Non-equilibrium dynamics of actively-driven viscoelastic networks

Federico S. Gnesotto

Munich 2020

© 2020 Federico S. Gnesotto

Non-equilibrium dynamics of actively-driven viscoelastic networks

Federico S. Gnesotto

A dissertation submitted

to the Faculty of Physics at the

Ludwig–Maximilians–Universität München

for the degree of

Doctor rerum naturalium

Munich, 3rd March 2020

First referee: Prof. Dr. Chase Broedersz
Second referee: Prof. Dr. Enzo Orlandini
Day of the oral examination: 16th April 2020

Zusammenfassung

Um ihre innere Organisation aufrechtzuerhalten, müssen lebende Systeme Energie auf molekularer Ebene dissipieren. Somit arbeiten sie weit entfernt vom thermodynamischen Gleichgewicht. Auf größeren Skalen kann sich Nichtgleichgewichtsverhalten in zirkulärer Bewegung im Phasenraum der mesoskopischen Koordinaten niederschlagen. Um diese Zirkulation zu erkennen und zu quantifizieren, wurden verschiedene Techniken und Methoden entwickelt. Es ist jedoch immer noch nicht klar, was diese Methoden über die physikalischen Eigenschaften des Systems aussagen und wie sie für nützliche Vorhersagen eingesetzt werden können. In dieser Arbeit werden wir zunächst die jüngsten Fortschritte bei der Erkennung und Quantifizierung mesoskopischer Ströme in Systemen aus weicher lebendender Materie untersuchen. Anschließend werden wir minimale Modelle aktiv getriebener viskoelastischer Netzwerke verwenden, um zu verstehen, wie die Nichtgleichgewichtsdynamik durch deren interne mechanische Struktur beeinflusst wird. Schließlich werden wir eine Methode zur Messung von Nichtgleichgewichtsfluktuationen aus Zeitraffermikroskopieaufnahmen, ohne tracking auskommt, einführen.

Die Arbeit ist in vier Kapitel unterteilt:

Kapitel 1 - Einführung
Hier ordnen wir unsere Arbeit innerhalb des allgemeinen Rahmens der “Physik aktiver Materie” ein. Dann stellen wir die biologischen Systeme vor, die unsere Arbeit motivieren, sowie die wichtigsten theoretischen Werkzeuge, die zum Verständnis der folgenden Kapitel erforderlich sind. Wir zeigen explizit, wie diese Werkzeuge für zwei gekoppelte aktive Teilchen (“two-beads model”) funktionieren, ein paradigmatisches Nichtgleichgewichtssystem, das in dieser Arbeit mehrfach auftaucht.

Kapitel 2
mit Federica Mura, Jannes Gladrow und Chase P. Broedersz.
Dieses Kapitel gibt einen Überblick über die jüngsten Fortschritte in der Erkennung und Quantifizierung von Nichtgleichgewichtsverhalten in weicher lebender Materie. Besonderes Augenmerk wird auf biologische Beispiele gelegt, die von Membranen und Gewebe, bis hin zu Zytoskelett-Netzwerken und Flagellen reichen.

Kapitel 3
mit Benedikt M. Remlein und Chase P. Broedersz.
Nach der Einführung in die Konzepte der Isostatizität, einem kritischen mechanischen Zustand mit einer divergierenden Längenskala, untersuchen wir in diesem Kapitel, wie die Nähe zum isostatischen Punkt die Nichtgleichgewichtsdynamik eines aktiv getriebenen viskoelastischen Netzwerks bestimmen kann. Wir zeigen, wie die Statistik der Kreisfrequenzen, eine neue Art der Quantifizierung von Zirkulation im Phasenraum, die ungeordnete, kritische Natur der zugrunde liegenden mechanischen Struktur widerspiegelt. Wir liefern eine Intuition für unsere Ergebnisse über ein mean-field Modell für das two-beads model. Kurz gesagt, verknüpft diese Arbeit das gut etablierte Gebiet der mechanischen Stabilität mit dem neueren Feld der statistischen Nichtgleichgewichtsmechanik.

Kapitel 4
mit Grzegorz Gradziuk, Pierre Ronceray und Chase P. Broedersz.
Im dritten Kapitel entwickeln wir eine neue Methode zur Ableitung von Nichtgleichgewichtseigenschaften eines Systems nur aus Beobachtungen mittels Zeitraffermikroskopie. Nach der Einführung eines neuen Werkzeugs zur Ableitung von Kraftfeldern aus stochastischen Trajektorien (Stochastic Force Inference), wenden wir diese Methode in Kombination mit einem prinzipienfesten Dimensionalitätsreduktionsansatz an. Damit können wir die Entropieproduktionsrate sowie die auf das System wirkenden deterministischen Kräfte ermitteln. Wir testen unsere Methode an einem two-beads model und an einem Netzwerk aktiver Fasern, das durch Strukturen im Zytoskelett inspiriert ist.

Summary

To maintain internal organization, living systems need to dissipate energy at the molecular level, thus operating far from thermodynamic equilibrium. At the larger scales, non-equilibrium behavior can be manifest through circulation in the phase space of mesoscopic coordinates and various techniques and measures have been developed to detect and quantify this circulation. It is however still not clear what these measures teach us about the physical properties of the system and how they can be employed to make useful predictions. In the following thesis, we will first review recent progress in detecting and quantifying mesoscopic currents in soft living systems; we will then employ minimal models of actively driven viscoelastic networks to understand how the non-equilibrium dynamics are affected by the internal mechanical structure. Finally, we will introduce a method of assessing non-equilibrium fluctuations in a tracking-free fashion via time-lapse microscopy imaging.

This work is divided into four chapters:

Chapter 1 - Introduction
Here, we first locate our work within the general setting of 'Active Matter Physics'. We then introduce the biological systems that constitute the motivation for our work, as well as the main theoretical tools needed to understand the following chapters. We explicitly show how these tools work on the 'two-beads model', a non equilibrium paradigm that recurs various times in this thesis.

Chapter 2
with Federica Mura, Jannes Gladrow, and Chase P. Broedersz.
This Chapter consists of a topical review of recent advances in the detection and quantification of non-equilibrium behavior in soft living matter. Particular emphasis is put on biological examples ranging from membranes, tissue, to cytoskeletal networks and flagella.

Chapter 3
with Benedikt M. Remlein, and Chase P. Broedersz.
After introducing the concepts of isostaticity, we study here how the vicinity to the isostatic point, a critical mechanical state with a diverging length scale, can determine the non-equilibrium dynamics of an actively-driven viscoelastic network. We show how the statistics of cycling frequencies, a novel way of quantifying phase space circulation, reflect the disordered, critical nature of the underlying mechanical structure. We provide intuition for our findings via a mean field two-beads model. Overall, this work connects the well-established field of mechanical stability to the novel field of non-equilibrium statistical mechanics.

Chapter 4
with Grzegorz Gradziuk, Pierre Ronceray, and Chase P. Broedersz.
In this Chapter, we develop a novel method of inferring non-equilibrium properties of a system by pure observation via time-lapse microscopy. After introducing a novel tool to infer force fields from stochastic trajectories (Stochastic Force Inference), we apply this method in combination with a principled dimensionality reduction approach, to reconstruct the entropy production rate and the deterministic forces acting on a system. We test our method on a two-beads model and an active fibrous network inspired by cytoskeletal assemblies.

Contents

1 Introduction

Nothing in life is to be feared, it is only to be understood.
Now is the time to understand more, so that we may fear less.
— Maria Skłodowska Curie

Life is possible due to constant dissipation at the molecular scale. In fact, metabolic activity avoids an otherwise inevitable decay of an organism towards equilibrium and death. In the words of Erwin Schrödinger: "What an organism feeds upon is negative entropy. Or, to put it less paradoxically, the essential thing in metabolism is that the organism succeeds in freeing itself from all the entropy it cannot help producing while alive" [1].

In recent years, an unprecedented effort to understand the mechanisms of life has given rise to a new field of study: Active Matter Physics [2–5]. In this field, physicists rethink standard approaches in soft condensed matter to account for the dissipative character of living entities. In contrast to standard non-equilibrium physics, where externally imposed fields maintain the system far from equilibrium, active matter is driven by dissipation of energy at the microscopic scale. For instance, in living structures such as the cytoskeleton or the membrane of a cell, the constant release of chemical potential energy by ATP hydrolysis guarantees that molecular motors are able to move and to generate forces on their surroundings [6–10]. Life mechanisms such as cell division [11], cell migration or muscle contraction [12–15] are the result of this constant interplay between enzymatic activity at the molecular scale and the viscoelastic structures that span the entire cell.

Although most of the individual pieces are there, we still have difficulties in reconstructing and understanding the puzzle of cellular life. In many cases we lack theoretical insights into how activity at the nanoscale emerges at the large scales, giving rise to order and patterns [16]. We are struggling to reliably measure non-equilibrium fluctuations at the cellular scale and, if we are able to measure them, it is not always clear what they can teach us about the underlying physical properties of the system [17–19].

This thesis addresses some aspects of these fundamental open questions by employing simple models of actively driven viscoelastic networks inspired by cytoskeletal systems. In these model networks, we systematically quantify and interpret the non-equilibrium dynamics at different lengthscales. Specifically, we aim to answer the following questions:

How does the internal viscoelastic structure of soft matter systems control their non-equilibrium properties?

Is it possible to directly detect and quantify forces and irreversibility in a living system only by observing its motion under a microscope?

As a preface to this thesis, we first introduce the biological systems that inspire our work and then briefly outline the main theoretical tools developed to study the non-equilibrium dynamics of these systems. In particular, we first touch upon the idea of measuring violations of the Fluctuation-Dissipation Theorem. We then continue by presenting some results of Stochastic Thermodynamics and the idea of Broken Detailed Balance. Finally, we conclude the Introduction by exemplifying these concepts and tools via an intuitive non-equilibrium paradigm, the two-beads model.

1.1 Cytoskeletal filaments

This introductory Section is a brief account of the properties of filaments that form the cell's cytoskeleton. The models presented in Chapter 3 and 4 are largely inspired by these structures.

Semiflexible polymers constitute the fundamental building blocks of the cell's scaffold, the cytoskeleton [20, 21]. In addition to giving the cell structure and rigidity, the cytoskeleton is fundamental for locomotion, intracellular transport ,and organization, as well as for cellular division [6, 22, 23]. As their name already indicates, semiflexible polymers are neither completely flexible and entropy-dominated as a random chain, nor totally stiff and only bending-dominated. Often, this defining property is expressed in term of a relevant length scale, the persistence length ℓ_p, that sets the scale at which thermal fluctuations balance bending stiffness. At room temperature, the persistence length of semiflexible polymers is of the same order of magnitude as their contour length, as noted in Fig. 1.1.

Although cytoskeletal filaments are usually separated into three main categories according to their characteristic thickness and function in the cell (Fig. 1.1), they all belong to the class of semiflexible polymers at the relevant cellular length scales. Microtubules are the stiffest among biopolymers: typically, the 13 polar protofilaments that compose a microtubule are arranged laterally in a helical fashion, forming a cylindrical structure of diameter $\approx$ 25 nm (Fig. 1.1a) [24]. Microtubules are polar filaments as a result of the head-to-tail arrangement of the α and β-tubulin dimers in a protofilament. Due to the polar nature of microtubules, processive, ATP-fueled motors such as kinesins and dyneins walk for large distances and transport cargo along these filaments. Other non-processive molecular motors (*e.g.* kinesin

14) can organize in groups that crosslink and exert forces on microtubules [25]. Although microtubules are crucial for the intracellular transport in the cell and for cell division, they do not play a fundamental role in determining the cell's viscoelastic behavior [20].

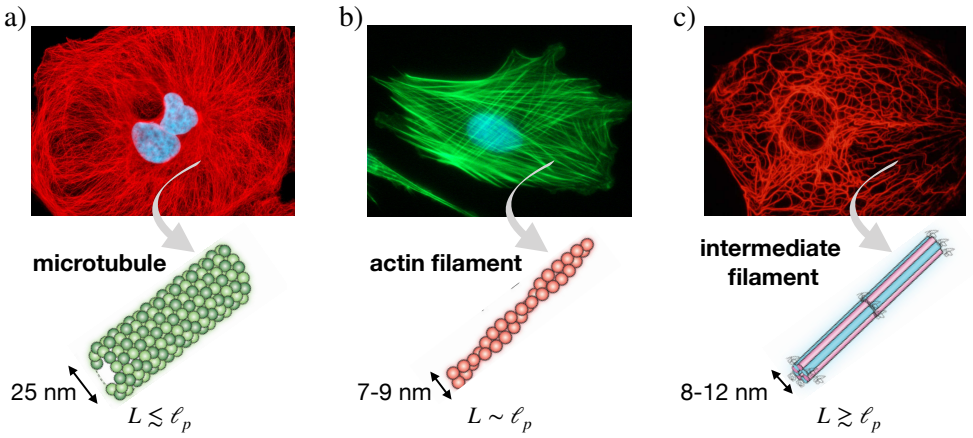

Figure 1.1 Top: Fluorescence microscopy images of a network of microtubules (a), the actin cytoskeleton (b) and an intermediate filaments network (c). Reproduced from MicroscopyU, microscopyu.com. Bottom: schematics of different kind of filaments with characteristic physical parameters. Reproduced from [26].

More relevant for our focus are intermediate filaments and microfilaments (Fig. 1.1 b-c), in particular F-actin [23]. An actin filament is composed of two parallel protofilaments of actin-monomers that twist around each other, forming a right handed double-helix of diameter between 7 and 9 nm (see Fig. 1.1b). Although if taken singularly an actin filament is much less rigid than a microtubule, actin can organize into stiff crosslinked networks and form bundles in the presence of crosslinking proteins such as fascin or α-actinin [6, 23, 27]. Another defining property of F-actin is that, similar to a microtubule, it is polar: this polar nature allows, for example, non-processive motors such as myosin II to bind with one head onto one actin filament and the other head onto a parallel actin filament with opposite polarity, thereby exerting opposite forces on the two filaments [28].

Cells rely on constant ATP consumption and thus energy dissipation to drive many of their internal processes. Thus, understanding the role of dissipation in shaping the efficiency of cellular processes, cellular response to external mechanical stimuli, as well as in cell migration, is of fundamental importance [17, 18, 29–31]. Although modern microscopy techniques have revealed that ATP-fueled motor proteins are the nano agents that drive cytoskeletal networks [32–34], it is not obvious how to detect and quantify the effects of their concerted activity at larger cellular scales, especially at steady-state conditions. Rather than because of deficient experimental techniques or noisy intracellular environment, it is in fact possible that the dynamics

of processes that break time reversal symmetry at the molecular level, appear instead to be time-reversible at the larger scales [19, 35–37]. This poses the question how one can reliably detect non-equilibrium at the larger mesoscopic scales in biological systems and distinguish active dissipative systems from passive equilibrium ones.

1.2 Probing the active dynamics: FDT violation

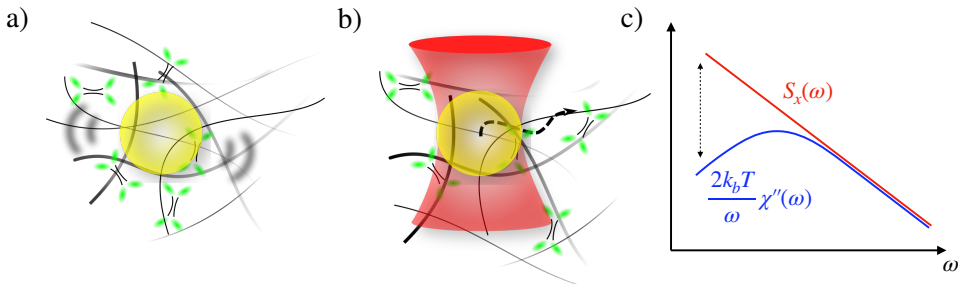

Figure 1.2 a) A bead fluctuating in a reconstituted biopolymer network with motors. The fluctuations of the bead's position are employed to measure the power spectrum $S_x(\omega)$. b) Forces can be exerted on an embedded bead via optical tweezers to measure the dissipative response $\chi''(\omega)$. c) Sketch of FDT violation: at low frequencies the power spectrum S_x deviates from the expected spectrum at equilibrium $\frac{2k_bT}{\omega}\chi''(\omega)$.

One of the first techniques to detect non-equilibrium features in biological systems hinges on measuring violations of the Fluctuation Dissipation Theorem, a fundamental result in equilibrium statistical mechanics. The Fluctuation Dissipation Theorem (FDT) in its simplest form is known as the Einstein-Smoluchowski [38, 39] relation for the diffusion coefficient of a Brownian particle:

$$D = \mu k_B T\,, \tag{1.1}$$

where k_B is Boltzmann's constant, T is the temperature of the fluid and μ the particle's mobility. The result Eq. (1.1) is derived on the hydrodynamic level by imposing balance of forces but can also be derived employing a Langevin description of Brownian motion at thermal equilibrium. In the latter case, Eq. (1.1) is usually known as the Stokes-Einstein relation: $\mu = 1/\gamma$ and the friction coefficient γ is given by the Stokes formula $\gamma = 6\pi\eta r$ with η being the fluid's viscosity and r the radius of the particle.

A generalization of Eq. (1.1), known as Fluctuation Dissipation Theorem, can be derived in the context of linear response theory [40]. The linear response of a particle's position $x(t)$ to a time-dependent force $f(t)$ switched on at $t = 0$ is defined by $\langle x(t)\rangle - \langle x(t)\rangle_0 = \int_0^t dt'\,\chi(t-t')f(t')$; $\langle x(t)\rangle_0$ denotes an ensemble average with

no force applied and $\chi(\omega)$ is the response function. The FDT relates the particle's fluctuations or power spectrum $S_x(\omega) = \int_{-\infty}^{\infty} \langle x(0)x(t)\rangle\, e^{i\omega t}$ to the dissipative part of the response $\chi''(\omega) = \mathrm{Im} \int_{-\infty}^{\infty} dt\, \chi(t) e^{i\omega t}$:

$$S_x(\omega) = \frac{2k_B T}{\omega} \chi''(\omega)\,. \tag{1.2}$$

To test whether the dynamics of cytoskeletal systems are out of thermodynamic equilibrium, microscopic beads embedded in reconstituted biopolymer assemblies [41], as well as in the cytoplasm of live cells [42], have been used to measure violations of the FDT as a result of motor activity. This has been possible by using a combination of two experimental techniques: Passive microrheology (PMR) and Active microrheology (AMR) [43–45]. While the former measures the fluctuations of the bead's position (*i.e.* the power spectrum $S_x(\omega)$, see Fig. 1.2a), the latter is able to measure the response function to a specific force (for example an oscillatory force) applied to the bead *e.g.* via optical tweezers, as shown in Fig. 1.2b.

Violations of the FDT have been reported in reconstituted cytoskeletal systems such as actin-myosin assemblies, as well as in live cells. Independent measurements of beads' power spectra in live cells reported $S_x(\omega) \sim 1/\omega^2$ at frequencies $\omega \lesssim 10$Hz [46, 47]. Importantly, this $1/\omega^2$ dependence of $S_x(\omega)$ is deceptively similar to the scaling of beads' power spectra measured in purely viscous systems at thermal equilibrium. However, the cytosplasm is not a viscous solvent, but a weak elastic medium [42]. Indeed it can be shown with a simple model of active forces in a viscoelastic medium, that at frequencies larger than the typical motor-frequency, but smaller than the system's characteristic frequency, such $\sim 1/\omega^2$ spectra arise naturally [48]. If only thermal forces are present, subdiffusive spectra are expected in a weakly elastic medium such as the cytoskeleton [19].

FDT violations can only be measured if *both* the fluctuations and the response function of the system are measured. Measuring response function requires *e.g.* dragging a silica bead through the medium and might thus not always be a feasible approach in fragile biological contexts. Furthermore, glassy rheological behavior has been measured in cellular environments too [49, 50] and violations of the FDT have been reported in glassy systems that are not microscopically driven [51].

Alternative methods of non-equilibrium probing have been developed in which only fluctuations of embedded probes or fluorescently labelled proteins are measured. These methods, however, rely on the comparison between spectra measured in unperturbed vs. perturbed conditions (for example via chemical perturbation such as myosin inhibition, ATP depletion or thermal perturbations) and are thus also intrinsically invasive. Ideally, one would like to devise protocols that enable probing of non-equilibrium properties and their links with biological functions, without interfering with the system's natural conditions. Before discussing these methods,

we give a brief account of the theoretical tools needed to measure irreversibility from single trajectories.

1.3 Stochastic Thermodynamics: measuring irreversibility from single trajectories

Entropy is the cost of structure.
— Ilya Prigogine

Stochastic Thermodynamics (ST) aims at scaling down the laws of thermodynamics to mesoscopic length scales. Concepts like heat, work, and entropy are defined on the trajectory level, thus offering a new way of interpreting and measuring thermodynamic quantities in stochastic physical systems. Importantly, ST does not rely either on linear-response assumptions or on close-to-equilibrium conditions, making it an ideal theory to study the behavior of strongly driven microscopic systems. The main assumption is that a separation of fast degrees of freedom (effect of a thermal bath) and slow observable degrees of freedom holds. We will here concentrate only on ST results that are relevant for our work and refer the reader to the excellent review [52] for an in-depth discussion of the vast field of ST.

The typical framework of ST is the overdamped Langevin equation for a Brownian particle:

$$\gamma \frac{dx}{dt} = F(x) + \xi(t), \tag{1.3}$$

where γ is the friction coefficient of the solvent, $F(x)$ is a generic force term comprising both internal conservative forces $-\partial_x V(x)$ and external forces $f(x)$ (conservative or not), while ξ is a Gaussian white noise term: $\langle \xi \rangle = 0$ and $\langle \xi(t)\xi(0) \rangle = 2\gamma^2 D\delta(t)$. At thermal equilibrium the Einstein relation implies $D = k_B T/\gamma$. Eq. (1.3) is valid in the limit in which inertial effect are negligible, *i.e.* if the time scales on which the position of the particle is considered are much longer than the momentum relaxation time: $\Delta t \gg m/\gamma$, with m being the mass of the particle.[1] This assumption is satisfied for all our applications and we will make extensive use of Eq. (1.3) throughout this thesis. Note that Eq. (1.3) is only valid in the case of space-independent diffusion coefficient (non-multiplicative noise): we will come back to this point in Chapter 4.

For single particles at the mesoscopic scales, traditional thermodynamic notions of heat and work are not applicable. These definitions are in fact only valid in the context of large numbers of particles where fluctuations are negligible. Instead, the Langevin Eq. (1.3) describes precisely how fluctuations shape the motion of

1 This of course implies in turn that the time resolution is much larger than the typical molecular times ($\mathcal{O}(10^{-12}s)$).

a Brownian particle: the concepts of heat and work must be thus readapted to this context. The generalisation of the first law of thermodynamics to a Brownian particle redefines heat at the mesoscopic scales and expresses conservation of energy by relating changes in the internal energy of a system to heat and work [52]:

$$du = \delta q + dw\,, \tag{1.4}$$

where $dw > 0$ is the infinitesimal work done on the particle, $\delta q > 0$ if heat is transferred from the environment to the particle, and du is the infinitesimal change of the internal energy of the particle. The change in internal energy of the particle is determined by its position in the potential landscape $du = \partial_x V(x) \circ dx$. Eq. (1.3) indicates that all external forces acting on the particle are $-\gamma \frac{dx}{dt} + \xi(t)$: the infinitesimal heat transferred to the particle can thus be defined as

$$\delta q = (-\gamma \frac{dx}{dt} + \xi(t)) \circ dx(t)\,, \tag{1.5}$$

where the $\circ$ indicates a Stratonovich product [52, 53]. Employing Eq. (1.3), we can express the heat change as $\delta q = -F \circ dx = \partial_x V \circ dx - f \circ dx$. Since the Stratonovich convention follows the usual rules of calculus, the first term is identified as the change in internal energy du, while the second term $-f \circ dx$ should be identified with the work done by the external force f (with a negative sign given our convention). For a trajectory of length τ the total heat and the total work can be obtained by integrating the respective infinitesimals along the trajectory:

$$q[x_\tau] = -\int_{x(0)}^{x(\tau)} F(x(t)) \circ dx(t)\,; \tag{1.6}$$

$$w[x_\tau] = -\int_{x(0)}^{x(\tau)} f(x(t)) \circ dx(t)\,. \tag{1.7}$$

The concept of heat is invevitably linked to dissipation and irreversibility. Scaling down the second law of thermodynamics to the Langevin level implies defining the concept of trajectory-dependent entropy [52]:

$$S[x(t)] = -k_B \ln p(x(t), t)\,. \tag{1.8}$$

The probability density $p(x(t), t)$ is the solution of the following one-dimensional Fokker-Planck (FP) equation for the Brownian particle

$$\partial_t p(x, t) = -\partial_x j(x, t) = -\partial_x(\mu F(x) - D\partial_x)p(x, t) \tag{1.9}$$

with $\mu = 1/\gamma$ being the particle's mobility. Importantly, averaging Eq. (1.8) over an ensemble of trajectories yields the Shannon entropy : $S(t) = \langle S[x(t)]\rangle$.

To analyze dissipation in the system, it is useful to consider the derivative w.r.t. time of the entropy defined by Eq. (1.8)[2]:

$$\dot{S}(t) = -\frac{1}{p(x(t),\,t)}\partial_t p(x(t),\,t) - \frac{1}{p(x(t),\,t)}\partial_x p(x,\,t)\Big|_{x=x(t)}\dot{x} \tag{1.10}$$

$$= -\frac{\partial_t p(x(t),\,t)}{p(x(t),\,t)} + D^{-1}\frac{j(x(t),\,t)}{p(x(t),\,t)}\dot{x} - \mu D^{-1}F(x(t))\dot{x} \tag{1.11}$$

where we have used the fact that $p(x,\,t)$ satisfies the FP Eq. (1.9). Recalling the definition Eq. (1.5) and the Einstein-Smoluchowski relation Eq. (1.1), the last term in Eq. (1.11) can be identified with the heat released into the medium per unit time or, equivalently, with the increase of the entropy of the medium per unit time:

$$\dot{S}_{\rm m} = \dot{q}/T = F(x(t))\dot{x}/T\,. \tag{1.12}$$

Thus, the total entropy production rate (EPR) $\dot{S}_{\rm tot}$ (sum of the system's own $\dot{S}$ and the medium's $\dot{S}_{\rm m}$ entropy production rates) is

$$\dot{S}_{\rm tot} = \dot{S} + \dot{S}_{\rm m} = -\frac{\partial_t p(x(t),\,t)}{p(x(t),\,t)} + \frac{D^{-1}j(x(t),\,t)}{p(x(t),\,t)}\dot{x}\,. \tag{1.13}$$

By first taking a conditional average on the positions and then integrating over all positions, we obtain the corresponding thermodynamic quantity (the first term of Eq. (1.13) vanishes upon averaging) [52]:

$$\left\langle \dot{S}_{\rm tot}\right\rangle = \left\langle \frac{D^{-1}j(x,\,t)}{p(x,\,t)}\dot{x}\right\rangle = \int dx \frac{j(x,\,t)D^{-1}j(x,\,t)}{p(x,\,t)} = \left\langle v(x,\,t)D^{-1}v(x,\,t)\right\rangle \geq 0\,, \tag{1.14}$$

where we have defined the phase space velocity field $v(x,\,t) = j(x,\,t)/p(x,\,t)$. Note that while $\dot{S}_{\rm tot}$ (Eq. (1.13)) can be negative, the total ensemble entropy production (Eq. (1.14)) is a semi-positive definite quantity that vanishes if and only if $j \equiv 0$ everywhere, *i.e.* at thermodynamic equilibrium. In a non-equilibrium steady state (NESS), the entropy production of the system is constant and the total entropy production is simply equal to the entropy production in the medium and can be written, in the limit $\tau \to \infty$, as a time average

$$\dot{S} = \lim_{\tau\to\infty}\frac{1}{\tau}\int_0^\tau \dot{S}_{\rm tot}dt\,. \tag{1.15}$$

2 $k_B = 1$ from now on.

In Chapter 4 we will compute the EPR by discretizing the time integral Eq. (1.15). Finally, we stress that when only partial information is available about the system (because of hidden/unobserved degrees of freedom), the partial entropy production is still a positive definite quantity that is a lower bound to the total entropy production rate. This property is crucial when dealing with multi-dimensional systems, as we will see in Chapter 4

The EPR as defined above can seem a difficult concept to grasp. However, informally speaking, the EPR quantifies how distinguishable a steady state trajectory is from its time-reversed counterpart and thus directly quantifies time-irreversibility in a physical system. The Kullback-Leibler divergence quantifies how distinguishable two distributions are, and, if computed for the distributions of the forward and backward trajectories, directly yields the EPR [54, 55]. Eq. (1.14) has also been employed to derive an energy-speed-accuracy relation for sensory adaptation in bacteria which has been tested in E. Coli [30]. Other results of ST, known as Fluctuation Theorems, such as the Jarzysnski equality and the Crooks theorem have been experimentally tested in single molecule experiments [56, 57]. Unfortunately, these approaches require invasive measurement protocols that might not be ideal when dealing with fragile biological structures. To explicitly avoid external manipulation when assessing the non-equilibrium character of biological systems, alternative approaches based on the concept of detailed balance have been developed.

1.4 Broken detailed balance and non-invasive measurements

Consider a stationary system described at thermal equilibrium by a general set of coordinates $\mathbf{y}$ that are *even* under time-reversal (*i.e.* positional coordinates); the detailed balance condition for the joint probability distribution reads [59]:

$$p(\mathbf{y}_2, t+\tau; \mathbf{y}_1, t) = p(\mathbf{y}_1, t+\tau; \mathbf{y}_2, t)\,, \tag{1.16}$$

where $\mathbf{y}_1$ and $\mathbf{y}_2$ are any pair of distinct phase space states. In words, Eq. (1.16) expresses the fact that, at thermal equilibrium, transitions between *any* pair of states of the system must be pairwise balanced (see Fig. 1.3a-b). If the system is also Markovian, detailed balance can be written as

$$p(\mathbf{y}_2, \tau|\mathbf{y}_1, 0)p(\mathbf{y}_1) = p(\mathbf{y}_1, \tau|\mathbf{y}_2, 0)p(\mathbf{y}_2)\,. \tag{1.17}$$

If the system is not only described by even variables under time reversal, but also by odd variables, the detailed balance condition (and the equivalent conditions on the FP equation) needs to be modified accordingly [59]. In this thesis we mostly deal

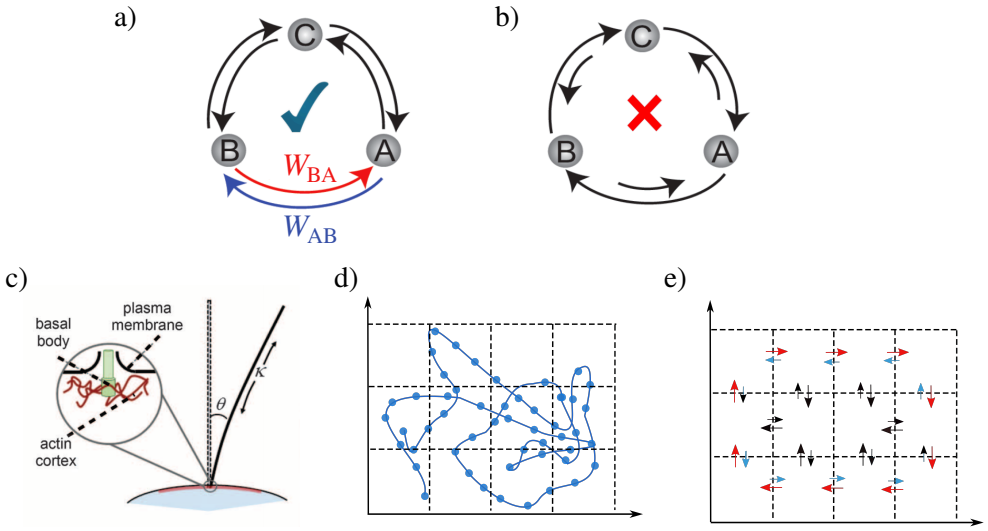

Figure 1.3 a) Detailed balance holds: transition rates are pairwise balanced. b) Broken detailed balance: the transition rates are not pairwise balanced. c) Schematic of a primary cilium with angle θ and curvature κ indicated. Reproduced from [58]. d) Continuous phase space trajectory (blue) and grid-discretization (dashed lines). e) Transition rates between each cell and its neighboring cells: with this coarse-grained desciption, when the rates are pairwise balanced (black arrows) there is no net current, while if the rates are unbalanced (red-blue arrows) a net current is revealed. Reproduced from [19].

with systems that obey overdamped Langevin dynamics (*i.e.* they are described by even variables under time reversal), hence Eq. (1.17) will suffice. Furthermore, most of the considered systems are Markovian and satisfy a FP equation (see for example Eq. (1.9)), implying that the detailed balance condition (in one dimension) is equivalent to [59]:

$$(\mu F(y) - D\partial_y)p(y) = j(y) = 0\,, \tag{1.18}$$

where j is the FP current. Importantly, the generalisation of Eq. (1.18) to a multi-dimensional system with a general state-dependent diffusion coefficient $D(y)$ has to be carried out carefully and necessitates the addition of a $\nabla \cdot D$ term on the right side of Eq. (1.3) in the Itô convention [60]. We will come back to this point in Chapter 4.

Live biological systems are typically multi-dimensional and subject to strong measurement-noise, making it challenging to distinguish a trajectory from its time reversed and thus to infer whether the system is out of thermodynamic equilibrium. Recently, a novel approach has been introduced that aims at detecting the presence of non-zero FP current or, more generally, at detecting broken detailed balance

with a non-invasive approach [58]. The dynamics of primary cilia of Madin-Darby Canine kidney cells (MDCK) have been analyzed in the phase space defined by two coordinates: the angle with respect to a chosen direction and the curvature (Fig. 1.3c). The phase space is discretized into a grid-like structure and transition probabilities between the grid cells are computed, as shown in Fig. 1.3d-e. These transition probabilities yield a discretized phase-space current which is found to be non-zero, thus providing evidence for the non-equilibrium character of primary cilia [58].

As a result of these experimental findings, various measures of phase space circulation have been proposed with the purpose of extracting relevant information about the underlying system without perturbing the system itself. A possible scalar quantity that serves this purpose is the average frequency with which a pair of observables circulates in phase space [19, 61–66] or the average area enclosed by these observables per unit time, the area enclosing rate [64, 67–70]. We will give next a brief analytical derivation of these quantities for a non-equilibrium paradigm, the two-beads model, and show how the cycling frequencies, the area enclosing rate, and the entropy production rate are closely related in a linear system. We will make extensive use of the two-beads model in Chapter 3 and Chapter 4.

1.5 A non-equilibrium paradigm: the two-beads model

The two-beads model (Fig. 1.4a) is a minimal model of a non-equilibrium system that displays phase space circulation. The overdamped Langevin equation for the displacement $\mathbf{x} = (x_1, x_2)$ of the beads from their rest position is [19, 63, 71, 72]

$$\dot{\mathbf{x}} = A\mathbf{x}(t) + \sqrt{2D}\boldsymbol{\xi}\,, \tag{1.19}$$

where the interaction matrix is $A_{ij} = (1 - 3\delta_{ij})k/\gamma$, the diffusion matrix is $D_{ij} = \delta_{ij}k_{\mathrm{B}}T_i/\gamma$ and $\boldsymbol{\xi}$ is a delta correlated Gaussian white noise.

The probability density function (pdf) for such a system obeys the FP equation

$$\partial_t p(\mathbf{x}, t) = -\nabla \cdot (A\mathbf{x}p(\mathbf{x}, t) - D\nabla p(\mathbf{x}, t)) = -\nabla \cdot \mathbf{j}(\mathbf{x}, t)\,. \tag{1.20}$$

In the long-time stationary limit the solution of the FP equation is independent of time and thus $\nabla \cdot \mathbf{j}(\mathbf{x}, t) = 0$. Given that the distribution of the noise is Gaussian and the interaction linear, the stationary solution of the FP equation will itself be a Gaussian pdf [73]:

$$p(\mathbf{x}) = \mathcal{N}(C)e^{-\mathbf{x}^T C^{-1}\mathbf{x}/2}\,, \tag{1.21}$$

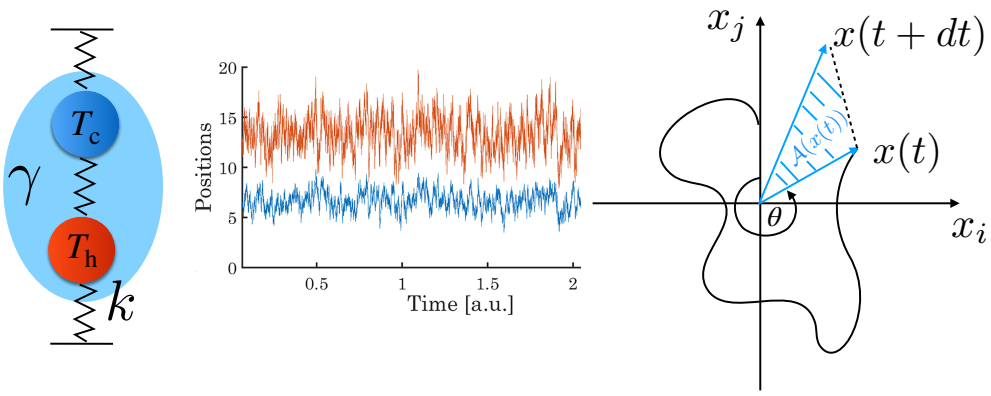

Figure 1.4 a) The two beads models: the cold bead (temperature T_c-blue) and the hot bead (temperature T_h-red) are coupled to one-another and anchored to two opposing walls by springs of constant k. The system is immersed in a fluid of friction coefficient γ. b) Sample trajectories of the hot bead (red) and cold bead (blue). c) Schematic showing the continuous phase space trajectory (black line) the area enclosed in one time step $\mathcal{A}(x(t))$ (shaded area) and the angle between the vertical axis and the phase-space position at time t.

where $\mathcal{N}$ is a normalization constant and C is the covariance matrix $C = \langle \mathbf{x}\mathbf{x}^T \rangle$. The latter is a solution of the following Lyapunov equation relating C, D and A [74]:

$$AC + CA^T = -2D\,. \tag{1.22}$$

The solution of the FP equation allows us to write the steady-state FP current as $j = A\mathbf{x}p(\mathbf{x}) - D\nabla p(\mathbf{x}) = (A + DC^{-1})\mathbf{x}p(\mathbf{x}) = \Omega\mathbf{x}p(\mathbf{x})$, where $\Omega\mathbf{x}$ is the velocity $v(\mathbf{x})$ with which probability is advected in phase space [61].

The circulating character of the FP current is manifest in covariance-identity-coordinates (cic) where $C = C^{-1} = \mathbb{1}$. In these coordinates in fact $\Omega_{\text{cic}} = (A_{\text{cic}} - A_{\text{cic}}^T)/2 = -\Omega_{\text{cic}}^T$. The eigenvalues of Ω_{cic} are either zero or purely imaginary $\lambda_{1,2} = \pm i\omega$, where ω is termed 'cycling frequency'. At the trajectory level, the time derivative of the angle-variable shown in Fig. 1.4c is

$$\dot{\theta}(t) = \frac{x_j(t)\dot{x}_i(t) - x_i(t)\dot{x}_j(t)}{x_i^2(t) + x_j^2(t)}\,. \tag{1.23}$$

By performing an ensemble average of Eq. (1.23) we can establish the equivalence $\langle\dot{\theta}\rangle \leftrightarrow \omega$ [52, 62, 66]. A direct calculation of ω for the two-beads model yields

$$\omega_{ij} = \frac{\sqrt{3}k(T_i - T_j)}{\gamma(T_i^2 + 14T_iT_j + T_j^2)} \tag{1.24}$$

which as expected vanishes at thermal equilibrium. In the limit of small temperature difference $T_i = T_j + \varepsilon$, with $\varepsilon \ll 1$, Eq. (1.24) reduces to:

$$\omega_{ij} = \frac{\sqrt{3}\varepsilon}{4T_j}, \tag{1.25}$$

which is then linear in the temperature difference ε.

Closely related to the Ω matrix is the average area enclosed by the trajectory in phase space per unit time, the area enclosing rate (AER) matrix $\mathcal{A}$ with elements:

$$\mathcal{A}_{ij} = \frac{1}{\tau}\int_0^\tau \frac{x_i dx_j - x_j dx_i}{2}. \tag{1.26}$$

Note that unlike Ω and the cycling frequency ω, the elements of $\mathcal{A}$ correspond exactly to the average area enclosed by the trajectory per unit time in the plane $\{i, j\}$. The relation between Ω and $\mathcal{A}$ is readily obtained by taking the average of Eq. (1.26):

$$\mathcal{A} = \frac{CA^T - AC}{2} = \Omega C, \tag{1.27}$$

where we have used the Lyapunov Eq. (1.22) in the last step. Taking the determinant on both sides of Eq. (1.27) allows us to relate the cycling frequency to the AER:

$$\mathcal{A}_{ij} = \omega_{ij}\sqrt{\det C}. \tag{1.28}$$

In Chapter 3 we will employ the cycling frequencies to quantify circulation between pairs of degrees of freedom in the system, while in Chapter 4 we will use the AER to find dissipative modes, *i.e.* special directions in phase space that account for maximal entropy production rate. Indeed for a linear system such as the two-beads model, there is a relation between the AER and the entropy production

rate $\dot{S}$ at steady state. Employing Eq. 1.13 and the relation $\mathbf{v}(\mathbf{x}) = \mathcal{A}C^{-1}\mathbf{x}$, we find

$$\dot{S} = \left\langle \mathbf{v}(\mathbf{x})^T D^{-1} \mathbf{v}(\mathbf{x}) \right\rangle \tag{1.29}$$

$$= \left\langle \mathrm{Tr}(\mathbf{x}^T C^{-1} \mathcal{A}^T D^{-1} \mathcal{A} C^{-1} \mathbf{x}) \right\rangle \tag{1.30}$$

$$= \mathrm{Tr}(\mathcal{A}^T D^{-1} \mathcal{A} C^{-1} \left\langle \mathbf{x}\mathbf{x}^T \right\rangle C^{-1}) \tag{1.31}$$

$$= \mathrm{Tr}(\mathcal{A} C^{-1} \mathcal{A}^T D^{-1}), \tag{1.32}$$

where in the second line we have used the fact the trace of a scalar is the scalar itself, in the third and last line we used the cyclic property of the trace and the fact that $\langle \mathrm{Tr}(\cdot) \rangle = \mathrm{Tr}(\langle \cdot \rangle)$. The EPR is invariant under coordinate changes, thus we can move to cic coordinates where $\dot{S} = \mathrm{Tr}(\mathcal{A}_{\mathrm{cic}} \mathcal{A}_{\mathrm{cic}}^T D^{-1}) = \mathcal{A}_{ij}^2 \mathrm{Tr}(D_{\mathrm{cic}}^{-1}) = \omega_{ij}^2 \mathrm{Tr}(D_{\mathrm{cic}}^{-1})$. This last expression establishes a direct link between EPR, AER and cycling frequencies.

The non-equilibrium tools introduced in this section will be largely employed throughout this thesis and can be readily generalized to higher dimensions.

1.6 Outline of this thesis

This thesis is outlined as follows:

Chapter 2

This chapter consists of a topical review on broken detailed balance and on non-equilibrium dynamics in living systems. We begin by illustrating different techniques to detect violations of the FDT, *e.g.* in reconstituted biopolymer networks and in live cells. We discuss some results of Stochastic Thermodynamics known as Fluctuation Theorems and uncertainty relations, together with some of their experimental validations. Next, we review in detail a novel way of inferring broken detailed balance that avoids invasive manipulation of the system by reconstructing coarse grained phase space currents directly from time-traces. Finally, we discuss extensions of this method to study actomyosin assemblies via the bending modes of semiflexible probe filaments embedded in the meshwork.

Chapter 3

Chapter 3 introduces a simple model of a marginal viscoelastic network driven out of equilibrium by molecular motors. Specifically, we model the elastic components of the system as Hookean springs and arrange them randomly between the nodes of a triangular network. At zero temperature and ss a function of the bond concentration, this network exhibits a critical phase transition from solid to floppy. We show with

simulations that when the network is locally driven out of equilibrium, the presence of a zero-temperature critical point affects the behavior of the cycling frequencies between pairs of network's node positions. We predict scaling exponents for the cycling frequencies near criticality and provide insight into this phenomenon with a simple mean field two-beads model. We conclude by showing that a divergent length scale present in the system also governs the scaling of the cycling frequencies with the distance between the nodes, thus providing a first step towards the understanding of the role of marginality in out of equilibrium systems.

Chapter 4

In the final chapter of this thesis we study actively driven viscoelastic networks directly via 'Brownian movies' of their dynamics. This tracking-free approach makes use of the intrinsic dissipative character of the system to infer a reduced set of relevant modes in the high-dimensional image phase space. Projecting the image dynamics on this set of modes allows us not only to reconstruct the partial entropy production of the system but also to infer the deterministic force field in image space. We benchmark our method onto the two-beads model and demonstrate its broader applicability onto a simulated viscoelastic network driven by a heterogeneous temperature distribution at the nodes and inspired by real biopolymer networks.

2 Non-equilibrium dynamics in living systems: topical review

Abstract of the chapter

This chapter reviews recent advances in theoretical and experimental approaches to the study of living systems. Examples range from beating flagella and cilia, to cellular membranes, reconstituted biopolymer networks, and live cells. We begin by reviewing methods that are based on violations of the fluctuation dissipation theorem (FDT), an equilibrium statistical mechanics result derived in linear response theory. We discuss rheological techniques that make the measurement of this violation possible in reconstituted assemblies such as acto-myosin, DNA gels and in live cellular environments such as the cellular cortex or the cytoplasm. We conclude this section by discussing assessments of FDT violations in the flickering motion of red blood cells and how measured fluctuation spectra of embedded probes can be intuitively understood with a minimal model of active force generation by molecular motors. In the following section we introduce the field of stochastic thermodynamics and present results known as 'fluctuation theorems' for the distribution, *e.g.*, of the entropy production along a stochastic trajectory. Such fluctuation theorems have been carefully verified using driven synthetic beads in controlled environment and have been successfully applied to the study of sensory adaptation and self-replication in bacteria, as well as to estimate the efficiency of single molecular motors. Interestingly, a universal bound relating current fluctuations and entropy production has also been established for generic systems in a non-equilibrium steady state (NESS). Systems in a NESS are the focus of the remaining of the review; in particular, we focus on a recently introduced method that aims at detecting non-equilibrium by inferring phase-space currents via a coarse-graining of phase space. The presence of currents implies breaking of detailed balance, a necessary and sufficient condition for equilibrium. This non-invasive method has been successfully employed to demonstrate the non-equilibrium character of the stochastic dynamics of isolated flagella and cilia. We conclude the review by discussing an analytically solvable 'toy model' for studying broken detailed balance and further analytical approaches to study the fluctuating motion of synthetic probe filaments in actively driven gels.

2.1 Publication

Broken detailed balance and non-equilibrium dynamics in living systems: a review

by

F. S. Gnesotto*[1], F. Mura*[1], J. Gladrow*[2], and C. P. Broedersz [1]

*equal contribution

[1]Department of Physics, Arnold Sommerfeld Center for Theoretical Physics and Center for NanoScience, Ludwig-Maximilians-Universität München, Theresienstraße 37, 80333 München, Germany,

[2]Cavendish Laboratory, University of Cambridge, Cambridge CB3 0HE, United Kingdom

reprinted on pages 21–52

with permission from

***Rep. Prog. Phys* 81, 066601 (2018)**,

DOI: 10.1088/1361-6633/aab3ed.

© 2018 IOP Publishing Ltd

IOP Publishing Reports on Progress in Physics
Rep. Prog. Phys. **81** (2018) 066601 (32pp) https://doi.org/10.1088/1361-6633/aab3ed

Review

Broken detailed balance and non-equilibrium dynamics in living systems: a review

F S Gnesotto[1,3], F Mura[1,3], J Gladrow[2,3] and C P Broedersz[1]

[1] Arnold-Sommerfeld-Center for Theoretical Physics and Center for NanoScience, Ludwig-Maximilians-Universität München, D-80333 München, Germany
[2] Cavendish Laboratory, University of Cambridge, Cambridge CB3 0HE, United Kingdom

E-mail: C.broedersz@lmu.de

Received 2 October 2017, revised 9 January 2018
Accepted for publication 5 March 2018
Published 18 April 2018

Corresponding Editor Professor Erwin Frey

Abstract

Living systems operate far from thermodynamic equilibrium. Enzymatic activity can induce broken detailed balance at the molecular scale. This molecular scale breaking of detailed balance is crucial to achieve biological functions such as high-fidelity transcription and translation, sensing, adaptation, biochemical patterning, and force generation. While biological systems such as motor enzymes violate detailed balance at the molecular scale, it remains unclear how non-equilibrium dynamics manifests at the mesoscale in systems that are driven through the collective activity of many motors. Indeed, in several cellular systems the presence of non-equilibrium dynamics is not always evident at large scales. For example, in the cytoskeleton or in chromosomes one can observe stationary stochastic processes that appear at first glance thermally driven. This raises the question how non-equilibrium fluctuations can be discerned from thermal noise. We discuss approaches that have recently been developed to address this question, including methods based on measuring the extent to which the system violates the fluctuation-dissipation theorem. We also review applications of this approach to reconstituted cytoskeletal networks, the cytoplasm of living cells, and cell membranes. Furthermore, we discuss a more recent approach to detect actively driven dynamics, which is based on inferring broken detailed balance. This constitutes a non-invasive method that uses time-lapse microscopy data, and can be applied to a broad range of systems in cells and tissue. We discuss the ideas underlying this method and its application to several examples including flagella, primary cilia, and cytoskeletal networks. Finally, we briefly discuss recent developments in stochastic thermodynamics and non-equilibrium statistical mechanics, which offer new perspectives to understand the physics of living systems.

Keywords: non-equilibrium, fluctuations, active living matter, fluctuation-dissipation theorem, detailed balance, cellular biophysics

(Some figures may appear in colour only in the online journal)

[3] These authors contributed equally.

 © 2018 IOP Publishing Ltd Printed in the UK

Contents

1. Introduction

Living organisms are inherently out of equilibrium. A constant consumption and dissipation of energy results in non-equilibrium activity, which lies at the heart of biological functionality: internal activity enables cells to accurately sense and adapt in noisy environments [1, 2], and it is crucial for high-fidelity DNA transcription and for replication [3, 4]. Non-equilibrium processes also enable subcellular systems to generate forces for internal transport, structural organization and directional motion [5–9]. Moreover, active dynamics can also guide spatial organization, for instance, through nonlinear reaction-diffusion patterning systems [10–12]. Thus, non-equilibrium dynamics is essential to maintain life in cells [13].

Physically, cells and tissue constitute a class of non-equilibrium many-body systems termed *active living matter*. Importantly, cellular systems are not driven out of equilibrium by external forces, as in conventional active condensed matter, but rather internally by enzymatic processes. While much progress has been made to understand active behavior in individual cases, the common physical principles underlying emergent active behavior in living systems remain unclear. In this review, we primarily focus on research efforts that combine recent developments in non-equilibrium statistical mechanics and stochastic thermodynamics [14–16] (see section 3) together with techniques for detecting and quantifying non-equilibrium behavior [17] (see sections 2 and 4). For phenomenological and hydrodynamic approaches to active matter, we refer the reader to several excellent reviews [18–21].

A characteristic feature of living systems is that they are driven out of equilibrium at the molecular scale. For instance, metabolic processes, such as the citric acid cycle in animals and the Calvin cycle for carbon fixation in plants, generally involve driven molecular reaction cycles. Such closed-loop fluxes break detailed balance, and are thus forbidden in thermodynamic equilibrium (figures 1(A) and (B) [23]. Similar directed chemical cycles also power reaction-diffusion patterning systems in cells [11] and molecular motors, including myosins or kinesins [24]. Indeed, such molecular motors can generate mechanical force by coupling the hydrolysis of adenosine triphosphate (ATP) to conformational changes in a mechano-chemical cycle [24, 25]. The dissipation of this chemical energy drives unidirectional transitions between molecular states in this cycle. Such unbalanced transitions break detailed balance and result in directional motion of an individual motor.

One of the central theoretical challenges in the field of active living matter is to understand how the non-equilibrium dynamics of individual molecular components act in concert to drive collective non-equilibrium behavior in large interacting systems, which in general is made of both active and passive constitutents. Motor activity may drive sub-components of cells and tissue [17, 26, 27], but it remains unclear to what extent this activity manifests in the dynamics at large scales. Interestingly, even for systems out of equilibrium, broken detailed balance, for instance, does not need to be apparent at the supramolecular scale. In fact, at large scales, specific driven systems may even effectively regain thermodynamic equilibrium and obey detailed balance [28, 29].

There are, of course, ample examples where the dynamics of a living system is manifestly out of equilibrium, such as cell division or cell migration. In many cellular systems, however, one can observe stationary stochastic processes that appear at first glance thermally driven. Indeed, for many macromolecular assemblies in cells such as chromosomes [30], the nucleus [31], the cytoplasm [32–34], membranes [35–39], primary cilia [22, 40], and tissue [41] it has been debated to what extent non-equilibrium processes dominate their dynamics. Such observations raise the fundamental and practical question how one can distinguish non-equilibrium dynamics from dynamics at thermal equilibrium. To address this question, a variety of methods and approaches have been developed to detect and quantify non-equilibrium in biological systems. When active and passive microrheology are combined, one can compare spontaneous fluctuations to linear response functions, which are related to each other

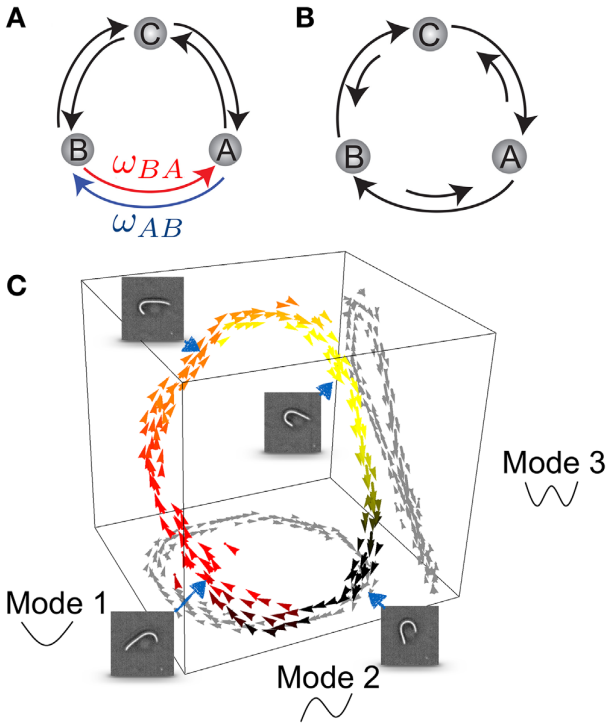

Figure 1. (A) In thermodynamic equilibrium, transitions between microscopic states are pairwise-balanced, precluding net flux among states. (B) Non-equilibrium steady states can break detailed balance and exhibit flux loops. (C) Snapshots of an isolated *Chlamydomonas* flagellum's beat cycle together with the 3D probability flux map of flagellar dynamics in a coarse grained phase space spanned by the first three modes. From [22]. Reprinted with permission from AAAS.

through the Fluctuation-Dissipation theorem (FDT) when the system is at thermal equilibrium [42–45]. Thus, the extent to which a system violates the FDT can provide insight into the non-equilibrium activity in a system. We will discuss this approach in detail in section 2. Other methods employ temperature or chemical perturbations to test the extent to which thermal or enzymatic activities primarily drive the behavior of a system, but such experiments are invasive and are often difficult to interpret. More recently, a non-invasive method to discriminate active and thermal fluctuations based on detecting broken detailed balance was proposed to study the dynamics of mesoscopic systems. This new approach has been demonstrated for isolated flagella (see figure 1(C)) and primary cilia on membranes of living cells [22]. The ideas underlying this method will be detailed in section 4 after briefly reviewing related work in stochastic thermodynamics in section 3.

Additional important insights on the collective effects of internal activity came from studies on a host of simple reconstituted biological systems. Prominent examples include a variety of filamentous actin assemblies, which are driven internally by myosin molecular motors. 2D actin-myosin assays have been employed to study emergent phenomena, such as self-organization and pattern formation [46, 47]. Moreover, actin-myosin gels have been used as model systems to study the influence of microscopic forces on macroscopic network properties in cellular components [43, 48–51]. Microrheology experiments in such reconstituted actin cytoskeletal networks have revealed that motor activity can drastically alter the rigidity of actin networks [52–54] and significantly enhance fluctuations [43, 55]. Importantly, effects of motor forces observed *in vitro*, have now also been recovered in their native context, the cytoplasm [34, 45, 55] and membranes [35, 36]. Further experimental and theoretical developments have employed fluorescent filaments as multiscale tracers, which offer a spectrum of simultaneously observable variables: their bending modes [56–58]. The stochastic dynamics of these bending modes can be exploited to study non-equilibrium behavior by looking for breaking of detailed balance or breaking of Onsager symmetry of the corresponding correlations functions [59, 60]. This approach will be discussed further in section 4.3.

2. Non-equilibrium activity in biological systems and the fluctuation-dissipation theorem

Over the last decades, a broad variety of microrheological methods have been developed to study the stochastic dynamics and mechanical response of soft systems. Examples of such systems include synthetic soft matter [61–65], reconstituted biological networks [26, 66–73], as well as cells, tissue, cilia and flagella [21, 22, 43, 71, 74–77]. In this section, we discuss how the combination of passive and active microrheology can be used to probe non-equilibrium activity in soft living matter. After briefly introducing the basic framework and the most commonly used microrheological techniques, we will discuss a selection of recent studies employing these approaches in conjunction with the fluctuation-dissipation theorem to quantify non-equilibrium dynamics.

2.1. The violation of the FDT as a non-equilibrium measure

Microscopic probes embedded in soft viscoelastic environments can not only be used to retrieve data about the spontaneous fluctuations of the surrounding medium, but can also be employed to measure the mechanical response of this medium to a weak external force. In the absence of an applied force, the average power spectrum $S_x(\omega) = \langle|\Delta x^2(\omega)|\rangle$ of fluctuations in the bead position $x(t)$ can be directly measured. The brackets here indicate an ensemble average. The same bead can, in principle, be used to extract the linear response function $\chi_x(\omega) = \langle\Delta x(\omega)\rangle/f(\omega)$ by measuring the average displacement induced by a small applied force $f(\omega)$. In systems at thermal equilibrium, these two quantities are related through the Fluctuation-Dissipation theorem (FDT), derived in the context of *linear response theory* [78, 79] (see figure 2). In frequency space, the FDT relates the autocorrelation function of position fluctuations of an embedded probe particle in the absence of external forces, to the imaginary part of the associated response function:

$$S_x(\omega) = \frac{2k_BT}{\omega}\chi_x''(\omega). \quad (1)$$

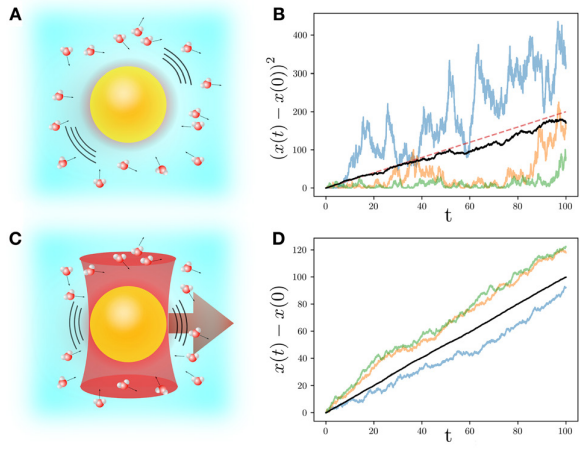

Figure 2. The fluctuation dissipation theorem implies a relation between thermal forces exerted by the molecules of the fluid on a Brownian bead and drag forces due to the viscosity of the fluid. (A) Cartoon of a freely diffusing Brownian particle. (B) Mean square displacement of the particle obtained by performing a Brownian simulation (black), and comparison with the analytical prediction $<(x(t)-x(0))^2>=2Dt$ (red). (C) Schematic of an external force f in the positive x direction applied on the particle via an optical tweezer. (D) The average displacement for the driven particle (black), obtained from Brownian dynamics simulation, increases linearly with time, as $<x(t)-x(0)>=\mu ft$, where μ is the mobility. In this simple cases, the FDT reduces to the Einstein relation: $D=\mu k_{\mathrm{B}}T$.

Importantly, a system that is actively driven into a non-equilibrium steady-state will typically not satisfy this equality; this fact can be used to our advantage to study activity in such a system. Indeed, the violation of the FDT has proven to be a useful method to assess the stochastic non-equilibrium nature of biological systems, for instance, by providing direct access to the active force spectrum in cells [45].

One of the first efforts to investigate deviations from the FDT in a biological system was performed on hair bundles present in the aural canal of a frog [80]. Hair bundles are thought to be primarily responsible for the capability of the ear to actively filter external inputs and emit sound [80, 81]. To trace the dynamics of the hair bundle, a flexible glass fiber was attached to the bundle's tip to measure both the position autocorrelation function and the associated response to periodic external stimuli. Interestingly, the magnitude of position fluctuations was observed to largely exceed the linear-reponse-based levels for a purely thermal system. This violation of the FDT indicates the presence of an internal energy source driving the system out of equilibrium.

A suggested measure of the degree of violation of the FDT is a frequency-dependent 'effective temperature' $T_{\mathrm{eff}}(\omega)$ [80, 82–86], defined as the ratio between fluctuations and dissipation: $T_{\mathrm{eff}}(\omega)\equiv\omega S_x(\omega)/2k_{\mathrm{B}}\chi_x''(\omega)$. For a system at thermal equilibrium $T_{\mathrm{eff}}=T$. However, this quantity can be drastically modified for an actively driven bundle: Close to its spontaneous oscillation frequency ω_0, the imaginary part of the response function of the hair bundle becomes negative. This implies that T_{eff} is frequency dependent and can also assume negative values.

Even though this example illustrates how the dimensionless quantity T_{eff}/T provides a simple metric for non-equilibrium, the concept of an effective temperature in this context remains a topic of debate [36, 37, 80, 87, 88]. Note, the existence of an effective temperature should not be mistaken for the existence of a physical mapping between an active system and an equilibrium system at a temperature T_{eff}. While there certainly are examples where such a mapping exists, this will not be the case in general. Furthermore, although it is not obvious how to interpret negative or frequency dependent effective temperatures, an interesting perspective is offered by Cugliandolo *et al* [82]. These authors demonstrated for a class of systems that the effective temperature can indicate the direction of heat flow and that this quantity can act as a criterion for thermalization [82]. In a more recent study, conditions were derived for systems in non-equilibrium steady states to be governed by a quasi-FDT: a relation similar to the equilibrium FDT, but with the temperature replaced by a constant $T_{\mathrm{eff}}>T$ [89]. These conditions entail that the intrinsic relaxation time of the system is much longer than the characteristic time scale of the active forces. However, these conditions may become more complicated in systems with a viscoelastic response governed by a spectrum of timescales for which the thermal force spectrum is colored [90]. Beyond being a simple way of measuring deviations from the FDT, the concept of an effective temperature may thus provide insight into active systems, but this certainly requires further investigation. Alternative measures for non-equilibrium have been the subject of more recent developments based on phase spaces currents and entropy productions rates, which are discussed in sections 3 and 4.

2.2. Active and passive microrheology

The successful application of the FDT in an active unidimensional context, as in the case of the hair bundle described above, paved the road for new approaches: microscopic probes were embedded into increasingly more complex biological environments to study the mechanics and to detect activity inside reconstituted cytoskeletal systems [26, 42, 43, 70] and living cells [42, 75, 91].

Probing violations of the FDT in such soft biological systems relies on high-precision microrheological approaches. Conventional single particle microrheology is divided into two categories: passive microrheology (PMR) [92] and active microrheology (AMR) [93–95]. PMR depends on the basic assumption that both the FDT and the generalized Stokes relationship apply. This assumption ensures that a measurement of the position fluctuation spectrum directly yields the rheological properties of the medium. Indeed, the generalized Stokes relation connects the force-response function to the viscoelastic response of the medium [92],

$$\chi_x(\omega)=\frac{1}{6\pi aG(\omega)}, \tag{2}$$

where a is the radius of the bead. This equation is valid in the limit of Stokes' assumptions, i.e. overdamped spherical

particle embedded in a homogeneous incompressible continuum medium with no slip boundary conditions at the particle's surface. Here, $G(\omega) = G'(\omega) + iG''(\omega)$ describes the complex shear modulus, where the the real part is the storage modulus G' describing the elastic component of the rheological response, and the imaginary part, G'', is the loss modulus accounting for the dissipative contribution. Under equilibrium conditions, the imaginary part of the response function χ_x'' is also related to the position power spectral density via the FDT (equation (1)). Thus, in PMR, the response function and the shear modulus are measured by monitoring the mean square displacement (MSD) $\langle \Delta x^2 \rangle(t) \equiv \langle (x(t) - \langle x \rangle)^2 \rangle$ of the embedded beads. By contrast, in AMR the mechanical response is directly assessed by applying an external force on an embedded probe particle, usually by means of optical traps or magnetic tweezers. Within the linear response regime, the response function can be measured as $\chi_x = \langle \Delta x(\omega) \rangle / f(\omega)$, and the complex shear modulus can then be determined from the generalized Stokes relation (equation (2)).

Although one-particle PMR has proven to be a useful tool to determine the equilibrium properties of homogeneous systems, biological environments are typically inhomogeneous. Such intrinsic inhomogeneity can strongly affect the local mechanical properties [96, 97], posing a challenge to determine the global mechanical properties using microrheology. To circumvent this issue, two-point particle microrheology is usually employed [42, 98]. This method is conceptually similar to one-point microrheology, but it is based on a generalized Stokes-Einstein relation for the cross-correlation of two particles at positions $\mathbf{r}_1$ and $\mathbf{r}_2$ with a corresponding power spectral density $S_{r_1,r_2}(R,\omega)$ with $R = |\mathbf{r}_2 - \mathbf{r}_1|$. This correlation function depends only on the distance between the two particles and on the macroscopic shear modulus of the medium. Thus, S_{r_1,r_2} is expected to be less sensitive to local inhomogeneities of the medium [98].

PMR has been extensively employed to assess the rheology of thermally driven soft materials in equilibrium, such as polymer networks [44, 62, 92, 99–104], membranes and biopolymer-membrane complexes [36, 105, 106], as well as foams and interfaces [107–109]. However, a PMR approach cannot be employed by itself to establish the mechanical properties of non-equilibrium systems, for which the FDT generally does not apply. If the rheological properties of the active system are known, the power spectrum of microscopic stochastic forces $\Delta(\omega)$—with both thermal and active contributions—can be extracted directly from PMR data for a single sphere of radius a [42, 44, 110]

$$\Delta(\omega) = 6\pi a\, S_x(\omega) |G(\omega)|^2 . \tag{3}$$

The expression for the power spectrum of force fluctuations was justified theoretically [42, 111], considering the medium as a continuous, incompressible, and viscoelastic continuum at large length scales. The results discussed above laid out the foundations for a variety of studies that employed microrheological approaches to investigate active dynamics in reconstituted cytoskeletal networks and live cells, which will be discussed next.

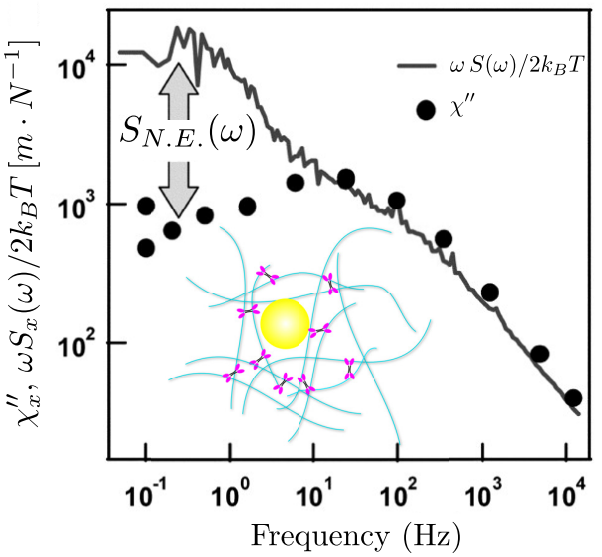

Figure 3. Violation of the FDT in reconstituted actin-myosin networks (inset). At frequencies below 10 Hz the response function estimated from spontaneous fluctuations of a probe bead via the FDT deviates significantly from the response χ'' measured directly using active microrheology (full circles). From [43]. Reprinted with permission from AAAS.

2.3. Activity in reconstituted gels

The cytoskeleton of a cell is a composite network of semiflexible polymers that include microtubules, intermediate filaments, F-actin, as well as associated proteins for cross-linking and force generation [6, 26, 112, 113]. The actin filament network is constantly deformed by collections of molecular motors such as Myosin II. These motors are able to convert ATP into directed mechanical motion and play a major role in the active dynamics of the cytoskeleton [8, 34, 43, 114, 115].

To develop a systematic and highly controlled platform for studying this complex environment, simplified cytoskeletal modules with a limited number of components were reconstituted *in vitro*, opening up a new field of study [26, 66, 116, 117]. Among these reconstituted systems, F-actin networks are perhaps the most thoroughly examined [20, 43, 68, 117–120]. Indeed, in the presence of motor activity, these networks display a host of intriguing non-equilibrium behaviors, including pattern formation [46–48, 121], active contractiliy and nonlinear elasticity [49, 52, 122–125], as well as motor-induced critical behavior [50, 53].

To study the steady state non-equilibrium dynamics of motor-activated gels, Mizuno *et al* constructed a three-component *in vitro* model of a cytoskeleton, including filamentous actin, an actin crosslinker, and Myosin II molecular motors [43]. The mechanical properties of the network were determined via AMR, while the activity-induced motion of an embedded particle was tracked via PMR. The measured imaginary component of the mechanical compliance, $\chi_x''(\omega)$, was compared to the response predicted via the FDT, i.e. $\omega S_x(\omega)/2k_BT$, as shown in figure 3. In the presence of myosin, the fluctuations in the low-frequency regime were

observed to be considerably larger than expected from the the measured response function and the FDT, indicating that myosin motors generate non-equilibrium stress fluctuations that rise well above thermally generated fluctuations at low frequencies.

These observations raise the question why motor-driven active fluctuations only dominate at low frequencies. This can be understood from a simple physical picture in which myosin motor filaments bind to the actin network and steadily build up a contractile force during a characteristic processivity time τ_p [126]. After this processivity time, the motor filament detaches from the actin polymers to which they are bound, producing a sudden drop in the force that is exerted locally on the network. Such dynamics generically generate a force spectrum $\Delta(\omega) \sim \omega^{-2}$ [111, 127], which can dominate over thermally driven fluctuations in an elastic network on time scales larger than the characteristic relaxation time of the network, but smaller than the processivity time of the motors (see section 2.6 for a more detailed discussion).

In addition to the appearance of non-equilibrium fluctuations, the presence of motors in the network led to a substantial ATP-dependent stiffening. It is well known that crosslinked semiflexible polymer networks stiffen under an external strain [67, 128–131]. Motors can effectively crosslink the network leading to stiffening, but they can also generate local contractile forces, and it is less clear how internal stress generation from such motor activity can induce large scale stresses and control network stiffness [54, 111, 123, 125, 132–136]. In a more recent experimental study, it was shown that motor generated stresses can induce a dramatic stiffening behavior of semiflexible networks [52]. This mechanism could be employed by cells and tissues to actively regulate their stiffness [132, 137–139].

An ensemble of beads dispersed in an active gel can not only be used to obtain fluctuation spectra, but also to infer the full probability distribution of the beads' displacements at a time-lag τ [88, 140, 141]. This distribution is typically observed to be Gaussian for a thermal systems, while non-Gaussian tails are often reported for an active system. In actin-myosin gels, for example, exponential tails in the particle position distributions are observed at timescales τ less than the processivity time of the motors. By contrast, at larger time lags, a Gaussian distributions is observed, in agreement with what was previously found for fluctuation spectra in frequency space [43]. Importantly however, non-Gaussianity is not a distinctive trait of non-equilibrium activity, since it can also appear in thermal systems with anharmonic potentials. In some cases, active systems are also governed by Gaussian distributions (see section 3.2).

The hallmarks of activity discussed above for actin-myosin gels are also observed in synthesized biomimetic motor-driven filament assemblies. For example, Betrand *et al* created a DNA-based gel composed of stiff DNA tubes with flexible DNA linkers [142]. As an active component, they injected FtsK50C, a bacterial motor protein that can exert forces on DNA. An important difference with the actin-based networks described above, is that here the motors do not directly exert forces on the DNA tubes, which constitute the filaments in the gel. Instead, the motors attach to long double-stranded DNA segments that were designed to act as cross-linkers between two stiff DNA tubes. Upon introduction of the motors, the MSD of tracer beads that were embedded in the gel was strongly reduced, even though the motors act as an additional source of fluctuations. This observation suggests a substantial stiffening of the gel upon motor activation. Furthermore, the power spectrum of bead fluctuations exhibited $\sim\omega^{-2}$ behavior, similar to results for *in vitro* actin-myosin systems and even for live cells, which we discuss next.

2.4. Activity in cells

The extensive variety of biological functions performed by living cells places daunting demands on their mechanical properties. The cellular cytoskeleton needs to be capable of resisting external stresses like an elastic system to maintain its structural integrity, while still permitting remodelling like a fluid-like system to enable internal transport as well as migration of the cell as a whole [113, 143]. The optimal mechanical response clearly depends on the context. An appealing idea is that the cell can use active forces and remodelling to dynamically adapt its (nonlinear) viscoelastic properties in response to internal and external cues [144–146]. In light of this, it is interesting to note that experiments on reconstituted networks suggest that activity and stresses can lead to responses varying from fluidization to actual stiffening [7, 52, 147]. Currently, however, it remains unclear how such a mechanical response plays a role in controlling the complex mechanical response of living cells [6, 143, 145, 148–151].

Important insights into the mechanical response of cells were provided by experiments conducted by Fabry *et al* via beads attached to focal adhesions near the cortex of human airway muscle cells. Their data indicate a rheological response where the loss and storage moduli are comparable, with a magnitude roughly in the range 100–1000 Pa around 1 Hz; also the moduli depend on frequency as a power law $|G(\omega)| \sim \omega^x$ with a small exponent $0.1 \leqslant x \leqslant 0.3$ [75], reminiscent of soft glassy rheology [84, 152–155].

The studies conducted by Lau *et al* [42] and Fabry *et al* [75] employed different probes at different cell sites for active and passive measurements, and determined a diffusive-like spectrum $\langle \Delta x^2 \rangle \sim \omega^{-2}$. A more recent assessment [74] was able to measure the cellular response and the fluctuation spectrum with the same probe and at the same cellular location. The rheological measurement of G was found to depend critically on the size of the engulfed magnetic beads and yielded a power law dependence on the applied torque-frequency $G(\omega) \sim \omega^{0.5-0.6}$. Furthermore, the conjuncted PMR and AMR assessments revealed a clear violation of the FDT, with the MSD of the beads increasing super diffusively with time. Measurements of the MSD of micron-size beads located around the nucleus of a living fibroblast also exhibited super-diffusive spectra, with a $\sim t^{3/2}$ dependence [156]. Upon depolymerization of the microtubule network, diffusive behavior was restored suggesting that the rectifying action of microtubule-related molecular motors might be responsible for the super diffusive behavior. Furthermore, when the motors were inhibited without perturbing the polymer

network, subdiffusive behavior was observed, in accordance to what is expected in equilibrium for a Brownian particle diffusing in a viscoelastic environment [110].

A systematic measurement of both active and passive cytoplasmic properties was carried out by Guo *et al* via submicron colloidal beads injected into the cytoplasm of live A7 Melanoma cells. The probe beads were conveniently employed to perform both PMR and AMR with the use of optical tweezers. The active microrheology experiments indicated a response with a shear modulus around 1 Pa, softer than measured near the cortex in [75], but with a similar power-law dependence of the complex shear modulus on frequency $|G(\omega)| \sim \omega^{0.15}$ [45]. Passive microrheology was employed to measure the mean square displacement (MSD) of position fluctuations in the cytoplasm under the same conditions (figure 4(A)). At short time-scales, the MSD is almost constant, as expected for a particle embedded in a simple elastic medium. By contrast, at long time scales, the system can relax, resulting in a MSD that increases linearly with time, as would be expected for simple diffusion-like behavior of a probe particle in a viscous liquid [91, 157].

Although these observations are deceptively close to the features of simple Brownian motion, this is clearly not the correct explanation for this phenomenon, given that the mechanical response of the system measured by AMR is predominantly elastic at these time scales. Furthermore, by treating cells with blebbistatin, an inhibitor of Myosin II, the magnitude of fluctuations notably decreased in the long time regime. While this suggests an important role for motor generated activity in driving the fluctuations of the probe particle, Myosin inhibition could also affect the mechanical properties of the cytoplasm, and thereby also the passive, thermally driven fluctuations of the probe particle. Nonetheless, by combining AMR and PMR it became clear that the system violates the FDT at these long time scales, implying that the system is not only out of equilibrium, but also that non-equilibrium activity can strongly alter the spectrum of force fluctuations.

The combination of AMR and PMR measurements was employed to infer the spectrum of force fluctuations using a method called force spectrum microscopy (FSM). This method makes use of the relation $\Delta(\omega) = |k(\omega)|^2 \langle \Delta x^2 \rangle(\omega)$, where the complex spring constant $k \equiv 1/\chi_x$ is related to G by $k = 6\pi G a$ (see equation (2)). The measured force spectrum exhibited two different power-law regimes: at high frequencies $\Delta(\omega) \sim \omega^{-0.85}$, while at low frequencies ($\omega \lesssim 10$ Hz), $\Delta(\omega) \propto \omega^{-2}$, in agreement with what is expected for typical molecular motor power spectra, as depicted in figure 4(B).

The observed high-frequency behavior is in accordance with predictions for particle fluctuations driven by thermal forces in a nearly elastic medium. In fact, if $G \sim \omega^{\beta}$, then $\langle \Delta x^2 \rangle(\omega) \sim \omega^{-(\beta+1)}$ at thermal equilibrium [42]. This implies that $\Delta(\omega) \sim \omega^{-0.85}$, with the measured $\beta = 0.15$. By contrast, an active model predicts $\langle \Delta x^2 \rangle(t) \sim t^{1+2\beta}$ if $\Delta(\omega) \sim \omega^{-2}$, which is consistent with what is observed in reconstituted motorized gels at timescales shorter than the processivity time τ_p [52, 55]. These experiments and others [34, 158] have thus established the active

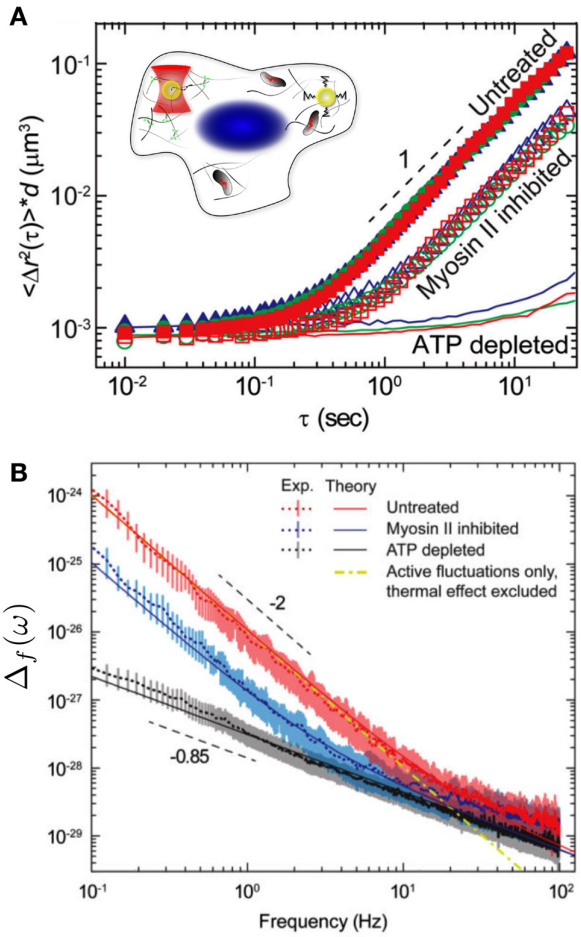

Figure 4. Fluctuations of probe particles inside living cells. (A) The MSD, $\langle \Delta x^2(\tau) \rangle$, of tracer beads rescaled by the particle diameter d, for untreated, Myosin inhibited, and ATP depleted cells. For untreated cells the MSD shows a plateau at short time scales, after which the MSD increases linearly with time. When Myosin is inhibited by blebbistatin, the power law does not change but the magnitude of the MSD is reduced. By depleting ATP in the cytoplasm, the dependence of the MSD on time becomes consistent with thermal motion in a viscoelastic environment at short times. A cartoon of AMR and PMR performed inside the cytoplasm is shown in the inset. (B) Measured force spectrum in the cytoplasm of untreated (red), blebbistatin treated (blue) and ATP-depleted (black) A7 cells. Adapted from [45], Copyright (2014), with permission from Elsevier.

nature and the characteristics of force spectra in the cytoplasm using embedded beads.

Various experiments employing PMR in live cells have been performed using alternative synthetic probes, such as nanotubes or embedded intracellular entities, including microtubules, vesicles, and fluorescently labeled chromosomal loci. In a recent study, Fakhri *et al* developed a new technology to investigate the stochastic dynamics of motor proteins along cytoskeletal tracks [34]. This cutting-edge method consists of imaging the near-infrared luminescence of single-walled carbon nanotubes (SWNT) targeted to kinesin-1 motors in live cells. Although traces of moving SWNT show long and relatively straight unidirectional runs, the dependence of the

tracers MSD on time exhibits several powerlaw regimes with an exponent that depends on the time range: At $t \approx 0.1$ s the exponent transitions from a value around 0.25 at short times to a value of 1 at larger times. By decomposing the MSD in motion along and perpendicular to the microtubule axis, it was shown that the dynamics of SWNT tracers originates from two distinct contributions: directed motion along the microtubules together with transverse non-directed fluctuations. The transverse fluctuations were attributed to bending fluctuations of the stiff microtubules, owing to motor-generated activity in the surrounding cytoskeleton, consistent with prior observations [158]. Indeed, the full time dependence of the MSD of traced kinesin motors could be described quantitatively with a model that assumes cytoskeletal stress fluctuations with long correlation times and sudden jumps. This is in agreement with a physical picture in which myosin mini-filaments locally contract the actin network during an attachment time set by the processivity time of the motors, followed by a sudden release.

Active bursts generated by Myosin-V are fundamental for nuclear positioning in mouse oocytes. In fact, active diffusion is here thought to create pressure gradients and directional forces strong enough to induce nuclear displacements [31, 159, 160]. As in the earlier studies discussed above, the FDT is sharply violated at low frequencies, while it is recovered at large ones [161].

To study the steady-state stochastic dynamics of chromosomes in bacteria, novel fluorescence-labelling techniques were employed on chromosomal loci in *E.Coli* cells. These experiments yielded sub-diffusive MSD behavior: $\langle \Delta x^2 \rangle(t) \sim t^{0.4}$ [30, 156, 162, 163]. Although purely thermal forces in a viscoelastic system, such as the cytoplasm or a nucleoid, can also generate sub-diffusive motion [164], Weber *et al* demonstrated a clear dependence of the MSD on ATP levels: When ATP was depleted from the cell, the MSD magnitude was reduced. Surprisingly however, the exponent, $\alpha = 0.4$, was not affected by varying ATP levels. Under the assumption that a change in the ATP level does not effect the dynamic shear modulus of the cytoplasm, this effect could be interpreted as resulting from active forces with a white noise spectrum and from a shear modulus that scales with frequency as $G \sim \omega^{0.7}$. While these results provide evidence for the existence of active diffusion by chromosomal loci, less invasive and more direct approaches are required to confirm and further study non-equilibrium behavior in the bacterial cytoplasm [165] and to understand the dynamics of the chromosome.

2.5. ATP-dependent elastic properties and membrane fluctuations in red blood cells

The elastic properties of cells play an important role in many biological systems. The unusually high deformability of red blood cells (RBCs) is a prominent example in this respect, lying at the heart of the cardiovascular system. RBCs have the astonishing capability to squeeze through micron-sized holes, which ensures seamless blood flow through tight capillaries. To explore how these astonishing properties emerge, a detailed understanding of passive and active behavior of the membrane enclosing RBCs and its connection to the underlying cytoskeleton is required.

The bending dynamics of membranes are largely determined by their curvature and their response to bending forces thus depends on their local geometry [166–169]. In flat membranes, the power spectral density of bending fluctuations is expected to scale as $\omega^{-5/3}$ for large ω [35, 169, 170]. A spectrum close to a $-5/3$-decay has indeed been reported in measurements of red blood cell membrane fluctuations [35]. Interestingly, the same experiments showed decreasing fluctuation amplitudes upon ATP-depletion, possibly indicating the role of non-equilibrium processes. The precise origin and nature of these processes, however, is difficult to determine due to the composite, ATP-dependent structure of erythrocyte membranes and cytoskeleton.

In addition, a flickering motion of RBC membranes observed in in microscopy experiments has sparked a discussion about the origin of these fluctuations. Indeed, the extent to which active processes determine the properties of RBCs is subject of intense research activity [35, 37, 171–177].

Although myosin is present in the cytoskeleton of human erythrocytes, mechano-chemical motors are not the only source of active forces in the cell. In the membrane of RBCs, actin forms triangular structures with another filamentous protein called spectrin. These structures are linked together by a protein known as 4.1R. Phosphorylation of 4.1R, an ATP-consuming process, causes the spectrin-actin complex to dissociate, which could lead to a softening of the cell. In accordance with this model, ATP-depletion was found to increase cell stiffness [38], and at the same time reduce membrane fluctuations on the $1-10$ s time scale. This is exemplified by the comparison between the green (ATP-depleted) and black (normal conditions) curves in figure 5(C).

In order to relate the magnitude of fluctuations to membrane stiffness κ and tension σ, Betz *et al* [35] employed a classical bending free-energy [178]

$$\mathcal{F}[h(r)] = \int \mathrm{d}^2 r \left[\frac{\kappa}{2} (\triangle h)^2 + \frac{\sigma}{2} (\nabla h)^2 \right]. \qquad (4)$$

A mode decomposition of the transverse displacement $h(\vec{q})$, evolving under thermal equilibrium dynamics of this energy functional leads to the correlator,

$$\langle h(\vec{q},t) h(\vec{q}\,',t') \rangle = \frac{(2\pi)^2 k_B T}{\kappa q^4 + \sigma q^2} \delta(\vec{q} + \vec{q}\,') \mathrm{e}^{-\frac{|t-t'|}{\tau_q}}, \qquad (5)$$

which is reminiscent of the correlator derived for semiflexible filaments (see section 4.3). The decorrelation time τ_q is given by $\tau_q = 4\eta q/(\kappa q^4 + \sigma q^2)$. A Fourier transformation of the correlator yields the theoretical prediction for the power spectral density shown in figure 5. This model was also generalized to consider membrane fluctuations in the presence of active forces [169, 174, 177].

The observed stiffening of the membrane upon ATP-depletion, presented a dilemma: membrane stiffening at low ATP could be the cause of the reduction of thermally driven membrane flickering, as apposed to a picture in which membrane flickering is primarily due to stochastic ATP-driven

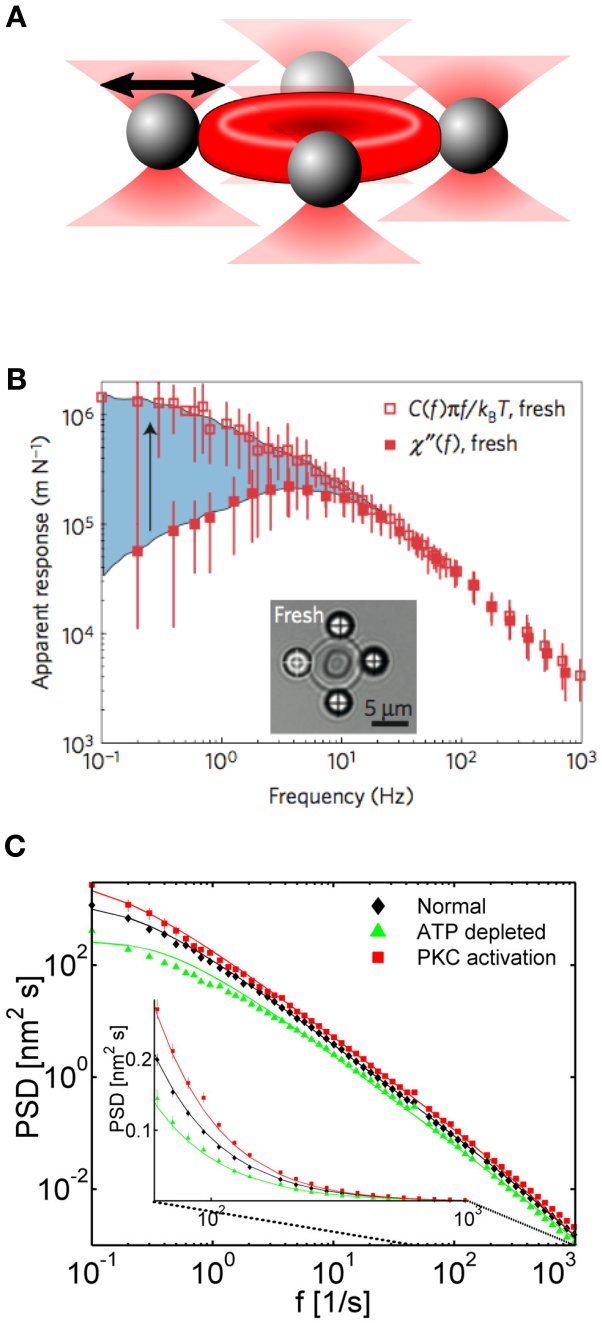

Figure 5. (A) Cartoon of a red blood cell whose membrane conformations and response are tracked via four attached microscopic beads. (B) The response and flickering spectrum of a red blood cell differ below 10 Hz, indicating a clear violation of the FDT. Adapted by permission from Macmillan Publishers Ltd: Nature Physics [36], Copyright (2016). (C) Power spectrum of RBC membrane fluctuations under normal conditions (black), after ATP-depletion (green) and after addition of a PKC (red). PKC stands for *protein kinase C*, which catalyzes the phosphorylation of 4.1R, leading to increased dissociation of actin-spectrin structures. Adapted from [35] with permission. Copyright © 2009 National Academy of Sciences.

processes. This conundrum was resolved in a subsequent study, in which RBC flickering motion was shown to violate the equilibrium FDT, providing strong evidence for an active origin of the flickering [36]. To demonstrate this, Turlier *et al* [36] attached four beads to live erythrocytes, three of them serving as a handle, while the remaining bead can either be driven by a force exerted by optical tweezers or the unforced bead motion can be observed to monitor spontaneous fluctuations. The complex response $\chi_x(\omega)$ is then obtained from the ratio of Fourier transformations of the position $x(\omega)$ and force $F(\omega)$. The equilibrium FDT in equation (1) relates these two quantities. The measured imaginary response $\chi_x''(\omega)$ is plotted together with the response calculated from equation (1) in figure 5(B). While the two curves exhibit stark differences at low frequencies, they become comparable for frequencies above 10 Hz. Thus, whatever the precise nature of active processes in erythocyte membranes is, the intrinsic timescales of these processes appear to be on the order of 1–10 Hz.

To explore the contributions to the mechanical properties of the membrane that arise specifically due to phosphorylation of 4.1R (and other molecules) in erythrocytes, the authors devised a semi-analytical non-equilibrium model for the elastic response of the membrane. Phosphorylation events are here modelled as on-off telegraph processes, which are added to an equilibrium description of membrane bending, such as in equation (4). The authors then decompose the membrane shape into spherical harmonic modes and calculate the single-mode power spectral density, which reads

$$S_x^{lm}(\omega) = \frac{2k_BT}{\omega}\chi_x^{lm}(\omega)'' + \frac{2\langle n_a\rangle(1-\langle n_a\rangle)\tau_a}{1+\omega\tau_a}\left|N^{lm}(\omega)\right|^2, \tag{6}$$

with $\tau_a = (k_a + k_i)^{-1}$ being the timescale, $n_a = k_a/(k_a + k_i)$ being the phosphorylation activity, and $N^{lm}(\omega)$ capturing the effects of tangential active noise on the membrane shape. The rate coefficients k_a and k_i characterize the simplified activate-inactivate (*a*-*i*) telegraph model, that the authors employ. The expression in equation (6) bears interesting similarities with the power spectrum of filament fluctuations (see section 4.3, equations (50) and (51)). The mode response here in equation (6) is also composed of independent thermal and non-equilibrium contributions. Interestingly, the model shows that the curvature of the membrane is crucial for it to sustain active flickering motions. Only a curved surface allows fluctuations of tangential stress to result in transversal motion. Modes that correspond to wavelengths too short to couple to tangential stresses also do not seem to be affected by non-equilibrium processes. The flickering therefore appears to be caused by a coupling of tangential stresses to transversal motion only within a certain window of spherical modes $2 \leqslant l \leqslant l^*$.

ATP-dependent fluctuations seem to contribute directly to the extraordinary mechanic properties of erythrocytes and may even help maintain their characteristic biconcave shape [175]. Recently, bending fluctuations of membranes have been implicated in general cell-to-cell adhesion [179]. The satisfactory agreement of theoretical and experimental fluctuation spectra in the examples discussed above highlights the merit of non-equilibrium statistical approaches to model and indeed explain properties of living biological matter.

In summary, the violation of the FDT is an elegant tool for the detection of activity in biological systems, as illustrated by the many examples discussed in the section above. That being said, for such a method to be applicable, the simultaneous

measurement of fluctuations *and* response is required. Even though this method gives information on the rheological properties of the system, its applicability can be challenging in contexts where the system is particularly delicate or poorly accessible such as chromosomes, the cytoskeleton, intracellular organelles, and membranes. Thus, in many cases a less invasive approach might be desired. These alternative approaches are further discussed in section 4.

2.6. Simple model for ω^{-2} active force spectra in biological systems

As illustrated by the examples discussed above, the mean square displacement of a probe particle in the cytoskeleton or in a reconstituted motor-activated gel has been widely observed to be surprisingly similar to a diffusive spectrum in a viscous medium: $\langle \Delta x^2 \rangle \sim t$. In a purely viscous environment, with only Brownian thermal forces, the force spectrum is well-described by white noise, which has a flat power spectrum over the whole frequency range by definition. The magnitude of the complex shear modulus for such a purely viscous fluid is $|G|^2 \sim \omega^2$. Such a simple rheological response, taken together with a white noise force spectrum, yields a displacement spectrum $\langle \Delta x^2 \rangle \sim \Delta/|G|^2 \sim \omega^{-2}$ *at all frequencies*. This mechanism, however, does not explain the effective diffusive behavior measured in cells below 10 Hz [7, 32, 34, 45, 88, 180]. Below, we illustrate with a simple model [111, 127, 180–182] that any active force with a sufficiently rapid decorrelation time can induce effective diffusive behavior of a bead in an elastic medium. The relevant range of time-scales is bound by the characteristic relaxation time of the network and by the processivity time of the motors.

Consider a particle moving in a simple viscoelastic solid with both active forces, f_A, and thermal forces, f_T. The stochastic motion of such a particle can be described by an overdamped Langevin equation [37, 42, 44, 65, 182–185]:

$$\gamma \dot{x}(t) = -kx(t) + f_T(t) + f_A(t)\,, \tag{7}$$

where k is the elastic stiffness and γ the friction coefficient of the gel, which is modelled as a Kelvin–Voigt medium [186]. For such a system, the thermal noise is described by:

$$\langle f_T(t) \rangle = 0\,,$$
$$\langle f_T(t') f_T(t) \rangle = 2\gamma k_B T \delta(t'-t).$$

By contrast, the independent active contribution, f_A, is modelled as a zero-average random telegraph process of amplitude f_0 [182, 187], whose autocorrelation function is

$$\langle f_A(t) f_A(s) \rangle = \frac{f_0^2}{4} e^{-|t-s|/\tau}.$$

The inverse time constant $\tau^{-1} = \tau_{on}^{-1} + \tau_{off}^{-1} \ll k/\gamma$ is the sum of the switching rates of the motors between *on* and *off* states.

Suppose we perform a PMR experiment in which we only have access to the power spectral density of the position, we would measure

$$S_x(\omega) = \frac{\langle f_T^2 \rangle + \langle f_A^2 \rangle}{k^2 + \gamma^2\omega^2} = \frac{2\gamma k_B T + \frac{f_0^2}{2}\frac{\tau}{(\omega\tau)^2+1}}{k^2+\gamma^2\omega^2}\,. \tag{8}$$

If we consider frequencies $\tau^{-1} \ll \omega \ll k/\gamma$ and assume that, in this frequency range, the magnitude of thermal fluctuations $2\gamma k_B T$ is negligible in comparison to the active force amplitude, the spectrum reduces to $S_x \approx f_0^2 \tau^{-1}/2(k\omega)^2$. In other words, to observe the characteristic ω^{-2} spectrum, the frequency needs to be higher than the operational frequency of the motors $1/\tau$, but smaller than the characteristic frequency of the medium k/γ. Note that the functional dependence on frequency in this limit is identical to the case of purely Brownian motion in a simple liquid. For frequencies $\omega \ll 1/\tau$, $S_x \sim$ const., consistent with experiments (see figure 6(A) of [45]). Thus, this simple model illustrates how active forces with a characteristic correlation time can account for the characteristic features of active particle motion in viscoelastic solids.

3. Entropy production and stochastic thermodynamics

3.1. Entropy production as a stochastic non-equilibrium measure

Put colloquially, entropy is about disorder and irreversibility: transitions that increase the entropy of the universe are associated with an exchange of heat and should not be expected to spontaneously occur in reverse. Historically, this picture was shaped by experiments on the macroscopic scale, where temperature and pressure are well-defined variables. However, on length scales ranging from nanometers to microns, where most cellular processes occur, fluctuations matter. Entropy, once thought to increase incessantly, here becomes a stochastic variable with fluctuations around its norm. These ideas sparked many new developments in stochastic thermodynamics [14–16].

In this section, we briefly introduce and motivate several recent theoretical and experimental advances of this stochastic approach, which has extended thermodynamics to the realm of small systems. In particular, we will discuss a class of results known as '*fluctuation theorems*' (FTs), together with a selection of general developments that highlight the applications of these results to living systems. In section 3.2 we discuss aspects of entropy production that are specific to linear multidimensional system, and in section 3.3, we review a recent study that demonstrates how these concepts can be used to understand noisy control systems in cells. Finally, in section 3.4, we discuss a recently introduced fundamental lower bound for fluctuations around the currents of probability, which are associated with out-of-equilibrium systems.

A key idea of stochastic thermodynamics is to extend the classical notion of ensembles and define ensemble averages of variables, such as heat, work, and entropy over specific stochastic time trajectories of the system [188]. These trajectories can be seen as realizations of a common generating process, associated with a particular thermodynamic state.

The distribution $P(\delta)$ of fluctuations δ is often of interest. Fluctuation theorems are usually applicable far from equilibrium and constrain the shape of this distribution. Most FTs derived so far adhere to the following form

$$\frac{P(\delta)}{P(-\delta)} = \mathrm{e}^{\delta}, \tag{9}$$

which is always fulfilled for Gaussian probability distributions $P(\delta) \propto e^{-1/2(\delta-\theta)^2/\sigma^2}$ with a mean θ that equals the variance $\theta = \sigma^2/2$. Other distributions may of course also fulfill this theorem. The fluctuation theorem governing the amount of entropy produced after a time Δt, $S(\Delta t) = \pm\omega$, $P(\omega)/P(-\omega) = \mathrm{e}^{\omega}$ has received particular attention. This result underlines the statistical nature of the second law of thermodynamics: a spontaneous decrease in the entropy of an isolated system is not prohibited, but becomes exponentially unlikely. However, since the entropy is an extensive quantity, negative fluctuations only become relevant when dealing with small systems, such as molecular machines.

The first fluctuation theorems were derived in a deterministic context [189], then extended to finite time transitions between two equilibrium states [190], and finally to microscopically reversible stochastic systems [191]. Later, mesoscopic stochastic approaches based on a Langevin descriptions were proposed. These descriptions turn out to be especially suitable in an experimental biological context were typically only mesoscopic degrees of freedom are tracked [192–195].

Further physical intuition for entropy production can be obtained in the description provided by Seifert [195]. Here, the 1D overdamped motion of a colloidal particle is treated as a model system. The particle moves in a medium at fixed temperature T and is subject to an external force $F(x, \lambda)$ at position x, which evolves according to a protocol λ. The entropy production associated with individual trajectories, $\Delta s_{\mathrm{tot}} = \Delta s_m + \Delta s$, is given by the sum of two distinct contributions: the change of entropy of the medium Δs_m and the change of entropy of the system Δs. The former is related to the amount of heat dissipated into the medium, $\dot{q} = F(x, \lambda)\dot{x}$, as $\Delta s_m = \int \mathrm{d}t'\, \dot{q}/T$. The entropy change of the system is obtained from a trajectory-dependent entropy:

$$s(t) = -k_{\mathrm{B}} \ln(P(x(t), t)). \tag{10}$$

where $P(x(t), t)$ is the probability of finding the particle at $x(t)$ at time t. Taking the average of $s(t)$ naturally leads to the Gibbs entropy, $S = -k_{\mathrm{B}}\langle \ln(P(x(t), t))\rangle$. Within this framework, the integral fluctuation theorem (IFT) for Δs_{tot} can be derived [195], which reads

$$\left\langle \mathrm{e}^{-\frac{\Delta s_{\mathrm{tot}}}{k_{\mathrm{B}}}} \right\rangle = 1. \tag{11}$$

The IFT expresses a universal property of entropy production, which is valid if the process can be captured by a Langevin or master equation description. Note, that in this context this theorem also implies the second law, since it implies $\langle \Delta s_{\mathrm{tot}} \rangle \geqslant 0$. In steady-state, a similar approach leads to the steady-state fluctuation theorem (SSFT)

$$P(-\Delta s_{\mathrm{tot}})/P(\Delta s_{\mathrm{tot}}) = \mathrm{e}^{-\frac{\Delta s_{\mathrm{tot}}}{k_{\mathrm{B}}}}, \tag{12}$$

which is a stronger relation from which equation (11) follows directly. In early studies [192, 196] this theorem was obtained only in the long time limit, but it has been now extended to shorter timescales [195]. To experimentally validate the fluctuation theorems discussed, Speck *et al* studied a silica bead maintained in a NESS by an optical tweezer. In this study, a single silica bead is driven along a circular path by an optical tweezer [197]. The forces felt by the bead fluctuate fast enough to result in an effective force f, which is constant along the entire circular path. The entropy production calculated directly from trajectories indeed adhered to the SSFT described above.

The development of fluctuation theorems has given a fresh boost to the field of stochastic thermodynamics and has led to a number of interesting studies. For example, several conditions for thermodynamic optimal paths have been established [198–200]. These optimal paths represent a protocol for an external control parameter that minimizes the mean work required to drive the system between two equilibrium states in a given amount of time. These results could provide insight into thermodynamic control of small biological systems. Recently, a fundamental trade-off between the amount of entropy produced and the degree of uncertainty in probability currents has been derived, which was considered in the context of sensory adaptation in bacteria. This trade-off is discussed in section 3.4.

Another important connection between energy dissipation and the spontaneous fluctuations of a system in a non-equilibrium steady-state was found by Harada and Sasa [201]. When a system is driven out of equilibrium, the fluctuation dissipation theorem (FDT) is violated (see section 2). A natural question to ask is what the violation of the FDT teaches us about the non-equilibrium state of a system. Starting from a Langevin description for a system of colloidal particles in a non-equilibrium steady state, a relation was derived between the energy dissipation rate and the extent of violation of the equilibrium FDT [201],

$$\langle \dot{W} \rangle = \sum_{i=0}^{N-1} \gamma_i \left\{ \bar{v}_i^2 + \int_{-\infty}^{+\infty} \left[\tilde{S}_{v,ii}(\omega) - 2T\tilde{\chi}'_{v,ii}(\omega) \right] \frac{\mathrm{d}\omega}{2\pi} \right\} \tag{13}$$

where $\langle \dot{W} \rangle$ is the average rate of energy dissipation and γ_i denotes the friction coefficient for the i_{th}-coordinate; $\tilde{S}_{v,ii}(\omega)$ and $\tilde{\chi}_{v,ii}(\omega)$ are the Fourier transform of the velocity correlation function and response function respectively. A remarkable feature of this relation is that it involves experimentally measurable quantities such as the correlation function and the response function, thereby allowing a direct estimate of the rate of energy dissipation. The violation of FDT has been measured, for instance, for molecular motors such as F_1 ATPase or Kinesin. Using the Harada–Sasa relation, it has been possible to infer information on the dissipated energy and efficiencies of such biological engines [202, 203].

Intuitively, any experimental estimate of the entropy production rate will be affected by the temporal and spatial resolution of the observation. In [204] a coarse-grained description of a system in terms of mesostates was considered. With this approach, it was shown how the entropy

production obtained from the mesoscopic dynamics, gives a lower bound on the total rate of entropy production. Interestingly, in systems characterized by a large separation of timescales [205] where only the slow variables are monitored, the hidden entropy production arising from the coupling between slow and fast degrees of freedom, can be recovered using equation (13). Another interesting notion in this context is the *partial entropy production*, which refers to the fraction of entropy production that can be recovered from a partial observation of the system, i.e. when only a subset of degrees of freedom is accessible. This concept is illustrated and discussed in [206, 207], and a partitioning of the entropy production related to the observed and hidden variables with relative FTs is derived in [208].

The entropy production rate appears to be a good way of quantifying the breakdown of time reversal symmetry and energy dissipation. However, it is still unclear how this quantity is affected by the timescales that characterize the system. To address this, a system of active Ornstein–Uhlenbeck particles was considered [87]. This system can be driven out of equilibrium by requiring the self-propulsion velocity of each particle to be a persistent Gaussian stochastic variable with decorrelation time τ, thereby providing a simple, yet rich theoretical framework to study non-equilibrium processes. Interestingly, to linear order in τ, an effective equilibrium regime can be recovered: This regime is characterized by an effective Boltzmann distribution and a generalized FDT, even though the system is still being driven out of equilibrium. Indeed, the leading order contribution of the entropy production rate only sets in at $\sim \tau^2$.

In complex systems, we may sometimes face limited information about local or global thermodynamic forces. In such situations, the direction in which processes evolve, that is, the direction of time itself may in principle become unclear. Due to micro-reversibility, individual backward and forward trajectories are indistinguishable in equilibrium. Thus, it is natural to ask‘ how much information is needed to tell if a given trajectory runs forward or backward in time?

This question was studied by Roldan *et al* [209] using decision-theory, a natural bridge between thermodynamic and information-theoretic perspectives. Entropy production is here defined as $\Delta s_{\rm tot}(t) = k_{\rm B}\ln(P(X_t)/P(\tilde{X}_t))$ with X_t and $\tilde{X}_t$ denoting a forward trajectory and its time-reversed counterpart . The unitless entropy production, $\Delta s(t)/k_{\rm B}$ assumes the role of a log-likelihood ratio $\mathcal{L}(t)$ of the probability associated with the forward-hypothesis $P(X_t|H_{\rightarrow})$ and the backward-hypothesis $P(X_t|H_{\leftarrow})$, that is, $\mathcal{L}(t) = \ln P(X_t|H_{\rightarrow})/P(X_t|H_{\leftarrow})$. In a sequential-probability ratio test, $\mathcal{L}(t)$ is required to exceed a pre-defined threshold L_1 or subceed a lower threshold L_0, to decide which of the respective hypotheses H_1, H_0 is to be rejected. The log-likelihood ratio $\mathcal{L}(t)$ evolves over time as more and more information is gathered from the trajectory under scrutiny.

Interestingly, for decision-thresholds placed symmetrically around the origin $L_0 = -L$, $L_1 = L$, the observation time $\tau_{\rm dec}$ required for $\mathcal{L}(t)$ to pass either threshold turns out to be distributed independently of the sign of L, i.e.

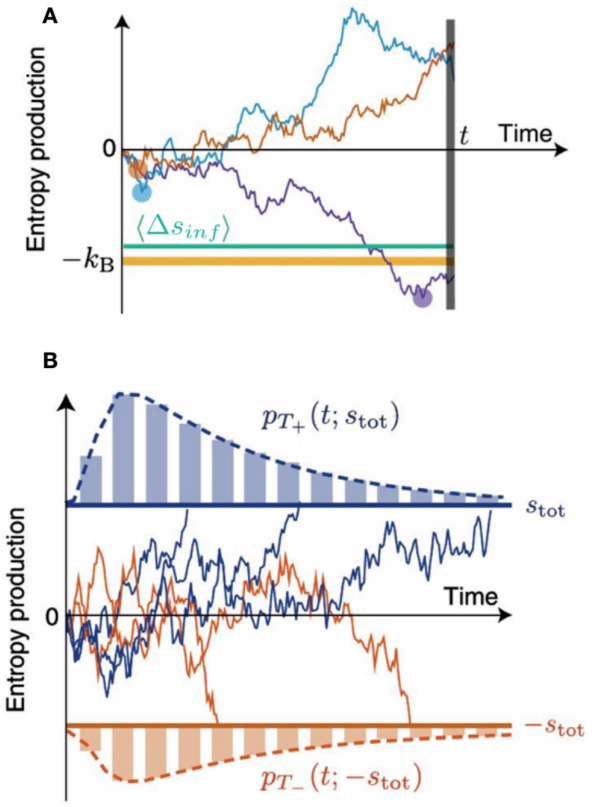

Figure 6. Entropy as a stochastic variable: illustration of the mean infimum inequality and the equivalence of entropy production stopping times. (A) The average of the minimum of an ensemble of entropy-trajectories (purple, red and blue) $\langle \Delta s_{\rm inf}(t) \rangle$ (cyan) is bound from below by $k_{\rm B}$ (thick yellow). (B) For entropy-bounds $\pm s_{\rm tot}$ that are symmetrically placed around 0 (thick red and blue), the stopping times T_+ and T_- share the same probability distribution (the figure shows unnormalized histograms). The stopping time T_+ (T_-) here is defined as the first-passage time of the entropy past the upper (lower) bound. Reproduced from [210]. CC BY 3.0.

$$P(\tau_{\rm dec}|\leftarrow) = P(\tau_{\rm dec}|\rightarrow). \tag{14}$$

From a thermodynamics perspective, this insight, implies that the average time it takes for a given process to produce a certain amount of entropy, must equal the average time it takes the same process to *consume* this amount of entropy. A process that consumes entropy takes up heat from the environment. This can only occur rarely, of course, so that the the second law is not violated.

In a related recent study, Neri *et al* [210] discuss the properties of ‘*stopping times*’ of entropy production processes using a rigorous mathematical approach. The stopping time here is defined as the time a process on average takes to produce or consume a certain amount of entropy relative to time t_0. This stopping time equivalence is sketched in figure 6(B). Importantly, stopping times are first passage times conditioned on the process actually reaching the threshold. The distribution of stopping times, therefore does not say anything about how probable it is for an observer to witness the process of reaching the threshold at all. Only *if* a trajectory reaches the

threshold, the conditional first passage time can be measured. Figure 6(A) depicts another property of the entropy $\Delta s(t)$: the average entropy is bounded from below by k_B.

These ideas were further illustrated by a few examples. The time a discrete molecular stepper, similar to the one illustrated in figure 9, would spend making N steps forward in a row, on average, is the same as it would spend making N steps backwards. This results from the way the entropy production for this system scales with the position, $\Delta s_{tot}(t) = -N(t)Fl/(k_BT)$, where F is the driving force and l denotes the step length. Related first-passage-time equivalences have been discussed in the context of transport [211], enzymes [212], molecular motors [213], and drift-diffusion processes [214]. Entropy stopping times, however, provide a unifying and fruitful perspective on first passage times of thermodynamic processes. Finally, we note that the properties of stochastic entropy production discussed above can also be derived from an Itô equation of the entropy that was recently derived [215].

Living systems form one of the most intriguing candidates to apply key concepts of stochastic thermodynamic. Several fluctuation relations have been experimentally verified for various biological processes[15, 216–222] and a stochastic thermodynamic description for chemical reaction networks have been developed [223] and applied, for instance, in catalytic enzymatic cycles [216]. A multitude of thermodynamic equalities and lower bound inequalities involving the entropy production have been used to investigate the efficiency of biological systems. This provides insight into the energy dissipation required for a system to perform its biological function at some degree of accuracy. Important contributions in this direction can be found, for instance, in [224] where the efficiency of molecular motors in transforming ATP-derived chemical energy into mechanical work is discussed. Following this line, we could ask how precise cells can sense their environment and use this information for their internal regulation. This was addressed in several works [1, 2, 225], highlighting a close connection between the amount of entropy produced by the cellular reaction network responsible for performing the 'measurement', and the accuracy of the final measured information (see section 3.3). In [226, 227] these concepts were further expanded and applied to more complex macroscopic systems, such as the self-replication of bacteria, whose description is not captured by a simple system of chemical reaction networks. Despite the system's complexity, insightful results were obtained by deriving the more general inequality:

$$\Delta S_m + \Delta S \geqslant -\ln \frac{\pi(II \to I)}{\pi(I \to II)}. \tag{15}$$

Here, the system's irreversibility, i.e the ratio of the probability of transition between two macrostates $\pi(II \to I)$ and the transition probability of the reversed process, represents a lower bound for the total entropy production: $\Delta S_m + \Delta S$, where ΔS is the internal entropy difference between the two macrostates and ΔS_m is the change of entropy of the bath. One can now identify the two macrostates I and II with an environment containing one and two bacterial cells respectively. Using probabilistic arguments it is then possible to express the probability ratio in equation (15) as a function of measurable parameters, which characterize the system's dynamics. With this approach, one can make a quantitative comparison between the actual heat produced by *E.coli* bacteria during a self-replication event and the physical lower bound imposed by thermodynamics constraints. These results may also have implications for the adaptation of internally driven systems, which are discussed in [227, 228].

3.2. Coordinate invariance in multivariate stochastic systems

Energy dissipation, variability, unpredictability are traits not exclusively found in biological systems. In fact, it was a meterologist, Edward Lorenz, who coined the term 'butterfly effect' to describe an unusually high sensitivity on initial conditions in what are now known as 'chaotic systems' [229]. In a fresh attempt to explain their large variability, stochastic models have been applied to periodically recurring meteorological systems. El-Niño, for example, is characterized by a slow oscillation of the sea surface temperature, which can cause violent weather patterns when the temperature is close to its maximum. Such a change in temperature can lead to new steady-states, in which the system is permanently driven out-of equilibrium under constant dissipation of energy and exhibits a rich diversity of weather 'states'. Out of equilibrium, transitions between states are still random, but certain transitions clearly unfold in a preferred temporal sequence.

Interestingly, in an effort to model meteorological systems stochastically, Weiss uncovered a direct link between energy dissipation and variability, which is intimately related to broken detailed balance [230]. More specifically, he found that out-of equilibrium systems can react more violently to perturbations than their more well-behaved equilibrium counterparts. This finding may be relevant in a much broader context, including biology, and we will therefore briefly summarize the main points here. Specifically, we will briefly explore this phenomenon of *noise amplification* from a perspective of coordinate-invariant properties [230].

In an open thermodynamic system in equilibrium, all state variables $\vec{x}$, are subject to the dialectic interplay of random forcing (noise) $\vec{\xi}$, relaxation, and dissipation. Consider an overdamped two-bead toy system at equilibrium, for example (see figure 12(A) and section 4.2.3), where the two beads are coupled by springs and are placed in contact with independent heat baths. Energy stored in the springs is permanently released and refuelled by the thermal bath, and flows back and forth between the two colloids in a balanced way. A sustained difference in temperature between the beads, $T_1 \neq T_2$, however, will permanently rectify the flow of energy and break this balance. Crucially, this temperature difference is a matter of perspective. If we set, for example, $T_1 = 0$, then bead 1 will not receive any noise any more and energy will flow to it from bead number 2. Interestingly, if we look at the normal coordinates of the beads $u_1(t) = (x_1(t) - x_2(t))/2$ and $u_2(t) = (x_1(t) + x_2(t))/2$, we find that their respective thermal noise has exactly the same temperature $T_2/2$. However,

if we could measure the fluctuations of noise in these coordinates, we would find that both noise terms correlate. Thus, in this case, mode 1 and 2 are driven not only by the same temperature, but by the very same white noise process.

Correlations amongst noise processes $\xi_1(t)$ and $\xi_2(t)$ exciting different variables $x_1(t)$ and $x_2(t)$ can, in principle, break detailed balance, even if the overall variance of the noise is equal in all directions, i.e. $\langle \xi_1^2 \rangle = \langle \xi_2^2 \rangle$. In other words, correlations in random forces in one coordinate system, result in differences in temperature in other coordinates and vice-versa. The simple temperature criterion $T_1 = T_2$ is thus insufficient to rule out broken detailed balance (see section 4.1); a comprehensive coordinate-invariant criterion is required.

Consider variables $\vec{x}(t)$ of a generic system, evolving stochastically according to a Langevin equation (16),

$$\frac{\mathrm{d}\vec{x}}{\mathrm{d}t}(t) = \mathbf{A}\vec{x}(t) + \mathbf{F}\vec{\xi}(t) \tag{16}$$

while the dynamics of the associated probability density $\rho(\vec{x}, t)$ is given by the corresponding Fokker-Planck equation (17).

$$\frac{\partial \rho}{\partial t}(\vec{x}, t) = -\nabla \cdot \left(\mathbf{A}\vec{x}\rho(\vec{x}, t) - \mathbf{D}\nabla\rho(\vec{x}, t)\right). \tag{17}$$

In the equations above, $\mathbf{F}$ denotes the forcing matrix, in which any noise variance is absorbed, such that $\vec{\xi}$ here has unit variance $\langle \vec{\xi}(t)\vec{\xi}^T(t') \rangle = \mathbf{1}\delta(t - t')$. The forcing matrix is directly related to the diffusion matrix $\mathbf{D} = \frac{1}{2}\mathbf{F}^T\mathbf{F}$, and the term $\mathbf{A}\vec{x}$ describes deterministic forces, and the matrix $\mathbf{A}$ therefore contains all relaxational timescales. Any linear system with additive, state-independent white noise $\vec{\xi}$ can be mapped onto these generic equations.

In an equilibrium system with independent noise processes, $\mathbf{D}$ is diagonal and fulfills the standard fluctuation-dissipation theorem $\mathbf{D} = k_\mathrm{B}T\mathbf{M}$, where $\mathbf{M}$ denotes the mobility matrix. In steady-state, the correlation matrix $\mathbf{C} = \langle \vec{x} \cdot \vec{x}^T \rangle$ both in and out of equilibrium, obeys the Lyanpunov equation $\mathbf{AC} + \mathbf{CA}^T = -2\mathbf{D}$, which can be thought of as a multidimensional FDT. The density ρ can therefore always be written as a multivariate Gaussian distribution $\rho(\vec{x}, t) = 1/\sqrt{|\mathbf{C}|}e^{-\frac{1}{2}\vec{x}^T\mathbf{C}^{-1}\vec{x}}$.

Apart from systems with temperature gradients, detailed balance is also broken in systems with non-conservative forces $\mathbf{A}\vec{x}$, which have a non-zero rotation $\partial_i (\mathbf{A}\vec{x})_j \neq \partial_j (\mathbf{A}\vec{x})_i$. Within our matrix framework, this condition simplifies to $A_{i,j} \neq A_{j,i}$ and thus requires $\mathbf{A}$ to be symmetric in equilibrium. In section 4.2.3 we give a detailed example for a 2D linear system of this framework and the bootstrapping technique discussed in section 4.2.2. In our example, $\mathbf{A}$ would represent a product between a mobility matrix and a stiffness matrix, both of which are symmetric resulting in a symmetric $\mathbf{A}$.

Note, this framework only applies to systems with dissipative coupling; reactive currents require a separate analysis. The two ways of breaking detailed balance in our case (temperature gradients and non-conservative forces) are reflected by a coordinate-independent commutation criterion for equilibrium [230]:

$$\mathbf{AD} - \mathbf{DA}^T = 0. \tag{18}$$

It was also argued that a system with broken detailed balance will sustain a larger variance than a similar system with the same level of noise, which is in equilibrium. This effect, referred to by Weiss as *noise amplification*, had previously been attributed to non-normality of the matrix $\mathbf{A}$, which is only true for diagonal $\mathbf{D}$. This type of noise amplification is now understood to be caused by broken detailed balance.

Although this amplification can be captured by different metrics, we here focus on the gain matrix $\mathbf{G} = \mathbf{1} + \mathbf{ACD}^{-1}$. The gain matrix is a measure of the variance of the system normalized by the amplitude of the noise input. To obtain a scalar measure, one can take, for example, the determinant of $\mathbf{G}$ which yields the gain g. It can be shown, that $g \geqslant g_0$ when detailed balance is broken, where g_0 is the gain of the same system in equilibrium. Finally, it is interesting to note, that the noise amplification matrix $\mathbf{G}$ is related to the average production of entropy in our generic model system. Let Π denote the production of entropy, then

$$\Pi = k_\mathrm{B}\,\mathrm{tr}\,(\mathbf{AG}), \tag{19}$$

providing a direct link between dissipation and increased variability in multivariate systems out of equilibrium.

3.3. Energy-speed-accuracy trade-off in sensory adaption

Energy dissipation is essential to various control circuits found in living organisms [231]. Faced with the noise inherent to small systems, cells are believed to have evolved strategies to increase the accuracy, efficiency, and robustness of their chemical reaction networks [232–234]. Implementing these strategies, however, comes at an energetic price, as is exemplified by Lan *et al* in the case of the energy-speed-accuracy (ESA) trade-off in sensory adaption [1, 235, 236]. This particular circuit is, of course, not the only active control in cell biology. The canonical example of molecular '*quality control*' is the kinetic proofreading process, in which chemical energy is used to ensure low error rates in gene transcription and translation [3]. Furthermore, fast and accurate learning and inference processes, which form the basis of sensing and adaptation, require some energy due to the inherent cost of information processing [2, 237–239]. A similar trade-off occurs in biochemical oscillations, which serve, for instance, as internal biological clocks. Here, the number of coherent cycles is linearly related to the energetic price that the system pays [240].

Sensory learning and adaptation at the cellular level involves chemical feedback circuits that are directly or indirectly driven by ATP hydrolysis, which provides energy input to break detailed balance. Examples of adaptation circuits are shown schematically in figures 7(B) and (C). These examples include the chemotactic adaption mechanism in *E. coli* (panel (B)), a well-established model system for environmental sensing. Common to all circuits is a three-node feedback structure, as depicted in figure 7(A). Conceptually, this negative feedback circuit aims to sustain a given level of activity a_0, independent of the steady amplitude of an external stimulus s, which here is assumed to be inhibitory. This adaptive behavior allows the circuit to respond sensitively to changes to the external stimulus over a large dynamic range in s.

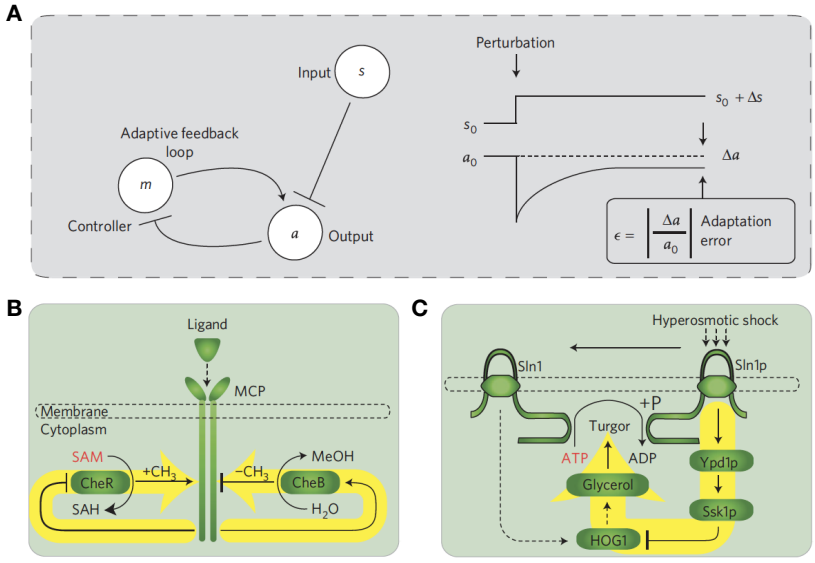

Figure 7. Models of adaptive feedback systems. (A) Simplified topology of a feedback circuit. The input s here is chosen to have an inhibitory effect. On the right the response of the output a is shown following a step in the input s. (B) Chemotactic circuit in *E. coli*. Ligand binding to a methyl-accepting-protein (MCP) causes further addition (mediated by CheR) or deletion (mediated by CheB) of methylgroups to MCP. This methylation counteracts the effects of ligand binding. (C) Osmotic sensing circuit in yeast. A reduction of osmolarity results in dephosphorylation of Sln1p→ Sln1, which activates the HOG1 (High osmolarity glycerol) mechanism. This mechanism acts to restore the tugor pressure inside the cell and eventually phosphorylates Sln1→Sln1p. Adapted by permission from Macmillan Publishers Ltd: Nature Physics [1], Copyright (2012).

The authors condense the dynamics of such a chemical network into a simple model (figure 7(A)) with abstract control $m(t)$ and activity $a(t)$ variables described by two coupled Langevin equations,

$$\dot{a} = F_a(a, m, s) + \xi_a(t) \tag{20}$$

$$\dot{m} = F_m(a, m, s) + \xi_m(t) \tag{21}$$

with F_a, F_m denoting the coarse-grained biochemical response and ξ_a, ξ_m being white-noise processes with different variances $2\Delta_a$ and $2\Delta_m$, respectively. Importantly, these biochemical responses do not fulfil the condition for conservative forces discussed in the previous section (above equation (18)). To function as an adaptive system with negative feedback, $\partial_m F_a$ and $\partial_a F_m$ must have different signs, which implies a breaking of detailed balance. Indeed, adaptation manifests in a sustained probability current $j = (j_a, j_m)$ in the phase space spanned by $a \times m$; the energetic cost to maintain this non-equilibrium steady-state is given by the amount of heat exchanged with the environment per unit time, which must equal the entropy production rate Π multiplied by the temperature T of the heatbath to which the system is coupled.

In general, a non-equilibrium system at steady-state that adheres to a Fokker-Planck equation produces entropy at a rate [14, 241],

$$\Pi = k_B \int \mathrm{d}\vec{x} \frac{1}{\rho(\vec{x}, t)} \vec{j}^T(\vec{x}, t) \mathbf{D}^{-1} \vec{j}(\vec{x}, t) \tag{22}$$

where $\rho(\vec{x}, t)$ is the probability density in phase space and $\mathbf{D}^{-1}$ is the inverse diffusion matrix. We note, that for linear systems equation (22) simplifies to equation (19).

Applying equation (22) to the model above for sensory adaption, yields the heat exchange rate $\dot{W} = \int \int \mathrm{d}m\mathrm{d}a \left[j_a^2/(\Delta_a \rho) + j_m^2/(\Delta_m \rho) \right]$. An assumed separation of timescales that govern the fast activity a and the slower control m, allows the authors to derive an *Energy-Speed-Accuracy* (ESA) relation, which reads

$$\dot{W} \approx (c_0 \sigma_a^2) \omega_m \log\left(\frac{\epsilon_0}{\epsilon}\right), \tag{23}$$

where, σ_a^2 represents the variance of the activity, and ϵ denotes the adaptation error defined as $\epsilon \equiv |1 - \langle a \rangle / a_0|$, while c_0 and ϵ_0 are constants that depend on details of the model. Here, ω_m parametrizes the rate of the control variable m. Therefore, an increase in ω_m or a reduction in ϵ requires an increased dissipation $\dot{W}$; put simply, swift and accurate adaptation can only be achieved at high energetic cost.

The authors argue that a dilution of chemical energy in living bacteria will mainly affect the adaptation rate, but leave the adaptation error unchanged. Starvation should therefore lead to lower adaptation rates to uphold the ESA relation. This prediction was tested in starving *E. coli* colonies under repeated addition and removal of MeAsp (see figure 8), an attractant which stimulates the chemotactic system shown in figure 7(B). The cells in this study were engineered to express fluorescent markers attached to two proteins involved in adaptation. Physical proximity between any of these two molecules is an indicator of ongoing chemosensing, and was measured using Foerster-resonance-energy transfer (FRET). Since the donor-acceptor distance correlates with the acceptor intensity, but anticorrelates with the donor intensity, the ratio of YFP (acceptor) and CFP (donor) intensities lends itself as a read-out signal to monitor adaptation. Indeed, after each addition/

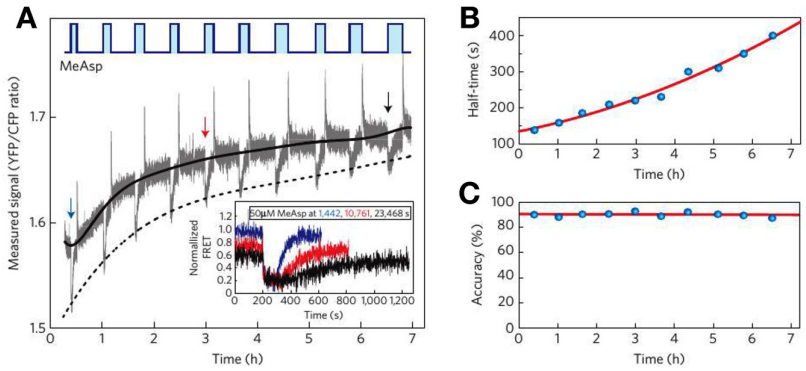

Figure 8. Experimental evidence for an energy-speed-accuracy (ESA) trade-off in *E. coli* chemotaxis. (A) Ratio of intensity of fluorescent reporters of adaptation. Changes in this signal are indicative of adaptation in the chemotatic circuit to external stimuli presented by the addition/removal of MeAsp. The inset illustrates the reduction of the FRET signal at the three different points in time indicated by arrows. (B) Half-times inferred from the responses to addition/removal cycles shown in (A). (C) Relative accuracies of adaptation. Adapted by permission from Macmillan Publishers Ltd: Nature Physics [1], Copyright (2012).

removal cycle of MeAsp, the signal recovers, albeit at a gradually decreasing pace, as is shown in the inset in figure 8(A). The decrease in the speed of adaptation is attributed to the progressing depletion of nutrition in the colony. In panels b and c, the adaptation half-time and relative accuracy are plotted. The graph in panel c clearly demonstrates the constancy of the accuracy of chemotatic system as nutrients are depleted over time, which is argued to be close to optimality.

3.4. Current fluctuations in non-equilibrium systems

Directed and chemically-specific transport of proteins, RNA, ions, and other molecules across the various membranes that foliate the cell is often achieved by active processes. A library of active membrane channel proteins has been described, which '*pump*' ions into and out of cells to control osmolarity, the electrical potential or the pH [242]. Furthermore, in eukaryotic cells, a concentration gradient of signalling molecules across the nuclear envelope causes messenger RNA (mRNA) molecules, expressed within the nucleus, to diffuse outwards through channels known as nuclear pore complexes (NPC) [112]. Outside of the nucleus, the mRNA is translated into proteins by the ribosomes, which are too large to traverse the NPCs. All these directed transport processes are essential to the cell. Thus, this raises the question of reliability of such processes [243, 244]. For example, how steady should we expect the supply of mRNA to the ribosomes to be [245]? Or, more generally, how predictable is the output rate of any given non-equilibrium process? Even active processes still endure fluctuations: molecular motors, at times, make a step backwards, or stall. Polymerizing filaments will undergo brief periods of sluggish growth or even shrinkage. Similarly, active membrane channels will sometimes transport more, and in other times fewer molecules. To illustrate this, an abstract example of such current fluctuations is depicted in figure 10, which will be further discussed below.

It seems intuitive, that predictability on the microscale always comes with an energy-price tag. In recent years, significant progress has been made to calculate the level of deviations from the average rate of a non-equilibrium process that is to be expected over finite times [199, 246–250]. More formally, a universal bound for finite-time fluctuations of a probability current in steady-state has been established. Such an uncertainty relation is perhaps best illustrated by the simple motor model discussed by Barato *et al* [247]: A molecular motor moves to the right at a rate k_+, and to the left at a rate k_-. The movement is biased, i.e. $k_+ > k_-$, driven by a free energy gradient $\Delta\mathcal{F} = k_\mathrm{B}T\log(k_+/k_-)$. A few trajectories for various values of k_+ are depicted in figure 9(A). As can be seen, the walker (shown in the inset), on average, moves with a constant drift $\langle x(t)\rangle = t(k_+ - k_-)$. Associated with this drift is a constant rate of entropy production $\Pi = (k_+ - k_-)\Delta\mathcal{F}/T$. Barato *et al* showed that the product of the total entropy produced $S(t) = \Pi t$ and the squared uncertainty $\epsilon^2 = \langle(x(t) - \langle x(t)\rangle)^2\rangle/\langle x(t)\rangle^2$ always fulfils the bound

$$TS(t)\epsilon(t)^2 \geqslant 2k_\mathrm{B}T. \tag{24}$$

For this particular model, the square uncertainty reads $\epsilon(t)^2 = (k_+ + k_-)/[(k_+ - k_-)^2 t]$, such that the product $TS(t)\epsilon(t)^2$ is constant in time. To further illustrate this point, we plotted the quantity $TS(t)\epsilon(t)^2$ for each choice of k_+ in figure 9(A), averaged over an ensemble of a hundred simulated trajectories in figure 9(B). Due to the finite ensemble size, the graphs fluctuate, but stay well above the universal lower bound of $2k_\mathrm{B}T$ for longer times t. So far, the theory underlying uncertainty relations was shown to be valid in the long time limit. Only recently, its validity has been extended to finite time scales [249, 250].

The bound in equation (24) can be generalized to any Markovian non-equilibrium steady-state [246, 248]. The four-node system in the inset in figure 10 is an example. Here, the integrated current $J_t = \int^t j(t')\mathrm{d}t'$ between any two nodes is distributed as $P(J_t = tj) \sim \mathrm{e}^{-tI(j)}$, with $I(j)$ denoting the large deviation function. This function therefore controls the variability of J_t. Interestingly, it can be shown that the large deviation function obtained in the linear response regime I_LR, is never exceeded by I, even far away from equilibrium [246]. Thus, an increase in currents is accompanied by an increase in the variability of these currents when a system is driven further

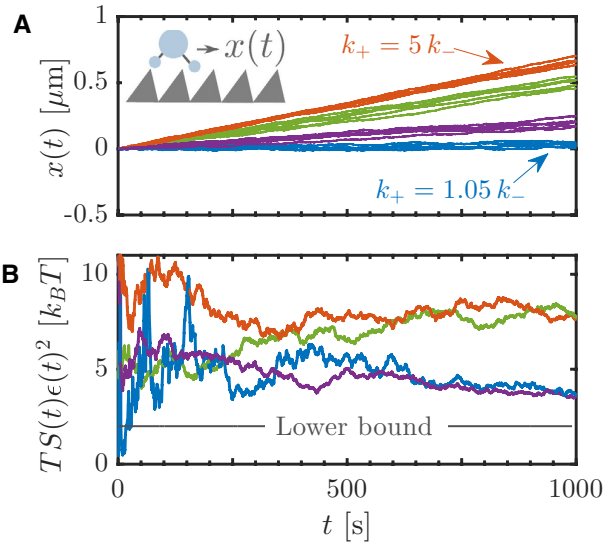

Figure 9. Variability of non-equilibrium steady states: (A) Example trajectories to show the spread in the average position $\langle x(t)\rangle$ after t steps. The inset depicts a simple model for a molecular motor in a sawtooth potential. (B) The products $TS(t)\epsilon(t)^2$ calculated over an ensemble of trajectories are bounded from below by the uncertainty relation. Despite the small size of the ensemble (100), equation (24) is fulfilled.

away from equilibrium. The relative uncertainty ϵ generalizes to $\epsilon^2 = \mathrm{var}(J)/\langle J\rangle^2$. The lower bound for this general ϵ^2 is similar in form to equation (24) and reads $2k_\mathrm{B}/(\Pi t)$, i.e. $\Pi t\epsilon^2 \geqslant 2k_\mathrm{B}$, where $\Pi = k_\mathrm{B}\sum_{m<n} j_{(m,n)} \log[(p^{(s)}_{(m)} r_{(m,n)})/(p^{(s)}_{(n)} r_{(n,m)})]$ is the average entropy production rate in the system in steady-state [246]. The steady-state probability distribution is denoted here by $p^{(s)}_{(m)}$. The relation above is a bound for the uncertainty of the entire system. A similar relation also applies to any individual edge between two nodes n and m, $\langle(j_{(m,n)} - \langle j_{(m,n)}\rangle)^2\rangle/\langle j_{(m,n)}\rangle^2 \geqslant 2k_\mathrm{B}/(\Pi_{(m,n)} t)$, where $\Pi_{(m,n)}$ denotes the entropy production associated with the edge (m,n). Recently, in an interesting connection to section 3, Gingrich *et al* [251] have found an uncertainty relation of the first-passage time T of a cumulative current J. More precisely, the time T it takes J to exceed a given threshold J_thr fulfils the relation

$$\frac{\mathrm{var}(T)}{\langle T\rangle}\Pi \geqslant 2k_\mathrm{B}. \tag{25}$$

While the uncertainty relations discussed above appear abstract at first, they may soon prove useful in studying transport or control systems in cellular biology due to their general applicability. Reminiscent of Carnot's efficiency for macroscopic engines, one implication of equation (24) is that a reduction in uncertainty can only be achieved by dissipating more energy when the system is close to optimality.

4. Detecting broken detailed balance in living systems

Up to this point we discussed intrinsically invasive methods to probe biological systems for non-equilibrium dynamics.

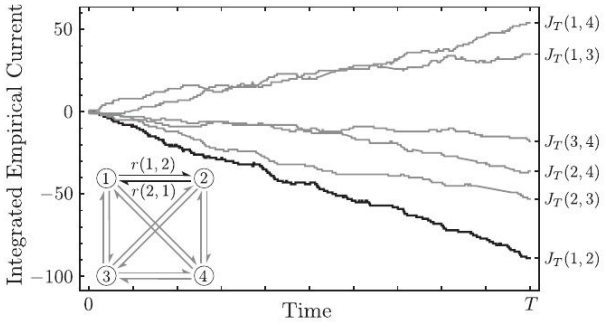

Figure 10. Variability of non-equilibrium steady states: Fluctuations of the cumulative probability current $J_T(m,n) = \int^T j_{m,n}(t)\mathrm{d}t$ along all nodes in the four state system shown in the inset. Fluctuations result in perturbations of the currents around their intrinsic rates $r(m,n)$. Adapted figure with permission from [246], Copyright (2016) by the American Physical Society.

For instance, to determine violations of the fluctuation-dissipation theorem a response function is required, which can only be measured by performing a perturbation in non-equilibrium systems (see section 2). Other methods that are used to probe for non-equilibrium involve thermal or chemical perturbations, and are therefore also inherently invasive. Such approaches are not ideal for investigating the stochastic dynamics of delicate sub-cellular system. Performing a controlled perturbation of such a system might not only be technically challenging, it may also be undesirable because of potential effects on the behavior or function of such a fragile system.

Ideally, we would like to avoid the technical and conceptual difficulties of invasive protocols to probe for non-equilibrium behavior. This raises the question: Could we perhaps measure a system's non-equilibrium behavior simply by looking at it? With this purpose in mind, we recently developed a method that indeed uses conventional video microscopy data of cellular and subcellular systems [22]. Detecting non-equilibrium behavior in the stochastic dynamics of mesoscopic coordinates of such systems can be accomplished by demonstrating that these dynamics break detailed balance. In this section, we will illustrate these ideas and discuss some recent related theoretical developments.

4.1. Equilibrium, steady state, and detailed balance

Suppose we can describe a system on a mesoscopic level by dividing phase space into small cells, such that the state of the system can be described by a state variable n. If the system is ergodic and irreducible, it will evolve towards a unique stationary solution $p^{(s)}_n$, which is constant in time. A necessary and sufficient requirement for such steady-state conditions is that the rate of transitions into any particular microstate, m, is balanced by the total rate of transitions from m to other microstates n:

$$\sum_n W_{n,m} = \sum_n W_{m,n}, \tag{26}$$

where $W_{n,m}$ describes the rate of transitions from state m to n. This result must hold for any system, at equilibrium or far

from equilibrium, that has reached steady state conditions. When the system is Markovian, equation (26) reduces to

$$\sum_n w_{nm} p_m^{(s)} = \sum_n w_{mn} p_n^{(s)}, \tag{27}$$

where w_{nm} describes the rate of transitions from state m to n, given that the system is in state m.

In thermodynamic equilibrium, it can be shown that a system must obey an even stronger condition: detailed balance. Classical closed ergodic systems are characterized by a time-independent Hamiltonian, which we will here restrict to be an even function of the momenta and independent of magnetic fields. The microscopic degrees of freedom of such a system obey deterministic dynamics described by Hamilton's equations, which are time reversal invariant. This has important implications also for the probability distribution of mesoscopic observables, which characterize the systems states at thermodynamic equilibrium. Consider, for instance, a mesoscopic variable y, which represents a generalized coordinate that either does not depend on the microscopic momenta, or that is an even functions of the microscopic momenta. Then, the transition between states must obey [187]

$$p_2^{(e)}(y_2, \tau; y_1, 0) = p_2^{(e)}(y_1, \tau; y_2, 0)\,. \tag{28}$$

Here we indicate with $p_2^{(e)}$ the two-point joint probability distribution. This result is referred to as the principle of detailed balance. Put simply, it means that the transitions between any two mesostates are pairwise balanced, and this result derives from the transition rates between any two microstates also being pairwise balanced. For Markovian systems we can write detailed balance more conveniently as

$$w(y_2|y_1)\, p^{(e)}(y_1) = w(y_1|y_2)\, p^{(e)}(y_2), \tag{29}$$

where the w's indicate the conditional rates between states. Finally, we note that if we add observables z, which are odd functions of the momenta, equation (28) needs to be generalized to

$$p_2^{(e)}(y_2, z_2, \tau; y_1, z_1, 0) = p_2^{(e)}(y_1, -z_1, \tau; y_2, -z_2, 0)\,. \tag{30}$$

It is important to note that for a system in steady state dynamics, broken detailed balance is direct evidence of non-equilibrium, but showing that a system obeys detailed balance in a subspace of coordinates is insufficient to prove equilibrium. Indeed, even for systems out of equilibrium, broken detailed balance is not necessarily apparent at the supramolecular scale [28, 29, 59, 60]. One can also often observe stationary stochastic processes in cells that, at first glance, appear to be thermally driven. Examples include the fluctuations of cytoskeletal filaments such as microtubuli, F-actin filaments or the fluctuations of intracellular organelles. These cases should be contrasted with obvious examples of mesoscopic non-equilibrium, non-stationary, irreversible processes such as cell growth, locomotion and mitosis. Thus, in general, it is unclear how and when broken detailed balance that realized on the molecular level also manifests at larger scales.

4.2. Probability flux analysis

In this section, we describe the basis and methodology that can be used to infer broken detailed balance from microscopy data. We consider a system, which is assumed to evolve according to stationary dynamics. This could, for instance, be a primary cilium or a flagellum [22]. In general, these systems exhibit stochastic dynamics, comprised of both a deterministic and a stochastic component. The dynamics of such systems can be captured by conventional video microscopy. To quantify this measured stochastic dynamics, we first need to parameterize the configuration of the system. The shape of a flagellum, for instance, could be conveniently decomposed into the dynamic normal modes of an elastic beam. In this example, the corresponding mode amplitudes represent time-dependent generalized coordinates of the system. Note, these mode amplitudes can be extracted from a single time frame and strictly represent configurational coordinates, which are independent of the microscopic momenta.

In general, a video microsocopy experiment can be used to extract time traces of D mesoscopic tracked coordinates $x_1, ..., x_D$, which represent the instantaneous configuration of the system. Clearly, this only represents a chosen subset of all coordinates that completely specify the whole system. Furthermore, only spatial or conformational degrees of freedom are considered in this discussion here. Indeed, fluctuations in momenta in a typical overdamped biological or soft-matter systems relax on very short time-scales, which are not resolved in typical video microscopy experiments. However, the basic methodology described below can readily be generalized to also include momentum-like variables.

We define a probability density, $\rho(x_1, ..., x_D, t)$, in terms of only the tracked degrees of freedom. This probability density can be obtained from the full joint probability density in terms of a complete set of variables, by integrating out all the untracked degrees of freedom. In the reduced configurational phase space of the tracked degrees of freedom, the dynamics of the system still obeys a continuity equation:

$$\frac{\partial \rho(x_1, ..., x_D, t)}{\partial t} = -\nabla \cdot \vec{j}(x_1, ..., x_D, t) \tag{31}$$

where $\vec{j}(x_1, ..., x_D, t)$ is the current density describing the net flow of transitions of the system in the D-dimensional configurational phase space. Here, we only consider systems with dissipative currents [90]. While at steady state the divergence of the current needs to vanish, in equilibrium any dissipative current itself must be identically zero.

4.2.1. Estimating phase space currents

Here we discuss one way of estimating currents from a set of time-traces. To provide a simple illustration of this approach, we consider a system with a 2D configurational phase space, as illustrated in figure 11(A). The dynamics of the system is captured by a time trace in this configurational phase space. It is convenient to analyze these trajectories using a discretized coarse-grained representation of the 2D phase space. This coarse-grained phase space (CGPS) consists of a collection of equally sized,

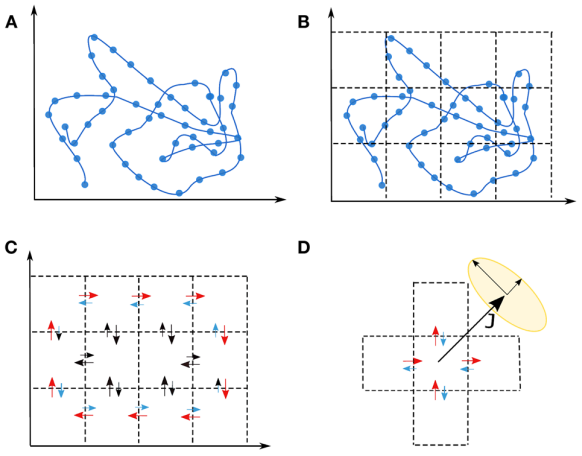

Figure 11. Schematic illustrating the coarse-graining procedure for the estimation of phase space currents and corresponding error bars. (A) Trajectory in continuous phase space. (B) Grid illustrating the discretization of the continuous phase space. (C) By counting transitions between first neighbour discrete states it is possible to estimate the currents (indicated by the arrows) across the boundaries. (D) Current error bars representation obtained through the bootstrapping procedure. From [22]. Reprinted with permission from AAAS.

rectangular boxes, each of which represents a discrete state figure 11(B). Such a discrete state in CGPS encompasses a continuous set of microstates, each of which belongs to a unique, discrete state. The primary reason for using this discretized representation of phase space is to be able to obtain informative results on experimental data with limited statistics.

In this 2D CGPS, a discrete state α has two neighboring states, respectively α_+ (larger x_i) and α_- (smaller x_i), along each direction x_i, resulting in four possible transitions. The dynamics of the system indeed satisfies the discrete continuity equation

$$\frac{\mathrm{d}p_\alpha}{\mathrm{d}t} = -\tilde{W}^{(x_1)}_{\alpha^-,\alpha} + \tilde{W}^{(x_1)}_{\alpha,\alpha^+} - \tilde{W}^{(x_2)}_{\alpha^-,\alpha} + \tilde{W}^{(x_2)}_{\alpha,\alpha^+}, \quad (32)$$

where $\tilde{W}_{\alpha,\beta} = W_{\alpha,\beta} - W_{\beta,\alpha}$ is the net rate of transitions from state β to α and p_α is the probability to be in discrete state α, which will become time independent when the system reaches steady-state conditions.

This probability p_α is related to the probability density $\rho(x_1, ..., x_2, t)$ defined above, and equation (32) can be obtained by integrating equation (31) on both sides over the volume of state α in CGPS. We can estimate this probability from a measured trajectory by using

$$p_\alpha = t_\alpha / t_{\mathrm{total}}, \quad (33)$$

where t_α is the accumulated time that the system spends in state α and t_{total} is the total duration of the experiment.

The net rates $\tilde{W}$ in CGPS can be estimated from the measured trajectories simply by counting the net number of transitions per unit time:

$$\tilde{W}^{(x_i)}_{\alpha,\beta} = \frac{N^{(x_i)}_{\alpha,\beta} - N^{(x_i)}_{\beta,\alpha}}{t_{\mathrm{total}}}. \quad (34)$$

Here $N^{(x_i)}_{\alpha,\beta}$ is the number of transitions from state β to state α along the direction x_i. In a mechanical system, the trajectories through phase space are continuous such that there can be only transitions between neighboring states. However, due to the discreteness in a measured time trajectory, it is possible that a transition between neighboring states is 'skipped', resulting in an apparent transition between non-neighboring states. In these cases, it is convenient to perform an interpolation of the time trace to estimate the intermediate transitions. It is important that this interpolation is performed in a time-symmetric way, so that the interpolation filter preserves time-reversal symmetry. In fact, this should be taken into account with any kind of filtering that is performed on measured time traces.

The currents in CGPS that describes back-and-forth transitions through all four boundaries of the box associated with a discrete state (figure 11(C)), can be defined by:

$$\vec{J}(\vec{x}_\alpha) = \frac{1}{2}\left(\tilde{W}^{(x_1)}_{\alpha^-,\alpha} + \tilde{W}^{(x_1)}_{\alpha,\alpha^+}, \tilde{W}^{(x_2)}_{\alpha^-,\alpha} + \tilde{W}^{(x_2)}_{\alpha,\alpha^+}\right). \quad (35)$$

Here, $\vec{x}_\alpha$ is the center position of the box associated with state α.

With this approach, prominent examples such as an isolated beating flagella of *Chlamydomonas reinhardtii* were examined [22] (see figure 1). Dynein motors drive relative axial sliding of microtubules inside the axoneme of the flagellum [77, 252, 253]. To quantify the non-equilibrium dynamics of this system, we decomposed the axoneme shapes measured using time-lapse microscopy into the dynamic normal modes of an elastic filament freely suspended in a liquid. Using this approach, we obtained the amplitudes of the projections coefficients for the first 3 modes. These amplitude time series were used to construct a trajectory in a phase space spanned by the three lowest-order modes, which were analyzed using PFA, as shown in figure 1(C). Here, the vector fields indicate the fluxes for the first three modes. Thus, this method can be used to quantify the non-equilibrium dynamics of the flagellum in a phase space of configurational degrees of freedom.

In addition, we considered primary cilia of Madin-Darby Canine Kidney (MDCK II) epithelial. Primary cilia are hair-like mechano and chemosensive organelles that grow from the periphery of certain eukaryotic cells [40, 254, 255]. At first glance the dynamics of the deflection angle and curvature of primary cilia appear to exhibit random fluctuations. Using probability flux analysis (PFA), however, it was demonstrated that there are significant circulating probability fluxes in a configurational phase space of angle and curvature, providing evidence for the non-equilibrium nature of primary cilia [22]. This approach is now gaining traction in variety of systems, ranging from the post translation Kai circadian clock [256] to motility phenotypes [257]. When the mobility of a system is known, a related approach can be used to estimate the heat dissipation [258]. However, in a non-equilibrium system, the mobility must be obtained by a perturbative measurement.

4.2.2. Bootstrapping. In practice, the finite length of experimental or simulated trajectories limits the accuracy with which we can estimate fluxes in phase space. This has an

important implication: even when considering a system at thermodynamic equilibrium, a measurement from finite data will typically result in apparent non-zero currents. In such a case we can not statistically distinguish the measured apparent current from a zero current. Therefore, it is important to asses if the estimated currents are statistically significant. Moreover, these current fluctuations may also be interesting to study in and of themselves (see section 3.4). In this section we briefly describe 'bootstrapping', a method that can be used to associate error bars to the measured currents.

The error bars on the probability flux can be determined by counting statistics of the number of transitions in equation (34). In general, however, there may be correlations between in-and-outward transitions for a given state, which renders it difficult to perform a simple estimate of the error-bar. A possible way around this, which naturally takes correlations into account, is to bootstrap trajectories from the experimentally measured or simulated trajectories.

To perform this bootstrapping procedure, we first determine all the transitions between discrete states in the CGPS from the measured trajectories. From this data, we construct a set A of n events, describing specific transitions of the system between two states, including the transition time. Given A, we can generate a new set of transitions, A', by randomly sampling n *single* events (with replacements) from A. This procedure, however, ignores possible correlations. To capture the effects of correlations on the accuracy of our current estimator, we bootstrap trajectories by randomly sampling a group of m consecutive events from A to construct a new set of transitions $A'_i(m)$ [259].

For each bootstrapped trajectory we calculate the current field and by averaging over all the realizations, we estimate the covariance matrix. To visualize the error bars (standard error of the mean) on the estimated currents, we depict an ellipse aligned with the principle components of this covariance matrix. The short and long axes of these error-ellipses are defined by the square roots of the small and large eigenvalues, respectively, of the covariance matrix, figure 11(D). Empirically, we found that the estimated error bars reduce substantially by including pairwise correlations, i.e. in going from $m = 1$ to $m = 2$, after which the error bars became largely insensitive to m. Such correlations can arise because of the coarse graining of phase space, which can introduce a degree of non-Markovianity.

4.2.3. Toy model: two stochastically driven coupled beads. To provide some basic intuition for stochastic non-equilibrium systems we next discuss a simple model, which can easily be solved both analytically and numerically. With this model, which was also studied in [260, 261], we illustrate how probability flux analysis (PFA) can be used on simulated data to obtain current densities in coarse grained phase space. The results are shown to be consistent with analytical calculations within error bars.

Consider a system consisting of two microscopic overdamped beads in a liquid connected to each other and to a rigid boundary by springs with elastic constant k, as depicted in figure 12(A). The two beads are assumed to be in contact with two independent heat baths, respectively at temperatures T_1 and T_2. The stochastic dynamics of this system is described by the overdamped equation of motion

$$\frac{\mathrm{d}\vec{x}}{\mathrm{d}t} = \mathbf{A}\vec{x} + \mathbf{F}\vec{\xi}, \tag{36}$$

where $\vec{x} = (x_1, x_2)^T$ represents the beads positions. The deterministic dynamics is captured by the matrix

$$\mathbf{A} = \frac{k}{\gamma}\begin{pmatrix} -2 & 1 \\ 1 & -2 \end{pmatrix}. \tag{37}$$

The drag coefficient γ, characterizing the viscous interactions between the beads and the liquid, is assumed to be identical for the two beads. The stochastic contribution, ξ_i, in the equation of motion is defined by

$$\langle\vec{\xi}\rangle = 0, \quad \langle\vec{\xi}(t)\otimes\vec{\xi}(t')\rangle = I\delta(t-t'), \tag{38}$$

and the amplitude of the noise is captured by the matrix

$$\mathbf{F} = \sqrt{\frac{2k_\mathrm{B}}{\gamma}}\begin{pmatrix} \sqrt{T_1} & 0 \\ 0 & \sqrt{T_2} \end{pmatrix}. \tag{39}$$

We can generate simulated trajectories for this system by numerically integrating equation (36). We will consider two exemplificative cases: (i) thermal equilibrium with $T_1 = T_2$, and (ii) non-equilibrium with $T_2 = 5T_1$. An example of the two simulated trajectories for this last case is shown in figure 12(A), where we note that the dynamics of individual trajectories appears to be, at first glance, indistinguishable from equilibrium dynamics. Interestingly however, the non-equilibrium nature of this system is revealed by applying PFA to these data, which gives coherently circulating probability fluxes in the phase space (figure 12(C)). By contrast, in the case of thermal equilibrium ($T_1 = T_2$) we find, as expected, that the flux vanishes, as shown in figure 12(B).

To compare these results of the estimated fluxes from simulations with analytical calculations, we next consider the time evolution for the probability density function $\rho(\vec{x}, t)$ of the system, which is described by the Fokker Planck equation:

$$\frac{\partial\rho(\vec{x},t)}{\partial t} = -\nabla\cdot[\mathbf{A}\vec{x}\rho(\vec{x},t)] + \nabla\cdot\mathbf{D}\nabla\rho(\vec{x},t), \tag{40}$$

where $\mathbf{D} = \frac{1}{2}\mathbf{F}\mathbf{F}^T$ is the diffusion matrix. The steady-state solution of this equation is a Gaussian distribution, with a covariance matrix, $\mathbf{C}$, which is found by solving the Lyapunov equation

$$\mathbf{A}\mathbf{C} + \mathbf{C}\mathbf{A}^T = -2\mathbf{D}. \tag{41}$$

The steady state probability flux density is given by $\vec{j} = \Omega\vec{x}\rho(\vec{x})$, where

$$\Omega = \frac{k(T_1 - T_2)}{\gamma c}\begin{pmatrix} 2(T_1+T_2) & -(7T_1+T_2) \\ (T_1+7T_2) & -2(T_1+T_2) \end{pmatrix} \tag{42}$$

with $c = (T_1^2 + 14T_1T_2 + T_2^2)$. As expected, the flux vanishes at thermal equilibrium when $T_1 = T_2$. In the near equilibrium regime, we can consider $T_1 = T$ and $T_2 = T + \epsilon$ with ϵ small. Within this limit, the current field can be written as

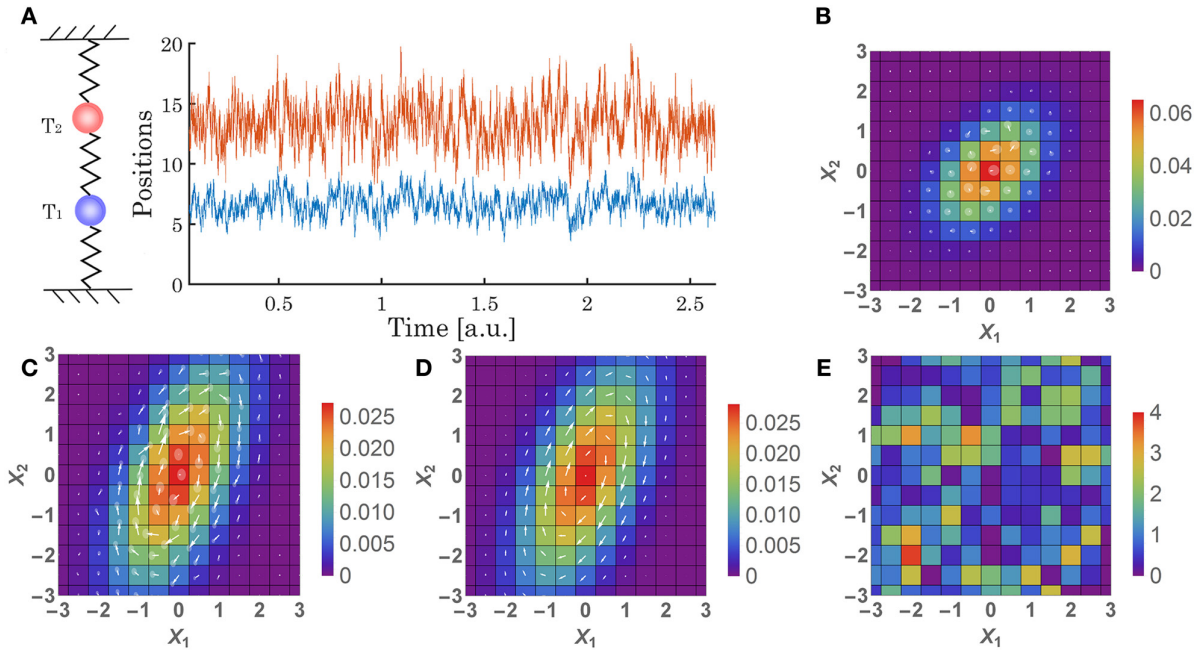

Figure 12. (A) Schematic of the two coupled beads system and simulated time series of the beads positions for $T_2 = 5T_1$. ((B) and (C)) Probability distribution (color) and flux map (white arrows) obtained by Brownian dynamics simulations at equilibrium ($T_1 = T_2$) (B) and non-equilibrium ($T_2 = 5T_1$) (C). Translucent discs represent a 2σ confidence interval for fluxes. (D) Analytical result for the probability distribution (color) and flux map (white arrows) obtained for a non-equilibrium case, ($T_2 = 5T_1$). From [22]. Reprinted with permission from AAAS. (E) Compatibility estimated from equation (45) between the estimated and theoretical second components of the currents.

$$\vec{j} \propto \frac{\epsilon}{T^2} e^{-\frac{k(x_1^2 - x_1 x_2 + x_2^2)}{k_B T}} \begin{pmatrix} x_1 - 2x_2 \\ -2x_1 + x_2 \end{pmatrix} + \mathcal{O}(\epsilon)^2 \qquad (43)$$

where we note how the amplitude and the direction of the flux are set by the ratio $\frac{\epsilon}{T^2}$, which vanishes at equilibrium. To gain some intuition on how the current decays with the distance in phase space, we can for example constrain equation (43) along the vertical direction ($x_1 = 0$),

$$\vec{j} \propto \frac{\epsilon}{T^2} e^{-\frac{kx_2^2}{k_B T}} \begin{pmatrix} -2x_2 \\ x_2 \end{pmatrix} + \mathcal{O}(\epsilon)^2. \qquad (44)$$

From equation (44) we can notice two opposite contributions to the amplitude, the linear dependence, dominant for small x_2 and the exponential dependence, dominant for larger x_2. This indicates an optimal distance from the origin at which the flux is maximum.

To compare the analytical expectation for the flux $\vec{j}$ with the results obtained using PFA on simulated trajectories, we calculate the compatibility $c_{ij,l}$ between the estimated $\hat{j}$ and the theoretical j values of the flux field in cell i,j, and in direction x_l:

$$c_{ij,l} = \frac{|\hat{j}_{ij,x_l} - j_{ij,x_l}|}{\sigma}, \qquad (45)$$

where σ is the error obtained from the bootstrapping analysis in PFA. The results for the second component of $\vec{j}$ yield an average compatibility of $\langle c_{ij} \rangle \simeq 1.02$ (figure 12(E)), indicating a good quantitative agreement between our estimation and the exact currents. A similar result is obtained in the equilibrium case ($T_1 = T_2$), for which the average compatibility is $\langle c_{ij} \rangle \simeq 0.95$. This concludes our analysis of probability fluxes in phase space for stochastic trajectories. These results illustrate how PFA can be used to infer accurate currents in coarse grained phase space from stochastic trajectories.

4.3. Probe filaments to study broken detailed balance across scales in motor-activated gels

While mesoscopic objects, such as cilia or flagella, can often be directly imaged, detecting non-equilibrium dynamics inside live cells on the microscale and below is more challenging. The cellular cytoskeleton, discussed in section 2, is a prominent example of active matter, which can best be described as a viscoelastic meshwork of biopolymers, activated by myosin motors [17, 21]. Random contractions of these myosin proteins fuelled by ATP hydrolysis can drive vigorous steady-state fluctuations in this polymer network. Such fluctuations can be quantified experimentally by embedding fluorescent probe particles. This technique has revealed multiple scaling regimes of the time dependence of the mean-squared displacement [32], which were attributed to a combination of the viscoelastic behavior of the network and the temporal dynamics of motor activity. In particular, endogenous embedded filaments such as microtubules, or added filaments such as single-walled carbon nanotubes have proved to be convenient probes [34, 55].

These experiments and others [45, 140, 262] have sparked a host of theoretical efforts [111, 185, 263–269] to elucidate the stochastic dynamics of probe particles and filaments in an active motorized gel. More recently, it has been suggested that

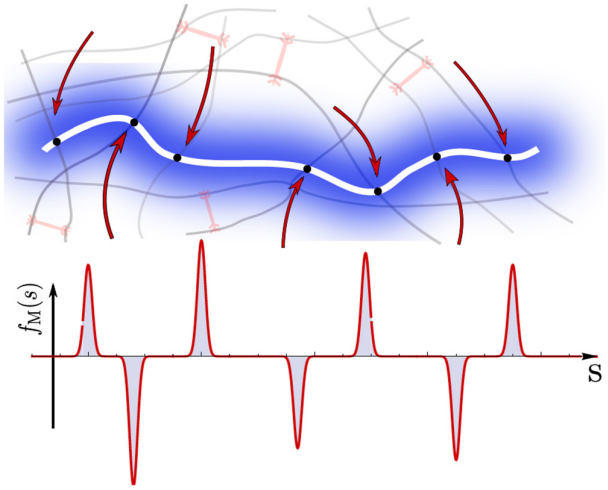

Figure 13. Fluctuations of a probe filament (blue) embedded in a viscoelastic actin (grey) network, driven out of equilibrium by random contractions of myosin (red, red arrows). Adapted figure with permission from [60], Copyright (2017) by the American Physical Society.

probe filaments can be also used as a multi-variable probe to discriminate active from thermal fluctuations using detailed balance [59, 60], and could be used to detect correlations in the profile of active forces along its backbone [58].

In the following, we lay out a framework to describe fluctuations of a semiflexible probe filament [56, 270–272], which is embedded in a motor-activated network [111, 127, 181]. We assume the probe filament to be weakly-bending, such that we can focus on the transverse coordinate $r_\perp(s,t)$, where the arclength $0 < s < L$ parametrizes the backbone, as shown in figure 13. The overdamped dynamics of such a probe filament is governed by a balance of (i) viscous and elastic forces of the surrounding viscoelastic medium, (ii) bending forces, (iii) thermal agitation, and (iv) motor-induced fluctuations, which read in this order as

$$\int_{-\infty}^{t} \mathrm{d}t'\, \alpha(t-t') r_\perp(s,t') + \kappa \frac{\partial^4 r_\perp}{\partial t^4}(s,t) = \xi(s,t) + f_M(s,t). \tag{46}$$

Terms on the left describe relaxation, while terms on the right contain stochastic contributions. For a predominantly elastic network, we can use the generalized Stokes equation, $\hat{\alpha}(\omega) = k_0 \hat{G}(\omega)$ to approximate the viscoelastic kernel on the left hand side as $\hat{G} = G_0 + i\eta\omega$, i.e. as a Kelvin–Voigt-type viscoelastic solid. The factor k_0 has a geometrical origin, and is given by $k_0 \approx 4\pi/\ln(L/d)$ for an infinitesimal rod segment of diameter d [126]. In a crosslinked actin network this approximation is reasonable for low frequencies typically below roughly 100 Hz, beyond which the network modulus exhibits a characteristic stiffening with frequency [45, 273, 274]. When the network is described as such a simple viscoelastic solid, the thermal noise is given by a Gaussian white-noise process $\xi(s,t)$, to which we add independent actively induced forces $f_M(s,t)$, specified in detail further below.

Bending forces can be conveniently studied from the perspective of bending modes of the probe filament. Following the approach in [59, 60], a description in terms of bending modes can be obtained from a decomposition of the backbone coordinates into orthogonal dynamic modes $r_\perp(s,t) = L\sum_q a_q(t) y_q(s)$ [56–58]. In this coordinate system, the multiscale character of probe filaments becomes apparent: each bending mode amplitude $a_q(t)$ is sensitive to a lengthscale corresponding to its wavelength. The precise form of bending modes, however, depends on the boundary conditions of the filament. The simplest case is a filament with zero transverse deflections at its end, where classical sine-modes $y_{q_m}(s) = \sqrt{2/L}\sin(q_m s)$ form an orthonormal set. Importantly, these modes are independent in equilibrium, due to their orthogonality. For fixed-end modes, mode number $m \in \{1,2,3,...\}$ and wave-vector q are related via $q(m) = m\pi/L$. The relaxational timescale of each mode is set by a balance between both elastic and viscous forces of the network and the bending rigidity of the filament. For inextensible filaments in purely viscous environments, this results in a strongly length-dependent decay

$$\tau_q = \frac{\eta}{\kappa q^4/k_0 + G_0}. \tag{47}$$

In the linear-response regime, we obtain the mode-response function to transverse deflections, $\chi_q(t)$, in fourier space $\hat{\chi}_q(\omega) = (\hat{\alpha}(\omega) + \kappa q^4)^{-1}$. This response function is related to mode variances in equilibrium via the mode fluctuation-dissipation theorem

$$\langle |\hat{a}_q(\omega)|^2 \rangle = \frac{2k_B T}{L^2 \omega} \hat{\chi}_q''(\omega). \tag{48}$$

Bending modes are thus ideally suited to not only detect motor activity, but also to measure their spatial and temporal characteristics. Perhaps for these reasons, bending mode fluctuations have been the subject of a number of studies in biological non-equilibrium systems.

In a study by Brangwynne *et al* [55], fluorescently labelled microtubuli were used to probe the active fluctuations in actin-myosin gels. The persistence lengths of microtubuli is on the order of millimeters [57], such that these filaments can be treated effectively as rigid on microscopic lengthscales under thermal conditions. By contrast, in actin-myosin gels, microtubuli exhibit significant fluctuations, caused by contractions of myosin, which deform the network in which the microtubules are embedded. A quantitative analysis of thermal bending mode fluctuations reveals a q^{-4}-decay in actin networks (without myosin). By contrast, adding myosin not only increases the amplitudes of fluctuations, but also results in a breakdown of the standard mode decay (see equation (47). The spatial extent of individual indentations in motor-agitated microtubuli can be used to extract forces induced by myosing. These force range between 0−30 pN, in accord with more recent studies in live cells [34, 45]. Importantly, the results also suggest a very narrow profile of the force exerted on the microtubules. Furthermore, in the cell cortex, microtubules often appear considerably more curved, despite their rigidity. Indeed, this curved microtubule structure is not due to

temporal bending fluctuations of the microtubule, but rather results from geometrical constraints that randomly deflect the microtubule tip during polymerization [158].

Motivated by these experimental observations, we can model the motor-induced force, exerted on the probe at the points where it is coupled elastically to the network, as a superposition of all active forces in the environment:

$$f_{\mathrm{M}}(s,t) = \sum_n f_n(s,t), \tag{49}$$

where each $f_n(s, t)$ denotes the force contribution from active motors, which affect the filament at the n_{th} entanglement point. Active forces have a characteristic spatial decay, since myosin motors exert forces in dipoles rather than in single directions [275]. The model in equation (49) does not account for such details; its main purpose is to provide a non-uniform force background $f(s)$ along the backbone s.

Measurements of myosin dynamics have revealed a Lorentzian power spectrum [111, 274]. A simple on-off telegraph process $\mathcal{T}(t)$ is in accord with these observations and appears to be adequate to model the stochastic force dynamics of individual motors. Taking furthermore into account the narrow profile of motor forces inferred from experiments [55], we arrive at a model for motor-induced forces, which reads $f_n(s,t) = f_n\delta(s-s_n)\mathcal{T}_n(t)$. Here $\mathcal{T}_n(t)$ is a telegraph process with exponential decorrelation $\langle\mathcal{T}(t)\mathcal{T}(t')\rangle = C_2\,\exp(-|t-t'|/\tau_M)$.

Using this simple description for the stochastic behavior of motor-generated forces together with equation (48), we compute the mode correlator, which decomposes into active and thermal contributions: $\langle a_q(t)a_w(t')\rangle = \langle a_q(t)a_w(t')\rangle^{\mathrm{Th}} + \langle a_q(t)a_w(t')\rangle^{\mathrm{M}}$, given by

$$\langle a_q(t)a_w(t')\rangle^{\mathrm{Th}} = \frac{k_{\mathrm{B}}T\tau_q}{L^2\gamma}\delta_{q,w}\mathrm{e}^{-\frac{|t-t'|}{\tau_q}} \tag{50}$$

$$\langle a_q(t)a_w(t')\rangle^{\mathrm{M}} = \frac{1}{L^2\gamma^2}\mathbf{F}_{q,w}C_2\mathcal{C}_{q,w}\,(t-t')\,. \tag{51}$$

$\mathbf{F}_{q,w}$ specifies the geometry of motor-induced forces in mode space and is defined by $\mathbf{F}_{q,w} = \sum_n f_n^2 y_q\,(s_n)\,y_w\,(s_n)$, where the sum runs over the filament-network contacts. The function $\mathcal{C}_{q,w}(\Delta t)$ denotes the temporal decorrelation of active mode fluctuations. In contrast to thermal equilibrium, active fluctuations decay as a double exponential

$$\mathcal{C}_{q,w}(t-t') = \tau_q\tau_w\left(\frac{\mathrm{e}^{-\frac{|t-t'|}{\tau_{\mathrm{M}}}}}{\left(1-\frac{\tau_q}{\tau_{\mathrm{M}}}\right)\left(1+\frac{\tau_w}{\tau_{\mathrm{M}}}\right)}\cdot\right.$$
$$\left.-2\frac{\tau_q}{\tau_{\mathrm{M}}}\frac{\mathrm{e}^{-\frac{|t'-t|}{\tau_q}}}{\left(1-\left(\frac{\tau_q}{\tau_{\mathrm{M}}}\right)^2\right)\left(1+\frac{\tau_w}{\tau_q}\right)}\right), \tag{52}$$

which indicates a competition between two decorrelating processes: mode relaxation and the internal decorrelation of the motor state. The correlator is not symmetric in the indices q and w as can be seen from equation (52), which results in a breaking of Onsager's time-reversal symmetry [60].

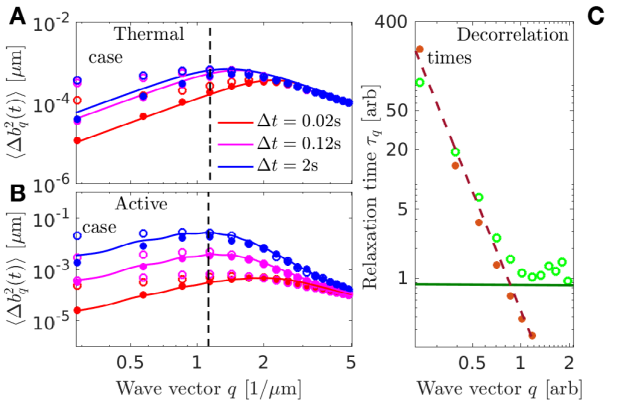

Figure 14. Mode fluctuations under (A) purely thermal agitated and (B) under additional influence of motor-induced forces. C) Convergence of mode decorrelation times onto the motor timescale. Different colors correspond to the different times Δt shown in the legend in panel (A). Adapted figure with permission from [55], Copyright (2008) by the American Physical Society.

This double exponential in equation (52) is the footprint of colour of the noise process, which we use to describe motor-induced forces. The q^{-4}-decay of mode amplitudes relaxation times, τ_q, levels off around τ_{M} as shown in figure 14(C). This saturation occurs because modes cannot decorrelate faster than the force that is driving them. Under coloured noise, the relaxation times cannot be directly inferred from decorrelation. This is indeed confirmed in Brownian dynamics simulations of filaments subject to active fluctuations [59]. To further illustrate these results, simulations of mode variances over mode vector in passive (figure 14(A)) and active (figure 14(B)) networks are shown together with theoretical predictions from equations (50) and (51). For comparison, experimentally obtained mode variances [55] are plotted over q in figure 15. As one would expect, in both cases mode variances are elevated in active environments.

In the long time regime $t \gg \tau_{\mathrm{M}}$, motor forces effectively appear as sources of white-noise. In this '*white-noise limit*', the motor correlator converges to a δ-function, $\langle\Delta\mathcal{T}(t)\Delta\mathcal{T}(t')\rangle \to C_2/2\tau_{\mathrm{M}}\delta(t-t')$ with a factor τ_{M}, which remains only as a scale of the variance of the motor process. The mode correlation function in the white-noise limit can be derived by a series expansion of $\mathcal{C}_{q,w}(t)$, which yields

$$\langle a_q(t)a_w(t')\rangle^{\mathrm{M}} = \frac{C_2\tau_M}{L^2\gamma^2}\mathbf{F}_{q,w}\frac{\tau_q\tau_w}{\tau_q+\tau_W}\delta(t-t'). \tag{53}$$

We can now contract the thermal and motor-white noise processes into a single process $\psi(t)$, with a correlator $\langle\psi_q(t)\psi_w(t')\rangle = (4k_{\mathrm{B}}T\gamma\delta_{q,w} + C_2\tau_{\mathrm{M}}\mathbf{F}_{q,w})\,\frac{\delta(t-t')}{2L^2}$.

It is useful at this stage to compare this scenario with that described in section 3.2: Here, mode variables are independent, but are subject to noise with a cross-mode correlations, such that different modes are simultanously excited by a motor event. By constrast, thermal noise is uniform in amplitude and uncorrelated throughout the system, giving rise to independent stochastic forces in mode-space. As we discussed in section 3.2, a correlation in the external noise in one coordinate system, may appear as a 'temperature'

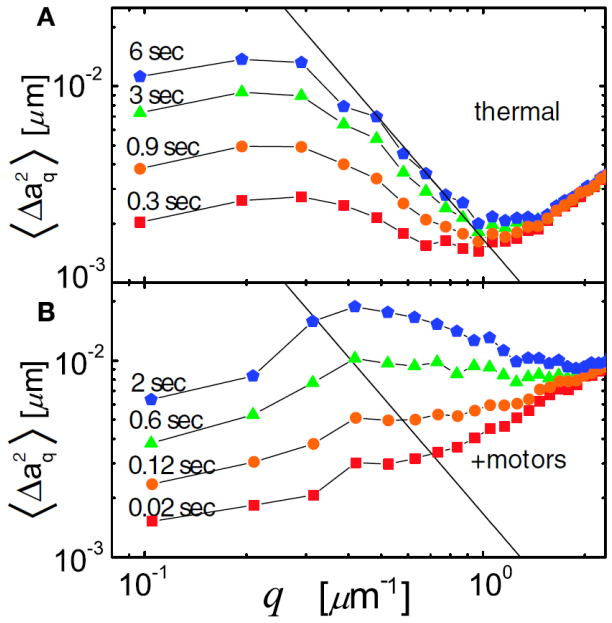

Figure 15. Mode amplitude variations in fluctuating microtubules embedded in actin-myosin gels over mode number q. (A) In ATP-depleted gels (purely thermal noise), mode variances follow a power law decay. (B) Active fluctuations result in enhanced mode variances in accord with the theory In figure 14. At high q-values measurement noise leads to an increase in mode variances. Adapted figure with permission from [59], Copyright (2016) by the American Physical Society.

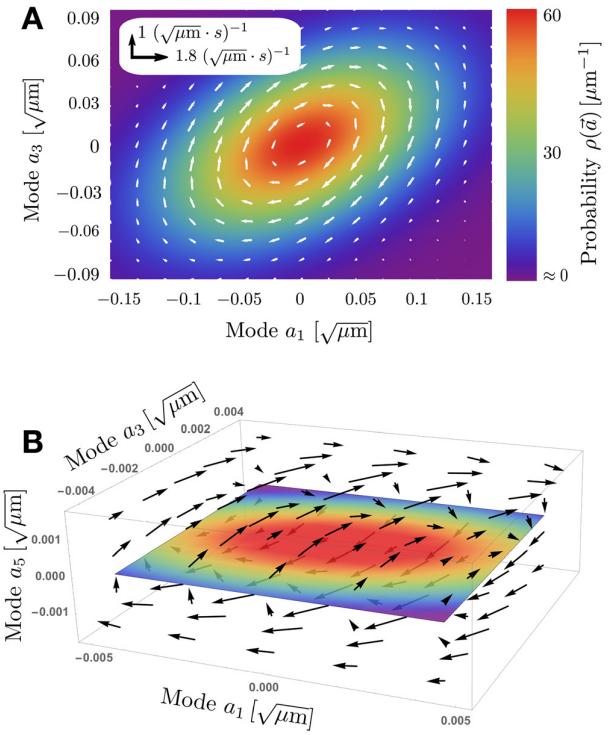

Figure 16. Steady-state probability currents in mode space. (A) Projection of the multidimensional current on the mode amplitude pair a_1 and a_3. (B) The same current in three dimensions a_1, a_3, and a_5. Due to the geometry of probe-network interactions in this example, only modes of similar number parity (e.g. odd–odd) couple. Adapted figure with permission from [59], Copyright (2016) by the American Physical Society.

gradient in different coordinates. It is this mechanism, which gives rise to a probability flux in mode space, which breaks detailed balance in the fluctuations of the probe filament. In other words, a motor-induced force background $\langle f_M(s,t)\rangle_{\text{temporal}} = \lim_{t_1\to\infty}\int_{t_0}^{t_1} \mathrm{d}t f_M(s,t)$ (see lower panel in figure 13), which varies along the filament, will lead to a breaking of detailed balance in a hyperplane spanned by the affected modes.

The magnitude and structure of this probability current, is given as a solution of the multivariate Fokker-Planck equation $\partial_t\rho(\vec{a},t) = -\vec{\nabla}\cdot\vec{j}(\vec{a},t)$ in mode space. The probability current, $\vec{j}(\vec{a})$, can be written in steady-state as

$$\vec{j}(\vec{a}) = (\mathbf{K} + \mathbf{D}\mathbf{C}^{-1})\vec{a}\rho(\vec{a}) \equiv \mathbf{\Omega}\vec{a}\rho(\vec{a}), \qquad (54)$$

where $\mathbf{K}_{q,w} = -1/\tau_q\delta_{q,w}$ is the deterministic matrix which defines the linear force field, and $\mathbf{D}$ and $\mathbf{C}$ represent respectively the diffusion and covariance matrices. Within this linear description, Ω is the matrix that captures the structure of the current [230, 276]. A rotational probability current in the Fokker-Planck picture is associated with a net rotation of variables in the Langevin description: On average, mode amplitudes cycle around the origin, when detailed balance is broken in steady-state, as illustrated in figure 16.

The circular character of the current is reflected mathematically by the skew-symmetry of $\mathbf{\Omega}^T = -\mathbf{\Omega}$ in the coordinate system where $\tilde{\mathbf{C}} = \mathbf{1}$ (‘*correlation-identity coordinates*’). This can be seen from equation (41), which dictates that $\tilde{\mathbf{K}} + \tilde{\mathbf{K}}^T = -2\tilde{\mathbf{D}}$ in this system, such that $\tilde{\mathbf{\Omega}} = \frac{1}{2}\left(\tilde{\mathbf{K}} - \tilde{\mathbf{K}}^T\right)$.

The eigenvalues of any skew-symmetric matrix $\mathbf{R}$ are either zero or purely imaginary, with the latter leading to rotational currents in a hypothetical dynamical system described by $\dot{\vec{x}} = \mathbf{R}\vec{x}$. Moreover, since $\mathrm{Tr}\,(\mathbf{\Omega}) = 0$, in two dimensions, this implies that the eigenvalues can be rewritten as $\lambda_{1,2} = \pm i\omega$. In a steady-state, the probability current $\vec{j}$ (in any dimension) has to be orthogonal to the gradient of the density $\rho(\vec{a},t)$, since $\vec{\nabla}\cdot\vec{j}(\vec{a}) = \rho(\vec{a})\vec{\nabla}\cdot(\mathbf{\Omega}\vec{a}) + (\mathbf{\Omega}\vec{a})\cdot\vec{\nabla}\vec{\rho}(\vec{a}) = \partial_t\rho = 0$. The first term must be zero, since it is proportional to $\mathrm{Tr}\,(\mathbf{\Omega})\,\vec{a}$, so that the second term has to vanish as well. This, however, implies that $\vec{\nabla}\rho \perp \mathbf{\Omega}\vec{a}$: the gradient of the density must be perpendicular to the flow field. In a linear system, the probability density is always Gaussian $\rho \propto e^{-\frac{1}{2}\vec{a}^T\mathbf{C}^{-1}\vec{a}}$, such that the flow field must have an ellipsoidal structure [230]. In correlation-identity coordinates, where the density has a radial symmetry, the profile of $\tilde{\vec{j}}$ would thus be purely azimuthal, and its magnitude would represent an angular velocity. An average over the angular movements $\langle\dot{\varphi}\rangle$ of the mode vector $\vec{a}(t)$ in the plane will yield the cycling frequency. The imaginary part of the positive eigenvalue of $\mathbf{\Omega}$ must therefore represent the average cycling frequency of the mode vector in the plane.

In a reduced 2D system consisting only of $a_q(t)$ and $a_w(t)$, the cycling frequency can be calculated analytically and reads

$$\omega^{2D}_{q,w} = \frac{(\tau_q - \tau_w)\,\mathbf{F}_{q,w}}{\sqrt{\tau_q\tau_w\left((\tau_q+\tau_w)^2\,\beta - 4\tau_q\tau_w\mathbf{F}^2_{q,w}\right)}} \tag{55}$$

where $\beta = (\frac{2k_BT\gamma}{C_2\tau_M})^2 + \frac{2k_BT\gamma}{C_2\tau_M}(\mathbf{F}_{q,q} + \mathbf{F}_{w,w}) + \mathbf{F}_{w,w}\mathbf{F}_{q,q}$.

Interestingly, equation (55) shows that in the case of equal relaxation times $\tau_q = \tau_w$, the cycling frequency would be zero and thus, detailed balance would be restored, regardless of differences between the modes in motor-induced fluctuations. This hints at an important role of relaxation times in determining the shape of the current in multidimensional systems. Furthermore, the denominator of equation (55) shows how an increase in overall temperature T could mask broken detailed balance by reducing the cycling frequency.

In summary, filaments as multi-scale and multi-variable probes offer a novel perspective on non-equilibrium phenomena in active matter and could be used in the future as 'non-equilibrium antennae'. As we illustrated in this section, a heterogeneous force background $f_M(s,t)$ created by motor-induced fluctuations leads to a breaking of detailed balance in mode space of embedded filaments. The intricate structure of the probability current in steady-state may contain a wealth of information about the geometric and, perhaps, temporal structure of impinging active forces.

The theory laid out in this section can be generalized to other objects, such as membranes [35, 36, 167, 172]. In principle, the membrane mode decomposition described in section 2 could be used to detect a breaking of detailed balance, since active processes in the cortex of red blood cells might result in noise input that correlates over different membrane modes.

5. Outlook

The examples discussed in this review illustrate how experimental measurements of non-equilibrium activity and irreversibility can provide a deeper conceptual understanding of active biological assemblies and non-equilibrium processes in cells. In many cases, non-equilibrium fluctuations have successfully been identified and quantified using the combination of active and passive microrheology techniques to study the violation of the fluctuation-dissipation theorem, [36, 43]. Such studies can for instance reveal the force spectrum inside cells, [45]. However, these approaches require invasive micromechanical manipulation. Furthermore, a complete generalization of the fluctuation-dissipation theorem for non-equilibrium system is still lacking, such that the response of a non-equilibrium system can not be inferred from its spontaneous fluctuations. However, this does not mean that the fluctuations of a non-equilibrium steady state do not contain valuable information about the nature of the system. Indeed, non-invasive approaches to measure broken detailed balance from stochastic dynamics have now been establishes to reveal phase space currents in mesoscopic degrees of freedom of biological systems, [22]. It remains an open question what information can be inferred about the underlying system from such phase space currents, [59, 60]. However, recently derived theoretical relations for energy dissipation and entropy production to characterize non-equilibrium activity are finding traction in various biological systems such as molecular motors and chemical control systems [1, 2, 225, 247].

Taken together, the research discussed in this review illustrate that the gap between fundamental approaches in stochastic thermodynamics and its application to real biological system is slowly closing. Indeed, studies of biological active matter are not only yielding insights in non-equilibrium physics, they have also suggested conceptually novel mechanisms in cell biology. For instance, the collective effect of forces exerted by molecular motors has been implicated in intracellular transport and positioning of the nucleus [31, 32, 34, 45, 110]. This novel mode of transport, known as *active diffusion*, is thought to complement thermal diffusion and directed, motor-driven modes of transport in cells. Another intriguing example is the role of DNA-binding ATPases, which have been suggested to be capable of generating forces on the chromosomes through a DNA-relay mechanism [277] or loop extrusion [278, 279]. ATP- or GTPases can also interact with membranes or DNA to play a role in pattern forming systems [10–12], for instance in the Min system in *E. coli* and CDC42 in yeast. In these systems, certain proteins can switch irreversibly between different conformational states, affecting their affinity to be in the cytosol or the membrane. This, together with nonlinear interactions between these different proteins, can result in non-equilibrium dynamic pattern formation.

Another important example in this respect is how cells break symmetry to form a polarity axes. Intracellular myosin activity has been implicated in establishing a sense of direction ('polarity') in cells. In order to divide, cells must 'decide' on the axis of the mytotic spindle, which is a crucial part of the cell division apparatus [280–283]. Cortical flows resulting from asymmetries in myosin activity have been shown to effectively polarize *C. elegans* cells and break the initial cellular symmetry [284].

Non-equilibrium phenomena also emerge at the multicellular scale: Groups of motile cells exhibit collective active dynamics, such as flocking, swarming, non-equilibrium phase transitions or the coordinated movements of cells during embryonic developments [285, 286]. More broadly, non-equilibrium physics is emerging as a guiding framework to understand phenomena related to self-replication and adaptation [226–228], the origin of life (see for example [287, 288]), as well as synthetic life-like systems (See [289] and references therein).

Acknowledgments

This work was supported by the German Excellence Initiative via the program NanoSystems Initiative Munich (NIM) and by the German Research Council (DFG) within the framework of the Transregio 174 'Spatiotemporal dynamics of bacterial cells'. FM is supported by a DFG Fellowship through the Graduate School of Quantitative Biosciences Munich (QBM). This project has received funding from the European Union's Horizon 2020 research and innovation

programme under European Training Network (ETN) grant 674979-NANOTRANS (JG) and was performed in part at the Aspen Center for Physics (CPB), which is supported by National Science Foundation grant PHY-1607611. We thank T Betz, G Berman, W Bialek, D Braun, D Brückner, C Brangwynne, G Crooks, N Fakhri, B Fabry, E Frey, N Gov, M Guo, G Gradziuk, R Granek, L Jawerth, F Jülicher, G Koenderink, K Kroy, M Lenz, T Liverpool, T Lubensky, B Machta, F MacKintosh, J Messelink, K Miermans, J Rädler, P Ronceray, J Shaevitz, D Schwab, M Sheinman, Y Shokef, C Schmidt, C Storm, J Tailleur, M Tikhonov, D Weitz, M Wigbers, and N Wingreen, for many stimulating discussions.

ORCID iDs

C P Broedersz https://orcid.org/0000-0001-7283-3704

References

[1] Lan G, Sartori P, Neumann S, Sourjik V and Tu Y 2012 The energy speed accuracy trade-off in sensory adaptation *Nat. Phys.* **8** 422–8
[2] Mehta P and Schwab D J 2012 Energetic costs of cellular computation *Proc. Natl Acad. Sci. USA* **109** 17978–82
[3] Hopfield J J 1974 Kinetic proofreading: a new mechanism for reducing errors in biosynthetic processes requiring high specificity *Proc. Natl Acad. Sci. USA* **71** 4135–9
[4] Murugan A, Huse D A and Leibler S 2012 Speed, dissipation, and error in kinetic proofreading *Proc. Natl Acad. Sci. USA* **109** 12034–9
[5] Needleman D and Brugues J 2014 Determining physical principles of subcellular organization *Dev. Cell* **29** 135–8
[6] Fletcher D A and Mullins R D 2010 Cell mechanics and the cytoskeleton *Nature* **463** 485–92
[7] Brangwynne C P, Koenderink G H, MacKintosh F C and Weitz D A 2008 Cytoplasmic diffusion: molecular motors mix it up *J. Cell Biol.* **183** 583–7
[8] Juelicher F, Kruse K, Prost J and Joanny J-F 2007 Active behavior of the cytoskeleton *Phys. Rep.* **449** 3–28
[9] Cates M E 2012 Diffusive transport without detailed balance in motile bacteria: does microbiology need statistical physics? *Rep. Prog. Phys.* **75** 042601
[10] Huang K C, Meir Y and Wingreen N S 2003 Dynamic structures in *Escherichia Coli*: spontaneous formation of MinE rings and MinD polar zones *Proc. Natl Acad. Sci. USA* **100** 12724–8
[11] Frey E, Halatek J, Kretschmer S and Schwille P 2017 Protein pattern formation *Physical Biology Members* ed P Bassereau and P C A Sens (Heidelberg: Springer)
[12] Halatek J and Frey E 2012 Highly canalized MinD transfer and MinE sequestration explain the origin of robust MinCDE-protein dynamics *Cell Rep.* **1** 741–52
[13] Bialek W 2012 *Biophysics: Searching for Principles* (Princeton, NJ: Princeton University Press)
[14] Seifert U 2012 Stochastic thermodynamics, fluctuation theorems and molecular machines *Rep. Prog. Phys.* **75** 126001
[15] Ritort F 2007 Nonequilibrium fluctuations in small systems: from physics to biology *Advances in Chemical Physics* ed S A Rice, vol 137 (Hoboken, NJ: Wiley) (https://doi.org/10.1002/9780470238080.ch2)
[16] Van den Broeck C and Esposito M 2015 Ensemble and trajectory thermodynamics: a brief introduction *Physica* A **418** 6–16
[17] MacKintosh F C and Schmidt C F 2010 Active cellular materials *Curr. Opin. Cell Biol.* **22** 29–35
[18] Marchetti M C, Joanny J F, Ramaswamy S, Liverpool T B, Prost J, Rao M and Simha R A 2013 Hydrodynamics of soft active matter *Rev. Mod. Phys.* **85** 1143–89
[19] Ramaswamy S 2010 The mechanics and statistics of active matter *Annu. Rev. Condens. Matter Phys.* **1** 323–45
[20] Joanny J-F and Prost J 2009 Active gels as a description of the actin-myosin cytoskeleton *HFSP J.* **3** 94–104
[21] Prost J, Julicher F and Joanny J-F F 2015 Active gel physics *Nat. Phys.* **11** 111–7
[22] Battle C, Broedersz C P, Fakhri N, Geyer V F, Howard J, Schmidt C F and MacKintosh F C 2016 Broken detailed balance at mesoscopic scales in active biological systems *Science* **352** 604–7
[23] Zia R K P and Schmittmann B 2007 Probability currents as principal characteristics in the statistical mechanics of non-equilibrium steady states *J. Stat. Mech.* **2007** P07012
[24] Ajdari A, Prost J, Ju F and Jülicher F 1997 Modeling molecular motors *Rev. Mod. Phys.* **69** 1269–81
[25] Howard J 2001 Mechanics of motor proteins and the cytoskeleton *Sinauer* **7** 384
[26] Bausch A R and Kroy K 2006 A bottom-up approach to cell mechanics *Nat. Phys.* **2** 231–8
[27] Glaser J and Kroy K 2010 Fluctuations of stiff polymers and cell mechanics *Biopolymers* 509–34
[28] Egolf D A 2000 Equilibrium regained: from nonequilibrium chaos to statistical mechanics *Science* **287** 101–4
[29] Rupprecht J-F and Prost J 2016 A fresh eye on nonequilibrium systems *Science* **352** 514–5
[30] Weber S C, Spakowitz A J and Theriot J A 2012 Nonthermal ATP-dependent fluctuations contribute to the *in vivo* motion of chromosomal loci *Proc. Natl Acad. Sci. USA* **109** 7338–43
[31] Almonacid M, Ahmed W W, Bussonnier M, Mailly P, Betz T, Voituriez R, Gov N S and Verlhac M-H 2015 Active diffusion positions the nucleus in mouse oocytes *Nat. Cell Biol.* **17** 470–9
[32] Brangwynne C P, Koenderink G H, MacKintosh F C and Weitz D A 2009 Intracellular transport by active diffusion *Trends Cell Biol.* **19** 423–7
[33] Brangwynne C P, Mitchison T J and Hyman A A 2011 Active liquid-like behavior of nucleoli determines their size and shape in Xenopus laevis oocytes *Proc. Natl Acad. Sci. USA* **108** 4334–9
[34] Fakhri N, Wessel A D, Willms C, Pasquali M, Klopfenstein D R, MacKintosh F C and Schmidt C F 2014 High-resolution mapping of intracellular fluctuations using carbon nanotubes *Science* **344** 1031–5
[35] Betz T, Lenz M, Joanny J-F and Sykes C 2009 ATP-dependent mechanics of red blood cells *Proc. Natl Acad. Sci. USA* **106** 15320–5
[36] Turlier H, Fedosov D A, Audoly B, Auth T, Gov N S, Sykes C, Joanny J-F, Gompper G and Betz T 2016 Equilibrium physics breakdown reveals the active nature of red blood cell flickering *Nat. Phys.* **12** 513–9
[37] Ben-Isaac E, Park Y, Popescu G, Brown F L H, Gov N S and Shokef Y 2011 Effective temperature of red-blood-cell membrane fluctuations *Phys. Rev. Lett.* **106** 238103
[38] Tuvia S, Almagor A, Bitler A, Levin S, Korenstein R and Yedgar S 1997 Cell membrane fluctuations are regulated by medium macroviscosity: evidence for a metabolic driving force *Proc. Natl Acad. Sci.* **94** 5045–9
[39] Monzel C, Schmidt D, Kleusch C, Kirchenbüchler D, Seifert U, Smith A-S, Sengupta K and Merkel R 2015 Measuring fast stochastic displacements of bio-membranes with dynamic optical displacement spectroscopy *Nat. Commun.* **6** 8162

[40] Battle C, Ott C M, Burnette D T, Lippincott-Schwartz J and Schmidt C F 2015 Intracellular and extracellular forces drive primary cilia movement *Proc. Natl Acad. Sci. USA* **112** 1410–5

[41] Fodor É, Mehandia V, Comelles J, Thiagarajan R, Gov N S, Visco P, van Wijland F and Riveline D 2015 From motorinduced fluctuations to mesoscopic dynamics in epithelial tissues **1** 1–5 (arXiv:1512.01476)

[42] Lau A W C, Hoffman B D, Davies A, Crocker J C and Lubensky T C 2003 Microrheology, stress fluctuations, and active behavior of living cells *Phys. Rev. Lett.* **91** 198101

[43] Mizuno D, Tardin C, Schmidt C F and MacKintosh F C 2007 Nonequilibrium mechanics of active cytoskeletal networks *Science* **315** 370–3

[44] Mizuno D, Head D A, MacKintosh F C and Schmidt C F 2008 Active and passive microrheology in equilibrium and nonequilibrium systems *Macromolecules* **41** 7194–202

[45] Guo M, Ehrlicher A J, Jensen M H, Renz M, Moore J R, Goldman R D, Lippincott-Schwartz J, Mackintosh F C and Weitz D A 2014 Probing the stochastic, motor-driven properties of the cytoplasm using force spectrum microscopy *Cell* **158** 822–32

[46] Schaller V, Weber C, Semmrich C, Frey E and Bausch A R 2010 Polar patterns of driven filaments *Nature* **467** 73–7

[47] Schaller V, Weber C A, Hammerich B, Frey E and Bausch A R 2011 Frozen steady states in active systems *Proc. Natl Acad. Sci. USA* **108** 19183–8

[48] Soares e Silva M *et al* 2011 Active multistage coarsening of actin networks driven by myosin motors *Proc. Natl Acad. Sci. USA* **108** 9408–13

[49] Murrell M P and Gardel M L 2012 F-actin buckling coordinates contractility and severing in a biomimetic actomyosin cortex *Proc. Natl Acad. Sci. USA* **109** 20820–5

[50] Alvarado J, Sheinman M, Sharma A, MacKintosh F C and Koenderink G H 2013 Molecular motors robustly drive active gels to a critically connected state *Nat. Phys.* **9** 591–7

[51] Lenz M 2014 Geometrical origins of contractility in disordered actomyosin networks *Phys. Rev.* X **4** 041002

[52] Koenderink G H, Dogic Z, Nakamura F, Bendix P M, MacKintosh F C, Hartwig J H, Stossel T P and Weitz D A 2009 An active biopolymer network controlled by molecular motors *Proc. Natl Acad. Sci. USA* **106** 15192–7

[53] Sheinman M, Broedersz C P and MacKintosh F C 2012 Actively stressed marginal networks *Phys. Rev. Lett.* **109** 238101

[54] Broedersz C P and MacKintosh F C 2011 Molecular motors stiffen non-affine semiflexible polymer networks *Soft Matter* **7** 3186–91

[55] Brangwynne C P, Koenderink G H, MacKintosh F C and Weitz D A 2008 Nonequilibrium microtubule fluctuations in a model cytoskeleton *Phys. Rev. Lett.* **100** 118104

[56] Aragon S R and Pecora R 1985 Dynamics of wormlike chains *Macromolecules* **18** 1868–75

[57] Gittes F, Mickey B, Nettleton J and Howard J 1993 Flexural rigidity of microtubules and actin filaments measured from thermal fluctuations in shape *J. Cell Biol.* **120** 923–34

[58] Brangwynne C P, Koenderink G H, Barry E, Dogic Z, MacKintosh F C and Weitz D A 2007 Bending dynamics of fluctuating biopolymers probed by automated high-resolution filament tracking *Biophys. J.* **93** 346–59

[59] Gladrow J, Fakhri N, MacKintosh F C, Schmidt C F and Broedersz C P 2016 Broken detailed balance of filament dynamics in active networks *Phys. Rev. Lett.* **116** 248301

[60] Gladrow J, Broedersz C P and Schmidt C F 2017 Nonequilibrium dynamics of probe filaments in actin-myosin networks *Phys. Rev.* E **96** 022408

[61] Cicuta P and Donald A M 2007 Microrheology: a review of the method and applications *Soft Matter* **3** 1449–55

[62] Mason T G, Ganesan K, van Zanten J H, Wirtz D and Kuo S C 1997 Particle tracking microrheology of complex fluids *Phys. Rev. Lett.* **79** 3282–5

[63] MacKintosh F and Schmidt C 1999 Microrheology *Curr. Opin. Colloid Interface Sci.* **4** 300–7

[64] Waigh T A 2005 Microrheology of complex fluids *Rep. Prog. Phys.* **68** 685

[65] Levine A J and Lubensky T C 2000 One- and two-particle microrheology *Phys. Rev. Lett.* **85** 1774–7

[66] Jensen M H, Morris E J and Weitz D A 2015 Mechanics and dynamics of reconstituted cytoskeletal systems *Biochim. Biophys. Acta* **1853** 3038–42

[67] Lieleg O, Claessens M M A E, Heussinger C, Frey E and Bausch A R 2007 Mechanics of bundled semiflexible polymer networks *Phys. Rev. Lett.* **99** 88102

[68] Lieleg O, Claessens M M A E and Bausch A R 2010 Structure and dynamics of cross-linked actin networks *Soft Matter* **6** 218–25

[69] Mahaffy R E, Shih C K, MacKintosh F C and Käs J 2000 Scanning probe-based frequency-dependent microrheology of polymer gels and biological cells *Phys. Rev. Lett.* **85** 880–3

[70] Gardel M L, Valentine M T, Crocker J C, Bausch A R and Weitz D A 2003 Microrheology of entangled F-actin solutions *Phys. Rev. Lett.* **91** 158302

[71] Tseng Y, Kole T P and Wirtz D 2002 Micromechanical mapping of live cells by multiple-particle-tracking microrheology *Biophys. J.* **83** 3162–76

[72] Keller M, Tharmann R, Dichtl M A, Bausch A R and Sackmann E 2003 Slow filament dynamics and viscoelasticity in entangled and active actin networks *Phil. Trans. R. Soc.* **361** 699–712

[73] Uhde J, Keller M, Sackmann E, Parmeggiani A and Frey E 2004 Internal motility in stiffening actin-myosin networks *Phys. Rev. Lett.* **93** 268101

[74] Wilhelm C 2008 Out-of-equilibrium microrheology inside living cells *Phys. Rev. Lett.* **101** 28101

[75] Fabry B, Maksym G N, Butler J P, Glogauer M, Navajas D and Fredberg J J 2001 Scaling the microrheology of living cells *Phys. Rev. Lett.* **87** 148102

[76] Bausch A R, Möller W and Sackmann E 1999 Measurement of local viscoelasticity and forces in living cells by magnetic tweezers *Biophys. J.* **76** 573–9

[77] Ma R, Klindt G S, Riedel-Kruse I H, Jülicher F and Friedrich B M 2014 Active phase and amplitude fluctuations of flagellar beating *Phys. Rev. Lett.* **113** 048101

[78] Callen H B and Welton T A 1951 Irreversibility and generalized noise *Phys. Rev.* **83** 34–40

[79] Kubo R 1966 The fluctuation-dissipation theorem *Rep. Prog. Phys.* **29** 255

[80] Martin P, Hudspeth A J and Jülicher F 2001 Comparison of a hair bundle's spontaneous oscillations with its response to mechanical stimulation reveals the underlying active process *Proc. Natl Acad. Sci. USA* **98** 14380–5

[81] Van Dijk P, Mason M J, Schoffelen R L, Narins P M and Meenderink S W 2011 Mechanics of the frog ear *Hear. Res.* **273** 46–58

[82] Cugliandolo L F, Kurchan J and Peliti L 1997 Energy flow, partial equilibration, and effective temperatures in systems with slow dynamics *Phys. Rev.* E **55** 3898–914

[83] Loi D, Mossa S and Cugliandolo L F 2008 Effective temperature of active matter *Phys. Rev.* E **77** 51111

[84] Bursac P, Lenormand G, Fabry B, Oliver M, Weitz D A, Viasnoff V, Butler J P and Fredberg J J 2005 Cytoskeletal remodelling and slow dynamics in the living cell *Nat. Mater.* **4** 557–61

[85] Prost J, Joanny J-F and Parrondo J M R 2009 Generalized fluctuation-dissipation theorem for steady-state systems *Phys. Rev. Lett.* **103** 090601

[86] Cugliandolo L F 2011 *J. Phys. A Math. Theor.* **44** 483001
[87] Fodor É, Nardini C, Cates M E, Tailleur J, Visco P and van Wijland F 2016 How far from equilibrium is active matter? *Phys. Rev. Lett.* **117** 038103
[88] Fodor É, Guo M, Gov N S, Visco P, Weitz D A and van Wijland F 2015 Activity-driven fluctuations in living cells *Europhys. Lett.* **110** 48005
[89] Dieterich E, Seifert U, Ritort F, Camunas-Soler J, Ribezzi-Crivellari M, Seifert U and Ritort F 2015 Single-molecule measurement of the effective temperature in non-equilibrium steady states *Nat. Phys.* **11** 1–8
[90] Chaikin P M and Lubensky T C 1995 *Principles of Condensed Matter Physics* (Cambridge: Cambridge University Press)
[91] Yamada S, Wirtz D and Kuo S C 2000 Mechanics of living cells measured by laser tracking microrheology *Biophys. J.* **78** 1736–47
[92] Mason T G and Weitz D A 1995 Optical measurements of frequency-dependent linear viscoelastic moduli of complex fluids *Phys. Rev. Lett.* **74** 1250–3
[93] Ziemann F, Rädler J and Sackmann E 1994 Local measurements of viscoelastic moduli of entangled actin networks using an oscillating magnetic bead micro-rheometer *Biophys. J.* **66** 2210–6
[94] Amblard F, Maggs A C, Yurke B, Pargellis A N and Leibler S 1996 Subdiffusion and anomalous local viscoelasticity in actin networks *Phys. Rev. Lett.* **77** 4470–3
[95] Schmidt F G, Ziemann F and Sackmann E 1996 Shear field mapping in actin networks by using magnetic tweezers *Eur. Biophys. J.* **24** 348–53
[96] Beroz F, Jawerth L M, Münster S, Weitz D A, Broedersz C P and Wingreen N S 2017 Physical limits to biomechanical sensing in disordered fibre networks *Nat. Commun.* **8** 16096
[97] Jones C A R, Cibula M, Feng J, Krnacik E A, McIntyre D H, Levine H and Sun B 2015 Micromechanics of cellularized biopolymer networks *Proc. Natl Acad. Sci. USA* **112** E5117–22
[98] Crocker J C, Valentine M T, Weeks E R, Gisler T, Kaplan P D, Yodh A G and Weitz D A 2000 Two-point microrheology of inhomogeneous soft materials *Phys. Rev. Lett.* **85** 888–91
[99] Schnurr B, Gittes F, MacKintosh F C and Schmidt C F 1997 Determining microscopic viscoelasticity in flexible and semiflexible polymer networks from thermal fluctuations *Macromolecules* **30** 7781–92
[100] Addas K M, Schmidt C F and Tang J X 2004 Microrheology of solutions of semiflexible biopolymer filaments using laser tweezers interferometry *Phys. Rev.* E **70** 021503
[101] Gittes F and MacKintosh F C 1998 Dynamic shear modulus of a semiflexible polymer network *Phys. Rev.* E **58** R1241–4
[102] Gittes F, Schnurr B, Olmsted P D, MacKintosh F C and Schmidt C F 1997 Microscopic viscoelasticity: shear moduli of soft materials determined from thermal fluctuations *Phys. Rev. Lett.* **79** 3286–9
[103] Chen D T, Weeks E R, Crocker J C, Islam M F, Verma R, Gruber J, Levine A J, Lubensky T C and Yodh A G 2003 Rheological microscopy: local mechanical properties from microrheology *Phys. Rev. Lett.* **90** 108301
[104] Mason T G 2000 Estimating the viscoelastic moduli of complex fluids using the generalized Stokes–Einstein equation *Rheol. Acta* **39** 371–8
[105] Helfer E, Harlepp S, Bourdieu L, Robert J, MacKintosh F C and Chatenay D 2000 Microrheology of biopolymer-membrane complexes *Phys. Rev. Lett.* **85** 457
[106] Fedosov D A, Caswell B and Karniadakis G E 2010 A multiscale red blood cell model with accurate mechanics, rheology, and dynamics *Biophys. J.* **98** 2215–25
[107] Lee M H, Reich D H, Stebe K J and Leheny R L 2010 Combined passive and active microrheology study of protein-layer formation at an AirWater interface *Langmuir* **26** 2650–8
[108] Prasad V, Koehler S A and Weeks E R 2006 Two-particle microrheology of quasi-2D viscous systems *Phys. Rev. Lett.* **97** 176001
[109] Ortega F, Ritacco H and Rubio R G 2010 Interfacial microrheology: particle tracking and related techniques *Curr. Opin. Colloid Interface Sci.* **15** 237–45
[110] Caspi A, Granek R and Elbaum M 2000 Enhanced diffusion in active intracellular transport *Phys. Rev. Lett.* **85** 5655
[111] MacKintosh F C and Levine A J 2008 Nonequilibrium mechanics and dynamics of motor-activated gels *Phys. Rev. Lett.* **100** 18104
[112] Vella F 1994 Molecular biology of the cell (third edition): By B Alberts, D Bray, J Lewis, M Raff, K Roberts and J D Watson. pp 1361. Garland Publishing, New York and London. 1994 *Biochem. Educ.* **22** 164
[113] Kasza K E, Rowat A C, Liu J, Angelini T E, Brangwynne C P, Koenderink G H and Weitz D A 2007 The cell as a material *Curr. Opin. Cell Biol.* 19 101–7
[114] Köhler S and Bausch A R 2012 Contraction mechanisms in composite active actin networks *PLoS One* **7** e39869
[115] Stricker J, Falzone T and Gardel M L 2010 Mechanics of the F-actin cytoskeleton *J. Biomech.* **43** 9–14
[116] Lin Y-C, Koenderink G H, MacKintosh F C and Weitz D A 2007 Viscoelastic properties of microtubule networks *Macromolecules* **40** 7714–20
[117] Kasza K E, Broedersz C P, Koenderink G H, Lin Y C, Messner W, Millman E A, Nakamura F, Stossel T P, MacKintosh F C and Weitz D A 2010 Actin filament length tunes elasticity of flexibly cross-linked actin networks *Biophys. J.* **99** 1091–100
[118] Gardel M L, Kasza K E, Brangwynne C P, Liu J and Weitz D A 2008 Mechanical response of cytoskeletal networks *Methods Cell Biol.* **89** 487–519
[119] Pelletier V, Gal N, Fournier P and Kilfoil M L 2009 Microrheology of microtubule solutions and actin-microtubule composite networks *Phys. Rev. Lett.* **102** 188303
[120] Murrell M, Oakes P W, Lenz M and Gardel M L 2015 Forcing cells into shape: the mechanics of actomyosin contractility *Nat. Rev. Mol. Cell Biol.* **16** 486–98
[121] Schaller V, Weber C, Frey E and Bausch A R 2011 Polar pattern formation: hydrodynamic coupling of driven filaments *Soft Matter* **7** 3213–8
[122] Bendix P M, Koenderink G H, Cuvelier D, Dogic Z, Koeleman B N, Brieher W M, Field C M, Mahadevan L and Weitz D A 2008 A quantitative analysis of contractility in active cytoskeletal protein networks *Biophys. J.* **94** 3126–36
[123] Ronceray P, Broedersz C P and Lenz M 2016 Fiber networks amplify active stress *Proc. Natl Acad. Sci. USA* **113** 2827–32
[124] Lenz M, Thoresen T, Gardel M L and Dinner A R 2012 Contractile units in disordered actomyosin bundles arise from F-actin buckling *Phys. Rev. Lett.* **108** 238107
[125] Wang S and Wolynes P G 2012 Active contractility in actomyosin networks *Proc. Natl Acad. Sci. USA* **109** 6446–51
[126] Howard J 2002 Mechanics of motor proteins *Physics of Bio-Molecules and Cells Physics des Biomolfégcules des Cellules* (New York: Springer) pp 69–94
[127] Levine A J and MacKintosh F C 2009 The mechanics and fluctuation spectrum of active gels *J. Phys. Chem.* B **113** 3820–30
[128] Storm C, Pastore J J, MacKintosh F C, Lubensky T C and Janmey P A 2005 Nonlinear elasticity in biological gels *Nature* **435** 191–4
[129] Gardel M L 2004 Elastic behavior of cross-linked and bundled actin networks *Science* **304** 1301–5

[130] Kasza K E, Koenderink G H, Lin Y C, Broedersz C P, Messner W, Nakamura F, Stossel T P, Mac Kintosh F C and Weitz D A 2009 Nonlinear elasticity of stiff biopolymers connected by flexible linkers *Phys. Rev.* E **79** 41928

[131] Lin Y-C, Yao N Y, Broedersz C P, Herrmann H, MacKintosh F C and Weitz D A 2010 Origins of elasticity in intermediate filament networks *Phys. Rev. Lett.* **104** 58101

[132] Shokef Y and Safran S A 2012 Scaling laws for the response of nonlinear elastic media with implications for cell mechanics *Phys. Rev. Lett.* **108** 178103

[133] Ronceray P and Lenz M 2015 Connecting local active forces to macroscopic stress in elastic media *Soft Matter* **11** 1597–605

[134] Hawkins R J and Liverpool T B 2014 Stress reorganization and response in active solids *Phys. Rev. Lett.* **113** 28102

[135] Xu X and Safran S A 2015 Nonlinearities of biopolymer gels increase the range of force transmission *Phys. Rev.* E **92** 032728

[136] Chen P and Shenoy V B 2011 Strain stiffening induced by molecular motors in active crosslinked biopolymer networks *Soft Matter* **7** 355–8

[137] Tee S-Y, Bausch A R and Janmey P A 2009 The mechanical cell *Curr. Biol.* **19** R745–8

[138] Lam W A, Chaudhuri O, Crow A, Webster K D, Li T-D, Kita A, Huang J and Fletcher D A 2011 Mechanics and contraction dynamics of single platelets and implications for clot stiffening *Nat. Mater.* **10** 61

[139] Jansen K A, Bacabac R G, Piechocka I K and Koenderink G H 2013 Cells actively Stiffen Fibrin networks by generating contractile stress *Biophys. J.* **105** 2240–51

[140] Toyota T, Head D A, Schmidt C F and Mizuno D 2011 Non-Gaussian athermal fluctuations in active gels *Soft Matter* **7** 3234–9

[141] Stuhrmann B, Soares e Silva M, Depken M, MacKintosh F C and Koenderink G H 2012 Nonequilibrium fluctuations of a remodeling *in vitro* cytoskeleton *Phys. Rev.* E **86** 20901

[142] Bertrand O J N, Fygenson D K and Saleh O A 2012 Active, motor-driven mechanics in a DNA gel *Proc. Natl Acad. Sci. USA* **109** 17342–7

[143] Deng L, Trepat X, Butler J P, Millet E, Morgan K G, Weitz D A and Fredberg J J 2006 Fast and slow dynamics of the cytoskeleton *Nat. Mater.* **5** 636–40

[144] Ahmed W W and Betz T 2015 Dynamic cross-links tune the solid–fluid behavior of living cells *Proc. Natl Acad. Sci. USA* **112** 6527–8

[145] Ehrlicher A J, Krishnan R, Guo M, Bidan C M, Weitz D A and Pollak M R 2015 Alpha-actinin binding kinetics modulate cellular dynamics and force generation *Proc. Natl Acad. Sci. USA* **112** 6619–24

[146] Yao N Y, Broedersz C P, Depken M, Becker D J, Pollak M R, MacKintosh F C and Weitz D A 2013 Stress-enhanced gelation: a dynamic nonlinearity of elasticity *Phys. Rev. Lett.* **110** 18103

[147] Humphrey D, Duggan C, Saha D, Smith D and Kas J 2002 Active fluidization of polymer networks through molecular motors *Nature* **416** 413–6

[148] Fernández P and Ott A 2008 Single cell mechanics: stress stiffening and kinematic hardening *Phys. Rev. Lett.* **100** 238102

[149] Wolff L, Fernández P and Kroy K 2012 Resolving the stiffening-softening paradox in cell mechanics *PLoS One* **7** 1–7

[150] Krishnan R *et al* 2009 Reinforcement versus fluidization in cytoskeletal mechanoresponsiveness *PLoS One* **4** e5486

[151] Trepat X, Deng L, An S S, Navajas D, Tschumperlin D J, Gerthoffer W T, Butler J P and Fredberg J J 2007 Universal physical responses to stretch in the living cell *Nature* **447** 592–5

[152] Sollich P, Lequeux F, Hébraud P and Cates M E 1997 Rheology of soft glassy materials *Phys. Rev. Lett.* **78** 2020–3

[153] Semmrich C, Storz T, Glaser J, Merkel R, Bausch A R and Kroy K 2007 Glass transition and rheological redundancy in F-actin solutions *Proc. Natl Acad. Sci. USA* **104** 20199–203

[154] Hoffman B D and Crocker J C 2009 Cell mechanics: dissecting the physical responses of cells to force *Annu. Rev. Biomed. Eng.* **11** 259–88

[155] Balland M, Desprat N, Icard D, Féréol S, Asnacios A, Browaeys J, Hénon S and Gallet F 2006 Power laws in microrheology experiments on living cells: comparative analysis and modeling *Phys. Rev.* E **74** 21911

[156] Sakaue T and Saito T 2017 Active diffusion of model chromosomal loci driven by athermal noise *Soft Matter* **13** 81–7

[157] Alcaraz J, Buscemi L, Grabulosa M, Trepat X, Fabry B, Farré R and Navajas D 2003 Microrheology of human lung epithelial cells measured by atomic force microscopy *Biophys. J.* **84** 2071–9

[158] Brangwynne C P, MacKintosh F C and Weitz D A 2007 Force fluctuations and polymerization dynamics of intracellular microtubules *Proc. Natl Acad. Sci. USA* **104** 16128–33

[159] Razin N, Voituriez R, Elgeti J and Gov N S 2017 Generalized Archimedes' principle in active fluids *Phys. Rev.* E **96** 032606

[160] Razin N, Voituriez R, Elgeti J and Gov N S 2017 Forces in inhomogeneous open active-particle systems *Phys. Rev.* E **96** 052409

[161] Ahmed W W, Fodor E, Almonacid M, Bussonnier M, Verlhac M-H, Gov N S, Visco P, van Wijland F and Betz T 2015 Active mechanics reveal molecular-scale force kinetics in living oocytes (arXiv:1510.08299)

[162] Weber S C, Spakowitz A J and Theriot J A 2010 Bacterial chromosomal loci move subdiffusively through a viscoelastic cytoplasm *Phys. Rev. Lett.* **104** 238102

[163] Vandebroek H and Vanderzande C 2015 Dynamics of a polymer in an active and viscoelastic bath *Phys. Rev.* E **92** 060601

[164] MacKintosh F C 2012 Active diffusion: the erratic dance of chromosomal loci *Proc. Natl Acad. Sci. USA* **109** 7138–9

[165] Parry B R, Surovtsev I V, Cabeen M T, O'Hern C S, Dufresne E R and Jacobs-Wagner C 2014 The bacterial cytoplasm has glass-like properties and is fluidized by metabolic activity *Cell* **156** 183–94

[166] Evans E A 1983 Bending elastic modulus of red blood cell membrane derived from buckling instability in micropipet aspiration tests *Biophys. J.* **43** 27–30

[167] Granek R 1997 From semi-flexible polymers to membranes: anomalous diffusion and reptation *J. Phys.* II **7** 1761–88

[168] Granek R 2011 Membrane surrounded by viscoelastic continuous media: anomalous diffusion and linear response to force *Soft Matter* **7** 5281

[169] Lin L C, Gov N and Brown F L H 2006 Nonequilibrium membrane fluctuations driven by active proteins *J. Chem. Phys.* **124** 074903

[170] Milner S T and Safran S A 1987 Dynamical fluctuations of droplet microemulsions and vesicles *Phys. Rev.* A **36** 4371–9

[171] Brochard F and Lennon J 1975 Frequency spectrum of the flicker phenomenon in erythrocytes *J. Phys.* **36** 1035–47

[172] Strey H, Peterson M and Sackmann E 1995 Measurement of erythrocyte membrane elasticity by flicker eigenmode decomposition *Biophys. J.* **69** 478–88

[173] Gov N 2004 Membrane undulations driven by force fluctuations of active proteins *Phys. Rev. Lett.* **93** 268104

[174] Gov N and Safran S 2005 Red blood cell membrane fluctuations and shape controlled by ATP-induced cytoskeletal defects *Biophys. J.* **88** 1859–74

[175] Park Y, Best C A, Auth T, Gov N S, Safran S A, Popescu G, Suresh S and Feld M S 2010 Metabolic remodeling of the human red blood cell membrane *Proc. Natl Acad. Sci. USA* **107** 1289–94

[176] Yoon Y Z, Kotar J, Brown A T and Cicuta P 2011 Red blood cell dynamics: from spontaneous fluctuations to non-linear response *Soft Matter* **7** 2042–51

[177] Rodríguez-García R, López-Montero I, Mell M, Egea G, Gov N S and Monroy F 2016 Direct cytoskeleton forces cause membrane softening in red blood cells *Biophys. J.* **111** 1101

[178] Helfrich W 1973 Elastic properties of lipid bilayers: theory and possible experiments *Z. Nat.forsch.* C **28** 693–703

[179] Fenz S F, Bihr T, Schmidt D, Merkel R, Seifert U, Sengupta K and Smith A-S 2017 Membrane fluctuations mediate lateral interaction between cadherin bonds *Nat. Phys. Nat. Phys.* **13** 906

[180] Gallet F, Arcizet D, Bohec P and Richert A 2009 Power spectrum of out-of-equilibrium forces in living cells: amplitude and frequency dependence *Soft Matter* **5** 2947

[181] Osmanović D and Rabin Y 2017 Dynamics of active Rouse chains *Soft Matter* **13** 963–8

[182] Samanta N and Chakrabarti R 2016 Chain reconfiguration in active noise *J. Phys. A: Math. Theor.* **49** 195601

[183] Romanczuk P, Bär M, Ebeling W, Lindner B and Schimansky-Geier L 2012 Active Brownian particles *Eur. Phys. J. Spec. Top.* **202** 1–162

[184] Gardel M L, Valentine M T and Weitz D A 2005 Microrheology *Microscale Diagnostic Technology* (New York: Springer) pp 1–49

[185] Ben-Isaac E, Fodor É, Visco P, van Wijland F and Gov N S 2015 Modeling the dynamics of a tracer particle in an elastic active gel *Phys. Rev.* E **92** 12716

[186] Doi M 2013 *Soft Matter Physics* (Oxford: Oxford University Press)

[187] Gardiner C 1985 *Stochastic Methods* (*Springer Series in Synergetics*) (Berlin: Springer)

[188] Jarzynski C 2017 Stochastic and macroscopic thermodynamics of strongly coupled systems *Phys. Rev.* X **7** 011008

[189] Gallavotti G and Cohen E G D 1995 Dynamical ensembles in nonequilibrium statistical mechanics *Phys. Rev. Lett.* **74** 2694–7

[190] Jarzynski C 1996 A nonequilibrium equality for free energy differences *Phys. Rev. Lett.* **78** 2690–3

[191] Crooks G E 1999 Entropy production fluctuation theorem and the nonequilibrium work relation for free energy differences *Phys. Rev.* E **60** 2721–6

[192] Kurchan J 1998 Fluctuation theorem for stochastic dynamics *J. Phys. A: Math. Gen.* **31** 3719

[193] Sekimoto K 1997 Kinetic characterization of heat bath and the energetics of thermal ratchet models *J. Phys. Soc. Japan* **66** 1234–7

[194] Sekimoto K 1998 Langevin equation and thermodynamics *Prog. Theor. Phys. Suppl.* **130** 17–27

[195] Seifert U 2005 Entropy production along a stochastic trajectory and an integral fluctuaction theorem *Phys. Rev. Lett.* **95** 14380–5

[196] Lebowitz J L and Spohn H 1999 A Gallavotti–Cohen-type symmetry in the large deviation functional for stochastic dynamics *J. Stat. Phys.* **95** 333–65

[197] Speck T, Blickle V, Bechinger C and Seifert U 2007 Distribution of entropy production for a colloidal particle in a nonequilibrium steady state *Europhys. Lett.* **79** 30002

[198] Schmiedl T and Seifert U 2007 Optimal finite-time processes in stochastic thermodynamics *Phys. Rev. Lett.* **98** 108301

[199] Machta B B 2015 Dissipation bound for thermodynamic control *Phys. Rev. Lett.* **115** 1–5

[200] Sivak D A and Crooks G E 2012 Thermodynamic metrics and optimal paths *Phys. Rev. Lett.* **108** 1–5

[201] Harada T and Sasa S-I 2006 Energy dissipation and violation of the fluctuation-response relation in nonequilibrium Langevin systems *Phys. Rev.* E **73** 026131

[202] Toyabe S, Okamoto T, Watanabe-Nakayama T, Taketani H, Kudo S and Muneyuki E 2010 Nonequilibrium energetics of a single F-ATPase molecule *Phys. Rev. Lett.* **104** 198103

[203] Ariga T, Tomishige M and Mizuno D 2017 Nonequilibrium energetics of molecular motor, kinesin-1 *Biophys. J.* **114** 509a

[204] Esposito M 2012 Stochastic thermodynamics under coarse graining *Phys. Rev.* E **85** 41125

[205] Wang S-W, Kawaguchi K, Sasa S-I and Tang L-H 2016 Entropy production of nanosystems with time scale separation *Phys. Rev. Lett.* **117** 70601

[206] Polettini M and Esposito M 2017 Effective thermodynamics for a marginal observer *Phys. Rev. Lett.* **119** 240601

[207] Shiraishi N and Sagawa T 2015 Fluctuation theorem for partially masked nonequilibrium dynamics *Phys. Rev.* E **91** 012130

[208] Bisker G, Polettini M, Gingrich T R and Horowitz J M 2017 Hierarchical bounds on entropy production inferred from partial information *J. Stat. Mech.* **2017** 093210

[209] Roldán É, Neri I, Dörpinghaus M, Meyr H and Jülicher F 2015 Decision making in the arrow of time *Phys. Rev. Lett.* **115** 250602

[210] Neri I, Roldán É and Jülicher F 2017 Statistics of infima and stopping times of entropy production and applications to active molecular processes *Phys. Rev.* X **7** 011019

[211] Berezhkovskii A, Hummer G and Bezrukov S 2006 Identity of distributions of direct uphill and downhill translocation times for particles traversing membrane channels *Phys. Rev. Lett.* **97** 020601

[212] Qian H and Sunney Xie X 2006 Generalized Haldane equation and fluctuation theorem in the steady-state cycle kinetics of single enzymes *Phys. Rev.* E **74** 010902

[213] Kolomeisky A B, Stukalin E B and Popov A A 2005 Understanding mechanochemical coupling in kinesins using first-passage-time processes *Phys. Rev.* E **71** 031902

[214] Stern F 1977 An independence in Brownian motion with constant drift *Ann. Probab.* **5** 571–2

[215] Pigolotti S, Neri I, Roldán É and Jülicher F 2017 Generic properties of stochastic entropy production *Phys. Rev. Lett.* **119** 140604

[216] Loutchko D, Eisbach M and Mikhailov A S 2017 Stochastic thermodynamics of a chemical nanomachine: the channeling enzyme tryptophan synthase *J. Chem. Phys.* **146** 025101

[217] Berg J 2008 Out-of-equilibrium dynamics of gene expression and the Jarzynski equality *Phys. Rev. Lett.* **100** 1–4

[218] Liphardt J 2002 Equilibrium information from nonequilibrium measurements in an experimental test of Jarzynski's equality *Science* **296** 1832–5

[219] Alemany A, Mossa A, Junier I and Ritort F 2012 Experimental free-energy measurements of kinetic molecular states using fluctuation theorems *Nat. Phys.* **8** 688–94

[220] Collin D, Ritort F, Jarzynski C, Smith S B, Tinoco I and Bustamante C 2005 Verification of the Crooks fluctuation theorem and recovery of RNA folding free energies *Nature* **437** 231–4

[221] Hayashi K, Ueno H, Iino R and Noji H 2010 Fluctuation theorem applied to F 1 -ATPase *Phys. Rev. Lett.* **104** 218103

[222] Ritort F 2006 Single-molecule experiments in biological physics: methods and applications *J. Phys.: Condens. Matter* **18** R531

[223] Schmiedl T and Seifert U 2007 Stochastic thermodynamics of chemical reaction networks *J. Chem. Phys.* **126** 044101

[224] Schmiedl T and Seifert U 2008 Efficiency of molecular motors at maximum power *Europhys. Lett.* **83** 30005

[225] Hartich D, Barato A C and Seifert U 2015 Nonequilibrium sensing and its analogy to kinetic proofreading *New J. Phys.* **17** 055026

[226] England J L 2013 Statistical physics of self-replication *J. Chem. Phys.* **139** 121923

[227] England J L 2015 Dissipative adaptation in driven self-assembly *Nat. Nanotechnol.* **10** 919–23

[228] Perunov N, Marsland R A and England J L 2016 Statistical physics of adaptation *Phys. Rev.* X **6** 021036

[229] Rouvas-Nicolis C and Nicolis G 2009 Butterfly effect *Scholarpedia* **4** 1720

[230] Weiss J B 2003 Coordinate invariance in stochastic dynamical systems *Tellus* A **55** 208–18

[231] Horowitz J M, Zhou K and England J L 2017 Minimum energetic cost to maintain a target nonequilibrium state *Phys. Rev.* E **95** 042102

[232] Barkai N and Leibler S 1997 Robustness in simple biochemical networks to transfer and process information *Nature* **387** 913–7

[233] Alon U, Surette M G, Barkai N and Leibler S 1999 Robustness in bacterial chemotaxis *Nature* **397** 168–71

[234] Qian H 2006 Reducing intrinsic biochemical noise in cells and its thermodynamic limit *J. Mol. Biol.* **362** 387–92

[235] Sartori P and Tu Y 2015 Free energy cost of reducing noise while maintaining a high sensitivity *Phys. Rev. Lett.* **115** 118102

[236] Lan G and Tu Y 2016 Information processing in bacteria: memory, computation, and statistical physics: a key issues review *Rep. Prog. Phys.* **79** 052601

[237] Ito S and Sagawa T 2013 Information thermodynamics on causal networks *Phys. Rev. Lett.* **111** 1–6

[238] Sartori P, Granger L, Lee C F and Horowitz J M 2014 Thermodynamic costs of information processing in sensory adaptation *PLoS Comput. Biol.* **10** e1003974

[239] Lang A H, Fisher C K, Mora T and Mehta P 2014 Thermodynamics of statistical inference by cells *Phys. Rev. Lett.* **113** 148103

[240] Cao Y, Wang H, Ouyang Q and Tu Y 2015 The free-energy cost of accurate biochemical oscillations *Nat. Phys.* **11** 772–8

[241] Tomé T and de Oliveira M J 2012 Entropy production in nonequilibrium systems at stationary states *Phys. Rev. Lett.* **108** 020601

[242] Stein W D and Litman T 2014 *Channels, Carriers and Pumps: an Introduction to Membrane Transport* (New York: Academic) pp 1–406

[243] Bezrukov S M, Berezhkovskii A M, Pustovoit M A and Szabo A 2000 Particle number fluctuations in a membrane channel *J. Chem. Phys.* **113** 8206–11

[244] Berezhkovskii A and Bezrukov S 2008 Counting translocations of strongly repelling particles through single channels: fluctuation theorem for membrane transport *Phys. Rev. Lett.* **100** 038104

[245] Grünwald D, Singer R H and Rout M 2011 Nuclear export dynamics of RNAprotein complexes *Nature* **475** 333–41

[246] Gingrich T R, Horowitz J M, Perunov N and England J L 2016 Dissipation bounds all steady-state current fluctuations *Phys. Rev. Lett.* **116** 120601

[247] Barato A C and Seifert U 2015 Thermodynamic uncertainty relation for biomolecular processes *Phys. Rev. Lett.* **114** 158101

[248] Pietzonka P, Barato A C and Seifert U 2016 Universal bound on the efficiency of molecular motors *J. Stat. Mech.* 124004

[249] Pietzonka P, Ritort F and Seifert U 2017 Finite-time generalization of the thermodynamic uncertainty relation *Phys. Rev.* E **96** 012101

[250] Horowitz J M and Gingrich T R 2017 Proof of the finite-time thermodynamic uncertainty relation for steady-state currents *Phys. Rev.* E **96** 020103

[251] Gingrich T R and Horowitz J M 2017 Fundamental bounds on first passage time fluctuations for currents *Phys. Rev. Lett.* **119** 170601

[252] Riedel I H, Hilfinger A, Howard J and Jülicher F 2007 How molecular motors shape the flagellar beat *HFSP J.* **1** 192–208

[253] Wan K Y and Goldstein R E 2014 Rhythmicity, recurrence, and recovery of flagellar beating *Phys. Rev. Lett.* **113** 238103

[254] Singla V 2006 The primary cilium as the cell's antenna: signaling at a sensory organelle *Science* **313** 629–33

[255] Barnes B G 1961 Ciliated secretory cells in the pars distalis of the mouse hypophysis *J. Ultrastruct. Res.* **5** 453–67

[256] Paijmans J, Lubensky D K and ten Wolde P R 2017 A thermodynamically consistent model of the post-translational Kai circadian clock *PLoS Comput. Biol.* **13** e1005415

[257] Kimmel J C, Chang A Y, Brack A S and Marshall W F 2018 Inferring cell state by quantitative motility analysis reveals a dynamic state system and broken detailed balance *PLoS Comput. Biol.* **14** e1005927

[258] Lander B, Mehl J, Blickle V, Bechinger C and Seifert U 2012 Noninvasive measurement of dissipation in colloidal systems *Phys. Rev.* E **86** 030401

[259] Shannon C E and Weaver W 1949 *The Mathematical Theory of Communication* (Urbana: University of Illinois Press) p 125

[260] Bérut A, Imparato A, Petrosyan A and Ciliberto S 2016 Theoretical description of effective heat transfer between two viscously coupled beads *Phys. Rev.* E **94** 052148

[261] Crisanti A, Puglisi A and Villamaina D 2012 Nonequilibrium and information: The role of cross correlations *Phys. Rev.* E **85** 061127

[262] Weber C A, Suzuki R, Schaller V, Aranson I S, Bausch A R and Frey E 2015 Random bursts determine dynamics of active filaments *Proc. Natl Acad. Sci. USA* **112** 10703–7

[263] Everaers R, Jülicher F, Ajdari A and Maggs A C 1999 Dynamic fluctuations of semiflexible filaments *Phys. Rev. Lett.* **82** 3717–20

[264] Liverpool T B 2003 Anomalous fluctuations of active polar filaments *Phys. Rev.* E **67** 031909

[265] Levine A J, Liverpool T B and MacKintosh F C 2004 Dynamics of rigid and flexible extended bodies in viscous films and membranes *Phys. Rev. Lett.* **93** 038102

[266] Kikuchi N, Ehrlicher A, Koch D, Kas J A, Ramaswamy S and Rao M 2009 Buckling, stiffening, and negative dissipation in the dynamics of a biopolymer in an active medium *Proc. Natl Acad. Sci. USA* **106** 19776–9

[267] Loi D, Mossa S and Cugliandolo L F 2011 Non-conservative forces and effective temperatures in active polymers *Soft Matter* **7** 10193

[268] Ghosh A and Gov N S 2014 Dynamics of active semiflexible polymers *Biophys. J.* **107** 1065–73

[269] Eisenstecken T, Gompper G and Winkler R G 2017 Internal dynamics of semiflexible polymers with active noise *J. Chem. Phys.* **146** 154903

[270] Kratky O and Porod G 1949 Röntgenuntersuchung gelöster fadenmoleküle *Recueil Travaux Chim. Pays-Bas* **68** 1106–22

[271] Goldstein R E and Langer S A 1995 Nonlinear dynamics of stiff polymers *Phys. Rev. Lett.* **75** 1094–7
[272] Hallatschek O, Frey E and Kroy K 2007 Tension dynamics in semiflexible polymers. I. Coarse-grained equations of motion *Phys. Rev.* E **75** 031905
[273] Koenderink G H, Atakhorrami M, MacKintosh F C and Schmidt C F 2006 High-frequency stress relaxation in semiflexible polymer solutions and networks *Phys. Rev. Lett.* **96** 138307
[274] Mizuno D, Bacabac R, Tardin C, Head D and Schmidt C F 2009 High-resolution probing of cellular force transmission *Phys. Rev. Lett.* **102** 168102
[275] Yuval J and Safran S A 2013 Dynamics of elastic interactions in soft and biological matter *Phys. Rev.* E **87** 042703
[276] Weiss J B 2007 Fluctuation properties of steady-state Langevin systems *Phys. Rev.* E **76** 061128
[277] Lim H C, Surovtsev I V, Beltran B G, Huang F, Bewersdorf J and Jacobs-Wagner C 2014 Evidence for a DNA-relay mechanism in ParABS-mediated chromosome segregation *Elife* **3** e02758
[278] Wang X, Llopis P M and Rudner D Z 2013 Organization and segregation of bacterial chromosomes *Nat. Rev. Genet.* **14** 191–203
[279] Wilhelm L, Bürmann F, Minnen A, Shin H C, Toseland C P, Oh B H and Gruber S 2015 SMC condensin entraps chromosomal DNA by an ATP hydrolysis dependent loading mechanism in Bacillus subtilis *Elife* **4** https://doi.org/10.7554/eLife.06659
[280] Grill S W, Gönczy P, Stelzer E H and Hyman A A 2001 Polarity controls forces governing asymmetric spindle positioning in the Caenorhabditis elegans embryo *Nature* **409** 630–3
[281] Grill S W 2003 The distribution of active force generators controls mitotic spindle position *Science* **301** 518–21
[282] Pecreaux J, Röper J C, Kruse K, Jülicher F, Hyman A A, Grill S W and Howard J 2006 Spindle oscillations during asymmetric cell division require a threshold number of active cortical force generators *Curr. Biol.* **16** 2111–22
[283] Ou G, Stuurman N, D'Ambrosio M and Vale R D 2010 Polarized myosin produces unequal-size daughters during asymmetric cell division *Science* **330** 677–80
[284] Mayer M, Depken M, Bois J S, Jülicher F and Grill S W 2010 Anisotropies in cortical tension reveal the physical basis of polarizing cortical flows *Nature* **467** 617–21
[285] Thutupalli S, Sun M, Bunyak F, Palaniappan K and Shaevitz J W 2015 Directional reversals enable Myxococcus xanthus cells to produce collective 1D streams during fruiting-body formation *J. R. Soc. Interface* **12** 20150049
[286] Peruani F, Starruß J, Jakovljevic V, Søgaard-Andersen L, Deutsch A and Bär M 2012 Collective motion and nonequilibrium cluster formation in colonies of gliding bacteria *Phys. Rev. Lett.* **108** 098102
[287] Frauenfelder H, Wolynes P G and Austin R H 1999 Biological physics *Rev. Mod. Phys.* **71** S419–30
[288] Agerschou E D, Mast C B and Braun D 2017 Emergence of life from trapped nucleotides? Non-equilibrium behavior of oligonucleotides in thermal gradients *Synlett* **28** 56–63
[289] Schwille P and Diez S 2009 Synthetic biology of minimal systems *Crit. Rev. Biochem. Mol. Biol.* **44** 223–42

3 Nonequilibrium dynamics of isostatic spring networks

Abstract of the chapter

In chapter 2 we reviewed recent advances and challenges in inferring non-equilibrium in living systems and in extracting relevant information from their fluctuating trajectories. We have highlighted how broken detailed balance at the molecular scale might manifest itself differently at the larger cellular scales and how, from the theoretical point of view, there is limited understanding of how non-equilibrium measures are affected by the system's intrinsic structural properties.

In this chapter we introduce a minimal framework to study how the non equilibrium dynamics of biological systems are affected by their underlying mechanical properties. In particular, we propose to do so by employing a model of diluted spring networks that displays non-trivial critical mechanical behavior. Our system is driven into a non-equilibrium steady state by stochastic forces induced by motors. We model these motor-forces as active white noise at the nodes as well as colored noise. We quantify the non-equilibrium dynamics between pairs of node trajectories via a two-point measure, the cycling frequency ω. Interestingly, as we lower the connectivity of our network, the cycling frequencies show similar qualitative features independently of the kind of active driving. Furthermore, we find that in the vicinity of the isostatic point the scaling of the distribution of cycling frequencies can be captured by a homogeneity relation typical of critical systems. We give insight into the origin of this result via a mean-field two-beads model. Finally, we demonstrate how a divergent length-scale present in the system governs the large length-scale behavior of cycling frequencies. Overall, our approach elucidates the role of the isostatic threshold in determining the non-equilibrium dynamics of active marginal systems and offers concrete predictions that could be experimentally tested in non-invasive ways.

Research question: How does isostaticity affect the non-equilibrium dynamics of spring networks?

3.1 Mechanics of disordered spring networks

We begin this chapter by reviewing the concepts of rigidity transition and of isostaticity in disordered networks of Hookean springs at zero temperature.

3.1.1 Rigidity and Isostaticity

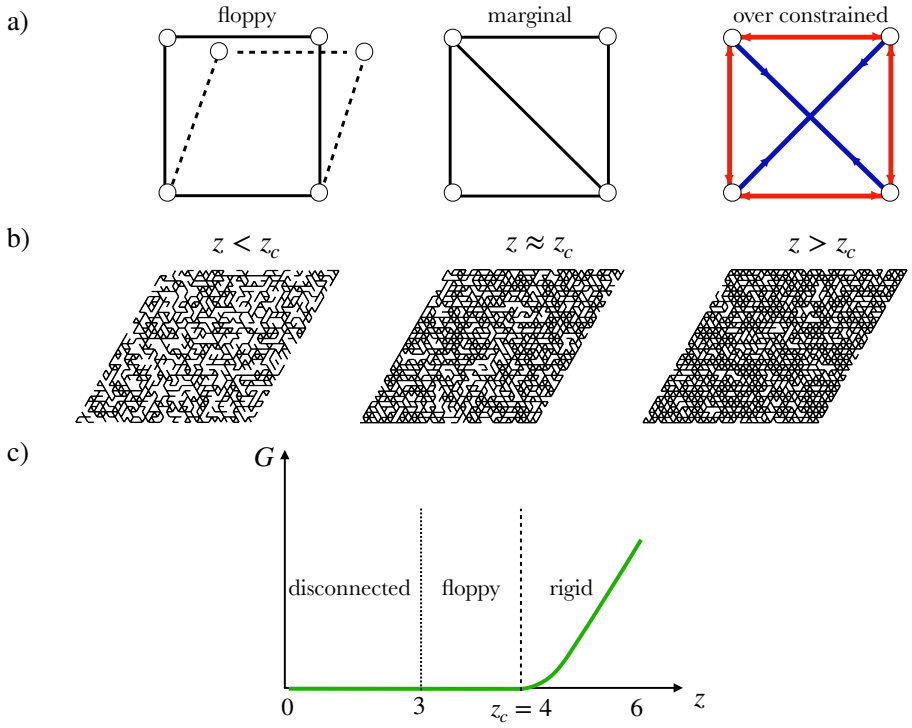

Figure 3.1 a) Left: example of a floppy structure where the number of internal degrees of freedom $Nd - d(d+1)/2$ is larger than the number of constraints N_c. Middle: an isostatic or marginal structure where $N_c = Nd - d(d+1)/2$ and the number of floppy modes N_0 is zero. Right: an over constrained structure with $N_c > Nd - d(d+1)/2$: a state of self stress is realized by imposing tensions on the external bonds and compressions on the cross-bonds. b) A sub-critical (left), a critical (middle) and a super-critical (right) randomly diluted triangular network. c) The shear modulus as a function of the connectivity for a diluted triangular network.

Isostaticity is a key concept to understand the structural rigidity not only of fiber networks, but also of foams, colloidal suspensions and granular packings close to jamming. A system is isostatic or marginal when it is, to linear order in the deformation, neither rigid or floppy. According to Maxwell's definition [75], in an isostatic structure of N vertices in d dimensions, the number of degrees of freedom

Nd is exactly balanced by the number of constraints N_c in the system. More precisely, Maxwell's counting argument states that the number of zero or floppy modes N_0 (*i. e.* zero-energy collective displacement modes) is given by

$$N_0 = Nd - d(d+1)/2 - N_c\,, \tag{3.1}$$

where $d(d+1)/2$ is the number of rigid body rotations and translations. A system is isostatic when $N_0 = 0$, which is a condition realized when the number of constraints N_c equals the number of *internal* degrees of freedom $Nd - d(d+1)/2$ (Fig. 3.1a middle). When the number of constraints is less than the number of internal degrees of freedom the structure is, to linear order, floppy and $N_0 > 0$ (Fig. 3.1a left). On the contrary, when the number of constraints exceeds the number of internal degrees of freedom the structure is overconstrained (See Fig. 3.1a right) and, according to Eq. (3.1) the number of zero modes is negative, which is unphysical. Maxwell's counting thus needs to be modified to include *states of self stress* N_s [76, 77]:

$$N_0 = Nd - \frac{d(d+1)}{2} - N_c + N_s\,. \tag{3.2}$$

A system is in a state of self stress if its bonds are under tension or compression in a way that the resulting force at the nodes is zero, as shown in Fig. 3.1a right. Importantly, if the system is isostatic ($N_c = Nd - d(d+1)/2$), a finite number of zero modes can arise because of states of self stress in the structure.

In this chapter we will focus on the properties of randomly diluted triangular networks in two dimensions, such as those shown in Fig. 3.1b. Eq. (3.1) can be expressed in terms of the connectivity z of the network by noting that $N_c = zN/2$: N is the total number of nodes in the network and periodic boundary conditions are realized. In the limit $N \gg 1$, we can neglect the number of rigid body motions and the isostaticity condition yields a critical connectivity $z_c = 4$. If disorder is realized in the lattice by randomly diluting bonds with probability $q = 1 - p$, $p \in [0, 1]$, then the average connectivity is $z = 6p$ and the critical dilution probability lies at $p_c = 2/3$. Similarly to Fig. 3.1a, different diluted network configurations in different elastic regimes are shown in Fig. 3.1b.

The linear elastic behavior of networks can be quantified by measuring their linear elastic moduli, such as the shear G modulus, when an infinitesimal external strain is imposed. As more and more bonds are removed, the system undergoes a mechanical phase transition, going from a rigid state where, *e.g.* G is non-zero and the system can resist strain deformations (Fig. 3.1b right), into a soft or floppy phase where G is zero (Fig. 3.1b left). Interestingly, G goes to zero continuously as the average connectivity z decreases from 1 (fully connected system) to 0 (fully disconnected system), as shown in Fig. 3.1 c. Moreover, this transition involves a diverging

length scale at the onset of rigidity, a connected set of critical exponents [78] and, more generally, contitutes a universality class known as *rigidity percolation* [79–81]. In a diluted triangular network, for $z > z_c$ the shear modulus scales linearly with the distance $z - z_c$ from the isostatic point, as shown in Fig. 3.1 c. The mean-field approach developed by Feng *et al.* known as Effective Medium Theory correctly predicts this scaling [81]. In the vicinity of z_c however, long range strain fluctuations induce a critical scaling regime that is not captured by EMT [78, 82]: $G \sim (z - z_c)^f$, $f \approx 1.4$ (3.1c). We will later on revisit the distinct critical regimes and EMT when investigating how non-equilibrium measures scale close to isostaticity. As a final remark, we note that although similar in form, the much better understood *connectivity percolation* problem constitutes a separate universality class. Indeed, while connectivity percolation ($z = 3$, $p = 0.5$ for the triangular network-Fig. 3.1c) identifies the point at which a cluster of connected nodes spans the system size, rigidity percolation occurs if the cluster is additionally rigid [80].

Given the limited number of parameters needed to describe such networks (namely the spring constant k and the dilution probability p), diluted spring networks have been one of the most employed model to study isostaticity. Their static linear response has been studied extensively both analytically and numerically at zero temperature [79, 80, 83], at finite non zero temperature [84], as well as in the presence of non-dissipative active stresses generated by contractile force dipoles [85]. Their rheology (dynamical response) when put in contact with a viscous fluid is also well understood [86]. Their well understood behavior at thermodynamic equilibrium makes spring networks an optimal ground to investigate what happens when dissipative, non-equilibrium driving is added to the system.

3.2 Actively driven disordered spring networks: the model

The field of active matter has been flourishing in the last years due to the possibility of investigating in a quantitative manner the properties of active systems such as membranes [87], tissues [88, 89], reconstituted cytoskeletal systems with motors [90], as well as active DNA gels [91]. Importantly, signatures of critical behavior have been detected in active systems such as actin-myosin assemblies, which can also self-organize and tune their connectivity close to a critical point [92, 93]. An accurate description of how motor-generated non-equilibrium driving affects the dynamics of critical biological networks is still lacking.

To bridge the gap between pre-existing theories of critical mechanical behavior and the thriving field of active matter, we introduce here a minimal theoretical model of a marginal elastic network where motors constantly exert contractile forces on the bonds. We consider a triangular network of spring-like bonds immersed in a

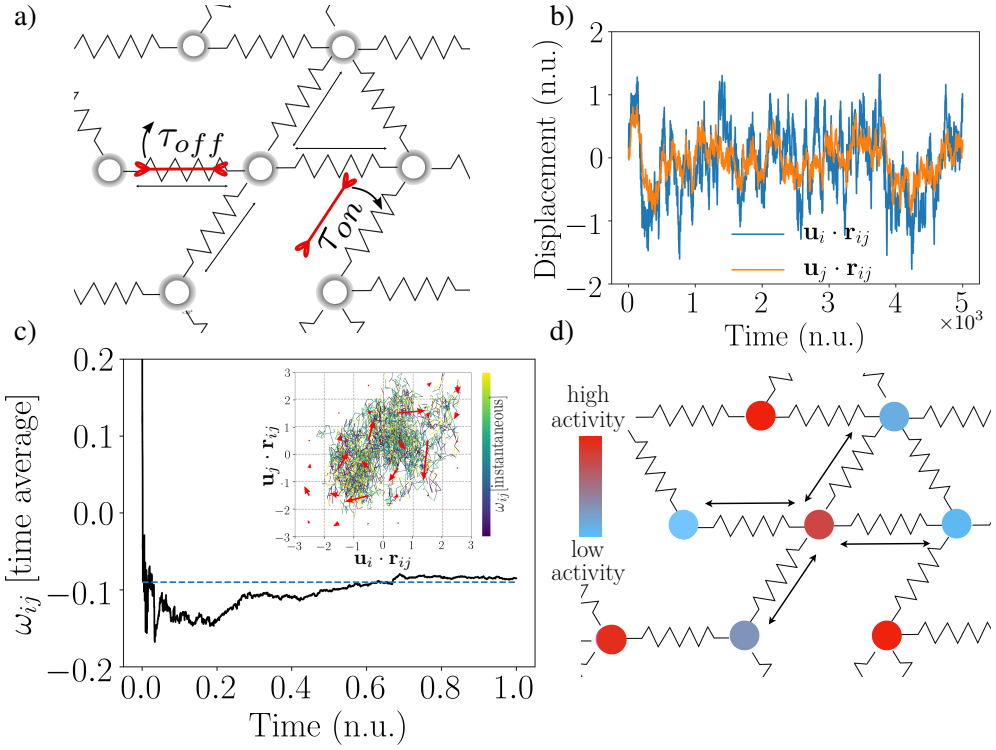

Figure 3.2 a) Schematic of a disordered triangular network of beads and springs with motors. Motors attach to bonds with rate τ_{on}^{-1} and detach with rate τ_{off}^{-1}. For simplicity, we assume $\tau_{\text{on}} = \tau_{\text{off}} = \tau$. b) Two stochastic trajectories of beads' displacements (projected along the distance-vector) as a function of time. All quantities are plotted in natural units (see main text). c) The time-averaged cycling frequency converges to a non-zero value as $t \to \infty$. Inset: Phase space trajectory (colored by the instantaneous cycling frequency) and probability current (red arrows) for the data in panel b. d) Sketch of a disordered triangular network with heterogeneous white noise activity at the nodes. The color indicates the different magnitude of white-noise activity in the system.

newtonian fluid at temperature T. The bonds of the network are removed with probability $1-p$, thereby introducing disorder in the system. The binding and unbinding of motors is modeled as a random telegraph process $\mathbf{f}^{\text{M}}$ with binding/unbinding rate τ_{on}/τ_{off} , while the amplitude of the motor contraction is drawn from a folded normal distribution of variance σ_M^2. A schematic of the model is shown in Fig. 3.2a.

We simulate the dynamics of the network with the following overdamped Langevin equation for the displacement at each node:

$$\gamma \frac{d\mathbf{x}_i}{dt}(t) = \mathbf{f}_i^{\text{E}}(t) + \mathbf{f}_i^{\text{M}}(t) + \sqrt{2\gamma k_B T}\boldsymbol{\eta}_i(t), \tag{3.3}$$

where γ is the drag coefficient.
The full elastic force on node i is $\mathbf{f}_i^{\mathrm{E}} = -\sum_{j\in \mathrm{NN}} k_{i,j}(\|\mathbf{x}_{i,j}(t)\| - \ell_0)\hat{\mathbf{x}}_{i,j}$, where $\mathbf{x}_{i,j} = \mathbf{x}_i - \mathbf{x}_j$, $\hat{\mathbf{x}}_{i,j}$ is the corresponding unit vector, and $k_{i,j} = k$ if the bond between nearest neighbor (NN) sites is present or else $k_{i,j} = 0$. Thermal forces act on the beads as Gaussian white noise ($\langle \eta_{ix}(t)\eta_{jy}(t')\rangle = \delta_{ij}\,\delta_{xy}\,\delta(t-t')$ and $\langle \eta_{ix}\rangle = \langle \eta_{iy}\rangle = 0$). Note, we neglect hydrodynamic interactions between beads and use fixed boundary conditions to prevent rigid body translation and rotation.[1] In addition, we employ natural units, measuring time in units of γ/k, lengths in units of ℓ_0 and temperature in units of $k\ell_0^2/k_B$, leaving T, σ_M and τ as the remaining free parameters.

We employ an Euler-Maruyama scheme to integrate the Brownian dynamics Eq. (3.3) and, after equilibration, we are able to record trajectories for all nodes in the network. Note that a trajectory is the projection of the displacement of the node $\mathbf{u}_i$ onto the distance vector between neighboring nodes $\mathbf{r}_{ij}$. A pair of recorded trajectories is shown in Fig. 3.2b. The non-equilibrium character of the system is manifest in the characteristic circulatory behavior of the probability current, as shown in the inset of Fig. 3.2c. To quantify the non-equilibrium character of the system we assign a simple pseudo-scalar measure, the cycling frequency ω (see Sec. 1.5 of the Introduction), to any pair of recorder trajectories. If detailed balance is broken in the phase space of the degrees of freedom, the time-averaged cycling frequency converges to a non-zero value, as shown in Fig. 3.2c. Importantly, we expect our chosen non-equilibrium measure to reflect not only the active driving of the motors, but also the spatial heterogeneity of the elastic structure of the network.

In the limit in which the typical relaxation times of the network are large compared to the on-off times of the motors,[2] we might consider the effect of multiple motors as a white noise process with heterogeneous amplitudes at different nodes (Fig. 3.2 d). As we will show later, this model exhibits statistics similar to the model with correlated motor activity, but has the great advantage of being analytically tractable. The nodes' fluctuations in this model are described by the following overdamped Langevin equation:

$$\gamma\frac{d\mathbf{x}_i}{dt}(t) = -\sum_{j\sim i} k_{i,j}(\|\mathbf{x}_{i,j}(t)\| - \ell_0)\hat{\mathbf{x}}_{i,j}(t) + a_i\boldsymbol{\eta}_i(t)\,. \tag{3.4}$$

The only difference between Eq. (3.4) and Eq. (3.3) is that now all fluctuating forces acting on the beads are described as Gaussian white noise. Thus, for nodes i and j, $\langle \eta_{ix}(t)\eta_{jy}(t')\rangle = \delta_{ij}\,\delta_{xy}\,\delta(t-t')$ and $\langle \eta_{ix}\rangle = \langle \eta_{iy}\rangle = 0$. Here, the white noise amplitude includes both thermal and active fluctuations: $a_i = \sqrt{2\gamma k_B(T + |\alpha_i|)}$. Im-

1 Using fixed instead of periodic boundary conditions slightly affects the value of p_c: we compute the corrected p_c in the Supplementary Material [63].

2 This limit is particularly relevant for large relaxation times of the network, *i.e.* close to a critical point.

portantly, while the amplitude of the thermal contribution is homogeneous throughout the system, the amplitude of the active noise is heterogeneous and is described using quenched disorder. Specifically, we draw the amplitudes α_i from a normal distribution with average μ_α and variance σ_α^2, such that $\sigma_\alpha \ll T + \mu_\alpha$. Note, when $\sigma_\alpha = 0$, the system obeys equilibrium dynamics. In what follows we use the natural units introduced for the model of Eq. (3.3) and we are left with only one free parameter $a_i = \sqrt{2(T + |\alpha_i|)}$ in Eq. (3.4).

3.3 Results

3.3.1 Understanding the local response: nearest-neighbor cycling frequencies

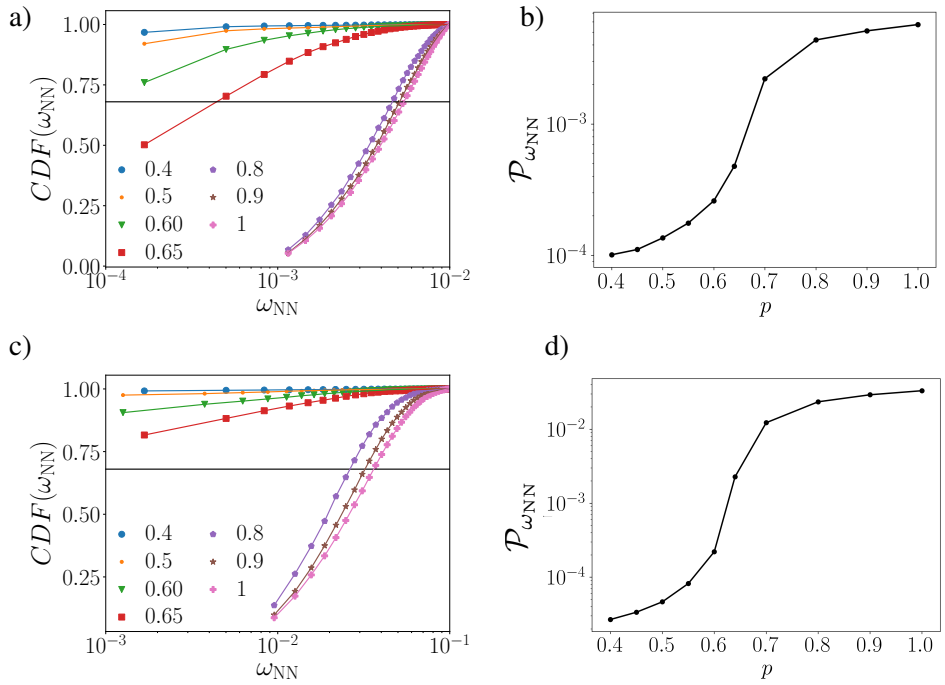

Figure 3.3 a) The cumulative distribution function (CDF) of ω_{NN} for different p and for the model with motors (Fig. 3.2 a) simulated using Eq. (3.3) with $\sigma_M = 10^{-3}$, $T = 10^{-5}$ and $\tau = 0.5$. b) The 68_{th} percentile of ω_{NN} as a function of p. (c-d) CDF and 68_{th} percentile for the full (nonlinear) model in (c) with $\sigma_\alpha = 10^{-6}$, $T + \mu_\alpha = 10^{-5}$.

To gain a first understanding of how the cycling frequencies are affected by the different elastic regimes induced by the bond-dilution protocol, we compute

the cumulative distribution function (CDF) of directly connected nearest-neighbor cycling frequencies ω_{NN} as a function of the dilution parameter p.[3] Results for the both models introduced in Sec. 3.2 are shown in Fig. 3.3a-b: as previously noted, the statistical features of the nearest-neighbor ω are, for the two models, qualitatively similar. For $p > 0.8$ the CDF gradually increases to 1, but only for large ω_{NN}. By contrast, below isostaticity ($p_c \approx 0.65$) the CDF immediately saturates to 1 at low values of ω_{NN}, indicating a large shift of the predominant cycling frequencies towards zero. We utilize the 68_{th} percentile $\mathcal{P}_{\omega_{\mathrm{NN}}}$ of the distribution as an order parameter to characterize this transition: $\mathcal{P}_{\omega_{\mathrm{NN}}}$ is non-zero in the rigid phase $p > p_c$, while it vanishes continuously when $p < p_c$ (Fig. 3.3c-d).

Although there have been analytical attempts to study, on the one hand, the non-linear elastic response of spring networks close to isostaticity [94] and, on the other hand, the non-equilibrium dynamics in the absence of dilution [64–66], it is particularly daunting to try to tackle analytically models that combine non-linear equation of motions such as Eq. 3.4 with intrinsic non-equilibrium activity. However, in the limit of modest driving (*i.e.* $\sigma_\alpha \ll (T + \mu_\alpha) \ll 1$) the displacements of the nodes will be small and we might linearize the elastic interaction $\mathbf{f}_i^{\mathrm{E}}$ to first order in the displacement. The force on node i now reads $-\sum_{j\sim i} A_{ij}\mathbf{u}_j$, with the interaction matrix A given by:

$$A_{i\alpha j\beta} = \begin{cases} -k_{i,j}\hat{r}_{i,j\alpha}\hat{r}_{i,j\beta}, & i \neq j \\ \sum\limits_{n\neq i} k_{in}\hat{r}_{i,n\alpha}\hat{r}_{i,n\beta}, & i = j \end{cases}, \tag{3.5}$$

where $\hat{\mathbf{r}}_{i,j}$ is the unit vector connecting the rest positions of nodes i and j and greek indices denote cartesian components. This linearized model captures the non-equilibrium fluctuations of the system, as shown by the good comparison of 68_{th} percentile curves for the full model and the linearized model (see Appx. E of [63]).

Thanks to the linearity of the problem, at steady state the covariance matrix $C_{i\alpha j\beta} = \langle u_{i\alpha}u_{j\beta}\rangle$ satisfies the Lyapunov equation (see Sec. 1.5 of the Introduction) :

$$AC + CA^T = -2D, \tag{3.6}$$

where D is the diffusion matrix $D_{i\alpha j\beta} = \frac{1}{2}a_i^2\delta_{ij}\delta_{\alpha\beta}$. While A is invertible for a fully connected network , zero-energy modes with diverging relaxation time appear as we remove network bonds. To avoid the resulting divergences in the covariance matrix, it is convenient to insert a weak ε-spring of elastic constant $\varepsilon \ll 1$ (ε is in units of k) whenever a k-spring is removed, as sketched in Fig. 3.4a top-left [82, 83]. In the limit $\varepsilon \to 0$ we expect to recover the dynamics of the simulated network. This

3 While the specific choice of neighbors connected by a bond may seem rather specific at this point, this choice will allow us to intuitively understand the local non-equilibrium behavior in terms of a simple two-beads model.

dilute-and-replace procedure allows us to stabilize the zero modes in a controlled way.

Once the network is stabilized it becomes possible to compute analytically the cycling frequencies directly from the covariance matrix (see Sec. 1.5 of the Introduction) and thus to study the behavior of the cycling frequencies as a function of ε, even at subcritical dilution values $p < p_c$. Compared to the simulated data (Fig. 3.3d), we find that the sharpness of the transition in $\mathcal{P}_{\omega_{\mathrm{NN}}}$ is softened by the stabilizing field ε, as shown in Fig. 3.4b. Thus, it appears as if ε acts as a scaling field driving the system away from criticality. To test this hypothesis, we test whether $\mathcal{P}_{\omega_{\mathrm{NN}}}$ obeys a homogeneity relation of the form:

$$\mathcal{P}_{\omega_{\mathrm{NN}}}(p, \varepsilon) = |\Delta p|^f P_{\pm}(\varepsilon |\Delta p|^{-\phi}), \tag{3.7}$$

where $\Delta p = p - p_c$ and $P_{\pm}$ is a universal function. By rescaling the data for different ε and p according to this relation we observe a good collapse (Fig. 3.4c). Based on this analysis, we identify three distinct scaling regimes: a super-critical, k-dominated regime where $\mathcal{P}_{\omega_{\mathrm{NN}}} \sim |\Delta p|^f$, a critical regime $\mathcal{P}_{\omega_{\mathrm{NN}}} \sim \varepsilon^{f/\phi}$, and a sub-critical one where $\mathcal{P}_{\omega_{\mathrm{NN}}} \sim \varepsilon^{1/2} |\Delta p|^{f-\phi/2}$. We find a reasonable collapse with the exponents $f = 0.45 \pm 0.05$, $\phi = 1.8 \pm 0.2$.

We can make progress in the analytical approach to this problem by considering a mean-field version of a two-beads model, shown in Fig. 3.4a bottom. The main idea is to first map the disordered network onto a uniform network with an effective stiffness μ_m (Fig. 3.4a top right–Effective Medium Theory, EMT [81]). Then, by requiring the dipole response of the disordered network (Fig. 3.4a top-left) to match the response in the effective medium (Fig. 3.4a top-right), we effectively map the problem onto a two-beads model for which we can analytically compute the cycling frequencies. As shown in the Appendix F and in Fig. 3 of our manuscript [63], we can expect this approach to work well in the low-activity limit. In this limit, fluctuations in the elastic constants of the two-beads model appear in fact only as a second order correction in the expression for the cycling frequency.

The two-beads EMT theory successfully predicts the scaling of $\mathcal{P}_{\omega_{\mathrm{NN}}}$ for the original, stabilized network with exponents $f = 1/2$, $\phi = 2$, as shown by the dashed purple line of Fig. 3.4c (see Appx. G of [63] for the derivation of the exponents). More than confirming our scaling ansatz (Eq. (3.7) and dashed purple line of Fig. 3.4c), this intuitive analytical approach provides insight into the non-equilibrium fluctuations of a disordered marginal system. The various phases and their boundaries predicted by this mean-field model are summarized in the phase diagram in Fig. 3.4d.

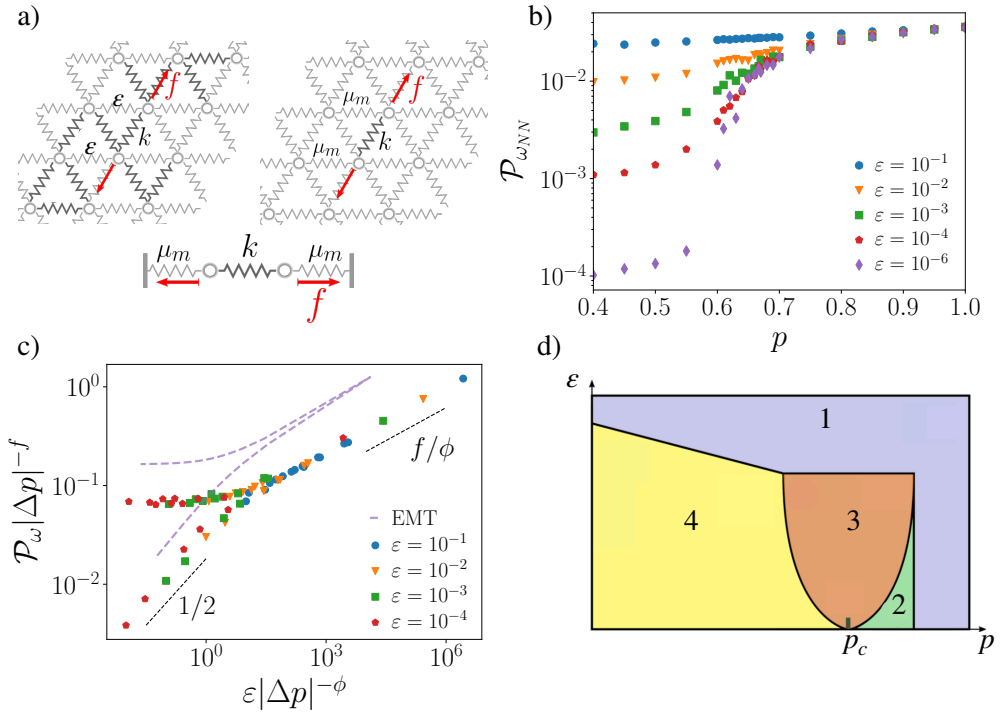

Figure 3.4 a) Top left: Schematic of network with ε-bond replacement (ε-bonds are light, k-bonds dark). Top right: Schematic of effective medium, with all bonds replaced by μ_m except where the dipole is applied. Bottom: Effective two-bead model with external spring constants μ_m. b) 68$_{\text{th}}$ percentile, $\mathcal{P}_{\omega_{\text{NN}}}$ for different p and ε. c) Scaling of the 68$_{\text{th}}$ percentile $\mathcal{P}_{\omega_{\text{NN}}}(p,\varepsilon) = |\Delta p|^f P(\varepsilon|\Delta p|^{-\phi})$ around p_c. The dashed purple line indicates the mean-field prediction. Results were obtained employing Eq. (3.6) for a lattice of size $W = 40\times 40$ and $\sigma_\alpha = 10^{-4}$, $T+\mu_\alpha = 10^{-3}$. d) Schematic phase diagram: (1) $\mathcal{P}_{\omega_{\text{EMT}}} \sim k$; (2) $\mathcal{P}_{\omega_{\text{EMT}}} \sim k^{1/2}|\Delta p|^{1/2}$; (3) $\mathcal{P}_{\omega_{\text{EMT}}} \sim k^{3/4}\varepsilon^{1/4}$; (4) $\mathcal{P}_{\omega_{\text{EMT}}} \sim k^{1/2}\varepsilon^{1/2}|\Delta p|^{-1/2}$.

3.3.2 From local to global: a diverging length scale sets the scaling properties of cycling frequencies

Critical phenomena are associated with a diverging length scale ξ. In isostatic networks, this phenomenon has been investigated via finite size scaling of the shear modulus and the non-affine measure [78]. Here, we show that a divergent length scale affects the radial scaling of cycling frequencies in the vicinity of the critical point. Results for uniform triangular networks showed that $\sqrt{\langle\omega^2(r)\rangle} \sim r^{-3}$, where r is the distance of any node from the center of the network and the average is over all nodes at the same distance (Fig. 3.5a) [65]. As p is lowered from one to the isostatic threshold, the scaling r^{-3} of $\sqrt{\langle\omega^2(r)\rangle}$ is at first robust, but starts deviating significantly from the uniform scaling once the vicinity of p_c is reached, as shown in

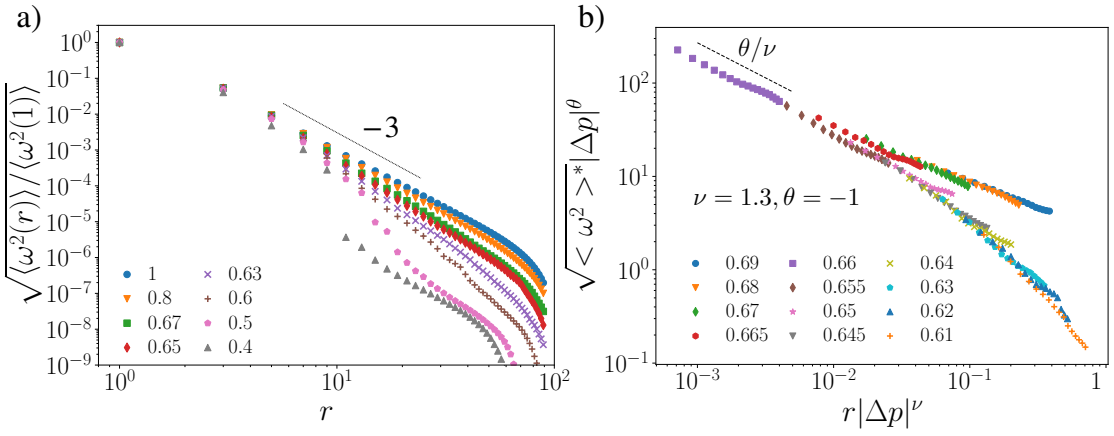

Figure 3.5 a) Scaling of $\sqrt{\langle\omega^2(r)\rangle/\langle\omega^2(1)\rangle}$ with r for different p values. b) Universal scaling with $|\Delta p|$ and r of the normalized root-mean-square value of the cycling frequencies around the critical point. Results were obtained from Eq. (3.6) for a lattice of size $W = 100 \times 100$ and $\sigma_\alpha = 10^{-6}$, $T + \mu_\alpha = 10^{-5}$.

Fig. 3.5a. To study if this intricate scaling behavior can be understood within the framework of rigidity percolation, we rescale r by ξ and test the following scaling relation near p_c

$$\sqrt{\langle\omega^2\rangle^*}(p, r) = |\Delta p|^{-\beta}\mathcal{S}_\pm(r|\Delta p|^\nu)\,. \tag{3.8}$$

In Eq. (3.8) We eliminated the r^{-3} scaling of a uniform network by defining $\sqrt{\langle\omega^2\rangle^*} := \sqrt{\langle\omega^2\rangle}(p, r)/\sqrt{\langle\omega^2\rangle}(p = 1, r)$. Remarkably, the rescaled cycling frequencies collapse onto a master curve with $\theta = -1 \pm 0.2$ and $\nu = 1.3 \pm 0.2$, as shown in Fig. 3.5b. Note that this value of ν is consistent with the exponent of the correlation length found in studies of rigidity percolation in diluted spring networks [78, 95]. In conclusion, we have shown how a diverging length-scale originally discovered for marginal athermal systems, also governs the large scale dynamics of actively driven diluted spring networks.

3.4 Summary and Discussion

In this chapter we investigated how measures of non-equilibrium, the cycling frequencies, can be controlled by the isostatic critical point. We proposed to do so by using a minimal framework of a randomly diluted spring network with active motor contractions.

Starting from the local nearest-neighbor dynamics, we have shown that the zero-temperature isostatic threshold which separates the floppy phase of the network from the rigid one, also regulates the statistics of cycling frequencies. Interestingly,

two different models of motor activity, one with time-correlated contractions of the springs, and one with white noise at the nodes, display similar non-equilibrium statistics as the average connectivity is varied across the critical value. This suggests that the presence in the network of zero-modes with diverging relaxation time dictates the behavior of cycling frequencies independently of the specific kind of active driving.

After identifying a viable order parameter, the 68-th percentile of the cycling frequencies' distribution, a simplified version of the model with linear interactions allowed us to compare numerical results with analytical ones obtained via an EMT-based two-beads model. While this theory yields accurate exponents for the nearest-neighbor scaling relation, the behavior at larger distances is not captured by the mean-field model.

Recent experimental developments in the field of active matter have made it possible to systematically study the non-equilibrium dynamics of disordered systems. Hence the need for non-equilibrium theories that make testable predictions. The scaling of cycling frequencies at different length-scales has been proposed as a non-invasive technique for investigating the features of the active driving as well as the structural features of nearly-ordered biological assemblies [64–66]. We have here shown how, for a diluted system, the presence of a diverging length-scale can induce different scaling behaviors of the cycling frequencies near criticality. Although we focused here on this single non-equilibrium measure, the relations between cycling frequencies and other two-point quantitites such as the area-enclosing-rate or the reduced entropy-production-rate are well established (see Sec. 1.5 of the Introduction) [66, 69, 70]. Our predictions might be particularly relevant in fragile biological contexts where structural disorder cannot be neglected and non-invasive measurement techniques are necessary.

3.5 Publication

Nonequilibrium dynamics of isostatic spring networks

by

F. S. Gnesotto*[1], B. M. Remlein*[1], and C. P. Broedersz [1]

*equal contribution

[1]Department of Physics, Arnold Sommerfeld Center for Theoretical Physics and Center for NanoScience, Ludwig-Maximilians-Universität München, Theresienstraße 37, 80333 München, Germany

reprinted on pages 67–76

with permission from

***Phys. Rev. E* 100, 013002 (2019)**,

DOI: 10.1103/PhysRevE.100.013002.

© 2019 American Physical Society

Nonequilibrium dynamics of isostatic spring networks

Federico S. Gnesotto,* Benedikt M. Remlein,* and Chase P. Broedersz†
Arnold Sommerfeld Center for Theoretical Physics and Center for NanoScience, Ludwig-Maximilians-Universität München, D-80333 München, Germany

(Received 14 September 2018; revised manuscript received 17 June 2019; published 11 July 2019)

Marginally stable systems exhibit rich critical mechanical behavior. Such isostatic assemblies can be actively driven, but it is unclear how their critical nature affects their nonequilibrium dynamics. Here, we study the influence of isostaticity on the nonequilibrium dynamics of active spring networks. In our model, heterogeneously distributed white or colored, motorlike noise drives the system into a nonequilibrium steady state. We quantify the nonequilibrium dynamics of pairs of network nodes by the characteristic cycling frequency ω—an experimentally accessible measure of the circulation of the associated phase space currents. The distribution of these cycling frequencies exhibits critical scaling, which we approximately capture by a mean-field theory. Finally, we show that the scaling behavior of ω with distance is controlled by a diverging length scale. Overall, we provide a theoretical approach to elucidate the role of marginality in active disordered systems.

DOI: 10.1103/PhysRevE.100.013002

I. INTRODUCTION

The concept of isostaticity has been central in providing a unifying understanding of the mechanics of soft disordered systems [1–4]. A system is isostatic when its degrees of freedom are exactly balanced by its internal constraints, poising the system at the verge of mechanical stability [5,6]. Examples of such marginal matter include colloidal suspensions, granular packings and foams near the jamming transition [7,8], spring lattices [9–11], and fiber networks [3,4,12–14]. Recently, a variety of nonequilibrium dynamics have been reported in such soft matter systems with active driving, ranging from active colloidal suspensions [15,16] and biopolymer networks with molecular motors [17–20] to living systems such as cells, tissues, and bacterial populations [21–25]. In particular, actin-myosin cortical networks extracted from cells can self-organize in highly responsive, nonequilibrium steady states with marginal connectivity [26]. Moreover, in weakly connected reconstituted networks of actin filaments, myosin motor activity can drive the system into a critical state [17,27]. However, a theoretical framework to describe the nonequilibrium fluctuations of such marginal disordered systems is still lacking.

Active systems cannot be fully characterized by conventional equilibrium measures. To study fragile biological systems, a noninvasive approach based on measuring broken detailed balance has been proposed [28]: a nonequilibrium steady state is characterized by the presence of steady-state probability currents. Consequently, the trajectory of a pair of mesoscopic observables revolves, on average, with a characteristic cycling frequency ω in a two-dimensional phase space (see Fig. 1) [29–31]. In linear systems, the cycling frequencies are directly related to another popular measure of irreversibility: the entropy production rate [32]. It has now become possible to experimentally determine such nonequilibrium measures in active biological gels such as actin-myosin networks [33]. However, it is unclear how nonequilibrium measures are affected by the system's architecture and by the onset of mechanical rigidity.

To provide conceptual insight into the stochastic dynamics of biological gels such as actin-myosin assemblies, we here develop a theoretical approach to study the active dynamics of a marginal elastic network driven by motors [Fig. 2(a)]. Motors randomly bind and unbind to the network bonds where they exert contractile forces, thereby driving the system into a nonequilibrium steady state. By tuning network connectivity, we investigate how isostaticity controls nonequilibrium fluctuations. We quantify these steady-state fluctuations using the experimentally accessible cycling frequency ω associated with pairs of network nodes. Interestingly, we find that the cumulative distribution function of ω is highly sensitive to network connectivity, with a drastic transition near the isostatic point. We employ a generalized median, the 68th percentile of the distribution, as an order parameter to characterize this transition. The 68th percentile obeys universal scaling laws, which are captured approximately by a mean-field theory. To understand how isostaticity controls the nonequilibrium dynamics at different length scales, we employ a simplified model with white-noise activity. Specifically, we demonstrate how a diverging length scale impacts the scaling behavior of nonequilibrium cycling frequencies. Together, our results demonstrate how isostaticity can control the nonequilibrium fluctuations in disordered systems.

II. ACTIVELY DRIVEN RANDOMLY DILUTED TRIANGULAR NETWORKS

A. Model with motor activity

We start our analysis by considering a triangular network of springs, which is immersed in a viscous fluid at

*These authors contributed equally to this work.
†C.broedersz@lmu.de

 ©2019 American Physical Society

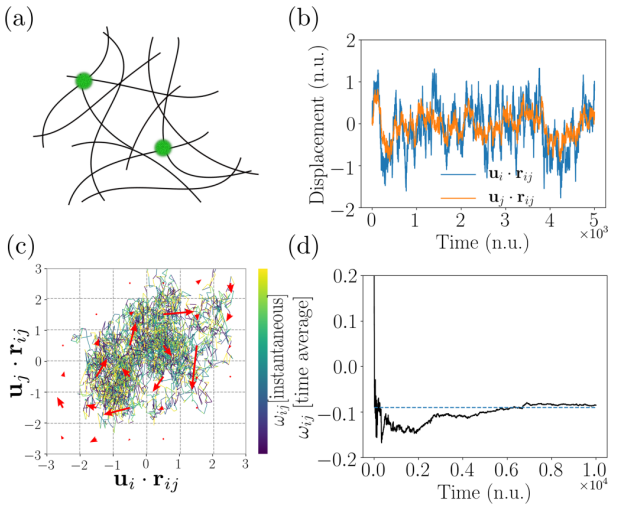

FIG. 1. (a) Schematic of two fluorescent tracer beads embedded in a motor-driven actin network: cycling frequencies can be calculated employing the positional trajectory of the two tracers in time. (b) Two stochastic trajectories of beads' displacements (projected along the distance vector) as a function of time. All quantities are plotted in natural units (see main text). (c) Phase space trajectory (colored by the instantaneous cycling frequency) and probability current (red arrows) for the data in panel (b). (d) The time-averaged cycling frequency converges to a nonzero value as $t \to \infty$.

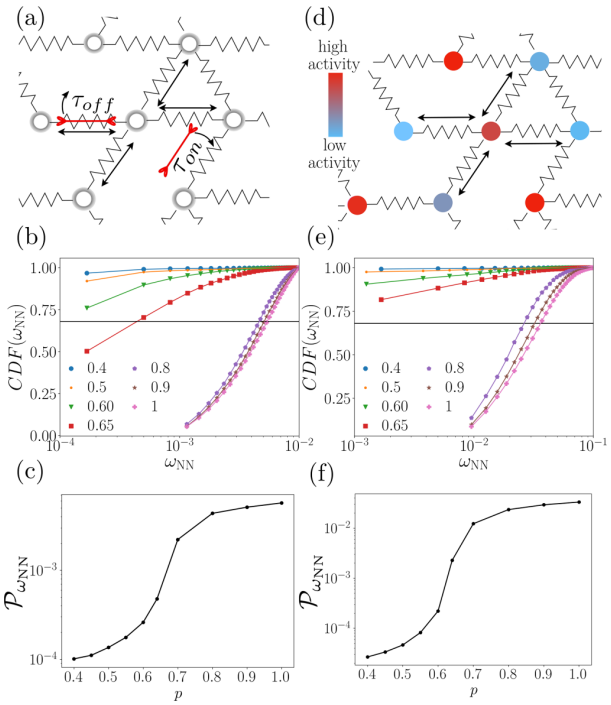

FIG. 2. (a) Schematic of a disordered triangular network of beads and springs with motors. Motors attach to bonds with the rate $\tau_{\rm on}^{-1}$ and detach with the rate $\tau_{\rm off}^{-1}$. For simplicity, we assume $\tau_{\rm on} = \tau_{\rm off} = \tau$. (b) The cumulative distribution function (CDF) of $\omega_{\rm NN}$ for different p for the full model in panel (a) simulated using Eq. (1) with $\sigma_{\rm M} = 10^{-3}$, $T = 10^{-5}$, and $\tau = 0.5$. (c) The 68th percentile of $\omega_{\rm NN}$ as a function of p. (d) Sketch of a disordered triangular network with heterogeneous white noise activity at the nodes. The color indicates the different magnitude of white-noise activity in the system. (e), (f) CDF and 68th percentile for the full (nonlinear) model in panel (c) with $\sigma_\alpha = 10^{-6}$ and $T + \mu_\alpha = 10^{-5}$.

thermodynamic equilibrium at temperature T [Fig. 2(a)]. Network connectivity is tuned by randomly diluting bonds with probability p. Molecular motors can attach to each bond of the network and exert a contractile force between two neighboring nodes. The random binding and unbinding of motors is modeled as a telegraph process (Appendix A) with rates $\tau_{\rm on}^{-1}$ and $\tau_{\rm off}^{-1}$ [34]; the local activity, i.e., the intensity of the motor force $|f_k^{\rm M}|$, is drawn from a folded Gaussian of variance $\sigma_{\rm M}^2$.

The overdamped stochastic equation for the position $\mathbf{x}_i$ of each network node reads

$$\gamma \frac{d\mathbf{x}_i}{dt}(t) = \mathbf{f}_i^{\rm E}(t) + \mathbf{f}_i^{\rm M}(t) + \sqrt{2\gamma k_B T}\,\boldsymbol{\eta}_i(t), \qquad (1)$$

where γ is the drag coefficient. The full elastic force on node i is $\mathbf{f}_i^{\rm E} = -\sum_{j\in {\rm NN}} k_{i,j}(\|\mathbf{x}_{i,j}(t)\| - \ell_0)\hat{\mathbf{x}}_{i,j}$, with $\mathbf{x}_{i,j} = \mathbf{x}_i - \mathbf{x}_j$; $\hat{\mathbf{x}}_{i,j}$ the corresponding unit vector; and $k_{i,j} = k$ if the bond between nearest neighbor (NN) sites is present or else $k_{i,j} = 0$. Thermal forces act on the beads as Gaussian white noise $[\langle \eta_{ix}(t)\eta_{jy}(t')\rangle = \delta_{ij}\,\delta_{xy}\,\delta(t-t')$ and $\langle \eta_{ix}\rangle = \langle \eta_{iy}\rangle = 0]$. Note that we neglect hydrodynamic interactions between beads and use fixed boundary conditions to prevent rigid body translation and rotation. In addition, we employ natural units, measuring time in units of γ/k, lengths in units of ℓ_0, and temperature in units of $k\ell_0^2/k_B$, leaving T, $\sigma_{\rm M}$, and τ as the remaining free parameters.

We employ a Brownian dynamics approach to simulate the network dynamics. Specifically, we determine the fluctuating displacements of various pairs of beads in the network. We quantify the nonequilibrium nature of these two-point fluctuations using the cycling frequency—the average number of revolutions, per unit time, in the two-dimensional configurational phase space of these beads [Figs. 1(c) and 1(d)]. By determining the cycling frequencies, we assign a simple pseudoscalar measure of nonequilibrium phase space currents to each pair of beads in our network. The cycling frequencies for distinct bead pairs will in general differ not only because of the heterogenous motor activities but also because of the disordered network structure.

To investigate the interplay between internal driving and disorder, we determine the cumulative probability distribution function, CDF($\omega_{\rm NN}$), of cycling frequencies $\omega_{\rm NN}$ for directly connected beads [Figs. 2(a) and 2(b)]. For $p > 0.8$ the CDF gradually increases to 1, but only for large $\omega_{\rm NN}$. By contrast, below isostaticity ($p_c \approx 0.65$, Appendix I) the CDF immediately saturates to 1 at low values of $\omega_{\rm NN}$, indicating a large shift of the predominant cycling frequencies towards zero. We utilize the 68th percentile $\mathcal{P}_{\omega_{\rm NN}}$ [Fig. 2(c)] of the distribution as an order parameter to characterize this transition: $\mathcal{P}_{\omega_{\rm NN}}$ is nonzero in the rigid phase $p > p_c$, while it vanishes continuously when $p < p_c$ [Fig. 2(c)]. These results indicate how the isostatic threshold can impact the statistics of nonequilibrium measures.

B. Model with spatially varying white-noise activity

We obtain further insight into these nonequilibrium dynamics by considering a simplified model in which the internal driving is modeled as white noise heterogeneously distributed over the network [Fig. 2(d)]. The dynamics of this model is simulated according to the following overdamped Langevin equation for the node positions:

$$\gamma \frac{d\mathbf{x}_i}{dt}(t) = -\sum_{\langle i,j\rangle} k_{i,j}(\|\mathbf{x}_{i,j}(t)\| - \ell_0)\hat{\mathbf{x}}_{i,j}(t) + a_i \boldsymbol{\eta}_i(t), \quad (2)$$

where γ is the drag coefficient of each bead in the fluid, $k_{i,j} = k$ if the bond is present or $k_{i,j} = 0$ if the bond is removed, $\mathbf{x}_{i,j} = \mathbf{x}_i - \mathbf{x}_j$, and $\hat{\mathbf{x}}_{i,j}$ is the corresponding unit vector. Internal fluctuating forces acting on the beads are described as Gaussian white noise. Thus, for nodes i and j, $\langle \eta_{ix}(t)\eta_{jy}(t')\rangle = \delta_{ij}\,\delta_{xy}\,\delta(t-t')$ and $\langle \eta_{ix}\rangle = \langle \eta_{iy}\rangle = 0$. Here, the white-noise amplitude includes both thermal and active fluctuations: $a_i = \sqrt{2\gamma k_B(T + |\alpha_i|)}$. Importantly, while the amplitude of the thermal contribution is homogeneous throughout the system, the amplitude of the active noise is heterogeneous and is described using quenched disorder. Specifically, we draw the amplitudes α_i from a normal distribution with average μ_α and variance σ_α^2, such that $\sigma_\alpha \ll T + \mu_\alpha$. Note that when $\sigma_\alpha = 0$ the system obeys equilibrium dynamics. In what follows we use the natural units introduced for the model of Eq. (1) and we are left with only one free parameter, $a_i = \sqrt{2(T + |\alpha_i|)}$, in Eq. (2).

Importantly, the statistics of the cycling frequencies of this simpler model [Figs. 2(e) and 2(f)] exhibits the same qualitative features as the model with explicit motor activity [Figs. 2(b) and 2(c)]. These results suggest that the transition in the statistics of cycling frequencies reflects the underlying elastic features of the marginal systems, independent of the specific internal driving.

III. THE TWO-BEAD MODEL PREDICTION FOR CYCLING FREQUENCIES

To provide physical intuition for which features determine the distribution of cycling frequencies in our system, we first ask: what sets the local value of $\omega_{\rm NN}$? To address this, we consider a network where all fluctuations are suppressed. We then determine the linear response to three force configurations applied to a pair of neighboring nodes in the network [Fig. 3(a)]. Using these responses, we map the disordered network onto an effective one-dimensional two-bead model [Fig. 3(b)], with spring constants k_1, k_2, and k_{12} set so that the effective system retains the local response of the full network.

While this procedure works well for the mechanics of the network, the mapping does not extend to the stochastic dynamics of the active system [35,36]. However, as a first approximation, we neglect the active fluctuations of all other beads in the network and include in our two-bead model only the activities, α_1 and α_2, of the considered pair of nodes [Fig. 3(b)]. We can now use the two-bead model to make a prediction for the cycling frequencies in the full network. In the limit of small activity difference, i.e., $\delta\alpha \ll T + \alpha$ with

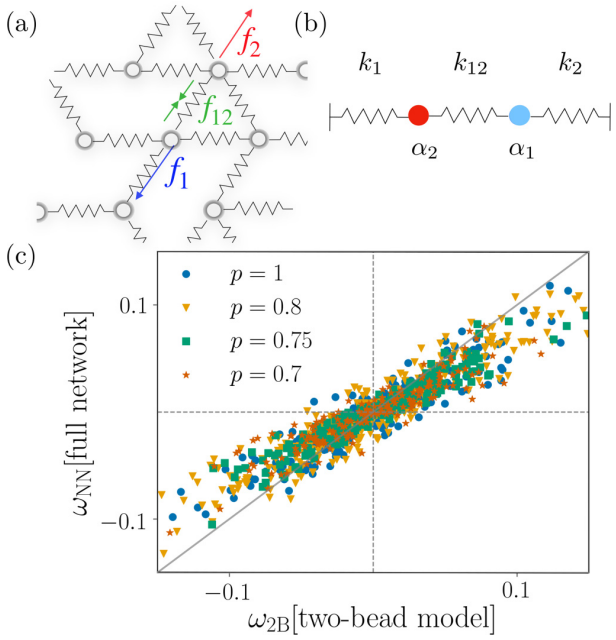

FIG. 3. (a) Two monopole forces, f_1 and f_2, and a dipole force, f_{12}, are applied at two neighboring network nodes. The response to the forces yields three different effective spring constants: k_1, k_2, and k_{12}. (b) Two-bead model with activities equal to those of the nodes in the full network. (c) Scatter plot of the cycling frequencies $\omega_{\rm NN}$ calculated for each pair of neighboring nodes for full networks with varying p (y axis) and the corresponding estimate from the two-bead model $\omega_{\rm 2B}$ (x axis).

$\alpha_1 = T + \alpha + \delta\alpha$ and $\alpha_2 = T + \alpha$ (Appendix B),

$$\omega_{\rm 2B} \approx k_{12}\frac{\sqrt{k_{12}(k_1+k_2)+k_1k_2}}{k_1+2k_{12}+k_2}\frac{\delta\alpha}{T+\alpha}. \quad (3)$$

The cycling frequencies $\omega_{\rm NN}$ for all pairs of neighbors in the full disordered network agree well on a case-by-case basis with the two-bead model prediction $\omega_{\rm 2B}$ [Fig. 3(c)]. Note, however, that $\omega_{\rm 2B}$ are in absolute value larger than $\omega_{\rm NN}$. We attribute this effect to the activities of the other network nodes (Appendix C), which are excluded in this simple model. Nonetheless, these results indicate that the local mechanical response together with the local activity difference sets the scale of the local cycling frequency.

IV. LINEAR MODEL

Next, we would like to build on the intuition provided by the two-bead model to fully understand the disordered network dynamics near isostaticity. Studying analytically the full system of Fig. 2(d) is arduous, as nonlinearities may become increasingly more important when the system is diluted and driven out of equilibrium by large noise. However, the elastic contribution to the force in our model can be linearized, resulting in a simplified equation of motion (in natural units),

$$\frac{d\mathbf{u}_i}{dt}(t) = -\sum_{\langle j\rangle} A_{ij}\mathbf{u}_j + a_i\boldsymbol{\eta}_i(t), \quad (4)$$

with $\mathbf{u}_i$ representing the displacement of node i from its rest position and the elastic-matrix A being defined as

$$A_{i\alpha j\beta} = \begin{cases} -k_{i,j}\hat{r}_{i,j\alpha}\hat{r}_{i,j\beta}, & i \neq j, \\ \sum_{n\neq i} k_{in}\hat{r}_{i,n\alpha}\hat{r}_{i,n\beta}, & i = j, \end{cases} \tag{5}$$

where $\hat{\mathbf{r}}_{i,j}$ is the unit vector connecting the rest positions of nodes i and j and Greek indices denote Cartesian components. This linearized model captures the nonequilibrium fluctuations of the system, as shown by the good comparison of 68th percentile curves for the full model and the linearized model (see Fig. 9 of Appendix E).

For such a linear system, we can extract nonequilibrium measures from the steady-state covariance matrix $C_{i\alpha j\beta} = \langle u_{i\alpha} u_{j\beta} \rangle$, which satisfies the Lyapunov equation [37]

$$AC + CA^T = -2D, \tag{6}$$

with $D_{i\alpha j\beta} = \frac{1}{2} a_i^2 \delta_{ij} \delta_{\alpha\beta}$ being the diffusion matrix. While A is invertible for a fully connected network, zero-energy modes with diverging relaxation times appear as we remove network bonds. To avoid the resulting divergences in the covariance matrix, it is convenient to insert a weak spring of elastic constant $\varepsilon \ll 1$ (ε is in units of k) whenever a k spring is removed, as sketched in Fig. 4(a) [10,38]. In the limit $\varepsilon \to 0$ we expect to recover the dynamics of the simulated network. This dilute-and-replace procedure allows us to stabilize the zero modes in a controlled way.

Because of the sixfold rotational symmetry of the lattice, we can obtain the cycling frequencies by considering a specific direction, say the x displacements of nodes connected by x-directed bonds, using [32]

$$\omega_{ij} = \frac{1}{2} \frac{(AC - CA^T)_{ixjx}}{\sqrt{C_{ixix}C_{jxjx} - C_{ixjx}C_{jxix}}}. \tag{7}$$

In the limit of modest activity: $\sigma_\alpha \ll (T + \mu_\alpha) \ll 1$, the nonlinear model is well approximated by its linearized version [Eq. (4)]. With this result, we can directly predict the CDFs [Fig. 2(e)] and in particular $\mathcal{P}_{\omega_{\mathrm{NN}}}$ (Appendix G). Moreover, the replacement of removed bonds by ε springs allows us to stabilize the rigidity of our network also below p_c. Using this approach, we find that the characteristic change in the shape of CDF(ω_{NN}) near the critical point p_c, is reflected by a sharp but continuous decrease of $\mathcal{P}_{\omega_{\mathrm{NN}}}$, as shown in Fig. 4(b) for varying ε.

Because the network is stabilized by the soft ε springs, the jump in $\mathcal{P}_{\omega_{\mathrm{NN}}}$ becomes less pronounced for larger ε. It appears as if ε acts as a scaling field taking the system away from criticality. To test this idea, we investigate if $\mathcal{P}_{\omega_{\mathrm{NN}}}$ obeys a homogeneity relation of the form

$$\mathcal{P}_{\omega_{\mathrm{NN}}}(p, \varepsilon) = |\Delta p|^f P_\pm(\varepsilon |\Delta p|^{-\phi}), \tag{8}$$

where $\Delta p = p - p_c$ and $P_\pm$ is a universal function. By rescaling the data for different ε and p according to this relation we observe a good collapse [Fig. 4(c)]. Based on this analysis, we identify three distinct scaling regimes: a supercritical, k-dominated regime where $\mathcal{P}_{\omega_{\mathrm{NN}}} \sim |\Delta p|^f$, a critical regime $\mathcal{P}_{\omega_{\mathrm{NN}}} \sim \varepsilon^{f/\phi}$, and a subcritical one where $\mathcal{P}_{\omega_{\mathrm{NN}}} \sim \varepsilon^{1/2} |\Delta p|^{f-\phi/2}$. We find a reasonable collapse with the exponents $f = 0.45 \pm 0.05$ and $\phi = 1.8 \pm 0.2$.

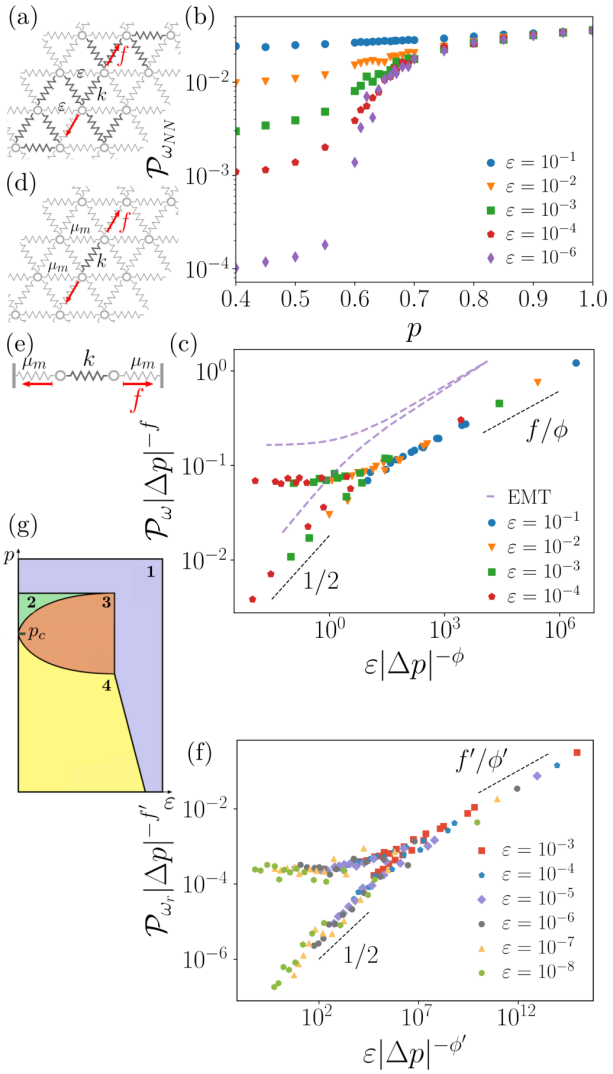

FIG. 4. (a) Schematic of network with ε-bond replacement. (b) The 68th percentile $\mathcal{P}_{\omega_{\mathrm{NN}}}$ for different p and ε. (c) Scaling of the 68th percentile $\mathcal{P}_{\omega_{\mathrm{NN}}}(p, \varepsilon) = |\Delta p|^f P(\varepsilon |\Delta p|^{-\phi})$ around p_c. The dashed purple (gray) line indicates the mean-field prediction. Results were obtained employing Eq. (6) for a lattice of size $W = 40 \times 40$, $\sigma_\alpha = 10^{-4}$, and $T + \mu_\alpha = 10^{-3}$. (d) Schematic of effective medium, with all bonds replaced by μ_m except for where the dipole is applied. (e) Effective two-bead model with external spring constants μ_m. (f) Scaling of the 68th percentile $\mathcal{P}_{\omega_r}(p, \varepsilon) = |\Delta p|^{f'} \tilde{P}(\varepsilon |\Delta p|^{-\phi'})$ around p_c for $r = 10$ ($f' = 1.4$, $\phi' = 4.8$, and $p_c = 0.63$). (g) Schematic phase diagram: (1) $\mathcal{P}_{\omega_{\mathrm{EMT}}} \sim k$, (2) $\mathcal{P}_{\omega_{\mathrm{EMT}}} \sim k^{1/2} |\Delta p|^{1/2}$, (3) $\mathcal{P}_{\omega_{\mathrm{EMT}}} \sim k^{3/4} \varepsilon^{1/4}$, and (4) $\mathcal{P}_{\omega_{\mathrm{EMT}}} \sim k^{1/2} \varepsilon^{1/2} |\Delta p|^{-1/2}$.

V. EFFECTIVE MEDIUM THEORY FOR THE TWO-BEAD MODEL

We obtain further insight into the origin of the critical scaling of the cycling frequency distribution by using the two-bead model [Fig. 3(b)] to develop a mean-field approach. In the case of $r = 1$, it is straightforward to construct an effective medium theory (EMT) [38,39] to predict the

statistical properties of the cycling frequencies in our system. The idea underlying the EMT is to map a lattice with randomly diluted bonds onto a network with uniform bond stiffness μ_m. Importantly, we anticipate this approach to work well in the low-activity limit because of the structure of Eq. (3): fluctuations in the elastic constants of the two-bead model only appear as a second-order correction to the cycling frequency (Appendix F).

By solving the following self-consistency equation we obtain the p-dependent effective spring constant μ_m for our system [38]:

$$\left\langle \frac{\mu_m - k}{\mu_m/a^* - \mu_m + k} \right\rangle = 0, \tag{9}$$

where the average $\langle\cdot\rangle$ is taken over the distribution of stiffnesses of the network bonds. In our case the distribution of bond stiffnesses is binary $P(k_{i,j} = k) = p$, $P(k_{i,j} = \varepsilon) = 1 - p$, and the constant $a^* = p_c = 2/3$ for a triangular network [39]. We then map the effective network onto a two-bead model by requiring the dipole-response of the network in Fig. 4(d) to be equivalent to the two-bead response in Fig. 4(e). Finally, we use Eq. (3) to find a mean-field estimate of the cycling frequency (Appendix F)

$$\omega_{\mathrm{EMT}} \approx \frac{k}{k + \mu_m} \sqrt{\mu_m(2k + \mu_m)} \frac{\delta\alpha}{2(T + \alpha)}. \tag{10}$$

By choosing $\alpha_1 = T + \alpha$ and $\alpha_2 = T + \alpha + \delta\alpha$—the activities of the two-bead model—to be distributed as the activities of the full network, we obtain the cycling frequency distribution and the 68th percentile $\mathcal{P}_{\omega_{\mathrm{EMT}}}$.

This mean-field model successfully predicts the scaling of the $\mathcal{P}_{\omega_{\mathrm{NN}}}$ for the original stabilized network with exponents $f = 1/2$ and $\phi = 2$ (Appendix G). Interestingly, the percentile $\mathcal{P}_{\omega_r}$ for non-nearest neighbor nodes is captured by the same scaling form [Eq. (8)], but with non-mean-field exponents [Fig. 4(f)] independent of r (Appendix H). More than confirming our scaling ansatz [Eq. (8), dashed purple (gray) line of Fig. 4(c)], this intuitive analytic approach provides insight into the nonequilibrium fluctuations of a disordered marginal system. The various phases and their boundaries predicted by this mean-field model are summarized in the phase diagram in Fig. 4(g).

VI. DIVERGING LENGTH SCALE AND DISTANCE SCALING OF CYCLING FREQUENCIES

The critical behavior of an isostatic network has an associated diverging length scale, $\xi \sim |\Delta p|^{-\nu}$ [6,13]. In uniform triangular networks with heterogenous driving it has been found that $\sqrt{\langle\omega^2(r)\rangle} \sim r^{-3}$ [Fig. 5(a)] [32]. To study how a diverging length scale affects this scaling behavior, we investigate how $\sqrt{\langle\omega^2(r)\rangle}$ depends on p. Interestingly, the scaling exponent of $\sqrt{\langle\omega^2(r)\rangle}$ is robust when p is lowered below 1. However, close to the rigidity percolation threshold, $\sqrt{\langle\omega^2(r)\rangle}$ exhibits a more intricate dependence on r, as shown in Fig. 5(a). To study if this intricate scaling behavior can be understood within the framework of rigidity percolation, we rescale r by ξ and test the following scaling relation near p_c:

$$\sqrt{\langle\omega^2\rangle^*}(p, r) = |\Delta p|^{-\beta} \mathcal{S}_{\pm}(r|\Delta p|^{\nu}). \tag{11}$$

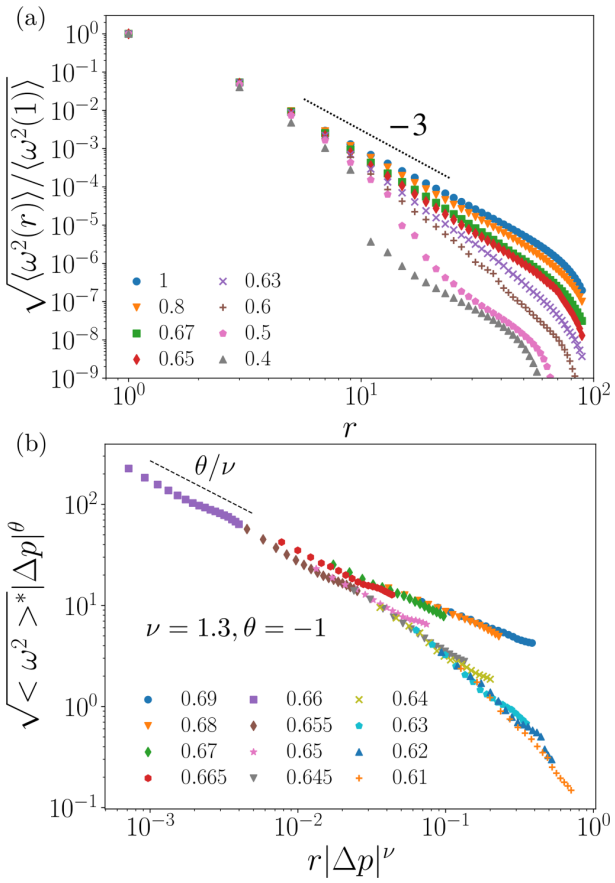

FIG. 5. (a) Scaling of $\sqrt{\langle\omega^2(r)\rangle/\langle\omega^2(1)\rangle}$ with r for different p values. (b) Universal scaling with $|\Delta p|$ and r of the normalized root-mean-square value of the cycling frequencies around the critical point. Results were obtained from Eq. (6) for a lattice of size $W = 100 \times 100$, $\sigma_\alpha = 10^{-6}$, and $T + \mu_\alpha = 10^{-5}$.

Here, we eliminated the scaling of a uniform network by normalizing $\sqrt{\langle\omega^2\rangle}(p, r)$ with $\sqrt{\langle\omega^2\rangle}(p = 1, r)$. Remarkably, the rescaled cycling frequencies collapse onto a master curve with $\theta = -1 \pm 0.2$ and $\nu = 1.2 \pm 0.2$, as shown in Fig. 5(b). Note that this value of ν is consistent with the exponent of the correlation length in rigidity percolation of spring networks [6,13]. Our results show how the presence of a diverging length scale in the system affects the distance scaling of the cycling frequencies and, more broadly, how nonequilibrium measures can show distinct characteristic distance scaling behaviors according to the different properties of the underlying elastic structure.

VII. CONCLUSIONS

In conclusion, we have determined theoretically how the dynamics of actively driven elastic networks are governed by the vicinity to an isostatic critical point. Interestingly, while the network in our model is driven out of equilibrium by active noise, we find that various statistics of nonequilibrium measures such as cycling frequencies are governed by

properties of the zero-temperature and zero-driving system. Our results show how experimentally accessible measures of nonequilibrium are sensitive to the different elastic regimes of the system. The scaling behavior of the cycling frequencies shows how nonequilibrium fluctuations determined by a two-point nonequilibrium measure manifest on different scales in an internally driven system. Considering that the scaling of cycling frequencies is governed by the elastic zero-temperature isostatic point, cycling frequencies provide a noninvasive alternative for assessing the underlying elastic properties of a nonequilibrium system and may thus prove particularly useful in fragile biological environments. These cycling frequencies are directly related to other nonequilibrium measures, such as the entropy production rate [32]. A detailed study of a realistic cytoskeletal-like system goes beyond the scope of this paper. Our findings, however, provide an important step towards establishing a general framework for understanding the dynamics of disordered nonequilibrium systems and might help in guiding experimental studies of active marginal matter in biological ensembles.

ACKNOWLEDGMENTS

We thank G. Gradziuk, K. Miermans, F. Mura, and P. Ronceray for helpful discussions. This work was supported by the German Excellence Initiative via the program NanoSystems Initiative Munich (NIM) and the Deutsche Forschungsgemeinshaft (DFG, German Research Foundation) under Grant. No. 418389167.

APPENDIX A: RANDOM TELEGRAPH PROCESS TO MODEL MOTOR CONTRACTIONS

We model the contraction of the springs of our network due to molecular motors as a telegraph process with on-off rates τ_{on}^{-1} and τ_{off}^{-1}. The contractile force of the jth motor on node i is given by $\mathbf{f}_i^{\text{M}}(t) = -\sum_{j\in NN} |f_j^{\text{M}}|\hat{\mathbf{x}}_{i,j}\mathcal{T}_j(t)$, where the telegraph process associated with each motor uncorrelates in time as $\langle \mathcal{T}_j(t)\mathcal{T}_j(t')\rangle = e^{-(\tau_{\text{on}}^{-1}+\tau_{\text{off}}^{-1})|t-t'|}$. An example of a contraction protocol in time is shown in Fig. 6.

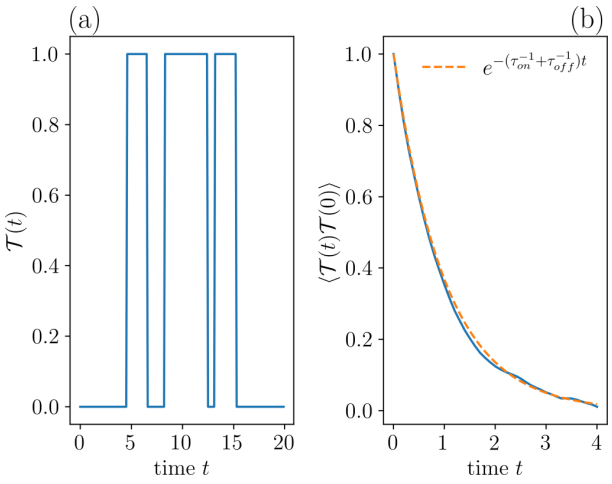

FIG. 6. (a) Realization of a random telegraph process between 0 and 1 with rates $\tau_{\text{on}}^{-1} = \tau_{\text{off}}^{-1} = 0.5$. (b) Autocorrelation function (solid blue line) for the telegraph process shown in panel (a) and the analytical prediction (dashed orange line).

APPENDIX B: DERIVATION OF EQ. (3)

In this Appendix we derive the expression for the cycling frequency of the system depicted in Fig. 3(b) of the main text. The linear equation of motion for the displacements u_i ($i = 1$ and 2) of the two beads is

$$\frac{d}{dt}\begin{pmatrix}u_1\\u_2\end{pmatrix} = A\begin{pmatrix}u_1\\u_2\end{pmatrix} + \begin{pmatrix}a_1\eta_1\\a_2\eta_2\end{pmatrix}, \tag{B1}$$

where

$$A = \begin{pmatrix}-(k_1+k_{12}) & k_{12}\\ k_{12} & -(k_{12}+k_2)\end{pmatrix}, \tag{B2}$$

$\langle \eta_i(t)\eta_j(t')\rangle = \delta_{ij}\delta(t-t')$, and $a_i = \sqrt{2\alpha_i}$ ($i \in \{1,2\}$) is the amplitude of the Gaussian white noise. This choice leads to the diffusion matrix

$$D = \begin{pmatrix}\alpha_1 & 0\\ 0 & \alpha_2\end{pmatrix}, \tag{B3}$$

which can then be inserted in the Lyapunov equation, $AC + CA^T = -2D$, to solve for the covariance matrix $C = \left(\begin{smallmatrix}C_{11} & C_{12}\\ C_{21} & C_{22}\end{smallmatrix}\right)$, where $C_{11} = \frac{2((\alpha_2-\alpha_1)k_{12}{}^2+(k_{12}+k_2)(k_1+2k_{12}+k_2)\alpha_1)}{(k_1+2k_{12}+k_2)[k_{12}k_2+k_1(k_{12}+k_2)]}$, $C_{12} = C_{21} = \frac{2k_{12}((k_{12}+k_2)\alpha_1+(k_1+k_{12})\alpha_2)}{(k_1+2k_{12}+k_2)[k_{12}k_2+k_1(k_{12}+k_2)]}$, and C_{22} is equal to C_{11} with all variables with index 1 replaced by variables of index 2 and vice versa.

By using Eq. (6) from the main text for $i = 1$ and $j = 2$, we obtain the cycling frequency

$$\omega_{12} = (\alpha_1-\alpha_2)k_{12}\sqrt{\frac{k_1(k_{12}+k_2)+k_{12}k_2}{4\alpha_1\alpha_2k_{12}(k_1+k_2)+\alpha_1\alpha_2(k_1+k_2)^2+(\alpha_1+\alpha_2)^2k_{12}{}^2}}. \tag{B4}$$

Replacing $\alpha_1 \to T+\alpha+\delta\alpha$ and $\alpha_2 \to T+\alpha$ (T is the temperature of the thermal bath) and Taylor-expanding for $\delta\alpha \ll 1$, we find

$$\omega_{12} = \omega_{2B} = k_{12}\frac{\sqrt{k_{12}k_2+k_1(k_{12}+k_2)}}{k_1+2k_{12}+k_2}\frac{\delta\alpha}{T+\alpha} + O(\delta\alpha^2). \tag{B5}$$

APPENDIX C: TWO-BEAD MODEL PREDICTION FOR THE CYCLING FREQUENCIES: NETWORKS WITH ACTIVITY RETAINED AT TWO NODES ONLY

The two-bead model estimates of the cycling frequencies for a network with heterogeneous activity distributions are larger (in absolute value) than the simulated cycling

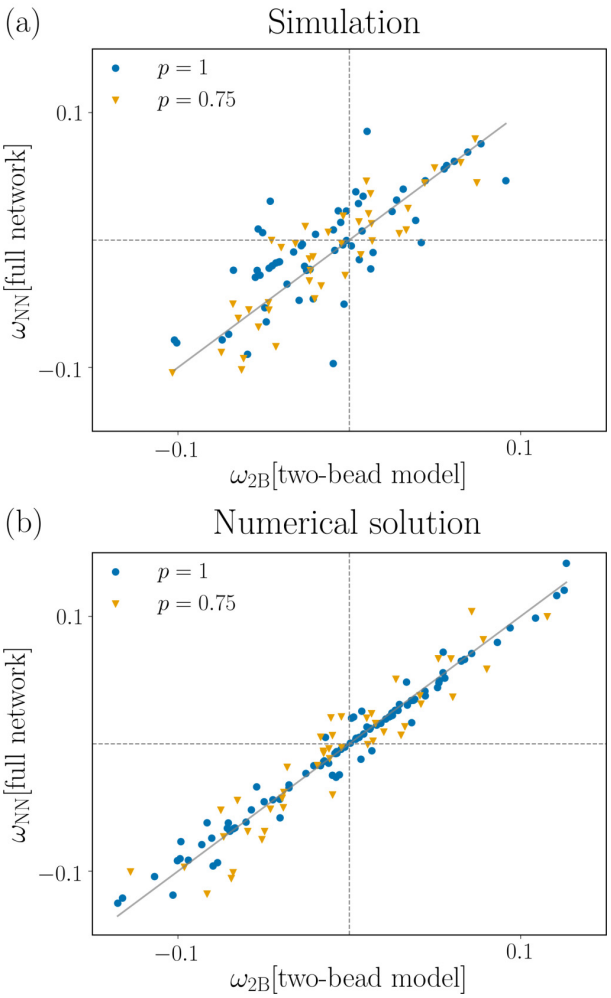

FIG. 7. (a) Scatter plot of cycling frequencies calculated from the two-bead model (x axis) and computed via multiple simulations of a 10×10 network with one active bead pair for $p = 1$ and $p = 0.75$ (y axis). (b) The same plot as in panel (a) but obtained employing the numerical solution of the Lyapunov equation for the linearized system.

frequencies, as mentioned in the main text and shown in Fig. 3(c). Here, we show that this deviation is due to the fluctuations of all other active beads in the network. Indeed, if we turn off the activities of all other nodes, we obtain cycling frequencies that are well predicted by the two-bead model without systematic deviations. To demonstrate this, we generate a configuration of the network where only one bead pair is "active"; all other beads are assigned zero activity, and for simplicity we set the temperature of the bath to be zero. To obtain all the cycling frequencies between different bead pairs we simulate different configurations and make a case-by-case comparison with the corresponding two-bead estimate. The results from the simulations and from the numerical solutions of the Lyapunov equation are shown in Fig. 7.

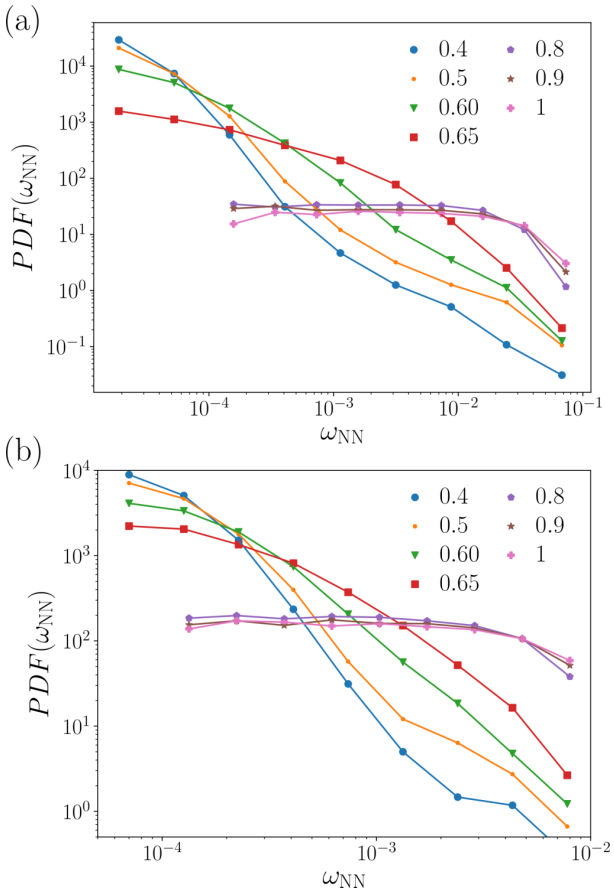

FIG. 8. (a) PDF of ω_{NN} for our model with motor generated noise [Fig. 2(a) of the main text]. (b) PDF of ω_{NN} for our model with heterogeneous active noise [Fig. 2(d) of the main text].

APPENDIX D: PROBABILITY DENSITY FUNCTION OF CYCLING FREQUENCIES

In the main text we discuss the cumulative distribution function of cycling frequencies [Figs. 2(b)–2(d)]: for completeness, we plot in Fig. 8 the probability density function (PDF) for the same data as in Figs. 2(b) and 2(e) of the main text.

APPENDIX E: COMPARISON OF 68th PERCENTILE CURVES FOR THE NONLINEAR MODEL AND THE LINEARIZED MODEL

As shown in Fig. 9, the 68th percentile curve for the full nonlinear model is well approximated by its linearised version for all p values.

APPENDIX F: DERIVATION OF EQ. (10)

The expression for the cycling frequency of our effective two-bead model follows directly from Eq. (B5) [Eq. (3)] by

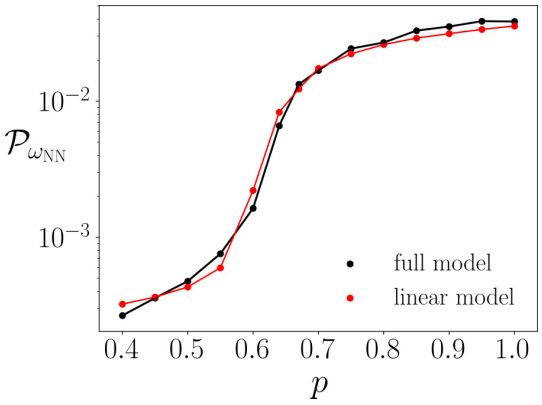

FIG. 9. The 68th percentile as a function of p for the full nonlinear model (black dots) and the linearized model [red (gray) dots]. The system size is 40×40, $\mu_\alpha + T = 10^{-5}$, and $\sigma_\alpha = 10^{-6}$. For the linear model the soft spring constant has a value of $\varepsilon = 10^{-5}$.

substituting $k_{12} \to k$ and $k_1, k_2 \to \mu_m$. This yields

$$\omega_{\rm EMT} = \frac{1}{2}\frac{k}{k+\mu_m}\sqrt{\mu_m(2k+\mu_m)}\frac{\delta\alpha}{T+\alpha} + O(\delta\alpha^2). \quad \text{(F1)}$$

Note that this equation follows from a first-order expansion in $\delta\alpha \ll 1$: corrections to the mean-field values of the spring constants contribute only to the second order, i.e.,

$$\omega_{\rm EMT} = f(k,\mu_m)\frac{\delta\alpha}{T+\alpha} + O\left(\delta k_1^2, \delta k_{12}^2, \delta k_2^2, \delta k_1\delta\alpha, \delta k_{12}\delta\alpha, \delta k_2\delta\alpha, \delta\alpha^2\right). \quad \text{(F2)}$$

As noted in the main text, this explains why our mean-field predictions are in good agreement with the numerically calculated values.

APPENDIX G: ANALYTICAL DERIVATION OF THE SCALING REGIMES FOR $\mathcal{P}_{\omega_{\rm EMT}}$

Here we describe the analytical procedure to retrieve the four different scaling regimes of $\mathcal{P}_{\omega_{\rm EMT}}$. First of all, note that the cycling frequency estimate in Eq. (9) is composed of two contributions: the stochastic contribution $\delta\alpha/(T+\alpha)$ and the elastic contribution that depends on k and μ_m. This elastic prefactor is completely deterministic and acts as a scale factor when computing the distribution of cycling frequencies.

For simplicity we rewrite Eq. (F1) in the following way:

$$\omega_{\rm EMT} = a(p,k,\varepsilon)\frac{\delta\alpha}{T+\alpha}. \quad \text{(G1)}$$

Note that $\delta\alpha \sim \mathcal{N}(0, \sqrt{2}\sigma_\alpha)$ and $T+\alpha \sim \mathcal{N}(T,\sigma_\alpha)$. We now have to compute the probability density distribution of $\omega_{\rm EMT}$: given that the stochastic part $\frac{\delta\alpha}{T+\alpha}$ of Eq. (F1) is a ratio of two Gaussian random variables, we can express the symmetric, strictly positive probability density ϱ_Z of $Z := \frac{\delta\alpha}{T+\alpha}$ as

$$\varrho_\omega(\omega) = \frac{1}{a(p,k,\varepsilon)}\varrho_Z[\omega/a(p,k,\varepsilon)],\ a>0, \quad \text{(G2)}$$

for the probability density of the cycling frequencies. Note that in general $\varrho_\omega(\omega)$ is not normal. We now have to compute the q percentile of the probability density, which is defined by

$$q = \int_{-\mathcal{P}_q}^{\mathcal{P}_q} \varrho_\omega(\omega)d\omega. \quad \text{(G3)}$$

An analytical calculation of $\mathcal{P}_q$ would require finding a closed-form solution of the integral appearing in Eq. (G3) and then an analytical inversion of the resulting function. Given that our goal is not to completely solve Eq. (G3), but only to find the scaling regimes of $\mathcal{P}_q$, we can proceed as follows. By fixing the distribution of activities in our system [i.e., we fix the distribution of z in Eq. (G2)], the percentiles of the ω distributions for two different sets of parameters of our system must satisfy

$$\int_{-\mathcal{P}_{q,1}/a_1}^{\mathcal{P}_{q,1}/a_1} \varrho_Z(z)dz = \int_{-\mathcal{P}_{q,1}}^{\mathcal{P}_{q,1}} \varrho_{\omega_1}(\omega_1)d\omega_1 = q \quad \text{(G4)}$$

$$= \int_{-\mathcal{P}_{q,2}}^{\mathcal{P}_{q,2}} \varrho_{\omega_2}(\omega_2)d\omega_2 = \int_{-\mathcal{P}_{q,2}/a_2}^{\mathcal{P}_{q,2}/a_2} \varrho_Z(z)dz. \quad \text{(G5)}$$

Since ϱ_Z is a positive function, this equation reduces to the following requirement:

$$\mathcal{P}_{q,1}/a_1 = \mathcal{P}_{q,2}/a_2. \quad \text{(G6)}$$

If we now choose realization 1 to be the fully connected network with the spring constant $k=1$, the elastic prefactor becomes $a_1(p=1,k=1,\varepsilon) = \frac{\sqrt{3}}{4}$ [at $p=1$, $\mu_m = k$, hence $a(p=1,k,\varepsilon) = \frac{\sqrt{3}}{4}k$; this follows immediately from Eq. (F1)]. Realization 2 is instead a general p-dependent configuration for which the percentile reads

$$\mathcal{P}_q(p,k,\varepsilon)/\mathcal{P}_q(p=1,k=1) = \frac{4}{\sqrt{3}}a(p,k,\varepsilon). \quad \text{(G7)}$$

Note that this equation implies that the scaling of $\mathcal{P}_{\omega_{\rm EMT}}$ is determined by the deterministic prefactor a, since $\mathcal{P}(p=1,k=1)$ is a number. The elastic prefactor depends on p through the effective spring constant μ_m, which is determined by solving the self-consistency equation

$$\left\langle \frac{\mu_m - k}{\mu_m/p_c - \mu_m + k} \right\rangle = 0, \quad \text{(G8)}$$

where the ensemble average $\langle\cdot\rangle$ is taken over the binary distribution

$$\varrho_k(x) = p\delta(x-k) + (1-p)\delta(x-\varepsilon). \quad \text{(G9)}$$

We thus have to solve the following equation for μ_m:

$$\frac{p(\mu_m - k)}{k + \mu_m/p_c - \mu_m} + \frac{(1-p)(\mu_m - \varepsilon)}{\mu_m/p_c + \varepsilon - \mu_m} = 0, \quad \text{(G10)}$$

for the different p, k, and ε regimes. This results in [38]

$$\mu_m \sim \begin{cases} k, & p \approx 1, \\ k\Delta p, & \Delta p > 0, \\ k^{1/2}\varepsilon^{1/2}, & \Delta p \approx 0, \\ |\Delta p|^{-1}\varepsilon, & \Delta p < 0. \end{cases} \quad \text{(G11)}$$

Plugging this scaling form into the definition of $a(p,k,\varepsilon)$ and employing Eq. (G7), we find that the 68th percentile of the

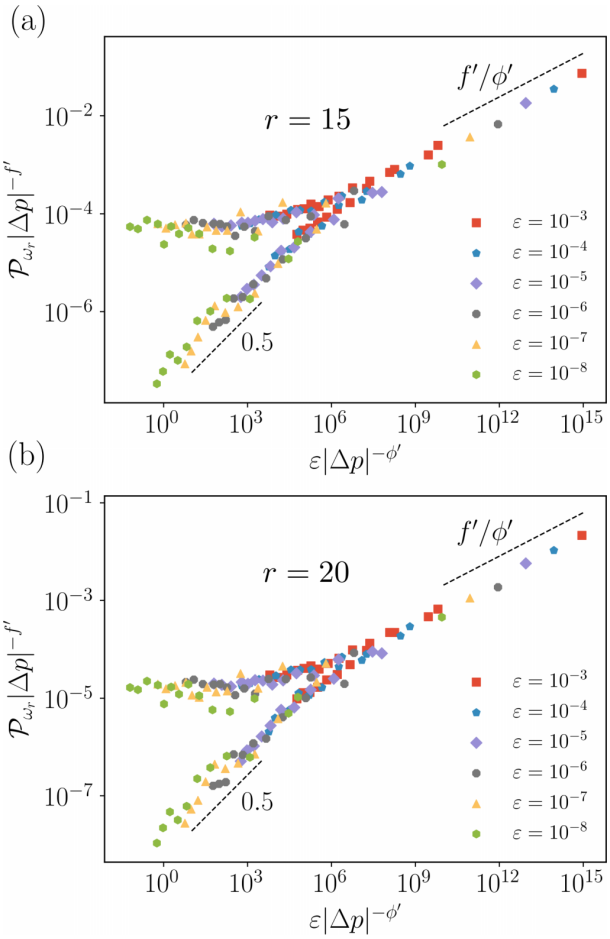

FIG. 10. Data collapse of $\mathcal{P}_{\omega_r}$ for $r = 15$ (a) and $r = 20$ (b).

ω_{EMT} scales as

$$\mathcal{P}_{\omega_{\mathrm{EMT}}}(p,k,\varepsilon) \sim \begin{cases} k, & p \approx 1, \\ k|\Delta p|^{1/2}, & \Delta p > 0, \\ k^{3/4}\varepsilon^{1/4}, & \Delta p \approx 0, \\ k^{1/2}|\Delta p|^{-1/2}\varepsilon^{1/2}, & \Delta p < 0. \end{cases} \quad \text{(G12)}$$

APPENDIX H: COLLAPSE OF 68th PERCENTILE FOR $r = 15$ AND $r = 20$

As noted in the main text, we observe that the exponents $f = 1.4'$ and $\phi' = 4.8$ do not depend on the distance r between the nodes, if the special case $r = 1$ is excluded. Figure 10 explicitly shows this for two additional r values.

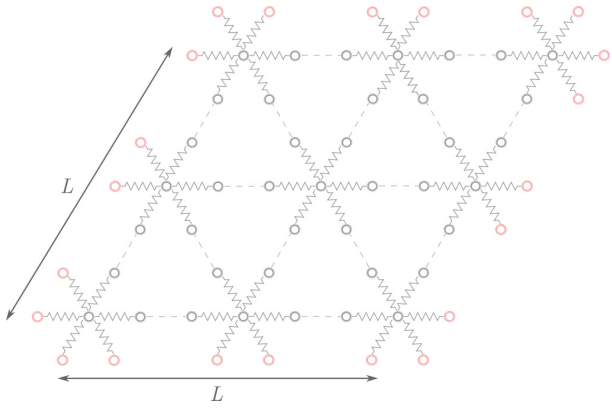

FIG. 11. Light red (gray) indicates the "frozen" nearest-neighbor degrees of freedom due to the fixed boundary conditions. The system size L refers to the nonfixed nodes. The different boundary scenarios of the lattice are shown: at the upper-left corner and at the lower-right corner three neighbors are fixed, while at the other two corners four neighbors are fixed. Along the four edges two neighboring nodes are absent and inside all six nearest neighbors are present.

APPENDIX I: CALCULATION OF p_c VIA COUNTING ARGUMENT

Following Maxwell's counting argument for a two-dimensional (2D) lattice with periodic boundary conditions [5], we count the degrees of freedom of a triangular lattice of size $L \times L$ with fixed boundaries. This results effectively in counting the fixed neighbors of the boundary nodes [highlighted in red (gray) in Fig. 11] and subtracting them from the result for a periodic lattice [39].

At the four corners of the lattice there are three or four fixed neighbors depending on the corner and along the four edges each node has two fixed neighbors. In the bulk of the lattice the counting is equivalent to Maxwell's formulation. Hence, due to the corners, 14 nearest neighbors are overcounted and have to be subtracted; along the four edges there are instead $4 \times 2(L-2)$ neighbors that need to be subtracted. The fraction of zero-frequency modes for a 2D triangular lattice is therefore given by

$$f = \frac{2L^2 - 3pL^2 - 8p(L-2) - 14p}{2L^2} = 1 - \frac{p}{p_c}, \quad \text{(I1)}$$

from which the critical connectivity or dilution probability is calculated to be

$$p_c = \frac{2L^2}{3L^2 + 8L - 2}. \quad \text{(I2)}$$

We used this to estimate p_c for the finite networks presented in the main text. Note that this result is consistent with Maxwell's result $p_c = 2/3$ in the limit of an infinite lattice.

[1] A. J. Liu and S. R. Nagel, Nature (London) **396**, 21 (1998).
[2] M. van Hecke, J. Phys.: Condens. Matter **22**, 033101 (2010).
[3] T. C. Lubensky, C. L. Kane, X. Mao, A. Souslov, and K. Sun, Rep. Prog. Phys. **78**, 073901 (2015).
[4] C. P. Broedersz and F. C. MacKintosh, Rev. Mod. Phys. **86**, 995 (2014).
[5] J. C. Maxwell, Philos. Mag. **27**, 294 (1864).
[6] D. J. Jacobs and M. F. Thorpe, Phys. Rev. E. **53**, 3682 (1996).

[7] M. E. Cates, J. P. Wittmer, J.-P. Bouchaud, and P. Claudin, Phys. Rev. Lett. **81**, 1841 (1998).
[8] A. J. Liu and S. R. Nagel, Annu. Rev. Condens. Matter Phys. **1**, 347 (2010).
[9] M. Thorpe, J. Non-Cryst. Solids **57**, 355 (1983).
[10] M. Wyart, H. Liang, A. Kabla, and L. Mahadevan, Phys. Rev. Lett. **101**, 215501 (2008).
[11] X. Mao, N. Xu, and T. C. Lubensky, Phys. Rev. Lett. **104**, 085504 (2010).
[12] C. Heussinger and E. Frey, Phys. Rev. Lett. **97**, 105501 (2006).
[13] C. P. Broedersz, X. Mao, T. C. Lubensky, and F. C. Mackintosh, Nat. Phys. **7**, 983 (2011).
[14] A. Sharma, A. J. Licup, K. A. Jansen, R. Rens, M. Sheinman, G. H. Koenderink, and F. C. MacKintosh, Nat. Phys. **12**, 584 (2016).
[15] I. Buttinoni, J. Bialké, F. Kümmel, H. Löwen, C. Bechinger, and T. Speck, Phys. Rev. Lett. **110**, 238301 (2013).
[16] B. van der Meer, W. Qi, R. G. Fokkink, J. van der Gucht, M. Dijkstra, and J. Sprakel, Proc. Natl. Acad. Sci. USA **111**, 15356 (2014).
[17] J. Alvarado, M. Sheinman, A. Sharma, F. C. MacKintosh, and G. H. Koenderink, Nat. Phys. **9**, 591 (2013).
[18] C. P. Brangwynne, G. H. Koenderink, F. C. MacKintosh, and D. A. Weitz, Phys. Rev. Lett. **100**, 118104 (2008).
[19] V. Schaller, C. Weber, C. Semmrich, E. Frey, and A. R. Bausch, Nature (London) **467**, 73 (2010).
[20] L. Huber, R. Suzuki, T. Krüger, E. Frey, and A. R. Bausch, Science **361**, 255 (2018).
[21] T. E. Angelini, E. Hannezo, X. Trepat, M. Marquez, J. J. Fredberg, and D. A. Weitz, Proc. Natl. Acad. Sci. USA **108**, 4714 (2011).
[22] D. Bi, J. H. Lopez, J. M. Schwarz, and M. L. Manning, Nat. Phys. **11**, 1074 (2015).
[23] S. Thutupalli, M. Sun, F. Bunyak, K. Palaniappan, and J. W. Shaevitz, J. R. Soc., Interface **12**, 20150049 (2015).
[24] S. Garcia, E. Hannezo, J. Elgeti, J.-F. Joanny, P. Silberzan, and N. S. Gov, Proc. Natl. Acad. Sci. USA **112**, 15314 (2015).
[25] M. Delarue, J. Hartung, C. Schreck, P. Gniewek, L. Hu, S. Herminghaus, and O. Hallatschek, Nat. Phys. **12**, 762 (2016).
[26] T. H. Tan, M. Malik-Garbi, E. Abu-Shah, J. Li, A. Sharma, F. C. MacKintosh, K. Keren, C. F. Schmidt, and N. Fakhri, Sci. Adv. **4**, eaar2847 (2018).
[27] J. Alvarado, M. Sheinman, A. Sharma, F. C. MacKintosh, and G. H. Koenderink, Soft Matter **13**, 5624 (2017).
[28] C. Battle, C. P. Broedersz, N. Fakhri, V. F. Geyer, J. Howard, C. F. Schmidt, and F. C. MacKintosh, Science **352**, 604 (2016).
[29] J. B. Weiss, Tellus, Ser. A: Dyn. Meteorol. Oceanogr. **55**, 208 (2003).
[30] J. Gladrow, N. Fakhri, F. C. MacKintosh, C. F. Schmidt, and C. P. Broedersz, Phys. Rev. Lett. **116**, 248301 (2016).
[31] J. Gladrow, C. P. Broedersz, and C. F. Schmidt, Phys. Rev. E **96**, 022408 (2017).
[32] F. Mura, G. Gradziuk, and C. P. Broedersz, Phys. Rev. Lett. **121**, 038002 (2018).
[33] D. S. Seara, V. Yadav, I. Linsmeier, A. P. Tabatabai, P. W. Oakes, S. M. A. Tabei, S. Banerjee, and M. P. Murrell, Nat. Commun. **9**, 4948 (2018).
[34] N. G. Van Kampen, *Stochastic Processes in Physics and Chemistry*, Vol. 1 (Elsevier, Amsterdam, 1992).
[35] J. Mehl, B. Lander, C. Bechinger, V. Blickle, and U. Seifert, Phys. Rev. Lett. **108**, 220601 (2012).
[36] M. Uhl, P. Pietzonka, and U. Seifert, J. Stat. Mech. (2018) 023203.
[37] A. M. Lyapunov, Intl. J. control **55**, 531 (1992).
[38] E. J. Garboczi and M. F. Thorpe, Phys. Rev. B **33**, 3289 (1986).
[39] S. Feng, M. F. Thorpe, and E. Garboczi, Phys. Rev. B **31**, 276 (1985).

4 Learning the nonequilibrium dynamics of "Brownian movies"

Abstract of the chapter

In the previous chapter we explored how the critical mechanical nature of diluted spring networks that are close to isostaticity modifies their non-equilibrium dynamics. To do so, we recorded the node's positions in time and, under different mechanical conditions, computed the cycling frequencies. We then described in which way the cycling frequencies carry information about the critical mechanics of the network.

In this chapter we take a different perspective to study non-equilibrium dynamics and lift two fundamental assumptions about the system of interest: 1) that tracking the positions of embedded objects or of specific regions of the system is always feasible; 2) that the degrees of freedom we arbitrarily decide to track (for example the positions of the nodes) are informative about the non-equilibrium dynamics of the system. Being able to lift such assumptions might be particularly relevant for biological contexts where the dynamics is intrinsically stochastic, the system comprises of many degrees of freedom that are not easy to track, and measurements are affected by noise in the imaging apparatus. After introducing the topic and defining what "Brownian movies" are, we develop our tracking-free analysis method and extract relevant non-equilibrium information directly from a movie of a physical system. Specifically, we are able to directly infer a relevant set of "image-modes" from the movie and to project the high-dimensional image frames onto this set, thus performing a dimensionality reduction. By virtue of reduced dimensionality, we are then able to infer non-equilibrium quantities such as the entropy production rate and the deterministic image-forces acting on the system. We first test our idea with a simple two-beads model. Then, we demonstrate the broader applicability of our method by considering a complex spring-network system comprising multiple degrees of freedom. In the latter example we introduce a novel, principled way of selecting for the most dissipative modes of the system: Dissipative Component Analysis. Finally, we introduce a scalable version of our force-inference method that exploits locality of interactions, therefore addressing the problem of force-inference in systems with a large number of degrees of freedom. We thus provide a real alternative to tracking-based methods in assessing microscopic forces and irreversibility in soft living matter.

Research question Given time-lapse microscopy data of a soft matter system, how can one identify relevant degrees of freedom and infer intrinsic non-equilibrium properties of the system?

4.1 Inferring force and dissipation from trajectories: Stochastic Force Inference

The foundations of Brownian motion lie deep in physics: it is in fact the thermal motion mesoscopic particles that determines the erratic motion of pollen grains observed by Brown in 1827 [96] and successfully explained by Einstein in 1905 [38]. In general, the dynamics of Brownian particles comprises of deterministic and stochastic forces. Being able to separately measure these forces given finite trajectories of multiple relevant degrees of freedom is challenging. This problem is made even harder by the presence of uncorrelated noise that corrupts the measurement. In the first section of this chapter, we present a tool developed in [67] to address this problem and to reliably infer forces and related observables from trajectories of Brownian systems, Stochastic Force Inference (SFI). We will here only highlight some of the main results of [67] and we refer the reader to the original manuscript for a complete discussion of the topic. We will employ SFI extensively throughout this chapter and in the related manuscript [70].

We consider a Brownian system governed by an overdamped Langevin equation for some general coordinates $\mathbf{x} = (x_1, \cdots, x_d)$ in a d-dimensional space :

$$\dot{x}_\mu = F_\mu(\mathbf{x}) + \sqrt{2D}_{\mu\nu}\xi_\nu(t)\,. \tag{4.1}$$

In Eq. (4.1) the mobility has been absorbed in the definition of F_μ, $D_{\mu\nu}$ is the diffusion coefficient, ξ_μ a delta-correlated Gaussian white noise term, and the Einstein notation for repeated indices is understood. The goal of SFI is to reliably estimate the force field $F_\mu(\mathbf{x})$ acting on such a system and the diffusion coefficient $D_{\mu\nu}$. Furthermore, if the system is out of equilibrium, phase space currents, velocities, and entropy production rate are also relevant quantities that can be inferred.

The main idea of the method is to infer the deterministic part of the steady-state dynamics by projecting the unknown force field onto a known basis of functions. Starting from a given basis of n_b known functions $\{b_\alpha(\mathbf{x})\}_{\alpha=1,\cdots,n_b}$ (*e.g.* polynomials or Fourier modes), a basis $\{\hat{c}_\alpha(\mathbf{x})\}$ of functions that are orthonormal with respect to the measure induced by the empirical probability density function $\hat{p}_\tau(\mathbf{x}) = \frac{1}{\tau}\int_0^\tau \mathrm{d}t\delta(\mathbf{x}-\mathbf{x}(t))$ can be constructed. Given $\hat{c}_\alpha(\mathbf{x})$, the projection of the force field onto this function is

$$F^\tau_{\mu\alpha} = \frac{1}{\tau}\int_0^\tau \mathrm{d}t F_\mu(\mathbf{x}(t))\hat{c}_\alpha(\mathbf{x}(t))\,. \tag{4.2}$$

Employing the Langevin Eq. (4.1), we find

$$F^\tau_{\mu\alpha} = \frac{1}{\tau}\int_0^\tau \dot{x}_\mu(t)\hat{c}_\alpha(\mathbf{x}(t))\mathrm{d}t - \frac{1}{\tau}\int_0^\tau \sqrt{2D}_{\mu\nu}\xi_\nu(t)\hat{c}_\alpha(\mathbf{x}(t))\mathrm{d}t\,. \tag{4.3}$$

Since the second term on the right side of Eq. (4.3) goes to zero in the long time limit (here we always employ the Itô convention unless stated otherwise), we can identify the first term on the right-hand side of Eq. (4.3) with the inferred projection coefficient $\hat{F}_{\mu\alpha}$. With a discrete set of time measurements, we can compute the force projection coefficient as $\hat{F}_{\mu\alpha} = 1/\tau \sum_{i=1}^{N} \Delta x_\mu(t_i)\hat{c}_\alpha(\mathbf{x}(t_i))$. Studying the statistics of the second term on the right hand side of Eq. (4.3), yields a self consistent estimate of the error on the projection coefficient. This error quantifies how the inferred projection coefficient $\hat{F}_{\mu\alpha}$ deviates from the projection coefficient of the exact force field $F^{\tau}_{\mu\alpha}$; this error does not instead estimate how well the exact force field is represented in the chosen basis. Indeed, the exact force field is in general unknown. If the diffusion coefficient $D_{\mu\nu}$ is known, the error on the force projection coefficients goes as $\sim \sqrt{N_b/2\hat{I}_b}$ where N_b is the total number of coefficients to infer and $\hat{I}_b = \frac{\tau}{4} D^{-1}_{\mu\nu}\hat{F}_{\mu\alpha}\hat{F}_{\nu\alpha}$.[1] Thus, as customary for average quantities, the error on the force decreases with the length of the trajectory as $\sim 1/\sqrt{\tau}$.

If $D_{\mu\nu}$ is not know a priori and if it is space-independent, it can be easily estimated via the MSD:

$$\hat{D}_{\mu\nu} = \frac{1}{2\tau} \sum_{i=1}^{N} \Delta x_\mu(t_i)\Delta x_\nu(t_i)\,. \tag{4.4}$$

The phase space velocity (defined in Eq. (1.3) of the introduction) can be estimated via a projection-procedure equivalent to the procedure used to project the force field.[2] The inferred projection coefficients for the velocity then read:

$$\hat{v}_{\mu\alpha} = \frac{1}{\tau}\int_0^{\tau} \hat{c}_\alpha(\mathbf{x}(t)) \circ dx_\mu(t) \approx \frac{1}{\tau}\sum_{i=1}^{N-1} \hat{c}_\alpha\left[\frac{\mathbf{x}(t_i)+\mathbf{x}(t_{i+1})}{2}\right]\Delta x_\mu(t_i)\,, \tag{4.5}$$

where the symbol $\circ$ denotes a Stratonovich integral. Note that these projection coefficients are odd under time reversal, reflecting the analogous symmetry of the phase space velocity. Consistent with this, all coefficients go to zero at equilibrium. Having inferred the phase space velocity and the diffusion tensor, the entropy production rate (see Eq. 1.14 of the Introduction) can also be inferred as:

$$\widehat{\dot{S}} = \hat{v}_{\mu\alpha}\hat{D}^{-1}_{\mu\nu\alpha}\hat{v}_{\nu\alpha}\,. \tag{4.6}$$

The estimator for the EPR is biased, the bias being of order $2N_b/\tau$, and the remaining error is roughly $\mathcal{O}(\sqrt{\frac{2\widehat{\dot{S}}}{\tau}} + \frac{2N_b}{\tau})$. The errors are computed assuming that the diffusion

1 In two dimensions a second degree polynomial expansion requires inferring 6 coefficients.

2 The phase space velocity can be calculated from a trajectory as $v(\mathbf{x}) = \langle \dot{\mathbf{x}} | \mathbf{x}(t) = \mathbf{x}\rangle$, where the average along the trajectory is to be taken in a Stratonovich sense [52].

coefficient is known. If this is not the case, errors on the inference of the diffusion coefficient have repercussions on all other errors too.

Up to this point we have considered space-independent diffusion. Howver, diffusion is space-dependent in various cases such as diffusion close to walls in a confined geometry when hydrodynamic interactions cannot be neglected [60]. Importantly, in the-Langevin Eq. (4.1), if diffusion is space-dependent, an additional noise-induced drift arises when employing the Itô convention:

$$\dot{x}_\mu = F_\mu(\mathbf{x}) + \partial_\nu D_{\mu\nu}(\mathbf{x}) + \sqrt{2D(\mathbf{x})}_{\mu\nu}\xi_\nu(t)\,. \tag{4.7}$$

The same idea of projecting onto a known basis of function can be used to infer the diffusion tensor-field coefficients:

$$\hat{D}_{\mu\nu\alpha} = \frac{1}{2\tau}\sum_i \Delta x_\mu(t_i)\Delta x_\nu(t_i)\hat{c}_\alpha(t_i)\,, \tag{4.8}$$

the error on the projection coefficients being $\mathcal{O}(\sqrt{N_b\Delta t/\tau})$.

Experimental trajectories are often corrupted to a certain degree by measurement noise, meaning that the recorded time-trace is $y_\mu(t_i) = x_\mu(t_i) + \eta^i_\mu$, where the measurement noise η^i_μ is modeled as a zero-average time-uncorrelated white noise: $\left\langle \eta^i_\mu \right\rangle = 0$ and $\left\langle \eta^i_\mu \eta^j_\nu \right\rangle = \sigma^2_\eta \delta_{ij}\delta_{\mu\nu}$. In case of strong measurement noise, the force coefficients $\hat{F}_{\mu\alpha}$ and the diffusion projection coefficients $\hat{D}_{\mu\nu\alpha}$ (Eq. (4.8)) are biased by measurement noise, the bias being non-vanishing in the infinite time limit. Howver, a bias-corrected estimator of the diffusion coefficient can be obtained at the price of a larger error for short trajectories [67, 97]. Moreover, the coefficients of the phase space velocity (Eq. (4.5)) are not biased. Hence, to obtain an unbiased estimator of the force, it is possible to first infer the phase space velocity and then infer the force using the unbiased estimator for the diffusion coefficient. This approach exploits a relation existing between force and phase space velocity to obtain $\mathbf{F}$ from $\mathbf{v}$ and D[3]:

$$F_\mu(\mathbf{x}) = v_\mu(\mathbf{x}) - D_{\mu\nu}(\mathbf{x})\partial_\nu \log(p(\mathbf{x}))\,, \tag{4.9}$$

from which the inferred projection coefficients read

$$\hat{F}_{\mu\alpha} = \hat{v}_{\mu\alpha} - \sum_i \frac{\Delta t}{\tau}\partial_\nu \left[\hat{D}_{\mu\nu}\hat{c}_\alpha\right](\mathbf{x}(t_i))\,. \tag{4.10}$$

3 This relation is valid on the ensemble level and thus independently of the convention used at the Langevin level.

Unfortunately, correcting diffusion and forces for measurement noise adds an additional bias of order $\mathcal{O}(1/(\tau\Delta t))$ to the entropy production rate. To infer EPR in the presence of measurement noise we will thus need long enough trajectories with reasonably large Δt.

This final chapter of the thesis is dedicated to the analyses of time-lapse microscopy data. As we will see in Sec. 4.3, the stochastic dynamics that governs the time evolution of a sequence of images of a Brownian system must take into account the possibility of space-dependent diffusion and the presence of measurement noise. This means that we will always use the noise-corrected estimators for the diffusion coefficient and the force, even if this means increasing the errors for short trajectories.

4.2 To track or not to track? Selecting the relevant degrees of freedom

Traditional methods to analyze the non-equilibrium dynamics of biological systems rely on tracking the position of embedded objects or of fluorescently labeled regions [41, 42, 98, 99]. Once the object has been tracked, probability distributions, correlation functions and related quantities can be directly obtained from its time trace. If the dynamics of the tracked object satisfy Eq. (4.1) or (4.7), additional information such as the force field or the phase space currents can be inferred, as described in the previous section and shown in Fig.4.1a.[4] There might be situations, however, where tracking embedded objects is not feasible without altering the physical system of interest. Furthermore, we can imagine a scenario were the tracked object (for example a bead or a filament) is trapped in a region were little activity is present, as shown in Fig. 4.1b. In this case, tracking of the beads would lead to no observable non-equilibrium fluctuations in the trajectory. In general, even if tracking of embedded objects or fluorescently labeled regions is feasible, it is not clear a-priori which tracked coordinates will be most informative about the dissipative nature of the system. Ideally, one would like to study the non-equilibrium dynamics by employing the full image-data about the system (*e.g.* the full filamentous structure sketched in Fig. 4.1) without biasing the analysis towards tracking of embedded objects.

In the rest of this chapter we will present an alternative to tracking that directly employs all the information available from time-lapse microscopy imaging to infer dissipation and forces in the system.

4 We note that given a trajectory, verifying that the dynamics is correctly described by Eq. (4.1) or (4.7) is not easy, especially in the presence of strong measurement noise that obscures the Brownian dynamics. Here, we assume that this is the case and that our system is well described by Eq. (4.7).

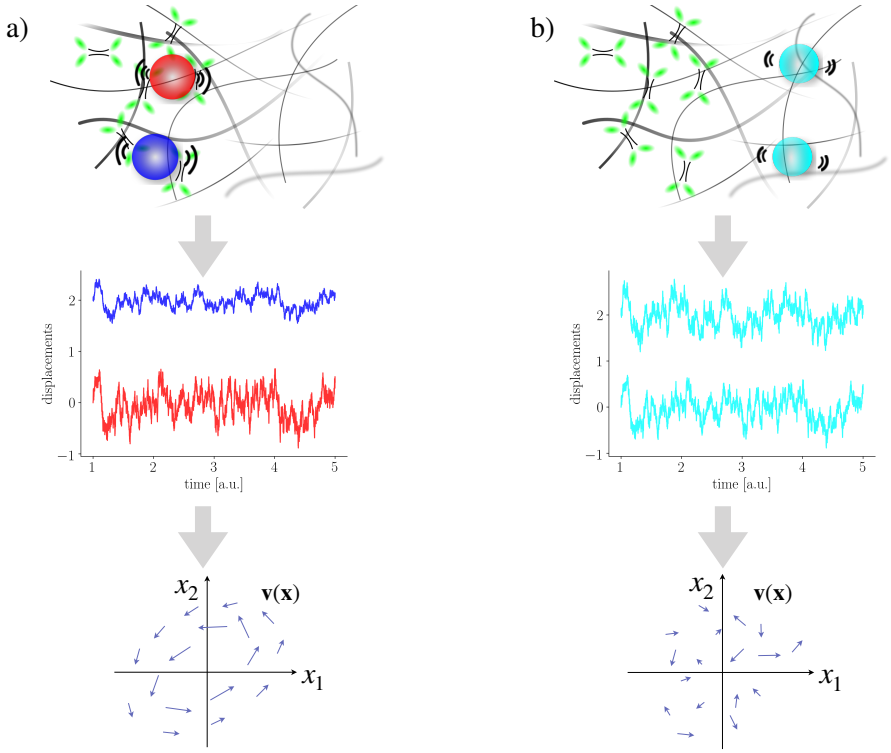

Figure 4.1 Panel a) and b) show two fictional cases of a motorized network where tracking two beads in an active region of the network can yield measurable phase space circulation (a) but tracking of the same beads in a region with little activity yields no measurable curculation (b). Top: Drawing of a motorized network with two embedded beads (the color of the beads reflects the intensity of the fluctuations). Center: the trajectories of the two beads. Bottom: Phase space circulation quantified by the phase space velocity $\mathbf{v}(\mathbf{x})$.

4.3 Learning by observing: principle of the method

As previously noted, our method is based on the assumption that the observed physical system (see Fig. 4.2 a) follows an overdamped Langevin equation such as Eq. (4.7). This assumption is not unjustified as the cytoplasm of cells has been shown to be mostly an elastic solid over a broad range of frequencies [42]. The Langevin Eq. for the state variables $\mathbf{x}$ is then

$$\frac{\mathrm{d}\mathbf{x}}{\mathrm{d}t} = \mathbf{\Phi}(\mathbf{x}) + \sqrt{2\mathbf{D}(\mathbf{x})}\xi(t), \tag{4.11}$$

where we have included force and noise induced drift in a general 'drift field' $\mathbf{\Phi}(\mathbf{x}) = \mathbf{F}(\mathbf{x}) + \nabla \cdot \mathbf{D}(\mathbf{x})$.

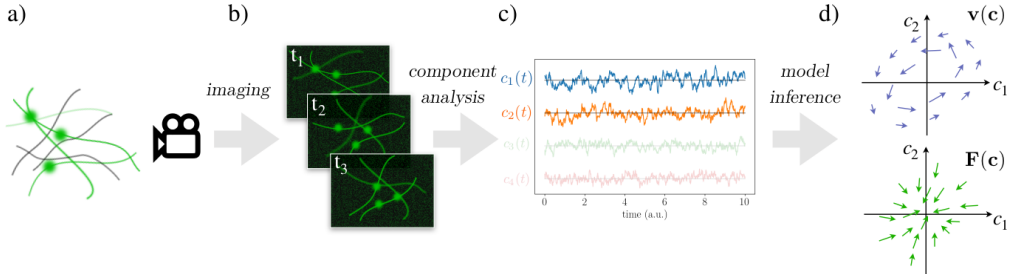

Figure 4.2 a) Sketch of a network of biopolymers (black) with embedded fluorescent filaments and beads (green). b) Image-frames of the fluorescent components in panel a) at three successive time points. c) The time trajectories of the projection coefficients $c_1(t)$, $c_2(t)$, $\cdots$: the coefficients and respective trajectories discarded by the dimensional reduction are faded. d) Sketch of the inferred velocity $\mathbf{v}(\mathbf{c})$ (top) and force field $\mathbf{F}(\mathbf{c})$ (bottom) in the space $\{c_1, c_2\}$.

We imagine to record a series of images $\{\mathcal{I}(t_0), \cdots, \mathcal{I}(t_N)\}$ ($L \times W$-dimensional vectors of real-valued pixel intensities) of the steady state dynamics (Eq. (4.11)) of the system at successive time-steps, as shown in Fig. 4.2b. This collection of successive images is a 'Brownian movie'. In general, the recorded images $\mathcal{I}$ will be an imperfect representation of the state of the system because of measurement noise. Here, the measurement noise $\mathcal{N}(t)$ is assumed to be time uncorrelated and added on top of the 'ideal' image $\bar{\mathcal{I}}$, such that the recorded images are given by $\mathcal{I}(t) = \bar{\mathcal{I}}(t) + \mathcal{N}(t)$. Furthermore, imaging the full state of the system might be impossible, as there could be regions of the systems that are hidden to the imaging apparatus. For this reason, we can only write a Markovian Langevin Eq. for the system comprised of visible degrees of freedom (the ideal image map $\bar{\mathcal{I}}$) and hidden ones $\mathbf{x}_\mathrm{h}$:

$$\frac{\mathrm{d}}{\mathrm{d}t}(\bar{\mathcal{I}}, \mathbf{x}_\mathrm{h}) = \phi(\bar{\mathcal{I}}, \mathbf{x}_\mathrm{h}) + \sqrt{2\mathcal{D}(\bar{\mathcal{I}}, \mathbf{x}_\mathrm{h})}\xi(t)\,. \tag{4.12}$$

Given the inevitable information loss in the imaging process, in the best-case scenario we would infer the average drift $\phi(\bar{\mathcal{I}}) := \left\langle \phi_{\bar{\mathcal{I}}}(\bar{\mathcal{I}}, \mathbf{x}_h)|\bar{\mathcal{I}}\right\rangle$, the average phase space velocity $\mathcal{V}(\bar{\mathcal{I}}) := \left\langle \mathcal{V}(\bar{\mathcal{I}}, \mathbf{x}_h)|\bar{\mathcal{I}}\right\rangle$, and the mean image diffusion tensor $\mathcal{D}(\bar{\mathcal{I}}) := \left\langle \mathcal{D}_{\bar{\mathcal{I}}}(\bar{\mathcal{I}}, \mathbf{x}_h)|\bar{\mathcal{I}}\right\rangle$, averaged over the hidden degrees of freedom $\mathbf{x}_h$. From the average drift and the average diffusion tensor we could immediately reconstruct force fields as $\mathcal{F}(\bar{\mathcal{I}}) = \phi(\bar{\mathcal{I}}) - \nabla \cdot \mathcal{D}(\bar{\mathcal{I}})$, as well as the 'apparent' entropy production rate $\dot{S}_\mathrm{apparent} = \left\langle \mathcal{V}^T(\bar{\mathcal{I}})\mathcal{D}^{-1}(\bar{\mathcal{I}})\mathcal{V}(\bar{\mathcal{I}})\right\rangle$, which is a lower bound to the total entropy production rate of the system.

Unfortunately, inferring observables directly in image space as suggested above is highly unpractical due to the high dimensionality of the image-data. We thus first seek to reduce the dimensionality of the problem by projecting the image dynamics on an appropriate set of 'modes' or 'components' (Fig. 4.2c). The number

of modes that we employ to describe our system is an important trade-off parameter of our method: by retaining few modes we have the advantage of having greatly reduced dimensionality, thus making inference in the reduced space simpler; however, retaining few modes implies greater loss of information about the actual image dynamics. In our manuscript [70] we elaborate on how to appropriately choose modes and we establish three truncation criteria. Once dimensionality has been reduced, we can employ SFI to disentangle the stochastic component of the dynamics from the deterministic one, thus obtaining the average drift $\mathbf{\Phi}(\mathbf{c}) \coloneqq \langle \mathbf{\Phi}_{\mathbf{c}}(\mathbf{c}, \mathbf{x}_h)|\mathbf{c}\rangle$, the average diffusion field $\mathbf{D}(\mathbf{c}) \coloneqq \langle \mathbf{D}_{\mathbf{c}}(\mathbf{c}, \mathbf{x}_h)|\mathbf{c}\rangle$, as well as the average force field $\mathbf{F}(\mathbf{c}) = \mathbf{\Phi}(\mathbf{c}) - \nabla \cdot \mathbf{D}(\mathbf{c})$ and velocity field $\mathbf{v}(\mathbf{c}) \coloneqq \langle \mathbf{v}_{\mathbf{c}}(\mathbf{c}, \mathbf{x}_h)|\mathbf{c}\rangle$ (see Fig. 4.2d). Importantly, now the hidden variables $\mathbf{x}_\mathrm{h}$ comprise also the variables discarded during the truncation procedure. The inferred observables in component space allow us to reconstruct directly the apparent entropy production rate (which, as previously remarked, is a lower bound to the total entropy production):

$$\dot{S}_{app.} = \left\langle \mathbf{v}(\mathbf{c})^T \mathbf{D}(\mathbf{c})^{-1} \mathbf{v}(\mathbf{c}) \right\rangle . \tag{4.13}$$

Moreover, by transforming force fields from component space back to image space we can reconstruct pixel force-maps that are informative about the deterministic component of the dynamics.

4.4 Benchmarking the method onto a minimal non-equilibrium system

Before applying our movie analysis to model systems and discuss the results, we briefly introduce the first dimensional reduction method that we will employ in this section: Principal Component Analysis (PCA).

4.4.1 Principal Component Analysis

Principal Component Analysis is a well established dimensionality reduction method that has been successfully applied both to structured data (such as an ensemble of particle positions) and unstructured data (series of images such as our movies). The idea of PCA is to infer orthogonal 'components' or vectors in such a way that, by projecting the data onto the linear space defined by these vectors, we retain maximal variance [100] (see Fig. 4.3). Given a set of length N of d-dimensional column-vectors $\mathbf{x}_n$, $n = 1, \cdots, N$, we seek to find a transformation that projects our data onto a space of dimensionality $m < d$ and that maximizes the variance of the projections. First, we compute the covariance matrix C from the data centered

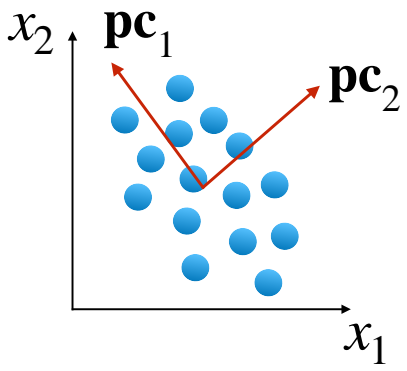

Figure 4.3 PCA maximizes the variance of the data (blue dots) projected along the principal components $\mathbf{pc}_1$ and $\mathbf{pc}_2$.

around the mean $\bar{\mathbf{x}} = \sum_{n=1}^{N} \mathbf{x}_n/N$:

$$C = \sum_{n=1}^{N} \frac{1}{N}(\mathbf{x}_n - \bar{\mathbf{x}})(\mathbf{x}_n - \bar{\mathbf{x}})^T \,. \tag{4.14}$$

The covariance matrix C is a $d \times d$ real symmetric matrix and thus, by the spectral theorem, there exists an orthonormal basis of d eigenvectors $\mathbf{v}_i$, $i = 1, \cdots, d$ of C in which C is diagonal. We will sort the eigenvectors in order of decreasing magnitude of the associated eigenvalue λ_i and rename them $\mathbf{pc}_i$. The variance of the data $\mathbf{x}_n$ projected onto the first eigenvector $\mathbf{pc}_1$ is:

$$\frac{1}{N}\sum_n (\mathbf{pc}_1^T\mathbf{x}_n - \mathbf{pc}_1^T\bar{\mathbf{x}})^2 = \frac{1}{N}\sum_n \mathbf{pc}_1^T(\mathbf{x}_n - \bar{\mathbf{x}})(\mathbf{x}_n - \bar{\mathbf{x}})^T\mathbf{pc}_1 = \mathbf{pc}_1^T C\mathbf{pc}_1 = \lambda_1^2 \,. \tag{4.15}$$

Thus, the variance of the data projected onto the first principal component $\mathbf{pc}_1$ is λ_1^2, which is maximal.

4.4.2 Brownian movie of the two-beads model: analysis results

Having introduced PCA, we can employ it to reduce the dimensionality of a Brownian movie (Fig. 4.4a) of the two-beads model (Sec. 1.5 of the Introduction).[5] While the first two principal components $\mathbf{pc}_1$, $\mathbf{pc}_2$ seem to reflect the collective in - and out-of-phase motion of the two-beads, components three $\mathbf{pc}_3$ and four $\mathbf{pc}_4$ highlight

5 For details on how the two-beads model is simulated and how the movies are generated see the Supplement to [70].

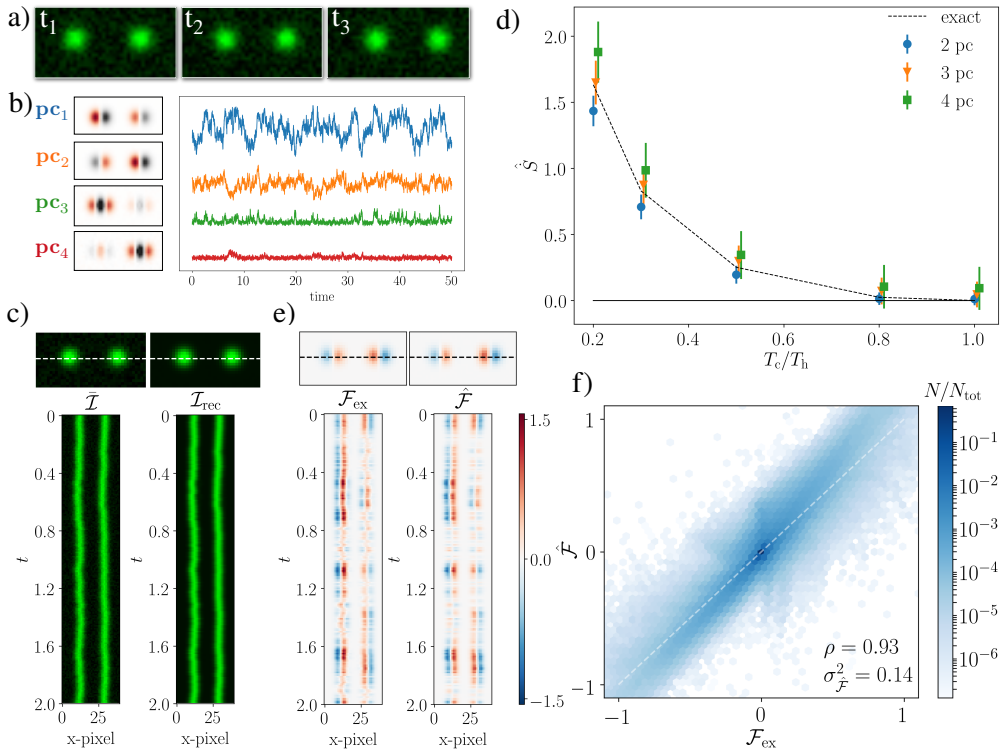

Figure 4.4 a) 40×20 Frames of the noisy (10% noise) Brownian movie for the two-beads model at successive time-points. b) The first 4 principal components with time-traces of respective projection coefficients. The color map displays negative values in black and positive values in red. c) Top: Snapshot of the original image $\mathcal{I}$ (left) and of the reconstructed image $\mathcal{I}_{\rm rec}$ (right) reconstructed with the first four principal components. Bottom: associated kymographs. We compare pixel intensities along the superimposed horizontal dashed line. d) Inferred entropy production rate $\widehat{\dot{S}}$ for varying temperature ratio T_c/T_h and number of included principal components. e) Top: comparison of inferred $\hat{\mathcal{F}}$ and exact $\mathcal{F}_{\rm ex}$ image-space force fields. Bottom: associated kymographs. f) Scatter plot of the exact image force field $\mathcal{F}_{\rm ex}$ vs. inferred image force field $\hat{\mathcal{F}}$ for different pixels and time points (data has been binned for visualization purposes). Results are obtained using the first four principal components. Panels c)-e)-f) have been obtained with $T_c/T_h = 0.5$ and for a trajectory of length $t_{\rm tot} = 10^5 \Delta t$, $\Delta t = 0.01$. Panel d) with $t_{\rm tot} = 5 \times 10^4 \Delta t$. The SFI routine was employed with a first order polynomial basis for the inference of forces and diffusion fields. The noise-corrected estimator was used to infer the diffusion fields [67].

the isolated fluctuations of the two beads, as shown in Fig. 4.4b. The first four principal components lead to an accurate reconstruction of the images in time, as reported in Fig. 4.4c. Interestingly however, when we compute the entropy production rate for different number of included principal components, we find that the first two components suffice to almost fully infer the entropy production of

the system. Furthermore, if $\mathbf{pc}_3$ and $\mathbf{pc}_4$ are included, the analysis overestimates the total entropy production rate, as shown in Fig. 4.4d. This behavior is not only consistent with the intuitive picture by which the first two components are enough to reconstruct the dynamics of the imaged physical system, but also with our truncation criteria (see Supplement of [70]).

Our procedure allows us to reconstruct force pixel-maps by transforming force fields in component space to force maps in the original image space. An adequate reconstruction of the images $\mathcal{I}_{\text{rec}}$ is possible by including the first four components, as shown in Fig. 4.4c; we thus employ the first four PCs to infer forces as well via the relation: $\widehat{\mathcal{F}}(\mathcal{I}(t)) \approx \sum_{i=1}^{4} \widehat{\mathbf{F}}_i(\mathbf{c}(t))\mathbf{pc}_i$. To assess whether our method accurately predicts force maps, we compare the inferred forces to the exact image force field obtained from the simulations as $\mathcal{F}_{\text{ex}}(t) = [\bar{\mathcal{I}}(\mathbf{x}(t) + \mathbf{F}(\mathbf{x}(t))\Delta t) - \bar{\mathcal{I}}(\mathbf{x}(t))]/\Delta t$. For different time points we compute the inferred $\widehat{\mathcal{F}}(t)$ and the exact force pixel map $\mathcal{F}_{\text{ex}}(t)$ and display the results in a kymograph (Fig. 4.4e) and in a scatter plot (Fig. 4.4f). To quantify the deviation of the inferred forces from the exact ones, we compute the relative squared error on the inferred image force field ($\sigma^2_{\widehat{\mathcal{F}}} = \sum_t \|\widehat{\mathcal{F}}(t) - \mathcal{F}_{\text{ex}}(t)\|^2 / \sum_t \|\widehat{\mathcal{F}}(t)\|^2$). Remarkably, we find excellent correlation between exact and inferred force maps (Pearson correlation coefficient $\rho = 0.93$) and squared error $\sigma^2_{\widehat{\mathcal{F}}} = 0.14$ (Fig. 4.4f).

In this section we have tested the capabilities of our analysis-method on a simple two-beads model, reliably inferring the entropy production rate and the forces acting on the system. Although in this minimal scenario tracking seems to be a more straightforward approach, this is not necessarily the case for more complex scenarios that we will consider next.

4.5 Dissipative Component Analysis: learning the non-equilibrium dynamics of viscoelastic networks

In Chapter 3 of this thesis we have introduced a cytoskeleton-inspired model of a viscoelastic networks with heterogeneous temperature distribution at the nodes. While in that case the non-equilibrium dynamics were quantified via the recorded time-traces of the nodes' positions (which is a 'perfect' tracking of the nodes), here we wish to analyze Brownian movies of such networks and quantify, in our tracking-free way, the entropy production rate and the forces.

We simulate the steady state dynamics of the nodes of a 5×5 triangular network of springs (see Supplement of [70] for details) and at each time step we create an image where all neighboring nodes are connected by filament-segments, as shown

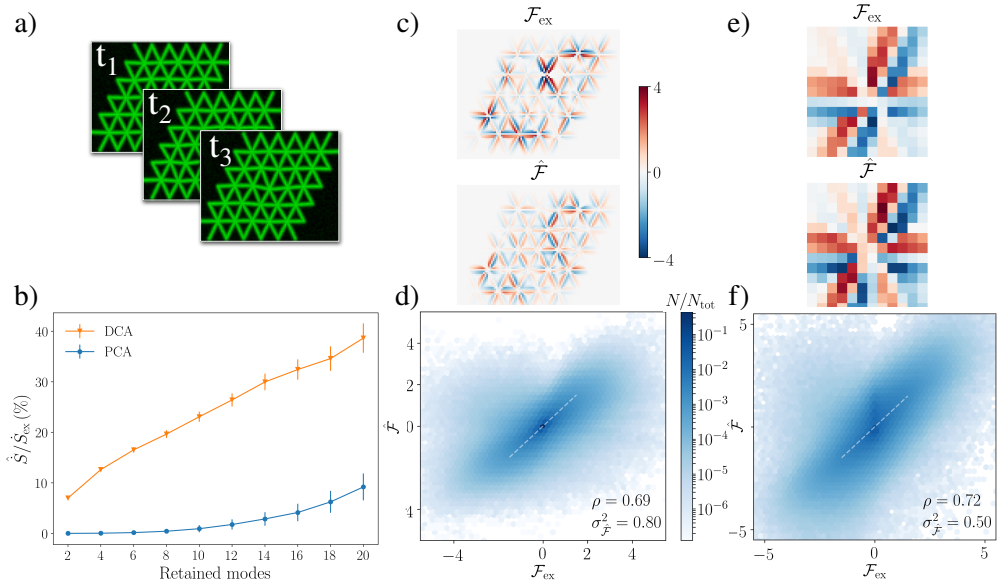

Figure 4.5 a) Three frames (100×80, 10% noise) of the spring network. b) Percentage of recovered entropy production rate $\widehat{\dot{S}}/\dot{S}_{\rm ex}$ via PCA (blued dots and line) and DCA (orange triangles and line) as a function of the number of retained components. c) Full network-50PCs included: Comparison between exact $\mathcal{F}_{\rm ex}$ and inferred $\widehat{\mathcal{F}}$ pixel force maps at $t = 7500\Delta t$. d) Full network-50PCs included: Scatter plot of inferred $\widehat{\mathcal{F}}$ vs. exact $\mathcal{F}_{\rm ex}$ force for the first 1000 time steps along the trajectory. e) Single cropped patch-20PCs included: Comparison between exact $\mathcal{F}_{\rm ex}$ and inferred $\widehat{\mathcal{F}}$ pixel force maps at $t = 7500\Delta t$. f) Full network force field via patch-wise inferene: Scatter plot of inferred vs. exact force pixel for the first 1000 time steps along the trajectory. All results have been obtained with a trajectory of 10^6 time steps, $\Delta t = 0.005$, and 100×80-pixels frames for the full network. The SFI routine was employed with a first order polynomial basis for the inference of forces and diffusion fields. Noise-corrected diffusion estimates have been employed.

in Fig. 4.5a. To reduce dimensionality, we first apply PCA to the movie and compute the entropy production rate for varying number of included components (4.5b blue dots/line). In this complex scenario PCA recovers less than 10% of the full entropy production rate: in fact, as proved in Sec. 4.4.1, PCA maximizes the projected variance and large variance does not imply large dissipation.

Ideally, one would like to devise a principled method to infer the *dissipative* components, *i.e.* components that yield maximal entropy production rate, and employ these dissipative components instead of principal components to reduce dimensionality. In what follows, we show that such a method ('Dissipative Component Analysis'-DCA) can indeed be rigorously derived for a linear system with homogeneous diffusion. Although the dynamics of our Brownian movie are neither

linear or with homogeneous diffusion, we will show that DCA is still capable of capturing substantial dissipation in the system and of greatly outperforming PCA.

To explain how Dissipative Component Analysis works, we consider a general scenario in which a system described by d coordinates $\mathbf{x} = (x_1, \cdots, x_d)$, obeys the Langevin equation

$$\dot{\mathbf{x}} = A\mathbf{x} + \sqrt{2D}\boldsymbol{\xi}\,, \tag{4.16}$$

where, as usual, $\boldsymbol{\xi}$ is a Gaussian delta-correlated white noise term, A is the interaction matrix, and D the constant diffusion matrix. As discussed in the Introduction (Chapter 2, Sec. 1.5), the Area Enclosing Rate (AER) matrix whose elements are defined by $\mathcal{A}_{ij} = \frac{1}{2\tau}\int_0^\tau (x_i dx_j - x_j dx_i)$, is related to the entropy production rate $\dot{S}$ by $\dot{S} = \mathrm{Tr}(\mathcal{A}C^{-1}\mathcal{A}^T D^{-1})$, where C is the covariance matrix. In covariance-identity-coordinates (cic), this relation simplifies to $\mathrm{Tr}(\mathcal{A}_{\mathrm{cic}}\mathcal{A}_{\mathrm{cic}}^T D^{-1})$. The matrix product $\mathcal{A}_{\mathrm{cic}}\mathcal{A}_{\mathrm{cic}}^T$ is a real symmetric matrix and can thus be diagonalised[6]: in the special-cic coordinates that diagonalize $\mathcal{A}_{\mathrm{cic}}\mathcal{A}_{\mathrm{cic}}^T$, the full EPR is decomposed into independent terms:

$$\dot{S} = \sum_{i\in odd} \lambda_i[(D^{-1}_{\mathrm{scic}})_{ii} + (D^{-1}_{\mathrm{scic}})_{i+1\,i+1}]\,, \tag{4.17}$$

where λ_i are the eigenvalues of $\mathcal{A}_{\mathrm{cic}}\mathcal{A}_{\mathrm{cic}}^T$. Importantly, the terms in the sum of Eq. (4.17) can be ordered according to their magnitude and the pairs of eigenvectors of $\mathcal{A}_{\mathrm{cic}}\mathcal{A}_{\mathrm{cic}}^T$ sorted accordingly. We term the ordered pairs of eigenvectors 'Dissipative Components' (DCs) and denote them by $\{\mathbf{dc}_1, \mathbf{dc}_2\}$, $\{\mathbf{dc}_3, \mathbf{dc}_4\}$, $\cdots$.

After applying PCA to our data both to reduce dimensionality and noise, we compute the dissipative components for the Brownian movie of the network (Fig. 4.5a), project the dynamics onto the DCs and compute the entropy production rate using SFI. Remarkably, we find that the EPR inferred with DCA allows to reconstruct up to 40% of the total EPR, performing about twenty times better than PCA, as shown in 4.5b.

Our method is not limited to inferring the entropy production rate ofthe system from phase space currents. Our PCA-based approach allows us in fact to infer pixel force maps both at equilibrium and out of equilibrium. By transforming the force fields inferred from PC-space back to image space, we construct force maps at each time step along the trajectory. Qualitatively, we capture the basic features of the force field, as shown in the comparison Fig. 4.5c. Then, we quantitatively compare the inferred and the exact force field maps pixel by pixel. For a selected portion of the trajectory we plot the inferred and exact pixel values one against the other and obtain the scatter plot shown in Fig. 4.5d. Due to the large dimensionality of

6 In the case of even dimension N of phase space, the matrix $\mathcal{A}_{\mathrm{cic}}\mathcal{A}_{\mathrm{cic}}^T$ has $d/2$ pairs of eigenvalues (each pair consists of equal eigenvalues) and $d/2$ associated pairs of eigenvectors. In the case of odd d there is at least one unpaired eigenvalue equal to zero.

the network, we need to include 50 PCs in our analysis in order to estimate forces. However, force inference performs rather poorly in this high dimensional context, as shown in Fig. 4.5d. Thus, this leaves little hope for reliable inference of force maps for even larger systems. Nevertheless, we can exploit the fact that in our system the interactions between the components are local and use this to infer forces for the full network. To this end, we divide each movie into disjoint 'patches' and apply our full inference method to each patch separately (see Fig. 4.5e and Supplement of [70]). Rejoining the inferred force maps in each patch, leads to a largely improved inference for the full network, as shown in Fig. 4.5f.

4.5.1 Two-beads model revisited: in and out-of-focus fluctuations

In section 4.4.2 we considered two beads that fluctuate in the focal plane of the microscope, tacitly assuming that the total intensity of each bead remained constant in time. Here, we would like to extend the two-beads model to simulate conditions in which the beads can also fluctuate out of the focal plane of the microscope in the z direction, as shown in Fig. 4.6a-b. When objects are out of focus they become blurry; to simulate this, we allow the intensity of each bead to decrease linearly with the displacement in the z direction. Importantly, we make no distinction between positive z direction (away from the camera/microscope in Fig. 4.6a) and negative z direction (towards the camera/microscope): the intensity of a bead always decreases by a factor $\sim 1 - |z|/z_{\max}$. Although from our movie it is possible to detect whether a bead is moving out of or in the focal plane, we expect some loss of information: it is in fact not possible to tell whether a bead is *e.g.* moving from $z = 0$ towards positive z-values or towards negative z-values. Nevertheless, an approach based on tracking would not be able to detect motion out of the focal plane, leading to complete loss of information about motion in the z direction.

Following the same approach as in Sec. 4.4.2, we perform PCA on the movie (Inset of Fig. 4.6c): while $\mathbf{pc}_1$ is analogous to the first principal component of Fig. 4.4b, $\mathbf{pc}_2$ is different. This second PC represents in-phase motion of the two beads in the z direction. We can understand why PCA select this kind of motion by realizing that the z direction is, to first order, floppy, leading to little restoring force and thus large variance.

If we assess the irreversibility of our system via PCA, we recover little EPR with the first two or three PCs (Fig. 4.6c). This is in contrast to the two-beads model (Fig. 4.4d) analyzed in Sec. 4.4.2 where the first two PCs mostly sufficed to recover the full EPR. Due to the aforementioned loss of information about motion in the z-direction, we do not recover the full EPR even if four PCs are included (Fig. 4.6c). We expect DCA to perform better than PCA and to be able to recover more EPR with fewer included components. Indeed, this is the case and with the first two DCs

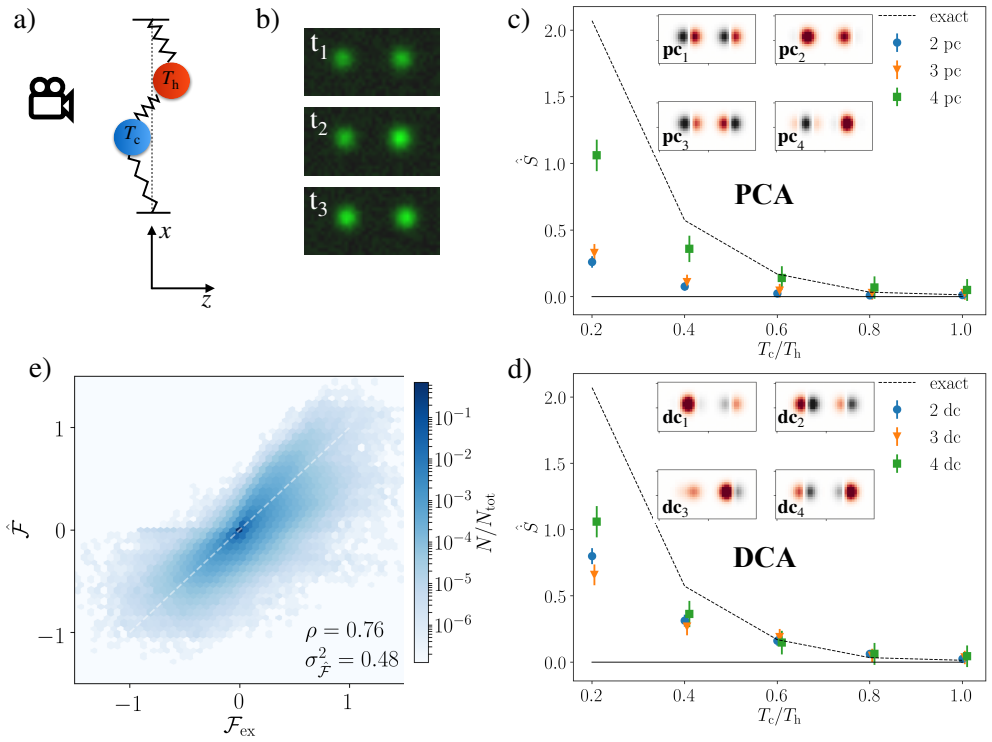

Figure 4.6 a) Schematics of the two-beads model with in-plane (x-direction, dashed line) and out of plane (z direction) fluctuations. b) Three 40×20 frames of the noisy (10% noise) Brownian movie: notice how at t_2, the left bead has weaker intensity than the right one due to motion in the z-direction. c) Inferred entropy production rate $\widehat{\dot{S}}$ as a function of the temperature ratio T_c/T_h for different number of PCs included. Inset: first four principal components for $T_c/T_h = 1/2$. d) Inferred entropy production rate $\widehat{\dot{S}}$ vs. T_c/T_h for different number of DCs included. Inset: first four dissipative components for $T_c/T_h = 1/2$. e) Comparison of inferred force field with exact force field using the first four PCs (or, equivalently, first four DCs). All results are obtained with spring constant $k = 2$, friction coefficient $\gamma = 1$ and for a trajectory of length $10^5 \Delta t$, $\Delta t = 0.01$.

we recover almost three times more EPR than with the first two PCs (Fig. 4.6d). Consistently, if all four DCs are included PCA and DCA are equivalent and they perform equally.

Finally, we also compare inferred image forces obtained with four PCs (or four DCs equivalently) and the exact image force in Fig. 4.6e: although the inclusion of more modes would presumably improve the results, force-inference still performs well ($\rho = 0.76$, $\sigma^2_{\widehat{\mathcal{F}}} = 0.48$). We remark once again that it is by construction impossible in this Brownian movie, to distinguish forces in the positive from forces in the negative z-direction.

Overall, we showed how PCA alone is not able to recover a substantial fraction of the EPR and we devised an alternative method, DCA, that succeeds at this task by identifying components that maximize the retained dissipation. We demonstrated the efficacy of our method on a challenging Brownian movie of a 5×5 viscoelastic triangular network and on an extension of the two-beads model that additionally includes fluctuations out of the focal plane of the microscope. Furthermore, we employed our method to reconstruct image force fields that are informative about the deterministic dynamics of the system: by showing, via a cropping procedure, that our approach is scalable, we can infer forces also in the case of large systems with local interactions.

4.6 Summary and Discussion

The goal of this chapter was to introduce a novel method to analyze the stochastic dynamics of time-lapse microscopy data. By employing the full information available in the recorded pixel intensity map, we developed a tracking free algorithm that is able to successfully quantify the non-equilibrium dynamics of model systems inspired by biological assemblies.

Our approach consists of three steps: *imaging* $\mapsto$ *component analysis* $\mapsto$ *model inference*. The first step maps the overdamped Langevin dynamics onto a noisy pixel map in a non-linear way. During the imaging process, only visible degrees of freedom are revealed, hence the resulting dynamics is non Markovian and only average observables can be inferred. The 'curse of dimensionality' prevents us from solving the inverse Brownian dynamics problem directly in image space; for this reason, the second step in our procedure consists of finding an appropriate reduced set of components onto which we can project our dynamics. We accomplish this via a combination of a traditional dimensionality reduction scheme –Principal components analysis– and Dissipative component analysis (DCA), the latter being an original way of finding components that maximize the retained entropy production rate. The reduced dimensionality of the problem after projection onto components makes it possible to infer a model (step three of our method) and hence to infer observables such as diffusion, force, and velocity fields, as well as the entropy production rate. To this end, we employ SFI: a data-efficient routine that, together with inference of average observables, provides estimates of inference errors and performs well in reasonably high dimensional spaces.

Having validated our PCA-based method on the two-beads model, we moved on to a challenging example of a viscoelastic network inspired by cytoskeletal structures. Here, PCA is not sufficient to recover a substantial fraction of the entropy production rate; DCA instead successfully selects the most dissipative components, yielding largely improved EPR inference. Furthermore, DCA also performs well in the realistic

scenario of two beads that fluctuate in and out of the focal plane of the microscope. Apart from quantifying the irreversible dynamics present in the movie, our approach is also able to extract image force fields, thus providing a novel way of assessing the microscopic forces acting on a physical system. In summary, we demonstrated how it is possible to extract and quantify non-equilibrium behavior directly from a Brownian movie, thus opening new doors to data-driven analyses of soft living matter.

4.7 Publication preprint

Learning the Non-Equilibrium Dynamics of Brownian Movies

by

F. S. Gnesotto[1], G. Gradziuk[1], P. Ronceray[2], and C. P. Broedersz [1]

[1]Department of Physics, Arnold Sommerfeld Center for Theoretical Physics and Center for NanoScience, Ludwig-Maximilians-Universität München, Theresienstraße 37, 80333 München, Germany

[2]Center for the Physics of Biological Function, Princeton University, Princeton, NJ 08544, USA

reprinted on pages 97–106

available at:

***ArXiv* 100, 013002 (2019)**.

Supplemental Material reproduced on pages 107–112.

Learning the Non-Equilibrium Dynamics of Brownian Movies

Federico S. Gnesotto,[1] Grzegorz Gradziuk,[1] Pierre Ronceray,[2,*] and Chase P. Broedersz[1,†]

[1] *Arnold-Sommerfeld-Center for Theoretical Physics and Center for NanoScience, Ludwig-Maximilians-Universität München, D-80333 München, Germany.*

[2] *Center for the Physics of Biological Function, Princeton University, Princeton, NJ 08544, USA*

(Dated: January 23, 2020)

Time-lapse microscopy imaging provides direct access to the dynamics of soft and living systems. At mesoscopic scales, such microscopy experiments reveal intrinsic fluctuations, which may have both thermal and non-equilibrium origins. These intrinsic fluctuations, together with measurement noise, pose a major challenge for the analysis of the dynamics of these "Brownian movies". Traditionally, methods to analyze such experimental data rely on tracking embedded or endogenous probes. However, it is in general unclear how to select appropriate tracers; it is not evident, especially in complex many-body systems, which degrees of freedom are the most informative about their non-equilibrium nature. Here, we introduce an alternative, tracking-free approach that overcomes these difficulties via an unsupervised analysis of the Brownian movie. We develop a dimensional reduction scheme that selects a basis of modes based on dissipation, and we subsequently learn the non-equilibrium dynamics in this basis and estimate the entropy production rate. In addition, we infer time-resolved force maps in the system and show that this approach is scalable to large systems, thus providing a potential alternative to microscopic force-probes. After benchmarking our method against a minimal two-beads model, we illustrate its broader applicability with an example inspired by active biopolymer gels.

Over the last two centuries, fundamental insights have been gleaned about the physical properties of biological and soft matter systems by using microscopes to image their dynamics [1, 2]. At the micrometer scale and below, however, this dynamics is inherently stochastic, as ever-present thermally driven Brownian fluctuations give rise to short-time displacements [3–5]. This random motion makes such "Brownian movies" appear jiggly and erratic; this randomness is further exacerbated by measurement noise and limited resolution intrinsic to, *e.g.*, fluorescence microscopy [6]. In light of all these sources of uncertainty, how can one best make use of measured Brownian movies of a systems dynamics, to learn the underlying physics of the fluctuating and persistent forces?

In addition to thermal effects, active processes can strongly impact the stochastic dynamics of a system [7–11]. Recently, there has been a growing interest in quantifying and characterizing the non-equilibrium nature of the stochastic dynamics in active soft and living systems [12–24]. In cells, molecular-scale activity, powered for instance by ATP hydrolysis, control mesoscale non-equilibrium processes in assemblies such as cilia [25, 26], flagella [27], chromosomes [28], protein droplets [29] or cytoskeletal networks [30–33]. The irreversible nature of such non-equilibrium processes can lead to measurable dissipative currents in a phase space of mesoscopic degrees of freedom [8, 16, 17, 34–36]. Such dissipative currents can be quantified by the entropy production rate [18, 19, 21, 23, 37], but it remains an outstanding challenge to accurately infer the entropy production rate by analyzing Brownian movies of such systems.

Traditional approaches to measure microscopic forces and analyze time-lapse microscopy data typically rely on tracking the position or shape of well-defined probes such as tracer beads, fluorescent proteins and filaments, or simply on exploiting the natural contrast of the intracellular medium to obtain such tracks [13–16, 28, 30, 33, 38–41]. The tracer trajectories can be studied through stochastic analysis techniques to extract an effective model for their dynamics and infer quantities like the entropy production [18, 19, 21, 23, 42–45]. There are, however, many cases in which tracking is impractical [46, 47], due to limited resolution or simply because there are no recognizable objects to use as tracers. Another, more fundamental limitation of tracking is that one then mostly learns about the dynamics of the tracked object—not of the system as a whole. Indeed, the dissipative power in a system might not couple directly to the tracked variables, and *a priori*, it might not be clear which coordinates will be most informative about such dissipation. This raises the question how one can identify which degrees of freedom best encode the forces and non-equilibrium dissipation in a given system.

Here we propose an alternative to tracking: learning the dynamics and inferring the entropy production directly from the unsupervised analysis of Brownian movies. We first decompose the movie into generic principal modes of motion, and predict which ones are the most likely to encode useful information through a "Dissipative Component Analysis" (DCA). We then perform a dimensional reduction, which leads to a representation of the movie as a stochastic trajectory in this component space. Finally, we employ a recently introduced method, Stochastic Force Inference (SFI) [23], to analyze such trajectories. Our approach not only yields an estimate of the entropy production rate of a Brownian movie, which is a

* ronceray@princeton.edu
† c.broedersz@lmu.de

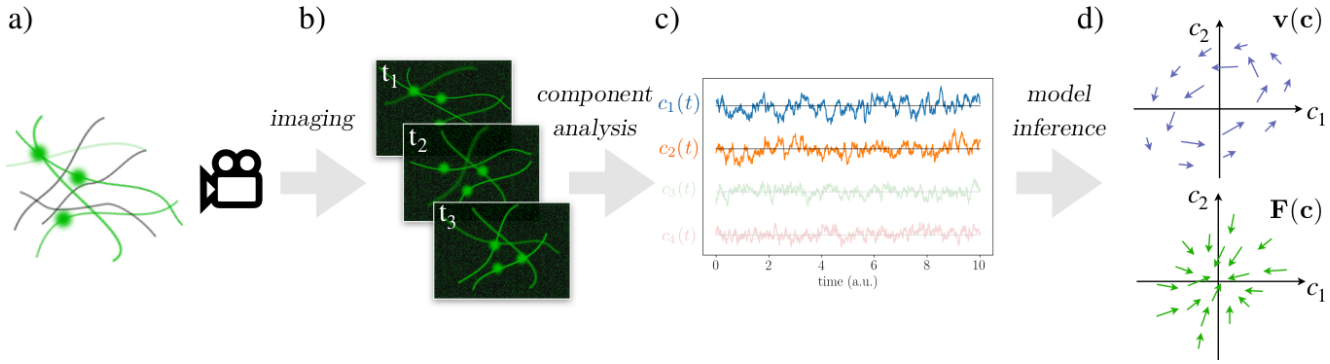

FIG. 1. **Schematic illustration of our approach to learn non-equilibrium dynamics from a Brownian movie.** a) Sketch of a network of biopolymers (black) with embedded fluorescent filaments and beads (green). b) Image-frames of the fluorescent components in panel a) at three successive time points. c) The time trajectories of the projection coefficients $c_1(t), c_2(t), \cdots$: the coefficients and respective trajectories discarded by the dimensional reduction are faded. d) Sketch of the the inferred velocity $\mathbf{v}(\mathbf{c})$ (top) and force field $\mathbf{F}(\mathbf{c})$ (bottom) in the space $\{c_1, c_2\}$.

controlled lower bound to the system's total entropy production, but also important dynamical information such as a time-resolved force map of the imaged system. Thus, our approach may provide an alternative to methods that use microcopic force sensors [40, 41, 48, 49]. In this article, we first present the method in its generality, then benchmark it on a simple two-beads model. Finally, we demonstrate the potential of our approach on simulated semi-realistic fluorescence microscopy movies of out-of-equilibrium biopolymer networks, and we show that the force inference approach is scalable to large systems.

I. PRINCIPLE OF THE METHOD

We begin by describing a tracking-free method to infer the dynamical equations of a system from raw image sequences. This approach allows us to determine a bound on the dissipation of a system, as well as the force-field in image space.

Our starting point is the assumption that the physical system we observe (Fig. 1a)—such as a cytoskeletal network or a fluctuating membrane—can be described by a configurational state vector $\mathbf{x}(t)$ at time t, undergoing steady-state Brownian dynamics in an unspecified d-dimensional phase space:

$$\frac{\mathrm{d}\mathbf{x}}{\mathrm{d}t} = \mathbf{\Phi}(\mathbf{x}) + \sqrt{2\mathbf{D}(\mathbf{x})}\xi(t), \tag{1}$$

where $\mathbf{\Phi}(\mathbf{x})$ is the drift field, $\mathbf{D}(\mathbf{x})$ is the diffusion tensor field, and throughout this article $\xi(t)$ is a Gaussian white noise vector ($\langle\xi(t)\rangle = 0$ and $\langle\xi_i(t)\xi_j(s)\rangle = \delta_{ij}\delta(t-s)$). Note that when diffusion is state-dependent, $\sqrt{2\mathbf{D}(\mathbf{x})}\xi(t)$ is a multiplicative noise term: we employ the Itô convention for the drift, *i.e.* $\mathbf{\Phi}(\mathbf{x}) = \mathbf{F}(\mathbf{x}) + \nabla\cdot\mathbf{D}(\mathbf{x})$, where $\mathbf{F}(\mathbf{x})$ is the physical force in the absence of Brownian noise [50, 51].

Our goal is to learn as much as possible about the process described by Eq. 1 from an experimental observation. In particular, we aim to measure if, and how far, the system is out-of-equilibrium by determining the irreversible nature of its dynamics. This irreversibility is quantified by the system's entropy production rate [37]

$$\dot{S}_{\mathrm{total}} = \left\langle \mathbf{v}(\mathbf{x})\mathbf{D}^{-1}(\mathbf{x})\mathbf{v}(\mathbf{x})\right\rangle, \tag{2}$$

where $\langle\cdot\rangle$ denotes a steady-state average, throughout this article we set Boltzmann's constant $k_{\mathrm{B}} = 1$, and $\mathbf{v}(\mathbf{x})$ is the mean phase space velocity field quantifying the presence of irreversible currents. Specifically, using the steady-state Fokker-Planck equation one can write $\mathbf{v}(\mathbf{x}) = \mathbf{F}(\mathbf{x}) - \mathbf{D}(\mathbf{x})\nabla\log P(\mathbf{x})$, where $P(\mathbf{x})$ is the steady-state probability density function, and flux balance imposes that $\nabla\cdot(P\mathbf{v}) = 0$.

The input of our method consists of a discrete time-series of microscopy images of the physical system $\{\mathcal{I}(t_0), \ldots \mathcal{I}(t_N)\}$—a "Brownian movie" (Fig. 1b). Each image $\mathcal{I}(t)$ is an imperfect representation of the state $\mathbf{x}(t)$ of the physical system as a bitmap, *i.e.* a $L\times W$ vector of real-valued pixel intensities [52]. Specifically, we model the imaging apparatus as a noisy nonlinear map $\mathcal{I}(t) = \bar{\mathcal{I}}(\mathbf{x}(t)) + \mathcal{N}(t)$, where $\mathcal{N}$ is a temporally uncorrelated noise representing measurement noise (such as the fluctuations in registered fluorescence intensities), and $\bar{\mathcal{I}}(\mathbf{x})$ is the "ideal image" returned on average by the microscope when the system's state is $\mathbf{x}$. We assume that this map $\bar{\mathcal{I}}(\mathbf{x})$ is time-independent (*i.e.* that the microscope settings are fixed and stable).

Importantly, if no information is lost by the imaging process, the ideal image $\bar{\mathcal{I}}(t)$ undergoes a Brownian dynamics equation determined by the nonlinear transformation of Eq. 1 through the map $\mathbf{x}\mapsto\bar{\mathcal{I}}(\mathbf{x})$, as prescribed by Itô's lemma [53]. In general, however, there is information loss and $\bar{\mathcal{I}}(\mathbf{x})$ is not invertible: due to finite resolution or because some elements are simply not visible, the imaging may not capture the full high-dimensional state of the system. For this reason, the dynamics in image space are not uniquely specified by the ideal image value

$\bar{\mathcal{I}}$; they also depend on "hidden" degrees of freedom $\mathbf{x}_h$ not captured by the image. In this case, a Markovian dynamical equation for $\bar{\mathcal{I}}$ alone does not exist, but by including the dynamics of $\mathbf{x}_h$, we can write

$$\frac{\mathrm{d}}{\mathrm{d}t}(\bar{\mathcal{I}}, \mathbf{x}_h) = \phi(\bar{\mathcal{I}}, \mathbf{x}_h) + \sqrt{2\mathcal{D}(\bar{\mathcal{I}}, \mathbf{x}_h)}\xi(t), \tag{3}$$

Here $\phi(\bar{\mathcal{I}}, \mathbf{x}_h)$ and $\mathcal{D}(\bar{\mathcal{I}}, \mathbf{x}_h)$ are the drift field and diffusion tensor, respectively, in the combined space of pixel intensities and hidden variables. Our Brownian movie analysis allows us to infer the mean image drift $\phi(\bar{\mathcal{I}}) \coloneqq \langle \phi_{\bar{\mathcal{I}}}(\bar{\mathcal{I}}, \mathbf{x}_h) | \bar{\mathcal{I}} \rangle$ and mean image diffusion tensor $\mathcal{D}(\bar{\mathcal{I}}) \coloneqq \langle \mathcal{D}_{\bar{\mathcal{I}}}(\bar{\mathcal{I}}, \mathbf{x}_h) | \bar{\mathcal{I}} \rangle$, averaged over the degrees of freedom $\mathbf{x}_h$ lost in the imaging process. From drift and diffusion fields we can directly obtain the mean image force field $\mathcal{F}(\bar{\mathcal{I}}) = \phi(\bar{\mathcal{I}}) - \nabla \cdot \mathcal{D}(\bar{\mathcal{I}})$. Similar to force and diffusion fields, the phase space currents $\mathbf{v}(\mathbf{x})$ in the d-dimensional physical phase space, transform into currents $\mathcal{V}(\bar{\mathcal{I}})$ in the $L \times W$-dimensional image space—again, averaged over unobserved degrees of freedom. These currents result in an apparent entropy production associated to the image dynamics [54],

$$\dot{S}_{\text{apparent}} = \left\langle \mathcal{V}(\bar{\mathcal{I}}) \mathcal{D}^{-1}(\bar{\mathcal{I}}) \mathcal{V}(\bar{\mathcal{I}}) \right\rangle . \tag{4}$$

Importantly, the function $(\mathcal{V}, \mathcal{D}) \mapsto \mathcal{V}\mathcal{D}^{-1}\mathcal{V}$ is multivariate convex, and thus by Jensen's inequality, $\dot{S}_{\text{apparent}} \leq \dot{S}_{\text{total}}$: the apparent entropy production is a lower bound to the total entropy production.

The goal of our method is to reconstruct the mean image-space dynamics $(\mathcal{F}(\bar{\mathcal{I}}), \mathcal{D}(\bar{\mathcal{I}}))$, and in particular the corresponding entropy production (Eq. 4). However, doing so in the high-dimensional image space is unpractical and would require unrealistic amounts of data. We therefore need to reduce the dimensionality of our system to a tractable number of relevant degrees of freedom.

Because each image represents a physical state of the system, we expect that the ideal images $\bar{\mathcal{I}}(t)$ all share similar structural features. Consequently, the Brownian movie occupies only a smaller subspace in the space of all configurations of pixel intensities. To restrict ourselves to the manifold of images representing the physical states, we can either perform only Principal Component Analysis (PCA) or, as we shall see later, reinforce PCA with an analysis which provides an additional basis transformation to select the most dissipative components. The idea behind this approach is that the components are hierarchically ordered according to how much they contribute to the entropy production, such that it becomes possible to truncate the basis and reduce the dimensionality of the problem, while retaining maximum information about the system's irreversibility.

We truncate the basis of components according to three criteria: 1) Noise floor—due to the finite amount of data and the measurement noise present in the Brownian movie, some modes are indistinguishable from the measurement noise. We only keep modes that rise above this noise floor. 2) Time resolution of the dynamics—we only consider the components whose statistical properties are consistent with Brownian dynamics, *i.e.* such that the short-time diffusive behavior can be resolved through the noise. 3) Dimension of phase space—for a physical system $\mathbf{x}(t)$ with d observable degrees of freedom the ideal images $\bar{\mathcal{I}}(\mathbf{x}(t))$ will form a d-dimensional manifold in the large $(L \times W)$-dimensional image space. Depending on the shape of the manifold it may be possible to project the images $\mathcal{I}(t)$ on an appropriate d-dimensional linear subspace, without losing any information about the dynamics of $\mathbf{x}(t)$. This restriction ensures that the dynamics is inferred in a space of dimensionality smaller or equal to that of the physical system, thus avoiding singularities in the inference of diffusion and related quantities. We determine the dimensionality of the manifold d by performing PCA locally, in a region where the manifold is approximately flat and keep only the first d principal components of the globally performed PCA (see Supplementary Material Sec. V). Note, while these first d components will be sufficient to represent the dynamics of $\mathbf{x}(t)$, more modes may be need to faithfully reconstruct configurational and dynamical quantities in image space.

Our task is now reduced to inferring the mean dynamics in component space,

$$\mathbf{\Phi}(\mathbf{c}) \coloneqq \langle \mathbf{\Phi}_{\mathbf{c}}(\mathbf{c}, \mathbf{x}_h) | \mathbf{c} \rangle \ , \ \mathbf{D}(\mathbf{c}) \coloneqq \langle \mathbf{D}_{\mathbf{c}}(\mathbf{c}, \mathbf{x}_h) | \mathbf{c} \rangle \tag{5}$$

where $\mathbf{c}(t) = (c_1(t), c_2(t), \cdots, c_n(t))$ are the components obtained after a linear transformation of the images (see Fig. 1c), and the hidden degrees of freedom $\mathbf{x}_h$ now also include those present in the image, but left out after the components' truncation. This procedure has reduced the system's dynamics to that of a smaller number of components, making it possible to learn $\mathbf{\Phi}(\mathbf{c})$ and $\mathbf{D}(\mathbf{c})$.

To this end, we employ a recently introduced method, Stochastic Force Inference [23] (SFI), for the inverse Brownian dynamics problem. Briefly, this procedure is based on a least-squares approximation of the diffusion and drift fields using a basis of known functions (such as polynomials). This method is data-efficient, not limited to low-dimensional signals or equilibrium systems, robust against measurement noise, and provides estimates of the inference error, making it well suited for our purpose. In practice, we use SFI in two ways: 1) we infer the velocity field $\mathbf{v}(\mathbf{c})$ (Fig. 1d) and the diffusion field $\mathbf{D}(\mathbf{c})$, which we use to measure the entropy production. 2) We infer the drift field $\mathbf{\Phi}(\mathbf{c})$, compute the image force $\mathbf{F}(\mathbf{c}) = \mathbf{\Phi}(\mathbf{c}) - \nabla \cdot \mathbf{D}(\mathbf{c})$ (Fig. 1d), and thus reconstruct the dynamics of the components. To render this deterministic dynamics more intelligible, we can transform $\mathbf{F}(\mathbf{c})$ back into image space by inverting the $\mathcal{I} \mapsto \mathbf{c}$ linear transformation: this results in a "pixel force" map, which indicates at each time step which pixel intensities tend to increase or decrease. This provides, we argue, a novel way to gain insight into the dynamics of Brownian systems and disentangle deterministic forces from Brownian motion without tracking.

Our analysis framework can thus be schematically summarized as: *imaging* → *component analysis* → *model*

inference (Fig. 1). This procedure allows the inference of entropy production and reconstruction of the dynamical equations from image sequences of a Brownian system.

II. A MINIMAL EXAMPLE: TWO-BEADS BROWNIAN MOVIES

Next, we test the performance of our procedure on a simple non-equilibrium model: two coupled beads moving in one dimension. The beads are coupled by Hookean springs with stiffness k and experience Stokes drag with friction coefficient γ, due to the surrounding fluid (Fig. 2a). In this two-bead model, the time-evolution of the bead displacements $\mathbf{x}(t) = (x_1(t), x_2(t))$ obeys the overdamped Langevin Eq. (1), with $\mathbf{F}(\mathbf{x}) = \mathbf{A}\mathbf{x}$ and $A_{ij} = (1-3\delta_{ij})k/\gamma$. The system is driven out of thermodynamic equilibrium by imposing different temperatures on the two beads: $D_{ij} = \delta_{ij} k_\mathrm{B} T_i/\gamma$ [8, 21, 55–57]. First, we obtain position trajectories for the two beads by discretizing their stochastic dynamics using an Euler integration scheme (see Supplementary Material Sec. I). Then, we use these position trajectories to construct a noisy Brownian movie (Fig. 2b) (cf. Supplementary Material Sec. II and Supplementary Movie 1). Note that by construction, the steady-state dynamics of the two-beads system in image space is governed by a nonlinear Langevin equation with multiplicative noise.

We seek to reduce the dimensionality of the data by finding relevant components. To this end, we employ Principal Component Analysis (PCA) [58] and determine the basis of n principal components $\mathbf{pc}_1, \mathbf{pc}_2, \cdots, \mathbf{pc}_n$ to expand each image around the time-averaged image $\langle \mathcal{I} \rangle$: $\mathcal{I}(t) = \langle \mathcal{I} \rangle + \sum_{i=1}^{n} c_i(t) \mathbf{pc}_i$. The dynamics of the projection coefficients are on average governed by the drift field $\mathbf{\Phi}(\mathbf{c})$ and diffusion tensor $\mathbf{D}(\mathbf{c})$ (see Eq. (5)).

In the simulated data of the two-bead model, the first four principal components satisfy criteria 1) and 2) introduced in Sec. I (Fig. 2c). Interestingly, $\mathbf{pc}_1$ and $\mathbf{pc}_2$ resemble the in-phase and out-of-phase motion of the two beads, respectively and should suffice to reproduce the dynamics of $(x_1(t), x_2(t))$, consistently with our third truncation criterion. The components $\mathbf{pc}_3$ and $\mathbf{pc}_4$ appear to mostly represent the isolated fluctuations of the hot and cold beads and mainly account for the nonlinear details of the image representation. The first four components, however, allow for an adequate reconstruction of the original images (Fig. 2d).

From the recorded trajectories in $\mathbf{pc}_1 \times \mathbf{pc}_2$ space we can already infer key features of the system's dynamics using SFI. Specifically, we infer the force and diffusion fields (Fig. 2e). In the phase space spanned by the first two principal components, we identify a stable fixed point at $(0, 0)$ (Fig. 2e). As may be expected in this case, the $\mathbf{pc}_1$-direction (in-phase motion) is less stiff than the $\mathbf{pc}_2$ direction (out-of-phase motion).

The temperature difference between the two beads results in phase-space circulation, as revealed by the inferred mean velocity field (Fig. 2f). To quantitatively assess the irreversibility associated with the presence of such phase space currents, we estimate the entropy production rate of the system $\widehat{\dot{S}}$, which converges for long enough measurement time (Fig. 2g-inset). Strikingly, already with two principal components we find good agreement between the inferred and the exact entropy production rate, capturing from $78 \pm 25\%$ at $T_\mathrm{c}/T_\mathrm{h} = 0.5$) to $88 \pm 7\%$ of the entropy production at $T_\mathrm{c}/T_\mathrm{h} = 0.2$ (Fig. 2g). Furthermore, the difference between the exact and inferred entropy production is consistent with the typical inference error predicted by SFI. As expected, the estimate of the entropy production rate increases with the number of included components. Note that including more modes than the dimension of the physical phase space (in this case 2) can lead to an overestimate of $\dot{S}$ (Fig. 2g). Finally, we note that the functional dependence of $\dot{S}$ on $T_\mathrm{c}/T_\mathrm{h}$ is fully recovered and, importantly, no significant entropy production is inferred when the bead temperatures are identical (equilibrium).

We can also use the information contained in the first four principal components to quantitatively infer forces in image-space via the relation $\widehat{\mathcal{F}}(\mathcal{I}(t)) = \sum_{i=1}^{4} \widehat{\mathbf{F}}_i(\mathbf{c}(t)) \mathbf{pc}_i$. Note that while two modes were sufficient to infer $\widehat{\dot{S}}$, more modes are needed to reconstruct the full images and image-force fields as a linear combination of modes. Importantly, when inferring forces we always subtract from the drift the spurious force $\nabla \cdot \mathbf{D}(\mathbf{c})$ arising in overdamped Itô stochastic differential equations with multiplicative noise. For comparison purposes, the exact image force field is obtained directly from the simulated data as: $\mathcal{F}_\mathrm{ex}(t) = [\bar{\mathcal{I}}(\mathbf{x}(t) + \mathbf{F}(\mathbf{x})\Delta t) - \bar{\mathcal{I}}(\mathbf{x}(t))]/\Delta t$. Remarkably, we find good qualitative agreement between inferred and exact image force fields for specific realizations of the system, as shown in the kymographs in Fig. 2i (see also Supplementary Movies 2 and 3). Moreover, we find a strong correlation (Pearson correlation coefficient $\rho = 0.93$) between inferred and exact image-forces. To further quantify the performance of force inference, we compute the relative squared error on the inferred image force field ($\sigma^2_{\widehat{\mathcal{F}}} = \sum_t \|\widehat{\mathcal{F}}(t) - \mathcal{F}_\mathrm{ex}(t)\|^2 / \sum_t \|\widehat{\mathcal{F}}(t)\|^2$), which in this case is modest $\sigma^2_{\widehat{\mathcal{F}}} = 0.14$ (Fig. 2h).

Thus, with sufficient information, we can use our approach to accurately predict at any instant of time the physical force fields in image space from the Brownian movie, even if the system is out of equilibrium. Moreover, the results for this simple two-bead system demonstrate the validity of our approach: we reliably infer the non-equilibrium dynamics of this system. Arguably, direct tracking of the two beads is, in this case, a more straightforward approach. However, this changes when considering more general soft assemblies comprised of many degrees of freedom.

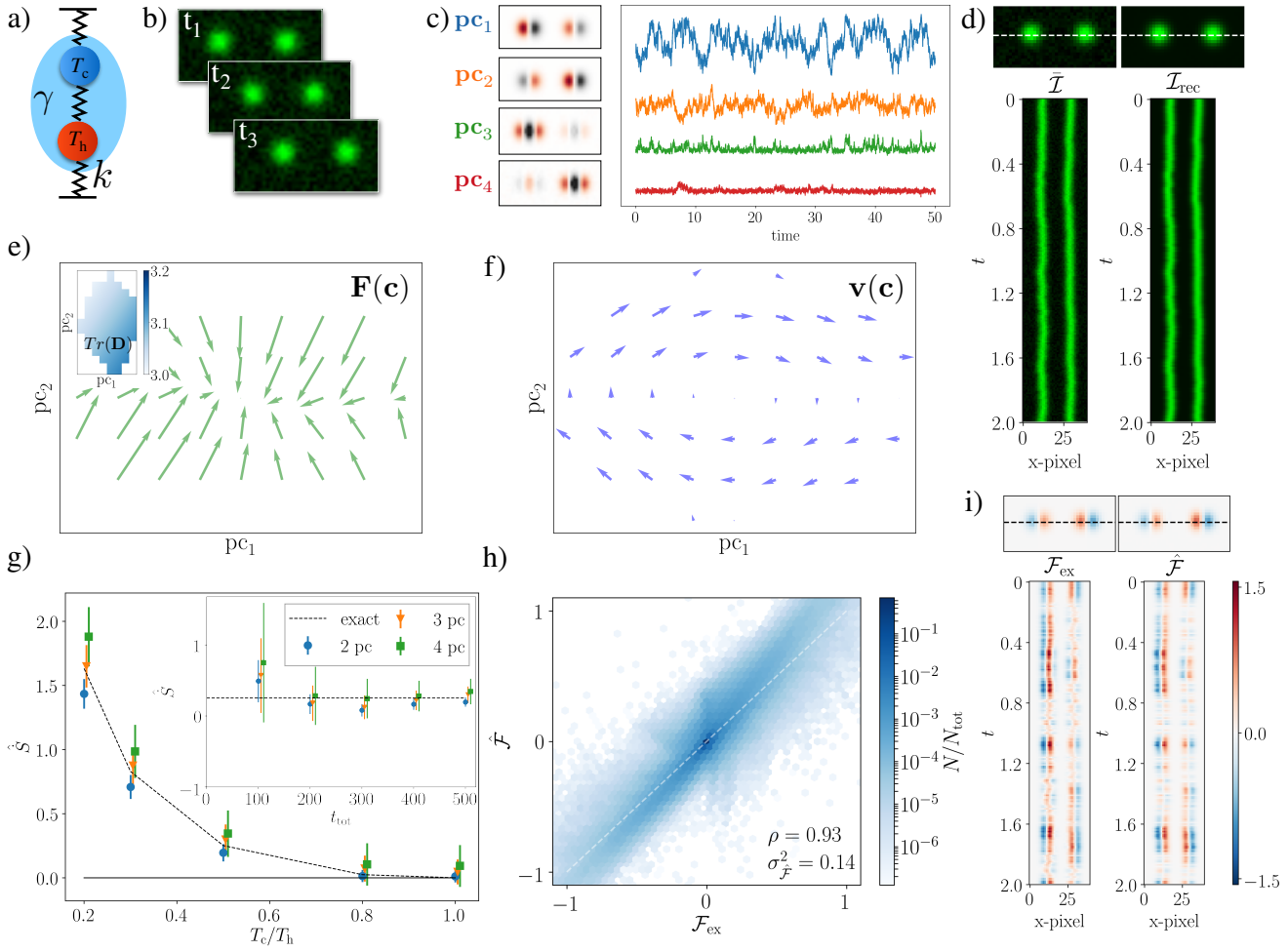

FIG. 2. **Benchmarking the Brownian movie learning approach with a simple toy model** a) Schematic of the two-bead model. We use $k = 2$, $\gamma = 1$, $k_B = 1$; the temperature of the hot bead $T_h = 1$ is fixed and the temperature of the cold bead $T_c \leq 1$ is varied. b) 40×20 Frames of the noisy (10% noise) Brownian movie for the two bead-model at successive time-points c) The first 4 principal components with time-traces of respective projection coefficients. The color map displays negative pixel values in black and positive pixel values in red. d) Top: Snapshot of the exact image $\mathcal{I}_{ex}$ (left) and the reconstructed image $\mathcal{I}_{rec}$ (right) reconstructed with the first four principal components. Bottom: associated kymographs. We compare pixel intensities along the superimposed horizontal dashed line. e) Force field in the space of the first two principal components $\mathbf{pc}_1 \times \mathbf{pc}_2$. Inset: trace of diffusion tensor $\mathrm{Tr}(\mathbf{D})$. f) The mean phase space velocity in $\mathbf{pc}_1 \times \mathbf{pc}_2$. g) Inferred entropy production rate $\hat{\dot{S}}$ for varying temperature ratio T_c/T_h and number of included principal components. Inset: $\hat{\dot{S}}$ as a function of trajectory length for a fixed $T_c/T_h = 0.5$. h) Scatter plot of the exact image force field $\mathcal{F}_{ex}$ vs. the inferred image force field $\hat{\mathcal{F}}$ for different pixels and time points (data has been binned for visualization purposes). Results are obtained using the first four principal components. i) Top: comparison of inferred $\hat{\mathcal{F}}$ and exact $\mathcal{F}_{ex}$ image-space force fields. Bottom: associated kymographs. Panels c)-d)-e)-f)-h)-i) have been obtained with $T_c/T_h = 0.5$ and for a trajectory of length $t_{tot} = 10^5 \Delta t$, $\Delta t = 0.01$. Panel g) with $t_{tot} = 5 \times 10^4 \Delta t$. The SFI routine was employed with a first order polynomial basis for the inference of forces and diffusion fields. The noise-corrected estimator was used to infer the diffusion fields [23].

III. DISSIPATIVE COMPONENT ANALYSIS: A PRINCIPLED APPROACH TO CONSTRUCT THE MOST DISSIPATIVE COMPONENTS

To expand the scope of our approach, we next consider a more complex scenario inspired by cytoskeletal assemblies: a network of elastic filaments (Fig. 3a). The filaments are modeled as Hookean springs that connect two neighboring nodes on a triangular network. The Langevin equation for the two-dimensional displacement $\mathbf{x}_i$ of the network's i-th node is given by Eq. 1. In this case, the force acting on node i is $\mathbf{F}_i(\mathbf{x}) = -\sum_{j\sim i} \frac{k}{\gamma}(\|\mathbf{x}_{i,j}(t)\| - \ell_0)\hat{\mathbf{x}}_{i,j}$, $\mathbf{x}_{i,j} = \mathbf{x}_i - \mathbf{x}_j$, $\hat{\mathbf{x}}_{i,j}$. is the corresponding unit vector, and the sum runs over nearest-

neighbors j of i. Similarly to the two-bead model (Fig. 2), we drive the system out of equilibrium by imposing spatially heterogeneous node temperatures drawn randomly from a uniform distribution, as shown in Fig. 3b. We impose rigid boundary conditions to avoid rotations and diffusion of the system as a whole.

We simulate the dynamics of a 5×5 network: for each time step we create an image in which neighboring nodes are connected by filament segments and measurement noise is added to generate a Brownian movie (see Supplementary Material Sec. II, Fig. 3a, and Supplementary Movie 4). In this spatially extended system, generated from an underlying dynamics with 50 degrees of freedom, it is not obvious based on the recorded Brownian movie how to select and analyze the relevant degrees of freedom.

We start our movie-based analysis by employing PCA to reduce the dimensionality of the image data (Fig. 3c). For this set of simulation data, our truncation criteria indicate that the maximum number of retainable components is roughly 50, consistent with the number of degrees of freedom in the underlying dynamics. Although we greatly reduced dimensionality of the image data using this truncation, it is still intractable to infer dynamics in a 50-dimensional space due to limited statistics. However, even a subset of these modes may suffice to glean useful information about the system's non-equilibrium dynamics. Therefore, as a first attempt, we identify the modes that retain most of the variance via PCA and infer the dynamics in increasingly larger PC-space via SFI. This allows us to infer the retained percentage of entropy production rate as a function of the number of principal components considered (Fig. 3e). In contrast to the two-beads case, we observe that in this more realistic scenario we recover less than 10% of the system's entropy production rate with the first twenty PCs. Indeed, PCA is designed to find modes that capture the most variance in the image data, and large variance, does not necessarily imply large dissipation. Thus, in this case, PCA fails at selecting components that capture a substantial fraction of the entropy production rate.

Our goal is to infer the system's non-equilibrium dynamics. We thus propose an alternative way of reducing data dimensionality that spotlights the time-irreversal contributions to the dynamics, which we term Dissipative Component Analysis (DCA). DCA represents a principled approach to determine the most dissipative pairs of modes for a linear system with state-independent noise (see Supplementary Material Sec. III). For such a linear system, there exists a set of component pairs for which the entropy production rate can be expressed as a sum of independent positive-definite contributions, which can be ranked by magnitude. After a suitable truncation, this basis ensures that the components with the largest entropy production rate are selected. While the approach is only rigorous for a linear system with state-independent noise, we demonstrate below that this method also performs well for more general scenarios.

DCA relies on the measurement of an intuitive trajectory-based non-equilibrium quantity: the area enclosing rate (AER) matrix $\mathcal{A}$ associated to a general set of coordinates $\mathbf{y}$. The elements of the AER matrix, in Itô convention, are defined by [23, 59–61]

$$\mathcal{A}_{ij} = \frac{1}{2}\langle y_j \dot{y}_i - y_i \dot{y}_j \rangle, \tag{6}$$

where y_i denotes the i-th coordinate centered around its mean value and $\langle\cdot\rangle$ a time average. This non-equilibrium measure quantifies the average area enclosed by the trajectory in phase space per unit time. Importantly, the AER is tightly linked to the entropy production rate. Specifically, for a linear system $\dot{S} = \mathrm{Tr}(\mathcal{A}C^{-1}\mathcal{A}^T D^{-1})$ where the covariance matrix $C_{ij} = \langle y_i y_j \rangle$. DCA identifies a basis of vector pairs $\{\mathbf{dc}_1, \mathbf{dc}_2; \mathbf{dc}_3, \mathbf{dc}_4; \ldots\}$ that simultaneously transforms C to the identity and diagonalizes $\mathcal{A}\mathcal{A}^T$ (see Supplement Sec. III). By doing so, DCA naturally separates the entropy production rate into independent contributions that can be readily ordered by magnitude, *i.e.* $\dot{S} = \dot{S}_{\mathbf{dc}_1,\mathbf{dc}_2} + \dot{S}_{\mathbf{dc}_3,\mathbf{dc}_4} + \cdots$ with $\dot{S}_{\mathbf{dc}_1,\mathbf{dc}_2} > \dot{S}_{\mathbf{dc}_3,\mathbf{dc}_4} > \cdots$. Truncating the basis of dissipative components using the aforementioned criteria, allows us to identify a few components that are assured to maximally contribute to the dissipation of the system.

To test the performance of DCA, we revisit the network simulations. We first perform PCA to reduce noise and dimensionality. Subsequently, we perform DCA with these first 50 principal component coefficients as input. The dissipative components are very different from the principal components (Fig. 3d): while the principal components seem to capture the collective displacement modes of the filaments, the dissipative components appear to reflect the local temperature inhomogeneities in the network. Strikingly, DCA allows us to recover a substantial portion of the total entropy production rate (almost 40% with 20 components) performing about twenty times better than the PCA-based approach, as shown in Fig. 3e.

Even when we recover only a fraction of the entropy production, our inference approach yields additional insightful information about the dynamics in the system, such as force field estimates. To investigate to what extent our movie-based learning approach reconstructs the elastic forces exerted by the network's filaments, we compare the inferred force field in image space to the exact one. For this purpose, we employ PCA in our dimensional reduction scheme, which can be used both in and out of equilibrium. Remarkably, even in this large network we find that the inferred force field in image space can capture the basic features of the exact force field, as shown in Fig. 3f-g and in Supplementary Movies 5 and 6. However, inferring image force fields with high accuracy for the full 5×5 network is challenging due to the curse of dimensionality [58], as confirmed by the sizeable force inference error reported in Fig. 3g.

To perform accurate force inference on large systems, we perform a piecewise learning of spatially cropped Brownian movies. Put simply, we can exploit the locality

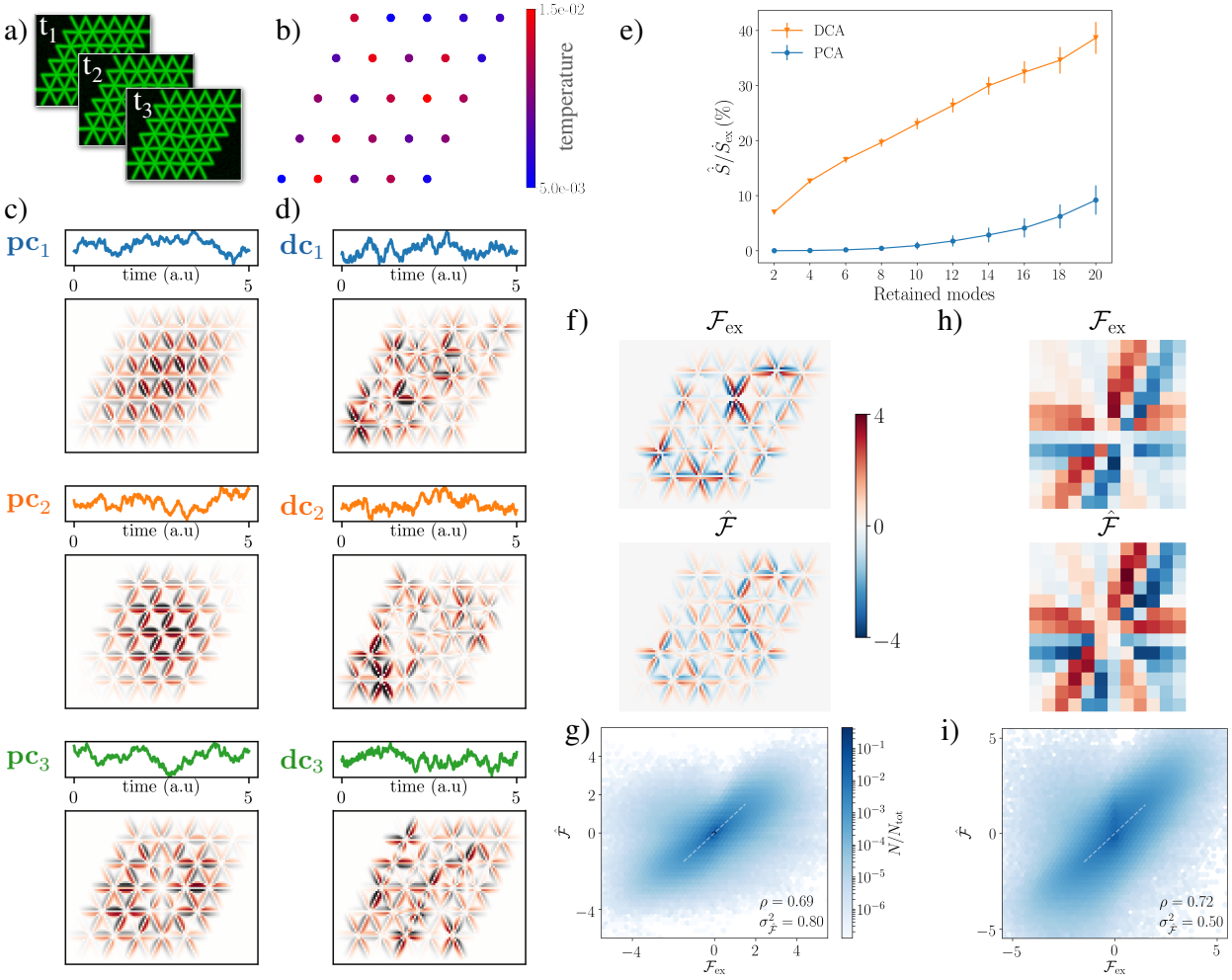

FIG. 3. **Learning the non-equilibrium dynamics of Brownian movies of simulated filamentous networks** a) 100×80 frames of a 5×5 filamentous network with fixed boundary conditions driven out of equilibrium by a heterogeneous temperature distribution. b) The temperatures at the nodes are indicated with a different color ranging from blue (low temperature) to red (high temperature). c-d) Trajectory of the projection coefficient (top) and image-component (bottom) for PCA (c) and DCA (d). e) The estimated entropy production rate $\widehat{\dot{S}}$ as a function of the number of components included in the analysis. See Supplementary Sec. IV for additional data at equilibrium and convergence of the estimates. f) Full network: Comparison of the exact image-force $\mathcal{F}_{\text{ex}}$ (top) to the inferred one $\hat{\mathcal{F}}$ (bottom) at a selected instant of time with 50 PCs. g) Scatter plot of the exact force field $\mathcal{F}_{\text{ex}}$ vs. the inferred force field $\hat{\mathcal{F}}$ for different pixels and time points with 50 PCs (data has been binned for visualization purposes). At the bottom right the Pearson correlation coefficient ρ and the relative error squared $\sigma^2_{\hat{\mathcal{F}}}$ are indicated. h) Single cropped patch: Comparison of the exact image-force $\mathcal{F}_{\text{ex}}$ (top) to the inferred one $\hat{\mathcal{F}}$ (bottom) at a selected instant of time with 20 PCs. Arrows indicate the deterministic velocity field. Colorbar same as in f). i) Piecewise reconstruction of force inference for full network from cropped patches: Scatter plot of the exact force field $\mathcal{F}_{\text{ex}}$ vs. the inferred force field $\hat{\mathcal{F}}$ for different pixels and time points with 20 PCs. Colorbar same as in g). All results have been obtained with a trajectory of 10^6 time steps, $\Delta t = 0.005$ and 100×80-pixels frames for the full network. The SFI routine was employed with a first order polynomial basis for the inference of forces and diffusion fields, and noise-corrected diffusion estimates.

of the interactions in the system to extract information about local forces from local dynamics in image space. More specifically, we divide each frame of the movie into disjoint cropped patches and reconstruct image-forces in each patch separately, as shown in Fig. 3h (see Supplementary Material Sec. VI). Then, we can use the force field inferred in each patch to reconstruct the force field for the full image and thus for the full network. This procedure not only improves force inference, as shown in Fig. 3i, but also has the advantage of being scalable: While image force inference for a whole system becomes unfeasible for large assemblies, the cropping procedure can yield accurate force estimates independent of system size.

In sum, we have demonstrated how a combination of PCA and DCA allows us to recover a substantial fraction of the entropy production in a complex scenario such as a 5×5 network with measurement noise. Note the dynamics in image space in this system is described by a non-linear Langevin equation with multiplicative noise. Despite this complexity, our scalable approach is able to infer the basic features of the force field.

IV. DISCUSSION

We considered the dynamics of movies of time-lapse microscopy data. Under the assumptions outlined in Sec. I, these movies undergo Brownian dynamics in image space: the image-field obeys an overdamped Langevin equation of the form of Eq. (3). Rather than tracking selected degrees of freedom, we propose to analyze the Brownian movie as a whole.

Our approach is based on constructing a reduced set of relevant degrees of freedom to reduce dimensionality, by combining PCA with a new method that we term Dissipative Component Analysis (DCA). In the limit of a linear system with state-independent noise, DCA provides a principled way of constructing and ranking independent dissipative modes. The order at which we truncate is an important trade-off parameter of this method: on the one hand we wish to significantly reduce the dimensionality of the data, on the other hand we need to include enough components to retain the information necessary to infer the system's dynamics. After the dimensional reduction, we infer the stochastic dynamics of the system, revealing the force field, phase space currents, and the entropy production rate in this basis. This information can then be mapped back to image-space to provide estimators for the stochastic dynamics of the Brownian movie. We illustrated our approach on simulated data of a minimal two-beads model and on filamentous networks in both equilibrium and non-equilibrium settings, and showed that it is robust in the presence of measurement noise. Beyond providing controlled lower bounds of the entropy production rates directly from the Brownian movie, our approach yields estimates of the force-fields in image space for an instantaneous snapshot of the system and we demonstrated that this approach can be scaled up to large systems. Thus, we provide in principle an alternative to microscopic force and stress sensing methods [40, 41, 48, 49].

We focused here on a class of soft matter systems termed "active viscoelastic solids" [8, 62]. Such systems include active biological materials such as cytoskeletal assemblies [30, 32, 33, 63], membranes [15, 64, 65], chromosomes [28], protein droplets [29], as well as active turbulent solids [66] and colloidal systems [9]. Although these structures are constantly fluctuating both due to energy-consuming processes (*e.g.* rapid contractions generated by molecular motors) and thermal motion, they do not exhibit macroscopic flow. Useful insights into the properties of such systems have been obtained via different non-invasive techniques. Typically, these techniques employ time traces of tracked object to extract information about the active processes governing the non-equilibrium behavior [15–19, 57, 64]. Often, however, it is not *a priori* obvious which physical degrees of freedom should be tracked, how tracking can be performed in fragile environments, and to what extent the dynamical information about the system of interest is encoded in the measured trajectories [46]. While tracking-free approaches have been proposed to obtain rheological information of a system under equilibrium conditions [47], our approach offers an alternative to tracking that can provide information on dissipative modes and the instantaneous force fields of a fluctuating non-equilibrium system.

In summary, we presented a viable alternative to traditional analysis techniques of high-resolution video-microscopy of soft living assemblies. Indeed, we envision experimental scenarios where our approach may serve as a guide, providing novel insights by disentangling the deterministic and stochastic components of the dynamics, and by helping to identify the source of thermal and active forces as well as the dissipation in the system. Overall, our movie-based approach constitutes an adaptable tool that paves the road for a systematic, non-invasive and tracking-free analysis of time-lapse data of soft and living systems.

ACKNOWLEDGEMENTS

We thank C. Schmidt, F. Mura, S. Ceolin and I. Graf for many stimulating discussions. This work was Funded by the Deutsche Forschungsgemeinschaft (DFG, German Research Foundation) under Germany's Excellence Strategy EXC-2094 390783311 and by the DFG grant 418389167.

[1] Stephens, D. J. & Allan, V. J. Light Microscopy Techniques for Live Cell Imaging. *Science* **300**, 82–86 (2003).

[2] Sahl, S. J., Hell, S. W. & Jakobs, S. Fluorescence nanoscopy in cell biology. *Nat Rev Mol Cell Biol* **18**, 685–701 (2017).

[3] Brown, R. XXVII. *A brief account of microscopical observations made in the months of June, July and August 1827, on the particles contained in the pollen of plants; and on the general existence of active molecules in organic and inorganic bodies*. *The Philosophical Magazine* **4**, 161–173 (1828).

[4] Einstein, A. Über die von der molekularkinetischen Theorie der Wärme geforderte Bewegung von in ruhenden Flüssigkeiten suspendierten Teilchen. *Ann. Phys.* **322**,

549–560 (1905).

[5] Frey, E. & Kroy, K. Brownian motion: A paradigm of soft matter and biological physics. *Annalen der Physik* **14**, 20–50 (2005).

[6] Waters, J. C. Accuracy and precision in quantitative fluorescence microscopy. *The Journal of Cell Biology* **185**, 1135–1148 (2009).

[7] MacKintosh, F. C. & Schmidt, C. F. Active cellular materials. *Current Opinion in Cell Biology* **22**, 29–35 (2010).

[8] Gnesotto, F. S., Mura, F., Gladrow, J. & Broedersz, C. P. Broken detailed balance and non-equilibrium dynamics in living systems: A review. *Rep. Prog. Phys.* **81**, 066601 (2018).

[9] Aranson, I. S. Active colloids. *Phys.-Usp.* **56**, 79 (2013).

[10] Cates, M. E. & Tailleur, J. Motility-Induced Phase Separation. *Annual Review of Condensed Matter Physics* **6**, 219–244 (2015).

[11] Fodor, É. *et al.* How Far from Equilibrium Is Active Matter? *Phys. Rev. Lett.* **117**, 038103 (2016).

[12] Martínez, I. A., Bisker, G., Horowitz, J. M. & Parrondo, J. M. R. Inferring broken detailed balance in the absence of observable currents. *Nat Commun* **10**, 1–10 (2019).

[13] Guo, M. *et al.* Probing the Stochastic, Motor-Driven Properties of the Cytoplasm Using Force Spectrum Microscopy. *Cell* **158**, 822–832 (2014).

[14] Fakhri, N. *et al.* High-resolution mapping of intracellular fluctuations using carbon nanotubes. *Science* **344**, 1031–1035 (2014).

[15] Turlier, H. *et al.* Equilibrium physics breakdown reveals the active nature of red blood cell flickering. *Nature Physics* **12**, 513–519 (2016).

[16] Battle, C. *et al.* Broken detailed balance at mesoscopic scales in active biological systems. *Science* **352**, 604–607 (2016).

[17] Gladrow, J., Fakhri, N., MacKintosh, F. C., Schmidt, C. F. & Broedersz, C. P. Broken Detailed Balance of Filament Dynamics in Active Networks. *Phys. Rev. Lett.* **116**, 248301 (2016).

[18] Mura, F., Gradziuk, G. & Broedersz, C. P. Nonequilibrium Scaling Behavior in Driven Soft Biological Assemblies. *Phys. Rev. Lett.* **121**, 038002 (2018).

[19] Seara, D. S. *et al.* Entropy production rate is maximized in non-contractile actomyosin. *Nature Communications* **9**, 1–10 (2018).

[20] Ma, R., Klindt, G. S., Riedel-Kruse, I. H., Jülicher, F. & Friedrich, B. M. Active Phase and Amplitude Fluctuations of Flagellar Beating. *Phys. Rev. Lett.* **113**, 048101 (2014).

[21] Li, J., Horowitz, J. M., Gingrich, T. R. & Fakhri, N. Quantifying dissipation using fluctuating currents. *Nat Commun* **10**, 1666 (2019).

[22] Sanchez, T., Chen, D. T. N., DeCamp, S. J., Heymann, M. & Dogic, Z. Spontaneous motion in hierarchically assembled active matter. *Nature* **491**, 431–434 (2012).

[23] Frishman, A. & Ronceray, P. Learning force fields from stochastic trajectories. *arXiv:1809.09650 [cond-mat]* (2019). 1809.09650.

[24] Roldán, É. & Parrondo, J. M. R. Estimating Dissipation from Single Stationary Trajectories. *Phys. Rev. Lett.* **105**, 150607 (2010).

[25] Sanchez, T., Welch, D., Nicastro, D. & Dogic, Z. Cilia-Like Beating of Active Microtubule Bundles. *Science* **333**, 456–459 (2011).

[26] Battle, C., Ott, C. M., Burnette, D. T., Lippincott-Schwartz, J. & Schmidt, C. F. Intracellular and extracellular forces drive primary cilia movement. *PNAS* **112**, 1410–1415 (2015).

[27] Riedel-Kruse, I. H., Hilfinger, A., Howard, J. & Jülicher, F. How molecular motors shape the flagellar beat. *HFSP Journal* **1**, 192–208 (2007).

[28] Weber, S. C., Spakowitz, A. J. & Theriot, J. A. Nonthermal ATP-dependent fluctuations contribute to the in vivo motion of chromosomal loci. *Proceedings of the National Academy of Sciences* **109**, 7338–7343 (2012).

[29] Brangwynne, C. P., Mitchison, T. J. & Hyman, A. A. Active liquid-like behavior of nucleoli determines their size and shape in Xenopus laevis oocytes. *PNAS* **108**, 4334–4339 (2011).

[30] Mizuno, D., Tardin, C., Schmidt, C. F. & MacKintosh, F. C. Nonequilibrium Mechanics of Active Cytoskeletal Networks. *Science* **315**, 370–373 (2007).

[31] Brangwynne, C. P., Koenderink, G. H., MacKintosh, F. C. & Weitz, D. A. Cytoplasmic diffusion: Molecular motors mix it up. *J Cell Biol* **183**, 583–587 (2008).

[32] Koenderink, G. H. *et al.* An active biopolymer network controlled by molecular motors. *PNAS* **106**, 15192–15197 (2009).

[33] Brangwynne, C. P., Koenderink, G. H., MacKintosh, F. C. & Weitz, D. A. Nonequilibrium Microtubule Fluctuations in a Model Cytoskeleton. *Phys. Rev. Lett.* **100**, 118104 (2008).

[34] Paijmans, J., Bosman, M., ten Wolde, P. R. & Lubensky, D. K. Discrete gene replication events drive coupling between the cell cycle and circadian clocks. *PNAS* **113**, 4063–4068 (2016).

[35] Kimmel, J. C., Chang, A. Y., Brack, A. S. & Marshall, W. F. Inferring cell state by quantitative motility analysis reveals a dynamic state system and broken detailed balance. *PLOS Computational Biology* **14**, e1005927 (16-gen-2018).

[36] Wan, K. Y. & Goldstein, R. E. Time Irreversibility and Criticality in the Motility of a Flagellate Microorganism. *Phys. Rev. Lett.* **121**, 058103 (2018).

[37] Seifert, U. Stochastic thermodynamics, fluctuation theorems and molecular machines. *Rep. Prog. Phys.* **75**, 126001 (2012).

[38] Crocker, J. C. & Grier, D. G. Methods of Digital Video Microscopy for Colloidal Studies. *Journal of Colloid and Interface Science* **179**, 298–310 (1996).

[39] Levine, A. J. & Lubensky, T. C. One- and Two-Particle Microrheology. *Phys. Rev. Lett.* **85**, 1774–1777 (2000).

[40] Sawada, Y. *et al.* Force Sensing by Mechanical Extension of the Src Family Kinase Substrate p130Cas. *Cell* **127**, 1015–1026 (2006).

[41] Grashoff, C. *et al.* Measuring mechanical tension across vinculin reveals regulation of focal adhesion dynamics. *Nature* **466**, 263–266 (2010).

[42] Mura, F., Gradziuk, G. & Broedersz, C. P. Mesoscopic non-equilibrium measures can reveal intrinsic features of the active driving. *Soft Matter* **15**, 8067–8076 (2019).

[43] Brückner, D. B. *et al.* Stochastic nonlinear dynamics of confined cell migration in two-state systems. *Nature Physics* **15**, 595–601 (2019).

[44] Selmeczi, D., Mosler, S., Hagedorn, P. H., Larsen, N. B. & Flyvbjerg, H. Cell Motility as Persistent Random Motion: Theories from Experiments. *Biophysical Journal*

89, 912–931 (2005).

[45] Stephens, G. J., Johnson-Kerner, B., Bialek, W. & Ryu, W. S. Dimensionality and Dynamics in the Behavior of C. elegans. *PLOS Computational Biology* **4**, e1000028 (25-apr-2008).

[46] Seara, D. S., Machta, B. B. & Murrell, M. P. Dissipative signatures of dynamical phases and transitions. *arXiv:1911.10696 [cond-mat, physics:physics, q-bio]* (2019). 1911.10696.

[47] Edera, P., Bergamini, D., Trappe, V., Giavazzi, F. & Cerbino, R. Differential dynamic microscopy microrheology of soft materials: A tracking-free determination of the frequency-dependent loss and storage moduli. *Phys. Rev. Materials* **1**, 073804 (2017).

[48] Lucio, A. A., Ingber, D. E. & Campàs, O. Chapter 20 - Generation of biocompatible droplets for in vivo and in vitro measurement of cell-generated mechanical stresses. In Paluch, E. K. (ed.) *Methods in Cell Biology*, vol. 125 of *Biophysical Methods in Cell Biology*, 373–390 (Academic Press, 2015).

[49] Han, Y. L. *et al.* Cell contraction induces long-ranged stress stiffening in the extracellular matrix. *PNAS* **115**, 4075–4080 (2018).

[50] Lau, A. W. C. & Lubensky, T. C. State-dependent diffusion: Thermodynamic consistency and its path integral formulation. *Phys. Rev. E* **76**, 011123 (2007).

[51] Risken, H. & Frank, T. *The Fokker-Planck Equation: Methods of Solution and Applications*. Springer Series in Synergetics (Springer-Verlag, Berlin Heidelberg, 1996), 2 edn.

[52] We neglect the discretization effect induced by the finite number of pixel intensities here.

[53] Øksendal, B. *Stochastic Differential Equations: An Introduction with Applications*. Universitext (Springer-Verlag, Berlin Heidelberg, 2003), 6 edn.

[54] Note that we consider here only the entropy production associated to apparent currents. The irreversible dynamics of unobserved degrees of freedom has repercussion on non-Markovian effects in the dynamics, which result in other contributions to the entropy production [24], which we neglect here.

[55] Crisanti, A., Puglisi, A. & Villamaina, D. Nonequilibrium and information: The role of cross correlations. *Phys. Rev. E* **85**, 061127 (2012).

[56] Bérut, A., Imparato, A., Petrosyan, A. & Ciliberto, S. Theoretical description of effective heat transfer between two viscously coupled beads. *Phys. Rev. E* **94**, 052148 (2016).

[57] Gnesotto, F. S., Remlein, B. M. & Broedersz, C. P. Nonequilibrium dynamics of isostatic spring networks. *Phys. Rev. E* **100**, 013002 (2019).

[58] Bishop, C. M. *Pattern Recognition and Machine Learning*. Information Science and Statistics (Springer, New York, 2006).

[59] Ghanta, A., Neu, J. C. & Teitsworth, S. Fluctuation loops in noise-driven linear dynamical systems. *Phys. Rev. E* **95**, 032128 (2017).

[60] Gonzalez, J. P., Neu, J. C. & Teitsworth, S. W. Experimental metrics for detection of detailed balance violation. *Phys. Rev. E* **99**, 022143 (2019).

[61] Gradziuk, G., Mura, F. & Broedersz, C. P. Scaling behavior of nonequilibrium measures in internally driven elastic assemblies. *Phys. Rev. E* **99**, 052406 (2019).

[62] Fletcher, D. A. & Geissler, P. L. Active Biological Materials. *Annu. Rev. Phys. Chem.* **60**, 469–486 (2009).

[63] Jensen, M. H., Morris, E. J. & Weitz, D. A. Mechanics and dynamics of reconstituted cytoskeletal systems. *Biochimica et Biophysica Acta (BBA) - Molecular Cell Research* **1853**, 3038–3042 (2015).

[64] Betz, T., Lenz, M., Joanny, J.-F. & Sykes, C. ATP-dependent mechanics of red blood cells. *PNAS* **106**, 15320–15325 (2009).

[65] Ben-Isaac, E. *et al.* Effective Temperature of Red-Blood-Cell Membrane Fluctuations. *Phys. Rev. Lett.* **106**, 238103 (2011).

[66] Hemingway, E. J. *et al.* Active Viscoelastic Matter: From Bacterial Drag Reduction to Turbulent Solids. *Phys. Rev. Lett.* **114**, 098302 (2015).

Learning the Non-Equilibrium Dynamics of Brownian Movies: Supplementary Material

I. NUMERICALLY INTEGRATING THE BROWNIAN DYNAMICS

We simulate the stochastic dynamics of the two-beads model by numerically integrating the overdamped Langevin equation for the beads' displacements $\mathbf{x} = (x_1, x_2)$ (Eq. 1 main text), with $\mathbf{F}(\mathbf{x}) = \mathbf{A}\mathbf{x}$, $A_{ij} = (1 - 3\delta_{ij})k/\gamma$, $D_{ij} = \delta_{ij}k_{\mathrm{B}}T_i/\gamma$. We discretize the equation of motion for the two beads using an Euler scheme with discretization step Δt. Thus, the discretized equation of motion after n time steps for the i-th bead reads: $x_i((n+1)\Delta t) = x_i(n\Delta t) + \sum_{j=1,2} A_{ij}x_j(n\Delta t)\Delta t + \sum_{j=1,2}\sqrt{2D_{ij}\Delta t}\xi_j$, where ξ_j is a random number drawn from a normal distribution with mean zero and average one. We initialize the simulation with the beads in their rest state and we only record the positions of the beads after an equilibration time $t_{\mathrm{eq}} = 10^5\Delta t$ to allow the dynamics to reach steady state. The parameters for the results of Fig. 2 of the main text are: $\Delta t = 0.01$, $k = 2$, $\gamma = 1$, $k_B = 1$, $T_1 = 1$ and $0.2 < T_2 \leq 1$.

The dynamics of the 5×5 spring network is generated in a similar way. In this case, we discretize the overdamped Langevin equation for the nodes' positions $\mathbf{x}$ with time step $\Delta t = 0.005$. For the network the elastic force acting on node i reads: $F_i(\mathbf{x}) = -\sum_{i\sim j}\frac{k}{\gamma}(\|\mathbf{x}_{i,j}(t)\| - \ell_0)\widehat{\mathbf{x}}_{i,j}$, $\mathbf{x}_{i,j} = \mathbf{x}_i - \mathbf{x}_j$, $\mathbf{x}_{i,j}$ is the unit vector between nodes i and j, $k = 4$, and $\ell_0 = \gamma = k_B = 1$. The heterogeneous temperatures at the different nodes are chosen randomly from 25 uniformly spaced values in the interval $[T_0 - T_0/2, T_0 + T_0/2]$ with $T_0 = 10^{-2}$. The simulation is initialized with the network in its rest state and we wait an equilibration time $t_{\mathrm{eq}} = 10^5\Delta t$ before recording trajectories.

II. GENERATING THE BROWNIAN MOVIES

We first outline the procedure to generate a Brownian movie for the two-beads model (see Fig. 2 of the main text). The input consists of the numerically generated position trajectories of the two beads. We then transform the trajectories from position space to image space into pixel units (we used a 40×20 pixel grid). Specifically, we set the image pixel intensities at a given time point by centering a radially symmetric Gaussian function centered at the bead's position, with amplitude 1 and variance 9 pixels . Finally, to simulate measurement noise in a simple way, we add uncorrelated white noise sampled uniformly from $[0, a]$ ($a = 0.1$, i.e. in Fig. 2 of the main text) independently at each pixel. As in real imaging devices, pixels are saturated at intensity 1, thus any intensity larger than 1 is truncated to one.

Next, we briefly explain how we generate a movie for the 5×5 network. The $N \times 50$-dimensional position array which is the output of the numerical integration of the Langevin equation is transferred to a custom Python routine that directly plots all lines connecting neighboring nodes at each time step onto a 100×80 grid. Specifically, the pixel intensities decay with the distance from each line as a Gaussian function with amplitude 0.8 and variance 2 pixels. Finally, to simulate measurement noise, we add uncorrelated white noise sampled uniformly from $[0, a]$ ($a = 0.08$–10% of the maximum intensity– in Fig. 3 of the main text).

III. INFERRING THE DISSIPATIVE MODES: DISSIPATIVE COMPONENT ANALYSIS

The aim of Dissipative Component Analysis (DCA) is to infer a set of modes that maximize dissipation or, more precisely, the entropy production rate. This method is a principled approach only for a linear dynamical system with constant diffusion. However, as we demonstrate in the main text, this method can be successfully employed in high-dimensional situations when dealing with image-data, when the dynamics is close to linear (close to the stable fixed points of the system). In such cases DCA can reduce the dimensionality by exploiting the non-equilibrium character of the system, as outlined below.

We consider a generic linear system described by an n-dimensional column-vector of coordinates $\mathbf{y}$ that obeys the Langevin equation

$$\frac{d\mathbf{y}}{dt}(t) = \mathbf{A}\mathbf{y}(t) + \sqrt{2D}\boldsymbol{\xi}(t)\,, \tag{S1}$$

where $\mathbf{A}$ is the interaction matrix and $\mathbf{D}$ the diffusion matrix. Note that $\mathbf{D}$ and $\mathbf{A}$ may in general not satisfy detailed balance and the system may thus be out of equilibrium.

As a preliminary step we perform principal component analysis (PCA) on data obtained simulating the time-evolution described by Eq. S1 for N time-steps: we first compute the covariance matrix $\mathbf{C} = \frac{1}{N}\sum_{t=1}^{N}(\mathbf{y}(t) - \langle\mathbf{y}\rangle)\cdot(\mathbf{y}^T(t) - \langle\mathbf{y}\rangle^T)$, where $\langle\mathbf{y}\rangle = \frac{1}{N}\sum_{t=1}^{N}\mathbf{y}(t)$. We then retain the first $m < n$ eigenvectors of $\mathbf{C}$ (see Sec. V for details on the truncation criteria), ordered by magnitude of the associated eigenvalues, and use them to construct the $m \times n$ transformation matrix $\mathbf{E}$. The time evolution of the system projected onto the PC-coordinates is then $\mathbf{y}_{pca}(t) = \mathbf{E}^T\mathbf{y}(t)$. In this basis, the covariance matrix $\mathbf{C}_{\mathrm{pca}}$ is diagonal with the ordered eigenvalues as diagonal entries. This preliminary step is useful for two reasons: it reduces dimensionality and it conveniently filters out measurement noise from the images. Next, we transform the data into covariance identity coordinates (cic), in which the covariance matrix is the identity. This is accomplished by $\mathbf{y}_{\mathrm{cic}}(t) = \mathbf{C}_{\mathrm{pca}}^{-1/2}\mathbf{E}^T\mathbf{y}(t)$.

In the next step, we focus on the non-equilibrium character of the system and compute the area-enclosing-rate matrix (AER) $\dot{\mathcal{A}}$ in CIC coordinates [1–3]:

$$\mathcal{A}_{\mathrm{cic,ij}} = \frac{1}{2t_{\mathrm{tot}}}\sum_{t=1}^{N}[y_{\mathrm{cic,i}}(t)\Delta y_{\mathrm{cic,j}}(t) - y_{\mathrm{cic,j}}(t)\Delta y_{\mathrm{cic,i}}(t)], \tag{S2}$$

where $t_{\mathrm{tot}} = N\Delta t$ is the total simulation time and Δy_i denotes the displacement of the i-th coordinate between two successive time-steps. Each element $\mathcal{A}_{ij}$ of the AER matrix corresponds to the area that the trajectory encloses on average in the plane (y_i, y_j) per unit time. This area enclosing rate quantifies broken detailed balance in the system and is zero in thermal equilibrium. Having defined the AER allows us to conveniently write the total entropy production of the system as [2, 4]:

$$\dot{S} = \mathrm{Tr}(\mathcal{A}_{\mathrm{cic}}\mathcal{A}_{\mathrm{cic}}^{\mathrm{T}}\mathbf{D}_{\mathrm{cic}}^{-1}), \tag{S3}$$

where $\mathbf{D}_{\mathrm{cic}} := \frac{1}{2t_{\mathrm{tot}}}\sum_t \Delta\mathbf{y}_{\mathrm{cic}}(t)\Delta\mathbf{y}_{\mathrm{cic}}^T(t)$. It is now key to observe that the matrix product $\mathcal{A}_{\mathrm{cic}}\mathcal{A}_{\mathrm{cic}}^T$, appearing in the expression for the entropy production rate Eq. S3, is real and symmetric and thus admits a real orthonormal basis of eigenvectors. Moreover, since $\mathcal{A}_{\mathrm{cic}}$ is antisymmetric, all non-zero eigenvalues of $\mathcal{A}_{\mathrm{cic}}\mathcal{A}_{\mathrm{cic}}^T$ are two-fold degenerate. Furthermore, note that the orthonormal basis of $\mathcal{A}_{\mathrm{cic}}\mathcal{A}_{\mathrm{cic}}^T$ is unique up to rotations in the two-dimensional eigenspaces that correspond to the same eigenvalue. Importantly, in these special covariance identity coordinates (scic), the total entropy production rate reads

$$\dot{S} = \sum_{i\in odd}\lambda_i[(\mathbf{D}_{\mathrm{scic}}^{-1})_{ii} + (\mathbf{D}_{\mathrm{scic}}^{-1})_{i+1\,i+1}], \tag{S4}$$

with λ_i being the eigenvalues of $\mathcal{A}_{\mathrm{cic}}\dot{\mathcal{A}}_{\mathrm{cic}}^T$. We refer to the corresponding eigenvectors as the dissipative components.

IV. DEPENDENCE OF ENTROPY PRODUCTION RATES ON THE TRAJECTORY LENGTH

The entropy production rate is a semi-positive definite quantity: at steady state $\dot{S} \geq 0$. Given finite-length data, the estimate of the entropy production rate will be biased. While this bias can be computed analytically for homogeneous diffusion coefficients [5], this may be difficult for space-dependent diffusion coefficients and in the presence of measurement noise. Given that we are here concerned with finite-size data of systems with multiplicative noise partially corrupted by measurement noise, we use the following approach to reduce the bias of the entropy production rate and, correspondingly, to avoid overfitting: We separate our data set of length N into two independent and successive sets, a training set of length m and a test set of length $n = N - m$. The results in Fig. 3 of the main text are obtained with $m = N/10$. We first infer relevant components using the training set, and we then project the test set onto these components and infer the corresponding entropy production rate, as shown in Supplementary Fig. 1a . Although entropy production rate estimates remain weakly positively biased for short trajectories, the bias approaches zero for long trajectories, as shown in Supplementary Fig. 1b for the spring network with uniform temperatures (equilibrium). Note, however that our error bar estimates always intersect zero for all trajectory lengths (Supplementary Fig. 1b). When the network is out of equilibrium, the entropy production rate estimates converge to non-zero values for long trajectories, as shown in Supplementary Fig. 1c.

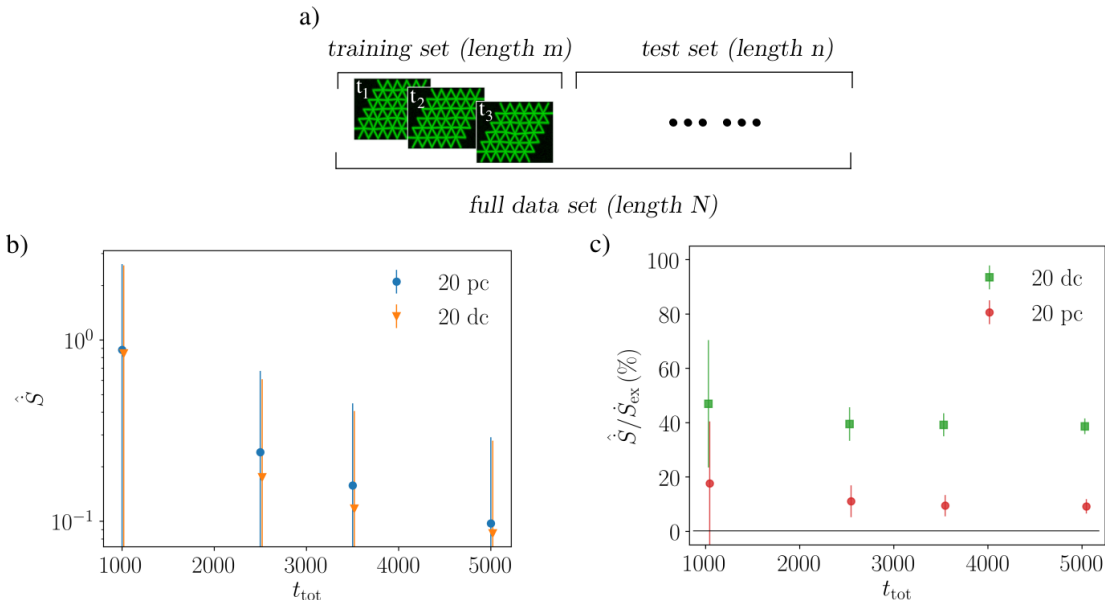

Supplementary Figure 1. a): Schematic of the training/test set splitting procedure: the full trajectory (length N) is split into a training set (length m) and into a test set (length n). b) Decay to zero of the entropy production rate bias (estimated with 20 pc-blue dots and 20 pc-orange triangles) as a function of the trajectory length at equilibrium. c) Convergence of the entropy production rate (estimated with 20 pc-red dots and 20dc-green squares) as a function of the trajectory length. The parameters of the simulations and noise level are the same as in Fig. 3 of the main text. Equilibrium is obtained by setting all temperatures equal to $T_0 = 10^{-2}$.

V. DIMENSIONAL REDUCTION: TRUNCATION CRITERIA

For the Brownian-movie learning procedure it is important to reduce the dimensionality of image data to a more tractable number of components. Therefore, we require criteria to decide on the maximum number of components that we consider in our analysis of the stochastic dynamics. Two main limiting effects arise due to the finite length of trajectories and measurement noise.

1) Noise floor

We start by asking what is the maximum number of components that we can distinguish from a noise floor set by the imaging noise and the finite length of the data. Our image data is a matrix $\mathbf{X}$ of $t_{\rm tot}$ (total simulation time) rows and $L \times W$ (total number of pixels in a single image) columns. We first estimate the principal components — the normalized eigenvectors of the covariance matrix of image data — and sort these components according to the magnitude of the corresponding eigenvalues. To determine the noise floor, we eliminate temporal correlations in the image data by shuffling the values of $\mathbf{X}$ separately along each of its columns [6]. What we obtain is a shuffled data set $\mathbf{X}_{\rm shuffled}$ for which we can also compute principal components and eigenvalues. The largest eigenvalue of the covariance matrix of $\mathbf{X}_{\rm shuffled}$ yields the noise floor. Thus, we truncate the basis of principled components to exclude components with eigenvalues below this noise floor. To illustrate this procedure, a plot of the eigenvalues for $\mathbf{X}$ together with the noise threshold is shown in Supplementary Fig. 2 a-b for the two beads model and for the filamentous network.

2) Resolution of the dynamics

Criterion 1) ensures that the components are distinguishable from imaging noise, which is a static property of the data. The Brownian-movie analysis is concerned with the dynamics. We thus want to make sure that we can resolve the dynamics of the components selected with criterion 1). This is a necessary condition to

infer force and diffusion fields in image-space. A criterion for selecting components whose dynamics can be resolved using SFI is based on computing the autocorrelation function of the projection coefficients ($\mathbf{c}$ in the main text) centered around their average value ($c_i(t) \to c_i(t) - \langle c_i \rangle$):

$$C_i(n\Delta t) = \frac{\sum_{t=1}^{N-n\Delta t} c_i(t+n\Delta t)c_i(t)}{\sum_{t=1}^{N} c_i^2(t)} \,. \tag{S5}$$

We are only able to resolve the dynamics if $c_i(t)$ does not decorrelate too fast, i.e. if $C_i(n\Delta t)$ does not decay to zero in a time comparable to the time-step Δt. We therefore employ the following criterion: we only retain components for which $|C_i(\Delta t) - C_i(0)| < 0.25$. We applied criterion 2) to the two-beads data and to the network data and plot the results in Supplementary Fig. 2 c-d. Criterion 2) is clearly sensitive both to the time resolution Δt and to the signal to noise ratio in the trajectories.

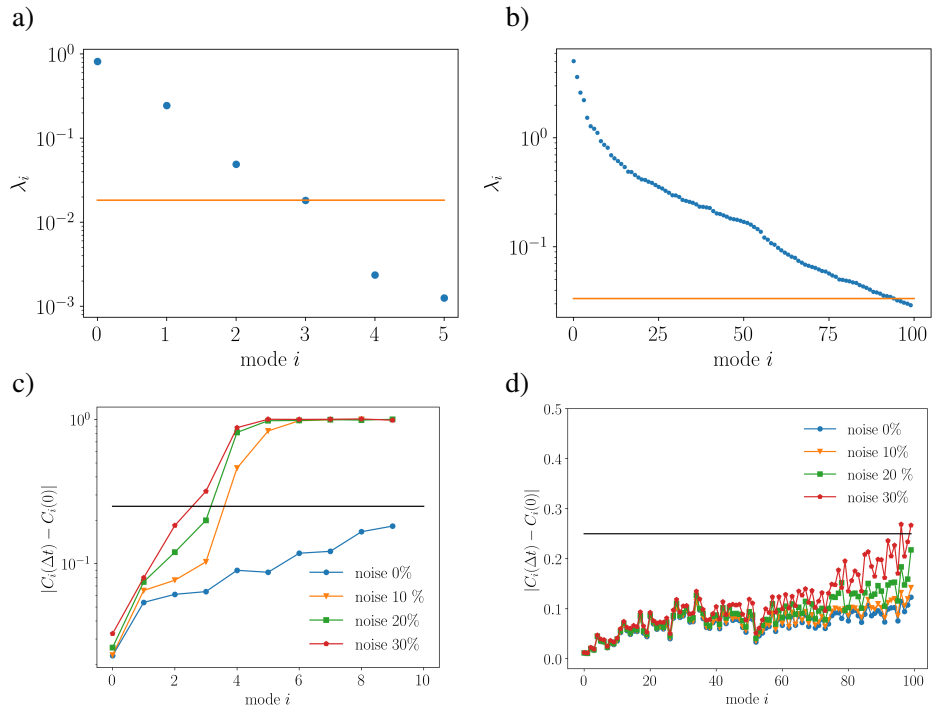

Supplementary Figure 2. a-b): Eigenvalues λ_i of the covariance matrix for the data $\mathbf{X}$ (blue markers) together with the noise floor (largest eigenvalue of $\mathbf{X}_{\text{shuffled}}$-orange line) for the two-beads model (a) and the filamentous network (b). In panels (a) and (b) the noise level on the image is 10%. c-d): Decrease (absolute value) of the autocorrelation function of principal component coefficients after one time-step at different noise levels for the two-bead model (c) and the filamentous network (d). The solid line indicates the 25% level used in our criterion. Panel a-c (Panel b-d): same simulation parameters as Fig. 2 (Fig. 3) of the main text.

3) Dimension of the physical phase space

For a physical system $\mathbf{x}(t)$ with d observable degrees of freedom, the ideal images of the system $\bar{\mathcal{I}}(t)$ form a d-dimensional manifold in the $(L \times W)$-dimensional image space. The registered images $\mathcal{I}(t)$, which include the measurement noise, lie in a neighborhood of the manifold. For this reason it may be possible to project the image-trajectory on a d-dimensional linear subspace, without loosing information about the original dynamics of $\mathbf{x}(t)$. To determine this linear subspace we perform PCA on the whole image set and order the principal modes according to their variance. Because of the curvature of the manifold such analysis may not reveal the physical phase space dimension d.

To resolve this problem we randomly choose an image $\mathcal{I}(t_0)$ and look for all the points of the image trajectory lying in a sphere of radius r around it. Having found the set $B_r[\mathcal{I}(t_0)] = \{\mathcal{I}(t) : \|\mathcal{I}(t_0) - \mathcal{I}(t)\|^2 \leq r^2\}$ we proceed to perform a local version of PCA on the sets $B_r[\mathcal{I}(t_0)]$. As we decrease the radius r, we begin to probe the manifold in a region where it is approximately flat. Consequently, we observe a gap appearing in the plot of the eigenvalues of the covariance matrix (see Supplementary Fig. 3), indicating the actual dimension of the manifold.

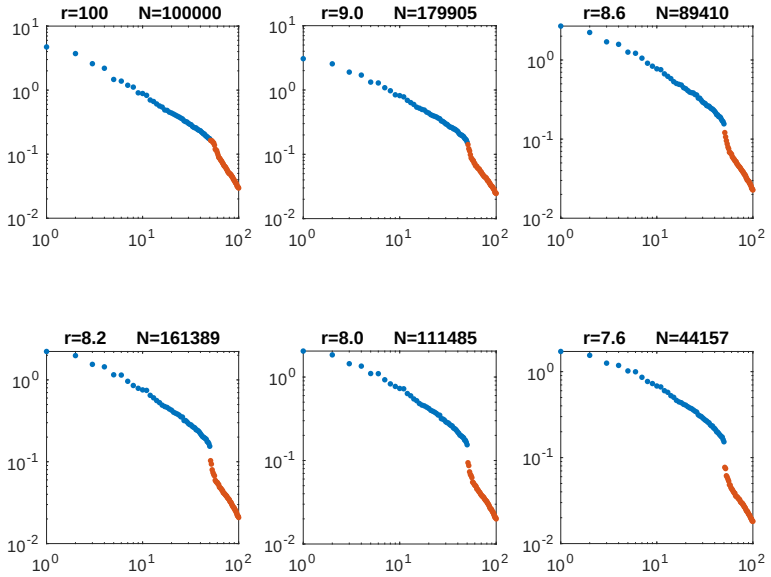

Supplementary Figure 3. Plots of the variances of the first 100 local PCA modes calculated for N images inside a sphere $B_r[\mathcal{I}(t_0)]$. The images used here represent the dynamics of the 5×5 network (50 degrees of freedom). The variances of the first 50 principal components are plotted in blue, the remaining ones in red. The distribution of the variances of the modes changes as we decrease the radius of the sphere r. For small radii a gap appears at the 50th mode.

VI. PATCHING PROCEDURE FOR FORCE INFERENCE

In this section, we briefly outline the patching procedure that allowed us to improve force inference for the network and make the approach scalable to large systems. First, we tessellate every frame of our movie into 25 disjoint patches, as shown in white in Supplementary Fig. 4. To infer forces inside a patch (for example the red patch in Supplementary Fig. 4), we learn the dynamics of a slightly larger region (indicated in blue in Supplementary Fig. 4. This region approximately encloses the parts of the image that interacts with those inside the patch. We then compare the inferred force field in the smaller patch (red in Supplementary Fig. 4). Repeating this procedure for every patch yields the plot of Fig. 3i of the main text.

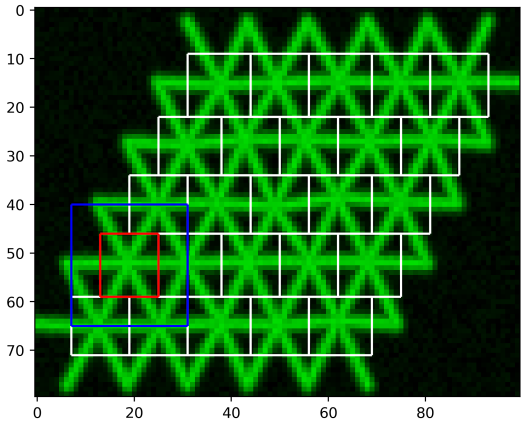

Supplementary Figure 4. Schematic of the patching procedure: The 25 patches in which every frame of the movie is divided are indicated in white. The dynamics is learned inside a larger blue patch and forces inferred in the smaller red patch (see Fig. 3h of the main text for the force pixel map in this patch).

[1] Ghanta, A., Neu, J. C. & Teitsworth, S. Fluctuation loops in noise-driven linear dynamical systems. *Physical Review E* **95**, 032128 (2017).

[2] Mura, F., Gradziuk, G. & Broedersz, C. P. Nonequilibrium Scaling Behavior in Driven Soft Biological Assemblies. *Physical Review Letters* **121**, 038002 (2018).

[3] Gonzalez, J. P., Neu, J. C. & Teitsworth, S. W. Experimental metrics for detection of detailed balance violation. *Physical Review E* **99**, 022143 (2019).

[4] Gradziuk, G., Mura, F. & Broedersz, C. P. Scaling behavior of nonequilibrium measures in internally driven elastic assemblies. *Physical Review E* **99**, 052406 (2019).

[5] Frishman, A. & Ronceray, P. Learning force fields from stochastic trajectories. *arXiv:1809.09650 [cond-mat]* (2019). ArXiv: 1809.09650.

[6] Berman, G. J., Choi, D. M., Bialek, W. & Shaevitz, J. W. Mapping the stereotyped behaviour of freely moving fruit flies. *Journal of The Royal Society Interface* **11**, 20140672 (2014).

Conclusions

This thesis focused on detecting, quantifying, and interpreting the non-equilibrium features of soft living matter. Inspired by cellular structures such as the actin cytoskeleton, we studied the stochastic, non-equilibrium dynamics of model viscoelastic networks via the cycling frequencies, the area enclosing rates between pairs of mesoscopic coordinates, as well as via the entropy production rate, a direct measure of time-irreversibility.

In Chapter 2 – *Non-equilibrium dynamics in living systems: topical review* – we reviewed progress made in recent years in detecting and quantifying non-equilibrium activity in living systems. We stressed that, although these systems break detailed balance via energy consumption at the molecular scale, their active behavior is not always manifestly irreversible at the larger scales relevant for biological functions. Hence, there is a need for reliable methods of activity detection at the mesoscopic scale. One of these methods relies on the idea of measuring violations of the Fluctuation Dissipation Theorem. Although its applications range from hair bundles inside the frog inner ear [101, 102], to the cytoplasm of live cells [42, 103], this technique requires external manipulation of the examined physical system. Promising alternatives to this approach stem from the field of 'Stochastic Thermodynamics' [52]. The goal of this recently developed field is to define thermodynamic quantities such as work, heat, and entropy production at the level of single trajectories. Inspired by the possibility of measuring meaningful physical quantities from single trajectories, a method to quantify broken detailed balance between pairs of mesoscopic observables in a non-invasive fashion was recently introduced in [58]. After reviewing this method and its applications to flagella and cilia in detail, we discussed how a more detailed quantification of non-equilibrium dynamics in motor-activated gels might be possible by measuring the cycling frequencies [62]. We noted, however, how further research was needed to highlight the link between the underlying physical properties of these gels and the cycling frequencies.

In Chapter 3 – *Nonequilibrium dynamics of isostatic spring networks* – we addressed the question of how the cycling frequencies between pairs of mesoscopic observables are informative of the underlying mechanical structure of the system. By employing a model of a disordered viscoelastic network driven by motors, we found that the distance from the zero-temperature isostatic threshold governs the scaling behavior of cycling frequencies at short, nearest-neighbors' scales, as well as at the larger scales. Therefore, we established an explicit link between the different elastic regimes of a our system and its non-equilibrium dynamics. Importantly,

experiments have found that an interplay between motor activity and connectivity can drive actomyosin assemblies into a critically connected state reminiscent of an isostatic state [104, 105]. Although our approach to this problem is still mainly conceptual, measurements of cycling frequencies require no external manipulation and could, therefore, be possibly employed in fragile biological essays to assess the underlying mechanical state of the system.

As shown in Chapter 1 and in [65, 66], the cycling frequencies are related to a 'reduced' entropy production rate between pairs of coordinates. Despite being difficult to interpret it physically, this reduced entropy production rate provides a lower bound to the full entropy production of the system. Future research could then study how the reduced and the full entropy production rate are affected by the system's connectivity. If successful, this research could shed light on the connection between the level of dissipation and the internal structure of biological assemblies and could help to conceive design principles to construct Brownian machines that perform work efficiently [106–108].

Finally, in Chapter 4 – *Learning the nonequilibrium dynamics of "Brownian movies"* – we took a radical approach to the study of stochastically-driven, non-equilibrium systems: we showed how it is possible to infer a lower bound to the entropy production rate and to infer the forces acting on a model viscoelastic network directly from a Brownian movie. Our approach is based on a principled way of finding image-modes (Dissipative Component Analysis-DCA) that retains maximal dissipation. By projecting the image-dynamics onto these components we were not only able to reduce dimensionality and to infer the entropy production rate, but also to infer the force field in component space. By transforming the force field back to image space we constructed pixel force-maps that visually represent the deterministic forces acting on the system. However, it is still unclear how to obtain the physical forces acting on the system from these pixel-force maps. Finally, we exploited local interactions in the systems examined here to make our force-inference approach scalable to large multi-component systems.

Extensions of this research that connect back to the work of Chapter 3 are imaginable: Will DCA still perform well and reconstruct a consistent fraction of the entropy produced when analyzing Brownian movies of diluted networks? Will our force-inference method detect different elastic regimes as the connectivity is varied? And will it be possible, from the movie, to measure the elastic moduli of the network in the fully connected state, as well as when connectivity is varied?

Our Brownian-movie analysis mainly examined systems that exhibit small fluctuations of their components around the rest state, rather than exhibiting macroscopic collective flow typical of other active matter systems [3]. Despite jammed states of active matter being reminiscent of the type of dynamics analyzed here [109–111], extending our movie-based approach to flowing systems would be of great interest and could help to characterize, for example, the types of interactions between

the system's components. Moreover, our approach could be used to distinguish between systems driven by temperature inhomogeneities combined with conservative forces (such as classical elastic interactions considered here), from those driven by non-conservative forces (such as active Brownian particles or driven colloids), thus identifying the source of activity in the system. In the current era of Big Data, in which large amounts of image-microscopy data of living systems' dynamics are readily available, our method constitutes a reliable way of harnessing as much non-equilibrium information as possible from such data and systematically analyzing the dynamics in an efficient, tracking-free, and non-invasive manner.

Bibliography

[1] E. Schrödinger. *What Is Life? The Physical Aspect of the Living Cell*. Cambridge University Press, 1944. (Cit. on p. 1).

[2] S. Ramaswamy. The Mechanics and Statistics of Active Matter. *Annual Review of Condensed Matter Physics* **1**(1), 323–345, 2010. DOI: 10.1146/annurev-conmatphys-070909-104101. (Cit. on p. 1).

[3] M. C. Marchetti, J. F. Joanny, S. Ramaswamy, T. B. Liverpool, J. Prost, M. Rao and R. A. Simha. Hydrodynamics of Soft Active Matter. *Rev. Mod. Phys.* **85**(3), 1143–1189, 2013. DOI: 10.1103/RevModPhys.85.1143. (Cit. on pp. 1, 114).

[4] G. Popkin. The Physics of Life. *Nature News* **529**(7584), 16, 2016. DOI: 10.1038/529016a. (Cit. on p. 1).

[5] É. Fodor and M. Cristina Marchetti. The Statistical Physics of Active Matter: From Self-Catalytic Colloids to Living Cells. *Physica A: Statistical Mechanics and its Applications* **504**, 106–120, 2018. DOI: 10.1016/j.physa.2017.12.137. (Cit. on p. 1).

[6] D. A. Fletcher and R. D. Mullins. Cell Mechanics and the Cytoskeleton. *Nature* **463**(7280), 485–492, 2010. DOI: 10.1038/nature08908. (Cit. on pp. 1–3).

[7] A. Mogilner. Mechanics of Motor Proteins and the Cytoskeleton. *Physics Today* **55**(3), 63–64, 2002. DOI: 10.1063/1.1472396. (Cit. on p. 1).

[8] F. Jülicher, K. Kruse, J. Prost and J. .-.-F. Joanny. Active Behavior of the Cytoskeleton. *Physics Reports* **449**(1), 3–28, 2007. DOI: 10.1016/j.physrep.2007.02.018. (Cit. on p. 1).

[9] F. C. MacKintosh and C. F. Schmidt. Active Cellular Materials. *Current Opinion in Cell Biology* **22**(1), 29–35, 2010. DOI: 10.1016/j.ceb.2010.01.002. (Cit. on p. 1).

[10] J.-F. Joanny and J. Prost. Active Gels as a Description of the Actin-myosin Cytoskeleton. *HFSP Journal* **3**(2), 94–104, 2009. DOI: 10.2976/1.3054712. (Cit. on p. 1).

[11] N. Pavin and I. M. Tolić. Self-Organization and Forces in the Mitotic Spindle. *Annu. Rev. Biophys.* **45**(1), 279–298, 2016. DOI: 10.1146/annurev-biophys-062215-010934. (Cit. on p. 1).

[12] R. Ananthakrishnan and A. Ehrlicher. The Forces Behind Cell Movement. *Int. J. Biol. Sci.* 303–317, 2007. DOI: 10.7150/ijbs.3.303. (Cit. on p. 1).

[13] G. H. Koenderink and E. K. Paluch. Architecture Shapes Contractility in Actomyosin Networks. *Current Opinion in Cell Biology* **50**, 79–85, 2018. DOI: 10.1016/j.ceb.2018.01.015. (Cit. on p. 1).

[14] H. E. Huxley. A Personal View of Muscle and Motility Mechanisms. *Annual Review of Physiology* **58**(1), 1–19, 1996. DOI: 10.1146/annurev.ph.58.030196.000245. (Cit. on p. 1).

[15] M. Murrell, P. W. Oakes, M. Lenz and M. L. Gardel. Forcing Cells into Shape: The Mechanics of Actomyosin Contractility. *Nature Reviews Molecular Cell Biology* **16**(8), 486–498, 2015. DOI: 10.1038/nrm4012. (Cit. on p. 1).

[16] C. Floyd, G. A. Papoian and C. Jarzynski. Quantifying Dissipation in Actomyosin Networks. *Interface Focus* **9**(3), 2019. DOI: 10.1098/rsfs.2018.0078. (Cit. on p. 1).

[17] D. S. Seara, V. Yadav, I. Linsmeier, A. P. Tabatabai, P. W. Oakes, S. M. A. Tabei, S. Banerjee and M. P. Murrell. Entropy Production Rate Is Maximized in Non-Contractile Actomyosin. *Nature Communications* **9**(1), 1–10, 2018. DOI: 10.1038/s41467-018-07413-5. (Cit. on pp. 1, 3).

[18] L. Kurzawa, B. Vianay, F. Senger, T. Vignaud, L. Blanchoin and M. Théry. Dissipation of Contractile Forces: The Missing Piece in Cell Mechanics. *MBoC* **28**(14), 1825–1832, 2017. DOI: 10.1091/mbc.e16-09-0672. (Cit. on pp. 1, 3).

[19] F. S. Gnesotto, F. Mura, J. Gladrow and C. P. Broedersz. Broken Detailed Balance and Non-Equilibrium Dynamics in Living Systems: A Review. *Rep. Prog. Phys.* **81**(6), 066601, 2018. DOI: 10.1088/1361-6633/aab3ed. (Cit. on pp. 1, 4, 5, 10, 11).

[20] A. R. Bausch and K. Kroy. A Bottom-up Approach to Cell Mechanics. *Nature Phys* **2**(4), 231–238, 2006. DOI: 10.1038/nphys260. (Cit. on pp. 2, 3).

[21] K. E. Kasza, A. C. Rowat, J. Liu, T. E. Angelini, C. P. Brangwynne, G. H. Koenderink and D. A. Weitz. The Cell as a Material. *Current Opinion in Cell Biology* **19**(1), 101–107, 2007. DOI: 10.1016/j.ceb.2006.12.002. (Cit. on p. 2).

[22] L. Blanchoin, R. Boujemaa-Paterski, C. Sykes and J. Plastino. Actin Dynamics, Architecture, and Mechanics in Cell Motility. *Physiological Reviews* **94**(1), 235–263, 2014. DOI: 10.1152/physrev.00018.2013. (Cit. on p. 2).

[23] J. Stricker, T. Falzone and M. L. Gardel. Mechanics of the F-Actin Cytoskeleton. *Journal of Biomechanics* **43**(1), 9–14, 2010. DOI: 10.1016/j.jbiomech.2009.09.003. (Cit. on pp. 2, 3).

[24] G. M. Cooper. Microtubules. *The Cell: A Molecular Approach. 2nd edition*, 2000. (Cit. on p. 2).

[25] K. Furuta, A. Furuta, Y. Y. Toyoshima, M. Amino, K. Oiwa and H. Kojima. Measuring Collective Transport by Defined Numbers of Processive and Nonprocessive Kinesin Motors. *PNAS* **110**(2), 501–506, 2013. DOI: 10.1073/pnas.1201390110. (Cit. on p. 3).

[26] C. P. Broedersz and F. C. MacKintosh. Modeling Semiflexible Polymer Networks. *Rev. Mod. Phys.* **86**(3), 995–1036, 2014. DOI: 10.1103/RevModPhys.86.995. (Cit. on p. 3).

[27] M. L. Gardel, K. E. Kasza, C. P. Brangwynne, J. Liu and D. A. Weitz. Chapter 19 Mechanical Response of Cytoskeletal Networks. en. *Methods in Cell Biology*. Vol. 89. Biophysical Tools for Biologists, Volume Two: In Vivo Techniques. Academic Press, Jan. 2008, pp. 487–519. DOI: 10.1016/S0091-679X(08)00619-5. (Cit. on p. 3).

[28] C. Bustamante, Y. R. Chemla, N. R. Forde and D. Izhaky. Mechanical Processes in Biochemistry. *Annual Review of Biochemistry* **73**(1), 705–748, 2004. DOI: 10.1146/annurev.biochem.72.121801.161542. (Cit. on p. 3).

[29] N. Perunov, R. A. Marsland and J. L. England. Statistical Physics of Adaptation. *Phys. Rev. X* **6**(2), 021036, 2016. DOI: 10.1103/PhysRevX.6.021036. (Cit. on p. 3).

[30] G. Lan, P. Sartori, S. Neumann, V. Sourjik and Y. Tu. The Energy–Speed–Accuracy Trade-off in Sensory Adaptation. *Nature Physics* **8**(5), 422–428, 2012. DOI: 10.1038/nphys2276. (Cit. on pp. 3, 9).

[31] M. Balland, A. Richert and F. Gallet. The Dissipative Contribution of Myosin II in the Cytoskeleton Dynamics of Myoblasts. *Eur. Biophys. J.* **34**(3), 255–261, 2005. DOI: 10.1007/s00249-004-0447-7. (Cit. on p. 3).

[32] J. Howard. *Mechanics of Motor Proteins and the Cytoskeleton*. Sinauer Associates, Publishers, 2001. (Cit. on p. 3).

[33] A. D. Mehta, M. Rief, J. A. Spudich, D. A. Smith and R. M. Simmons. Single-Molecule Biomechanics with Optical Methods. *Science* **283**(5408), 1689–1695, 1999. DOI: 10.1126/science.283.5408.1689. (Cit. on p. 3).

[34] A. B. Kolomeisky. Motor Proteins and Molecular Motors: How to Operate Machines at Nanoscale. *J Phys Condens Matter* **25**(46), 2013. DOI: 10.1088/0953-8984/25/46/463101. (Cit. on p. 3).

[35] C. Nardini, É. Fodor, E. Tjhung, F. van Wijland, J. Tailleur and M. E. Cates. Entropy Production in Field Theories without Time-Reversal Symmetry: Quantifying the Non-Equilibrium Character of Active Matter. *Phys. Rev. X* **7**(2), 021007, 2017. DOI: 10.1103/PhysRevX.7.021007. (Cit. on p. 4).

[36] É. Fodor, C. Nardini, M. E. Cates, J. Tailleur, P. Visco and F. van Wijland. How Far from Equilibrium Is Active Matter? *Phys. Rev. Lett.* **117**(3), 038103, 2016. DOI: 10.1103/PhysRevLett.117.038103. (Cit. on p. 4).

[37] D. A. Egolf. Equilibrium Regained: From Nonequilibrium Chaos to Statistical Mechanics. *Science* **287**(5450), 101–104, 2000. DOI: 10.1126/science.287.5450.101. (Cit. on p. 4).

[38] A. Einstein. Über die von der molekularkinetischen Theorie der Wärme geforderte Bewegung von in ruhenden Flüssigkeiten suspendierten Teilchen. *Annalen der Physik* **vol. 4, t. 17**, 1905. (Cit. on pp. 4, 78).

[39] M. von Smoluchowski. Zur Kinetischen Theorie Der Brownschen Molekularbewegung Und Der Suspensionen. 1906. DOI: 10.1002/andp.19063261405. (Cit. on p. 4).

[40] R. Kubo. The Fluctuation-Dissipation Theorem. *Rep. Prog. Phys.* **29**(1), 255–284, 1966. DOI: 10.1088/0034-4885/29/1/306. (Cit. on p. 4).

[41] D. Mizuno, C. Tardin, C. F. Schmidt and F. C. MacKintosh. Nonequilibrium Mechanics of Active Cytoskeletal Networks. *Science* **315**(5810), 370–373, 2007. DOI: 10.1126/science.1134404. (Cit. on pp. 5, 81).

[42] M. Guo, A. J. Ehrlicher, M. H. Jensen, M. Renz, J. R. Moore, R. D. Goldman, J. Lippincott-Schwartz, F. C. Mackintosh and D. A. Weitz. Probing the Stochastic, Motor-Driven Properties of the Cytoplasm Using Force Spectrum Microscopy. *Cell* **158**(4), 822–832, 2014. DOI: 10.1016/j.cell.2014.06.051. (Cit. on pp. 5, 81, 82, 113).

[43] A. W. C. Lau, B. D. Hoffman, A. Davies, J. C. Crocker and T. C. Lubensky. Microrheology, Stress Fluctuations, and Active Behavior of Living Cells. *Phys. Rev. Lett.* **91**(19), 198101, 2003. DOI: 10.1103/PhysRevLett.91.198101. (Cit. on p. 5).

[44] M. Gardel, M. Valentine and D. Weitz. Microrheology. en. *Microscale Diagnostic Techniques*. Ed. by K. S. Breuer. Springer, Berlin, Heidelberg, 2005, pp. 1–49. DOI: 10.1007/3-540-26449-3_1. (Cit. on p. 5).

[45] D. Wirtz. Particle-Tracking Microrheology of Living Cells: Principles and Applications. *Annual Review of Biophysics* **38**(1), 301–326, 2009. DOI: 10.1146/annurev.biophys.050708.133724. (Cit. on p. 5).

[46] S. Yamada, D. Wirtz and S. C. Kuo. Mechanics of Living Cells Measured by Laser Tracking Microrheology. *Biophysical Journal* **78**(4), 1736–1747, 2000. DOI: 10.1016/S0006-3495(00)76725-7. (Cit. on p. 5).

[47] J. Alcaraz, L. Buscemi, M. Grabulosa, X. Trepat, B. Fabry, R. Farré and D. Navajas. Microrheology of Human Lung Epithelial Cells Measured by Atomic Force Microscopy. *Biophysical Journal* **84**(3), 2071–2079, 2003. DOI: 10.1016/S0006-3495(03)75014-0. (Cit. on p. 5).

[48] A. J. Levine and F. C. MacKintosh. The Mechanics and Fluctuation Spectrum of Active Gels. *J. Phys. Chem. B* **113**(12), 3820–3830, 2009. DOI: 10.1021/jp808192w. (Cit. on p. 5).

[49] C. Semmrich, T. Storz, J. Glaser, R. Merkel, A. R. Bausch and K. Kroy. Glass Transition and Rheological Redundancy in F-Actin Solutions. *PNAS* **104**(51), 20199–20203, 2007. DOI: 10.1073/pnas.0705513104. (Cit. on p. 5).

[50] P. Bursac, G. Lenormand, B. Fabry, M. Oliver, D. A. Weitz, V. Viasnoff, J. P. Butler and J. J. Fredberg. Cytoskeletal Remodelling and Slow Dynamics in the Living Cell. *Nature Materials* **4**(7), 557–561, 2005. DOI: 10.1038/nmat1404. (Cit. on p. 5).

[51] A. Crisanti and F. Ritort. Violation of the Fluctuation–Dissipation Theorem in Glassy Systems: Basic Notions and the Numerical Evidence. *J. Phys. A: Math. Gen.* **36**(21), R181–R290, 2003. DOI: 10.1088/0305-4470/36/21/201. (Cit. on p. 5).

[52] U. Seifert. Stochastic Thermodynamics, Fluctuation Theorems and Molecular Machines. *Rep. Prog. Phys.* **75**(12), 126001, 2012. DOI: 10.1088/0034-4885/75/12/126001. (Cit. on pp. 6–8, 13, 79, 113).

[53] K. Sekimoto. *Stochastic Energetics*. en. Lecture Notes in Physics. Springer-Verlag, Berlin Heidelberg, 2010. DOI: 10.1007/978-3-642-05411-2. (Cit. on p. 7).

[54] É. Roldán and J. M. R. Parrondo. Entropy Production and Kullback-Leibler Divergence between Stationary Trajectories of Discrete Systems. *Phys. Rev. E* **85**(3), 031129, 2012. DOI: 10.1103/PhysRevE.85.031129. (Cit. on p. 9).

[55] É. Roldán and J. M. R. Parrondo. Estimating Dissipation from Single Stationary Trajectories. *Phys. Rev. Lett.* **105**(15), 150607, 2010. DOI: 10.1103/PhysRevLett.105.150607. (Cit. on p. 9).

[56] D. Collin, F. Ritort, C. Jarzynski, S. B. Smith, I. Tinoco and C. Bustamante. Verification of the Crooks Fluctuation Theorem and Recovery of RNA Folding Free Energies. *Nature* **437**(7056), 231–234, 2005. DOI: 10.1038/nature04061. (Cit. on p. 9).

[57] J. Liphardt, S. Dumont, S. B. Smith, I. Tinoco and C. Bustamante. Equilibrium Information from Nonequilibrium Measurements in an Experimental Test of Jarzynski's Equality. *Science* **296**(5574), 1832–1835, 2002. DOI: 10.1126/science.1071152. (Cit. on p. 9).

[58] C. Battle, C. P. Broedersz, N. Fakhri, V. F. Geyer, J. Howard, C. F. Schmidt and F. C. MacKintosh. Broken Detailed Balance at Mesoscopic Scales in Active Biological Systems. *Science* **352**(6285), 604–607, 2016. DOI: 10.1126/science.aac8167. (Cit. on pp. 10, 11, 113).

[59] C. Gardiner. *Stochastic Methods: A Handbook for the Natural and Social Sciences*. en. 4th ed. edition. Springer Series in Synergetics. Springer-Verlag, Berlin Heidelberg, 2009. (Cit. on pp. 9, 10).

[60] A. W. C. Lau and T. C. Lubensky. State-Dependent Diffusion: Thermodynamic Consistency and Its Path Integral Formulation. *Phys. Rev. E* **76**(1), 011123, 2007. DOI: 10.1103/PhysRevE.76.011123. (Cit. on pp. 10, 80).

[61] J. B. Weiss. Coordinate Invariance in Stochastic Dynamical Systems. *Tellus A* **55**(3), 208–218, 2003. DOI: 10.1034/j.1600-0870.2003.00014.x. (Cit. on pp. 11, 12).

[62] J. Gladrow, N. Fakhri, F. C. MacKintosh, C. F. Schmidt and C. P. Broedersz. Broken Detailed Balance of Filament Dynamics in Active Networks. *Phys. Rev. Lett.* **116**(24), 248301, 2016. DOI: 10.1103/PhysRevLett.116.248301. (Cit. on pp. 11, 13, 113).

[63] F. S. Gnesotto, B. M. Remlein and C. P. Broedersz. Nonequilibrium Dynamics of Isostatic Spring Networks. *Phys. Rev. E* **100**(1), 013002, 2019. DOI: 10.1103/PhysRevE.100.013002. (Cit. on pp. 11, 58, 60, 61).

[64] F. Mura, G. Gradziuk and C. P. Broedersz. Mesoscopic Non-Equilibrium Measures Can Reveal Intrinsic Features of the Active Driving. *Soft Matter* **15**(40), 8067–8076, 2019. DOI: 10.1039/C9SM01169B. (Cit. on pp. 11, 60, 64).

[65] F. Mura, G. Gradziuk and C. P. Broedersz. Nonequilibrium Scaling Behavior in Driven Soft Biological Assemblies. *Phys. Rev. Lett.* **121**(3), 038002, 2018. DOI: 10.1103/PhysRevLett.121.038002. (Cit. on pp. 11, 60, 62, 64, 114).

[66] G. Gradziuk, F. Mura and C. P. Broedersz. Scaling Behavior of Nonequilibrium Measures in Internally Driven Elastic Assemblies. *Phys. Rev. E* **99**(5), 052406, 2019. DOI: 10.1103/PhysRevE.99.052406. (Cit. on pp. 11, 13, 60, 64, 114).

[67] A. Frishman and P. Ronceray. Learning Force Fields from Stochastic Trajectories. *arXiv:1809.09650 [cond-mat]*, 2019. arXiv: 1809.09650 [cond-mat]. (Cit. on pp. 11, 78, 80, 86).

[68] A. Ghanta, J. C. Neu and S. Teitsworth. Fluctuation Loops in Noise-Driven Linear Dynamical Systems. *Phys. Rev. E* **95**(3), 032128, 2017. DOI: 10.1103/PhysRevE.95.032128. (Cit. on p. 11).

[69] J. P. Gonzalez, J. C. Neu and S. W. Teitsworth. Experimental Metrics for Detection of Detailed Balance Violation. *Phys. Rev. E* **99**(2), 022143, 2019. DOI: 10.1103/PhysRevE.99.022143. (Cit. on pp. 11, 64).

[70] F. S. Gnesotto, G. Gradziuk, P. Ronceray and C. P. Broedersz. Learning the Non-Equilibrium Dynamics of Brownian Movies. *arXiv:2001.08642 [cond-mat, physics:physics]*, 2020. arXiv: 2001.08642 [cond-mat, physics:physics]. (Cit. on pp. 11, 64, 78, 84, 85, 87, 90).

[71] A. Crisanti, A. Puglisi and D. Villamaina. Nonequilibrium and Information: The Role of Cross Correlations. *Phys. Rev. E* **85**(6), 061127, 2012. DOI: 10.1103/PhysRevE.85.061127. (Cit. on p. 11).

[72] A. Bérut, A. Imparato, A. Petrosyan and S. Ciliberto. Theoretical Description of Effective Heat Transfer between Two Viscously Coupled Beads. *Phys. Rev. E* **94**(5), 052148, 2016. DOI: 10.1103/PhysRevE.94.052148. (Cit. on p. 11).

[73] H. Risken and T. Frank. *The Fokker-Planck Equation: Methods of Solution and Applications*. en. 2nd ed. edition. Springer Series in Synergetics. Springer-Verlag, Berlin Heidelberg, 1996. DOI: 10.1007/978-3-642-61544-3. (Cit. on p. 11).

[74] A. M. Lyapunov. The General Problem of the Stability of Motion. *International Journal of Control* **55**(3), 531–534, 1992. DOI: 10.1080/00207179208934253. (Cit. on p. 12).

[75] J. Maxwell. On the Calculation of the Equilibrium and Stiffness of Frames. *The London, Edinburgh, and Dublin Philosophical Magazine and Journal of Science* **27**(182), 294–299, 1864. DOI: 10.1080/14786446408643668. (Cit. on p. 54).

[76] T. C. Lubensky, C. L. Kane, X. Mao, A. Souslov and K. Sun. Phonons and Elasticity in Critically Coordinated Lattices. *Rep. Prog. Phys.* **78**(7), 073901, 2015. DOI: 10.1088/0034-4885/78/7/073901. (Cit. on p. 55).

[77] C. L. Kane and T. C. Lubensky. Topological Boundary Modes in Isostatic Lattices. *Nature Phys* **10**(1), 39–45, 2014. DOI: 10.1038/nphys2835. (Cit. on p. 55).

[78] C. P. Broedersz, X. Mao, T. C. Lubensky and F. C. MacKintosh. Criticality and Isostaticity in Fibre Networks. *Nature Phys* **7**(12), 983–988, 2011. DOI: 10.1038/nphys2127. (Cit. on pp. 56, 62, 63).

[79] M. F. Thorpe. Rigidity Percolation in Glassy Structures. *Journal of Non-Crystalline Solids* **76**(1), 109–116, 1985. DOI: 10.1016/0022-3093(85)90056-0. (Cit. on p. 56).

[80] M. F. Thorpe. Rigidity Percolation. en. *Physics of Disordered Materials*. Ed. by D. Adler, H. Fritzsche and S. R. Ovshinsky. Institute for Amorphous Studies Series. Springer US, Boston, MA, 1985, pp. 55–61. DOI: 10.1007/978-1-4613-2513-0_5. (Cit. on p. 56).

[81] S. Feng, M. F. Thorpe and E. Garboczi. Effective-Medium Theory of Percolation on Central-Force Elastic Networks. *Phys. Rev. B* **31**(1), 276–280, 1985. DOI: 10.1103/PhysRevB.31.276. (Cit. on pp. 56, 61).

[82] E. J. Garboczi and M. F. Thorpe. Effective-Medium Theory of Percolation on Central-Force Elastic Networks. III. The Superelastic Problem. *Phys. Rev. B* **33**(5), 3289–3294, 1986. DOI: 10.1103/PhysRevB.33.3289. (Cit. on pp. 56, 60).

[83] M. Wyart, H. Liang, A. Kabla and L. Mahadevan. Elasticity of Floppy and Stiff Random Networks. *Phys. Rev. Lett.* **101**(21), 215501, 2008. DOI: 10.1103/PhysRevLett.101.215501. (Cit. on pp. 56, 60).

[84] M. Dennison, M. Sheinman, C. Storm and F. C. MacKintosh. Fluctuation-Stabilized Marginal Networks and Anomalous Entropic Elasticity. *Phys. Rev. Lett.* **111**(9), 095503, 2013. DOI: 10.1103/PhysRevLett.111.095503. (Cit. on p. 56).

[85] M. Sheinman, C. P. Broedersz and F. C. MacKintosh. Actively Stressed Marginal Networks. *Phys. Rev. Lett.* **109**(23), 238101, 2012. DOI: 10.1103/PhysRevLett.109.238101. (Cit. on p. 56).

[86] M. G. Yucht, M. Sheinman and C. P. Broedersz. Dynamical Behavior of Disordered Spring Networks. *Soft Matter* **9**(29), 7000–7006, 2013. DOI: 10.1039/C3SM50177A. (Cit. on p. 56).

[87] H. Turlier, D. A. Fedosov, B. Audoly, T. Auth, N. S. Gov, C. Sykes, J.-F. Joanny, G. Gompper and T. Betz. Equilibrium Physics Breakdown Reveals the Active Nature of Red Blood Cell Flickering. *Nature Phys* **12**(5), 513–519, 2016. DOI: 10.1038/nphys3621. (Cit. on p. 56).

[88] S. Garcia, E. Hannezo, J. Elgeti, J.-F. Joanny, P. Silberzan and N. S. Gov. Physics of Active Jamming during Collective Cellular Motion in a Monolayer. *PNAS* **112**(50), 15314–15319, 2015. DOI: 10.1073/pnas.1510973112. (Cit. on p. 56).

[89] D. Bi, J. H. Lopez, J. M. Schwarz and M. L. Manning. A Density-Independent Rigidity Transition in Biological Tissues. *Nature Phys* **11**(12), 1074–1079, 2015. DOI: 10.1038/nphys3471. (Cit. on p. 56).

[90] C. P. Brangwynne, G. H. Koenderink, F. C. MacKintosh and D. A. Weitz. Nonequilibrium Microtubule Fluctuations in a Model Cytoskeleton. *Phys. Rev. Lett.* **100**(11), 118104, 2008. DOI: 10.1103/PhysRevLett.100.118104. (Cit. on p. 56).

[91] O. J. N. Bertrand, D. K. Fygenson and O. A. Saleh. Active, Motor-Driven Mechanics in a DNA Gel. *Proceedings of the National Academy of Sciences* **109**(43), 17342–17347, 2012. DOI: 10.1073/pnas.1208732109. (Cit. on p. 56).

[92] J. Alvarado, M. Sheinman, A. Sharma, F. C. MacKintosh and G. H. Koenderink. Molecular Motors Robustly Drive Active Gels to a Critically Connected State. *Nature Phys* **9**(9), 591–597, 2013. DOI: 10.1038/nphys2715. (Cit. on p. 56).

[93] T. H. Tan, M. Malik-Garbi, E. Abu-Shah, J. Li, A. Sharma, F. C. MacKintosh, K. Keren, C. F. Schmidt and N. Fakhri. Self-Organized Stress Patterns Drive State Transitions in Actin Cortices. *Science Advances* **4**(6), eaar2847, 2018. DOI: 10.1126/sciadv.aar2847. (Cit. on p. 56).

[94] M. Sheinman, C. P. Broedersz and F. C. MacKintosh. Nonlinear Effective-Medium Theory of Disordered Spring Networks. *Phys. Rev. E* **85**(2), 021801, 2012. DOI: 10.1103/PhysRevE.85.021801. (Cit. on p. 60).

[95] D. J. Jacobs and M. F. Thorpe. Generic Rigidity Percolation in Two Dimensions. *Phys. Rev. E* **53**(4), 3682–3693, 1996. DOI: 10.1103/PhysRevE.53.3682. (Cit. on p. 63).

[96] R. Brown. A Brief Account of Microscopical Observations Made in the Months of June, July and August 1827, *on the Particles Contained in the Pollen of Plants; and on the General Existence of Active Molecules in Organic and Inorganic Bodies. The Philosophical Magazine* **4**(21), 161–173, 1828. DOI: 10.1080/14786442808674769. (Cit. on p. 78).

[97] C. L. Vestergaard, P. C. Blainey and H. Flyvbjerg. Optimal Estimation of Diffusion Coefficients from Single-Particle Trajectories. *Phys. Rev. E* **89**(2), 022726, 2014. DOI: 10.1103/PhysRevE.89.022726. (Cit. on p. 80).

[98] N. Fakhri, A. D. Wessel, C. Willms, M. Pasquali, D. R. Klopfenstein, F. C. MacKintosh and C. F. Schmidt. High-Resolution Mapping of Intracellular Fluctuations Using Carbon Nanotubes. *Science* **344**(6187), 1031–1035, 2014. DOI: 10.1126/science.1250170. (Cit. on p. 81).

[99] C. P. Brangwynne, G. H. Koenderink, F. C. MacKintosh and D. A. Weitz. Cytoplasmic Diffusion: Molecular Motors Mix It Up. *J Cell Biol* **183**(4), 583–587, 2008. DOI: 10.1083/jcb.200806149. (Cit. on p. 81).

[100] C. M. Bishop. *Pattern Recognition and Machine Learning*. Information Science and Statistics. Springer, New York, 2006. (Cit. on p. 84).

[101] P. Martin, A. J. Hudspeth and F. Jülicher. Comparison of a Hair Bundle's Spontaneous Oscillations with Its Response to Mechanical Stimulation Reveals the Underlying Active Process. *PNAS* **98**(25), 14380–14385, 2001. DOI: 10.1073/pnas.251530598. (Cit. on p. 113).

[102] B. Nadrowski, P. Martin and F. Jülicher. Active Hair-Bundle Motility Harnesses Noise to Operate near an Optimum of Mechanosensitivity. *PNAS* **101**(33), 12195–12200, 2004. DOI: 10.1073/pnas.0403020101. (Cit. on p. 113).

[103] C. Wilhelm. Out-of-Equilibrium Microrheology inside Living Cells. *Phys. Rev. Lett.* **101**(2), 028101, 2008. DOI: 10.1103/PhysRevLett.101.028101. (Cit. on p. 113).

[104] J. Alvarado, M. Sheinman, A. Sharma, F. C. MacKintosh and G. H. Koenderink. Molecular Motors Robustly Drive Active Gels to a Critically Connected State. *Nature Physics* **9**(9), 591–597, 2013. DOI: 10.1038/nphys2715. (Cit. on p. 114).

[105] J. Alvarado, M. Sheinman, A. Sharma, F. C. MacKintosh and G. H. Koenderink. Force Percolation of Contractile Active Gels. *Soft Matter* **13**(34), 5624–5644, 2017. DOI: 10.1039/C7SM00834A. (Cit. on p. 114).

[106] I. A. Martínez, É. Roldán, L. Dinis and R. A. Rica. Colloidal Heat Engines: A Review. *Soft Matter* **13**(1), 22–36, 2017. DOI: 10.1039/C6SM00923A. (Cit. on p. 114).

[107] P. Pietzonka and U. Seifert. Universal Trade-Off between Power, Efficiency, and Constancy in Steady-State Heat Engines. *Phys. Rev. Lett.* **120**(19), 190602, 2018. DOI: 10.1103/PhysRevLett.120.190602. (Cit. on p. 114).

[108] I. A. Martínez, É. Roldán, L. Dinis, D. Petrov, J. M. R. Parrondo and R. A. Rica. Brownian Carnot Engine. *Nature Physics* **12**(1), 67–70, 2016. DOI: 10.1038/nphys3518. (Cit. on p. 114).

[109] D. Bi, X. Yang, M. C. Marchetti and M. L. Manning. Motility-Driven Glass and Jamming Transitions in Biological Tissues. *Phys. Rev. X* **6**(2), 021011, 2016. DOI: 10.1103/PhysRevX.6.021011. (Cit. on p. 114).

[110] C. Bechinger, R. Di Leonardo, H. Löwen, C. Reichhardt, G. Volpe and G. Volpe. Active Particles in Complex and Crowded Environments. *Rev. Mod. Phys.* **88**(4), 045006, 2016. DOI: 10.1103/RevModPhys.88.045006. (Cit. on p. 114).

[111] C. Reichhardt and C. J. Olson Reichhardt. Active Matter Transport and Jamming on Disordered Landscapes. *Phys. Rev. E* **90**(1), 012701, 2014. DOI: 10.1103/PhysRevE.90.012701. (Cit. on p. 114).

Acknowledgements

Dear Chase, you have been to me in this journey like Virgilio has been to Dante[1]: my guide. Without you, I could have never made it to the top of the ladder. You have not only taught me how to be a scientist, but your joy, enthusiasm, commitment, and passion for everything you do have made me a better person. For all these reasons, I would like to thank you immensely.
A special Thank You to Federica Mura and Grześ Gradziuk for being such wonderful colleagues, friends and office mates (Grześ). Friends will be friends...
Thank You Enzo for, once again, reading my thesis and for coming all the way to Munich on my defense day.
Thanks to David Brückner, Francesco Gnesotto, Grześ Gradziuk, Isabella Graf, Felix Kempf, Federica Mura, and Joris Messelink for proofreading my thesis. I really appreciate it.
Thanks also to everyone at the wonderful LS Frey/Broedersz for all the discussions, all the fun, and for always making the atmosphere in the group so friendly.
An enormous Thank You to my parents, without whom none of this would have ever been possible. Thank you to my lovely family in Italy, Germany, and Singapore for always supporting me and believing in me.
To the BrochenOll gang in particular, and to all my Friends in Padova, Munich, and all over the world: Thank You for all the wonderful time we spent and will spend together!
Finally, I would like to thank the person with whom I decided to share my life, Lorraine. No matter what I do, where I am or where you are, I know that I can count on you and I will always have your shoulder to lay my head on when I feel like I am falling. Even if I am a little heavy. I love you.

To all of you that I have forgotten to mention, go my sincere apology and my deepest gratitude for everything you have done for me.

1 Dante Alighieri, Divina Commedia (1321).